Imperial College London

Hybridised Energy Storage Systems for Automotive Powertrain Applications

Wasim Sarwar

PhD Thesis

Mechanical Engineering

Supervisors:

Dr Gregory Offer	Imperial College London
Dr Monica Marinescu	Imperial College London
Mr Nick Green	Jaguar Land Rover
Mr Nigel Taylor	Jaguar Land Rover

Declaration of Originality

I hereby declare that this thesis and the work presented herein is my own work except where appropriately referenced or acknowledged.

Signed: Wasim Sarwar **Date**: 29/08/16

Copyright Declaration

The copyright of this thesis rests with the author and is made available under a Creative Commons Attribution Non-Commercial No Derivatives license. Researchers are free to copy, distribute or transmit the thesis on the condition that they attribute it, that they do not use it for commercial purposes and that they do not alter, transform or build upon it. For any reuse or redistribution, researchers must make clear to others the licence terms of this work.

Abstract

This study explores whether the requirements of the Energy Storage System (ESS) in electrified automotive powertrains can be more effectively met by Hybridised Energy Storage Systems (HESS) than by batteries alone, and aims to quantify the benefits. Given their complementary characteristics, this study focuses upon combinations of Lithium-ion Batteries (LIBs) and Supercapacitors (SCs). In order to develop a comprehensive understanding of HESS operation and capabilities, a literature review is conducted and experiments and modelling tools are designed to address knowledge gaps.

The electrochemical and thermal performance of SCs and LIBs is examined in detail, and the amassed knowledge is used to generate modelling tools. Following a review of HESS topologies, a model of a passive HESS is developed through combination of the SC and LIB models. The developed models are validated using experimental data for automotive drive-cycles. The degradation of a HESS is assessed using experimental analysis. The main findings of this study are split into three chapters:

Supercapacitors

This chapter explores the electrochemical and thermal characteristics of SCs and demonstrates how they vary with the operating conditions relevant for latter comparison with LIBs. Particular focus has been placed upon the attributes of SCs which affect their performance in a HESS, namely capacity and resistance variation with operating conditions, heat generation during operation, low temperature performance and performance degradation following extended use.

An understanding of these factors is used to develop a model capable of predicting SC performance over an array of operating conditions, enabling latter combination with a lithium ion battery model to predict HESS behaviour in both cell-level and high voltage systems. An emphasis was placed upon the development of a high fidelity thermal model as the academic literature provided a limited understanding of thermal management and the effect of thermal gradients within SCs. The development of a high fidelity thermal model led to novel findings with respect to heat generation with SCs during operation.

Lithium-ion Batteries

An understanding of the performance and characteristics of LIBs relative to SCs is necessary for the development of an understanding of a HESS. This chapter briefly explains why LIBs are the dominant form of energy storage in electrified passenger vehicles, and subsequently discusses how LIBs function. The relationship between each component within the LIB and its performance is reviewed, and common internal design trade-offs such as material selection and thicknesses are explained. LIB performance variation as a function of operating conditions is subsequently presented and described analytically. This knowledge is used to generate a model to predict battery performance over a range of operating conditions, with a particular focus placed upon performance over an automotive drive-cycle. The developed model enables estimation of internal temperature during use. The causes of long term performance degradation are examined and a summary of degradation methods and their causes is provided.

Hybridised Energy Storage Systems

This chapter investigates whether it is possible to combine supercapacitors suitable for a micro hybrid electric vehicle (mHEV) with high-energy batteries suitable for use in a battery electric vehicle (BEV) to create a Hybridised Energy Storage System (HESS) suitable for use in a hybrid electric vehicle (HEV). A passive HESS topology is investigated due to its low cost and complexity and therefore high reliability. A low cost HESS is found to be capable of meeting the electrical demands

of a HEV during a drive cycle. The operating principles of HESSs are discussed and factors limiting system performance are explored. The performance of the HESS is found to be significantly less temperature dependent than battery-only systems, however the heat generated suggests a requirement for thermal management. A correctly sized HESS is shown to generate less heat than a specialised HPB ESS. The HESS degrades at a similar rate to a specialised HPB. In a HESS, battery resistance rises faster than supercapacitor resistance; as a result, the supercapacitor provides a greater current contribution over time, therefore the energy throughput, temperature rise and rate of degradation of the batteries is reduced.

Acknowledgements

The successful completion of a PhD requires the support of numerous individuals, and I would like to extend genuine gratitude to my academic and industrial supervisors; Dr Gregory Offer, Dr Monica Marinescu, Mr Nick Green and Mr Nigel Taylor. In particular, I would like to thank Dr Gregory Offer for the opportunity to pursue a PhD, and for his guidance, support and availability throughout the previous three years.

I wish to express my gratitude to Dr Monica Marinescu for her technical guidance, for motivation and for her part in creating a fantastic working environment. I wish to thank Nick Green for his support, for his availability to have open and honest discussions on a wide range of topics, and for his expertise which helped to guide the project. Further, I would like to thank Nigel Taylor for his technical and professional guidance during the challenging early stages of the PhD, for his continual positive influence and for sharing his wealth of experience, for which I am greatly appreciative.

In addition, I wish to thank Dr Billy Wu and Dr Marie-Therese von Srbik for valuable discussions with regarding to modelling of electrochemical devices, and Dr Yatish Patel, Dr Vladimir Yufit, Ian Hunt and Timothy Engstrom for their support and assistance with experimentation. I would like to thank all past and present member of the research group for their contribution to a fantastic working environment, and whilst it is not possible to mention you all by name, I wish to extend particular thanks to Yuri, Alex, Ian C, Krishna, Harini, Farid, Masashi, Enrique, Paul, Christoph, Edmund and Teng.

I would like to thank Ioxus, Maxwell and Nesscap for their technical support, for numerous useful discussions and for their participation in joint investigations. In particular, from Ioxus, I would like to thank Dr George Lane & Alex Patsos for their support with degradation data and Chad Hall for his technical and commercial expertise. Of Maxwell, I would like to extend thanks to Priya Bendale & Stefan Werkstetter for their support, and Trisha Kirkham of Nesscap for her drive to help the project.

Great efforts were made by numerous individuals within the Warwick Manufacturing Group to support the project; specifically I would like to thank Dr Stefania Ferrari for her assistance in the creation of half-cells, Dr Michael Lain and Nasrin Khah for their assistance with cell disassembly, and Dr Ravichandra Tangirala for assistance with SC testing. Of JLR, I would like to thank Dr Gael Chouchelamane, Stephen Pickering and Paul Haney for their technical guidance, and Dr Phil Barber for his support.

I would like to thank Jaguar Land Rover, and Innovate UK for project funding, and Ms Jose Freeman for her tireless support through the Knowledge Transfer Partnership procedures, and her professional coaching.

Finally, I would like to thank my fiancée for her motivation, understanding and patience.

Project Outputs

Academic Journal Publications

"*Electro-thermal Modelling of Electrochemical Double-Layer Capacitors*", Journal of Energy Storage (2016), *Authors: Wasim Sarwar, Nick Green, Nigel Taylor, Gregory Offer*

"Experimental analysis of Hybridised Energy Storage Systems for automotive applications", Journal of Power Sources (2016). *Authors: Wasim Sarwar, Timothy Engstrom, Monica Marinescu, Nick Green, Nigel Taylor, Gregory Offer*

Conference Presentations

'**Modelling of Supercapacitors for Automotive Applications**', *Wasim Sarwar, Nick Green, Nigel Taylor, Gregory Offer* - Electrochemical Society (226th Meeting), Cancun, Mexico, 2014

'**High fidelity, multi-dimensional Supercapacitor Thermal Modelling**', *Wasim Sarwar, Nick Green, Nigel Taylor, Gregory Offer* - Supercapacitor USA, Santa Clara, USA, 2014

'**Electro-thermal Supercapacitor Modelling**', *Wasim Sarwar, Nick Green, Nigel Taylor, Gregory Offer* - UK Energy Storage 2015, Birmingham, UK, 2015

'**Hybridised Li-Ion/Supercapacitor Energy Storage Systems',** *Wasim Sarwar, Timothy Engstrom, Monica Marinescu, Nick Green, Nigel Taylor, Gregory Offer* – Modval 13, Lausanne, Switzerland, 2016

Poster Presentations

'The Benefits of Supplementing Lead-acid Batteries with Supercapacitors in Automotive Applications' – Future Powertrain Conference 2015 (Poster Prize), Catapult Energy Storage Conference 2014 (Poster Prize), Imperial College London Research Symposium 2014 (Poster Prize), Energy Futures Lab Annual Lecture 2014, *Authors: Wasim Sarwar, Monica Marinescu, Nick Green, Nigel Taylor, Gregory Offer*

'A Look Inside Supercapacitors: An Electro-thermal Model for Automotive Applications' - International Society of Electrochemistry (65th Meeting), *Authors: Wasim Sarwar, Monica Marinescu, Nick Green, Nigel Taylor, Gregory Offer*

'Hybridised Energy Storage' –Future Powertrain Conference 2016 (Poster Prize), *Authors: Wasim Sarwar, Timothy Engstrom, Monica Marinescu, Nick Green, Nigel Taylor, Gregory Offer*

Awards

"Powering up! Benefits of supplementing batteries with Supercapacitors" – Catapult Energy Storage Conference 2014 – Best Poster (1st Prize)

"Hybridised Energy Storage" – Future Powertrain Conference 2016 – Best Poster (2nd Prize)

"Powering up! Benefits of supplementing lead-acid batteries with Supercapacitors" – Future Powertrain Conference 2015 – Best Poster (2nd Prize)

"Powering up! Benefits of supplementing lead-acid batteries with Supercapacitors"– Imperial College London Research Symposium 2014 – Best Poster (3rd Prize)

Tutorials

Provided over 80 hours of training on the fundamental operating principles of a Supercapacitor, characteristics of commercial Supercapacitors, and electro-thermal modelling of Supercapacitors.

Table of Contents

Declaration of Originality i
Copyright Declaration i
Abstract ii
Acknowledgements iv
Project Outputs v
Academic Journal Publications v
Conference Presentations v
Poster Presentations v
Awards v
Tutorials v
List of Figures x
List of Tables xiv
Nomenclature & Acronyms xvi
1.0 Introduction 1
1.1 The need for alternate energy storage systems in automotive powertrains 1
1.2 Thesis Aims 3
1.2.1 Research Questions and Working Hypothesis 3
1.2.2 Scope of Work 3
1.3 Thesis Structure 4
2.0 Experimental Methodology & Modelling Requirements 6
2.1 Experimental Methodology 6
2.1.1 Cell Setup 6
2.1.2 Experimental Techniques 9
2.2 Modelling Targets and Requirements 12
3.0 Supercapacitors 13
3.1 Introduction 13
3.2 Operating Principle & Factors Affecting Performance 14
3.2.1 Operating Principle 14
3.2.2 Cell Constituents and Internal Structure 15
3.2.3 The Electric Double Layer 17
3.3 Factors Influencing Supercapacitor Performance 20
3.3.1 Variation with Voltage 20
3.3.2 Variation with Temperature 21
3.3.3 Variation with Current 22
3.4 Self Discharge & Degradation 22

3.4.1 Charge redistribution 23
3.4.2 Causes of Self-discharge 24
3.4.3 Degradation Literature Review 25
3.4.4 Independent Degradation Testing 27
3.5 Interim Conclusion 28
3.6 SC Model Development 30
3.6.1 Introduction 30
3.6.2 Heat Transfer Model 30
3.6.3 Electrical Model 33
3.6.4 Heat Generation Model 36
3.7 Model Parameterisation 38
3.7.1 Electrical Model 38
3.7.2 Thermal Model 40
3.7.3 Electro-thermal Model Configuration 40
3.7.4 Experimental Conditions for Validation 41
3.8 Model Results, Validation & Discussion 42
3.8.1 Electrical Model Validation 42
3.8.2 Thermal Model Validation 44
3.8.3 Predicted Internal Temperature 44
3.8.4 Comparison with Existing Works 46
3.9 Modelling Conclusion 48
4.0 Lithium-ion Batteries 49
4.1 Why use Lithium-ion Batteries in Automotive Applications 49
4.2 Principle of Operation 50
4.3 Battery Design 52
4.3.1 Anode 52
4.3.2 Cathode 54
4.3.3 Electrolyte 56
4.3.4 Separator 57
4.3.5 Current Collectors 57
4.3.6 Internal Design 57
4.4 Capability variation with operating conditions 59
4.5 Degradation 61
4.5.1 Anode Degradation 61
4.5.2 Cathode Degradation 65
4.5.3 Degradation in Hybridised Energy Storage Systems 66

4.6 Interim Conclusion 68
4.7 Battery Model Development 68
4.7.1 Models in Literature 68
4.7.2 Developed Model 70
4.7.3 Model Structure 70
4.8 Model Parameterisation & Validation 74
4.8.1 Electrical Model 74
4.8.2 Thermal Model 75
4.8.3 Model Validation 77
4.9 Modelling Conclusion 83
5.0 Hybridised Energy Storage System 85
5.1 Introduction 85
5.2 Evaluation Conditions 86
5.2.1 Drive Cycle Selection 86
5.2.2 Drive Cycle Analysis 87
5.3 System Configuration 88
5.3.1 Passive HESS 89
5.3.2 Semi-active HESS 89
5.3.3 Fully-active HESS 90
5.3.4 Topology Selection 90
5.4 Experimental Setup 90
5.4.1 Cell Selection 90
5.4.2 Equating Lab Scale Test to Module Level 91
5.4.3 Experimental Setup 91
5.5 System Performance 93
5.5.1 HESS Performance Analysis 93
5.5.2 HESS Performance relative to other systems 95
5.5.3 System Specification & Cost 100
5.6 Degradation 101
5.6.1 Capacity Loss & Resistance Rise 102
5.7 Interim Conclusion 105
5.8 HESS Modelling 106
5.8.1 Model Configuration 106
5.8.2 Model Validation 106
5.8.3 System analysis through Simulation 109
5.8.4 Modelling Conclusions 112

5.9 Suitability for use in Automotive Applications 113
6.0 Conclusion & Future Work 115
6.1 Conclusions 115
6.2 Future Work 117
References 119
Appendix 137
A1 – Battery Heat Transfer Area Calculation 137
A2 – Battery Model Electrical Parameters 139

List of Figures

Figure 1: Energy storage system requirements for electrified vehicles which fall under the broad categories of mHEV, HEV, PHEV and BEV. In addition to a numerical quantification of the requirement, a colour scale is used to indicate the most challenging factors in the design of an energy storage system for the particular application. The scale passes from green to red, with green requirements proving the least challenging for traditional battery technology, and red requirements the most challenging. Sources - [1–14] 1
Figure 2: Ragone plot showing the power and energy capability of electrochemical devices. Markers show requirements for electrified vehicle targets as defined by USABC – adapted from [15] 2
Figure 3: Schematic of cell connection using four-terminal sensing, with the potential drop between the terminals of the cell cycler indicated 6
Figure 4: Render of test rig used for 18650 cell testing – Image credit: Timothy Engstrom 7
Figure 5: Variation of contact resistance of pouch cell with surface treatment and tightening torque - [17] 8
Figure 6: (Left) SC voltammogram as scan rate is varied within cell ESW - [24], (Right) Variation of electrode potential limit to determine stability window - [25] 10
Figure 7: Typical EIS plot of a lithium-ion battery- [22,26] 11
Figure 8: Typical equivalent circuit used for fitting of LIB EIS data 12
Figure 9: Simplified illustration of the charging mechanism of a SC. Positive (+) and negative (-) signs indicate regions of charge of opposing polarity. 14
Figure 10: Image of cross section of a Maxwell 650F cell, including an illustration (not to scale) of the repeating element within the jelly roll 15
Figure 11: Schematic of EDL for a quasi-planar electrode – Created using the findings from [47,51,65,66] 18
Figure 12: (A) Variation of normalised capacitance with average pore size, schematic of ion (green) and solvent (blue) arrangement for ions of (B) 2-5nm, (C) 1-2nm, (D) 0.7-1nm – Source [60] 19
Figure 13: Schematic of evolution of the EDL for a sub-nano-meter porous electrode – Created using the findings from [47,51,65,66] 20
Figure 14: Capacitance & resistance variation of a Maxwell BCAP0650 cell with voltage 20
Figure 15: Measured capacitance & resistance variation of a Maxwell BCAP0650 cell with temperature 21
Figure 16: Available capacitance variation with applied current, measured during both a charge and discharge 22
Figure 17: Illustration of charge redistribution as no further charge is applied (left), when additional charge is applied (right) - [86] 23
Figure 18: Voltage decay of SC cells charged to 2.4V and held at constant voltage for varying time periods - [70] 24
Figure 19: Change of cell capacitance over time as cells are aged via holding at voltages from 2.75-4V - [93] 26
Figure 20:Change of capacitance and resistance of positive (a & c) and negative (b & d) electrodes as a result of holding cell at voltages between 2.75-4V, measured using three electrode setup - [93] 26
Figure 21: Capacitance loss (left) and resistance rise (right) following floating testing over a range of voltages at 65℃ presented alongside 120A cycling with 40℃ cell surface temperature for an Ioxus 3000F cell 28
Figure 22: Comparison of capacitance loss (left) and resistance rise (rise) during floating test at 65℃ and 85℃ conducted on an Ioxus 3000F cell 28

Figure 23: Illustration of the structure and discretisation of the jelly-roll in the developed pseudo-3D thermal model – [Top] Partially unwound jelly-roll with grey blocks illustrating the thermal model discretisation [for 'n' x 'm' elements] and a thermal equivalent circuit showing the thermal resistance and capacitance through a single electrode only, [Bottom] Illustration of the thermal connection between material layers, (heat transfer in the Z direction), in the jelly roll at discretisation segment (n-1,m) via a thermal equivalent circuit 32
Figure 24: [a] A generic electrical equivalent circuit model which has been discretised by time domain for the electrical modelling of an EDLC - adapted from Lajnef [117] [b] Highly simplified electrical equivalent circuit model, [c] Selected model to be used during electrical parameterisation, [d] Repeated ionic unit used within semi-physical high fidelity model. 34
Figure 25: Illustration aligning the transmission line ($\tau 1$) and the RC Branches ($\tau 2$ & $\tau 3$) with different degrees of charge saturation within a carbon pore. Illustrations depecit findings of [51,65,66] 35
Figure 26: Reduced schematic of high fidelity semi-physical electrical model. The positive and negative electrode resistor networks are connected at nodes via a repeated electrical circuit which is shown to connect co-ordinates (1,5) and (2,5) on the positive and negative electrodes 36
Figure 27: [a] Spatial current density variation through the jelly-roll whilst at a uniform temperature of 20°C during a 15 second 75A discharge - Top. [b] Radial current density variation through jelly-roll of non-uniform temperature during a 15 second 75A discharge. An artificial radial temperature gradient of 6K between the core and edge of the jelly-roll was applied - Bottom. 41
Figure 28a (Top) - Comparison of measured and simulated voltage of a Maxwell 650F EDLC over a highly transient load-cycle, using the complex model seen in Figure 24c with a constant temperature 43
Figure 29: Temperature rise at the positive terminal for charge and discharge events from 20-100A 44
Figure 30: Predicted temperature distribution within a cell during and following a 100A charge from 0.1-2.7V 44
Figure 31: Predicted radial (left) and axial (right) temperature distributions in the cell from the core to the surface – Presented data taken following 1700s of continuous charging and discharging at 50A with natural convective cooling 45
Figure 32: Comparison of temperature rise at the surface and core of the cell when in constant operation, i.e. continuous charge and discharge at 50A between 1.2-2.7V at 25°C 46
Figure 33: Comparison of temperature rise predicted by the lumped model and pseudo-3D model (positive terminal) when in constant operation, i.e. continuous charge and discharge at 50A between 1.2-2.7V at 25°C 47
Figure 34: Illustration of the internal structure of a cylindrical battery cell at cell and particle scale - [140] 50
Figure 35: Illustration of the internal structure within a lithium ion battery with ion and electron motion indicated for a discharge process – [141] 51
Figure 36: (a) Graphene sheet structure (b) ABAB stacking of graphene sheets –Source: [146] 53
Figure 37: Plot of graphite anode potential vs Li as a function of stoichiometry, with a graphic illustrating – Adapted from [144,147] 54
Figure 38: Raw commodity prices for metals as of January 2016 – Source: [151] 55
Figure 39: Potential of anode, cathode and full cell (Panasonic 18650) where potential of anode and cathode is against a lithium reference, and full cell potential difference is between the anode and cathode. Data acquired experimentally by author through creation of half-cells and discharge at a C/40 rate and 25°C 58
Figure 40: Estimated cost of high-power and high-energy cells in 2020 and 2030 - [168] 59

Figure 41: Capacity variation as a function of temperature and current where temperature is normalised around 25℃ and current is normalised against a C/120 discharge – Presented data acquired experimentally from a Panasonic 18650BD cell 60
Figure 42: OCV variation with temperature - adapted from [177] 61
Figure 43: Illustration of the degradation mechanisms which can occur within a lithium-ion battery - [184] 62
Figure 44: Anode degradation mechanisms - [157] 63
Figure 45: Summary of cathode degradation mechanisms – [157] 65
Figure 46: Typical battery equivalent circuit model –Source: [198] 69
Figure 47: Schematic of utilised equivalent circuit model 70
Figure 48: OCV as a function of state of charge at 25℃ determined through a constant current discharge at a rate of C/120 71
Figure 49: OCV transition between charge OCV and discharge OCV as SoC is varied - [197] 71
Figure 50: Graphical representation of heat transfer model showing the axial and radial discretisation and heat transfer paths 73
Figure 51: Charge curve with current of C/120, C/70 and C/40 between 0-100% SoC (left), and 3-10% SoC (right) where the greatest differences occur 74
Figure 52: Voltage profile during 10% SoC constant current pulse charge profile between 0-100% SoC for RC value estimation 75
Figure 53: Photographs of Panasonic 18650BD cell during various stages of disassembly 77
Figure 54: Comparison of experimental and simulated voltage for parameterised conditions - Experimental Conditions: Repeated application of 2C (6A) pulse load for 10% SoC (297mAh) at 25℃, Initial SoC – 0% 78
Figure 55: (Top) Comparison of experimental and simulated voltage for FTP drive cycle (Cycle 1), Initial SoC – 58%, Initial Temperature - 25℃, (Middle) Current profile of FTP drive cycle (Cycle 1), (Bottom) Residual between experimental and simulated voltage 79
Figure 56: (Top) Comparison of experimental and simulated voltage for battery in a HESS over a drive cycle (Cycle 2), Initial SoC – 25%, Initial Temperature - 25℃, (Middle) Current profile of a battery in a HESS over the FTP drive cycle (Cycle 2), (Bottom) Residual between experimental and simulated voltage 80
Figure 57: (Top) Comparison of experimental and simulated voltage for battery in a HESS over a drive cycle (Cycle 2), Initial SoC – 31%, Initial Temperature - 25℃, (Bottom) Residual between experimental and simulated voltage 81
Figure 58: (a) Comparison of experimentally determined and simulated surface temperature for a battery in a HESS over a drive cycle (Cycle 2), Initial SoC – 25%, Initial Temperature - 25℃ (b) Residual of surface temperatures 82
Figure 59: Plot of simulated temperature at the positive and negative terminal and at the core of the jelly-roll during cycle 2 82
Figure 60: Temperature distribution across the radial cross section of a battery cell during a 5C discharge predicted by (a) the developed model, (b) Somasundaram model - [225] 83
Figure 61: (a) Current request of a HEV during the NEDC drive cycle – orange line indicates the RMS current (25A), (b) Current request of a HEV during the FTP-72 drive cycle – orange line indicates the RMS current (28.5A), (c) Voltage evolution of a high power battery cell during the FTP drive cycle – Initial Conditions: 3.68V, 25℃ 87
Figure 62: Schematic of (a) Passive HESS Topology (b) Battery semi-active HESS Topology (c) SC semi-active HESS Topology (d) Fully active HESS Topology – Adapted from [261,262] 88

Figure 63: (a) Schematic of lab scale HESS (b) Photograph of lab scale HESS experimental setup (c) Comparative analysis of battery temperature in the HESS using I2KF SCs with and without the active thermal management system (ATM) operational 93
Figure 64: Comparison of HESS and battery current for 5 second square wave current pulses (top) and over the FTP drive-cycle (bottom). 'Battery current' denotes the total current provided by both cells. HESS uses I3kF SCs, operated at 25℃ with an initial voltage of 3.49V 94
Figure 65: (Top) Experimentally determined performance map showing the ability of different energy storage systems to meet the requirements of the FTP drive cycle in a hybrid electric vehicle as a function of state of charge, number of cells in parallel, temperature, and in the case of the HESS, capacitor size. Different shades of blue show the performance of the high power battery, different shades of red show the performance of the HESS, and different shades of green show the performance of the high energy battery system. Active thermal management system is used. (Bottom) Total current provided by batteries in HESS over the FTP drive cycle at different operating temperatures 96
Figure 66: (a) Battery current comparison between HESS using 2000F and 3000F Capacitors and high-energy cells in 8P configuration – Initial Conditions: 3.49V, 25℃, ATM on (b) Histograms showing the current distribution from a single battery within the HEB ESS in the 8P configuration (left) and a single battery in the I3kF HESS (right) 98
Figure 67: Battery temperatures at the negative terminal – Initial Conditions: HESS and HEB systems at 3.49V and HPB at 3.57V (corresponding to midpoint of usable SoC at 10℃), both systems at 25℃ 99
Figure 68: Comparison of new and aged cells through EIS: EIS Plots (Top) of HESS (inset shows the equivalent circuit to which data was fitted), (Mid-Left) HPB, (Mid-Right) HEB, (Bottom) Temperature and current over the FTP drive cycle at various stages of cell aging 104
Figure 69: HESS model structure in Simulink 106
Figure 70: Comparison of simulated and experimentally determined HESS (3000F SCs) voltage (Top), with a plot of voltage error (Bottom), during FTP drive cycle following the current profile shown in Figure 61b – Initial Conditions: SoC – 31%, Temperature - 25℃ 108
Figure 71: Comparison of simulated and experimentally determined battery current within the HESS (3000F SCs), during FTP drive cycle following the current profile shown in Figure 61b. – Initial Conditions: SoC – 31%, Temperature - 25℃ 108
Figure 72: Comparison of simulated and experimentally determined battery temperature within the HESS (3000F SCs), during FTP drive cycle following the current profile shown in Figure 61b. – Initial Conditions: SoC – 31%, Temperature - 25℃ 109
Figure 73: (Left) Available energy capacity between 281-186V, (Right) Gravimetric energy capacity with the application of a 12A load – Source: HESS and P18650BD data from simulation, Saft VL6P data acquired from experimentation 110
Figure 74: 5 second pulse power resulting in a minimum efficiency of 80% - HESS & P18650BD data from model, Saft data from experimental analysis – Initial conditions - 25℃ 111
Figure 75: HESS configuration trade-off expressed as a Penrose triangle 113

List of Tables

Table 1: Modelling Targets 12
Table 2: Summary of causes of SC degradation – Sources: [54,80,94–96] 25
Table 3: List of tests complete to evaluate degradation, *surface temperature, internal temperature is assumed to be higher 27
Table 4: Parameter values used in electrical model for Maxwell 650F Cell at 25℃ 39
Table 5: Material properties for the parameterisation of the thermal model 40
Table 6: Maximum cell temperature and maximum temperature difference for charging currents from 75-400A 45
Table 7: Comparison of temperature gradients predicted by this study with experimental works conducted by Gualous et al [106] 46
Table 8: Cell mass and volume required to replicate the performance of mHEV with a usable energy of 240Wh and power of 12kW that satisfies IEC standard 60038 50
Table 9: Overview of cathode material attributes for commercialised technologies – adapted from [144] ,[15] and [143] 56
Table 10: A comparison of the attributes of high power and high energy NCA lithium-ion battery cells – Data Sources: Manufacturer supplied datasheets 59
Table 11: Table summarising the causes of degradation at the anode, and factors affecting these causes – Adapted from [157] 64
Table 12: Table summarising the causes of degradation at the cathode, and factors affecting these causes 67
Table 13: Voltage difference as a result of varying current compared to a baseline of C/120 74
Table 14: Jelly-roll parameters used for thermal model 75
Table 15: Measured cell parameters 76
Table 16: Table of parameters used for the generation of Figure 54 78
Table 17: Comparison of peak and RMS battery current over the FTP cycle at 25℃ for each system under consideration 95
Table 18: Experimentally determined effect of temperature on usable SoC range to run the FTP drive – values in brackets show difference between minimum and maximum SoC 97
Table 19: Cumulative heat generation for each ESS over the FTP drive cycle - Initial Conditions: HESS and HEB systems at 3.49V and HPB at 3.57V (corresponding to midpoint of usable SoC at 10℃), both systems at 25℃ 99
Table 20: Energy throughput for each ESS during the FTP drive cycle - Initial Conditions: HESS and HEB systems at 3.49V and HPB at 3.57V, temperature of 25℃ with active thermal management system enabled. (* calculated with respect to the ET of each system) 100
Table 21: Specification of modules consisting of HPB, HEB and HESSs using 2000F and 3000F SCs – Usable energy capacity at 25℃ 101
Table 22: Specification of modules consisting of HPB, HEB and HESSs using 2000F and 3000F SCs for higher energy capacity HEVs - Usable energy capacity at 25℃ 101
Table 23: Capacity loss during degradation testing determined via a C/20 discharge 102
Table 24: Series, SEI and Charge Transfer Resistance of new and aged cells, as determined through EIS 102
Table 25: Comparison of HESS (3000F) simulated and experimentally measured minimum and maximum voltage during FTP drive cycle at multiple initial SoC points with an initial temperature of 25℃ 107
Table 26: Table of capacitance, resistance, mass and volume as specified by the manufacturer for I2kF and I3kF SC cells and estimated values for the cell that would provide the equivalent performance to the I3kF when the lab-scale test is up-scaled to the module level 111

Table 27: Measured jelly-roll and can properties for the I2kF and I3kF cells, and estimated values for the cell that would provide the equivalent performance to the I3kF when the lab-scale test is up-scaled to the module level..... 112
Table 28: Comparison of mass and volume of HESS using the I3kF and equivalent cell SCs..... 112
Table 29: Battery Model Electrical Parameters - Capacitor C1 (F), 40℃..... 140
Table 30: Battery Model Electrical Parameters - Capacitor C2 (F), 40℃..... 140
Table 31: Battery Model Electrical Parameters - Capacitor C3 (F), 40℃..... 140
Table 29: Battery Model Electrical Parameters - Capacitor C1 (F), 25℃..... 141
Table 30: Battery Model Electrical Parameters - Capacitor C2 (F), 25℃..... 141
Table 31: Battery Model Electrical Parameters - Capacitor C3 (F), 25℃..... 141
Table 31: Battery Model Electrical Parameters - Resistor R0 (Ω), 40℃..... 142
Table 31: Battery Model Electrical Parameters - Resistor R1 (Ω), 40℃..... 142
Table 31: Battery Model Electrical Parameters - Resistor R2 (Ω), 40℃..... 142
Table 31: Battery Model Electrical Parameters - Resistor R3 (Ω), 40℃..... 143
Table 31: Battery Model Electrical Parameters - Resistor R0 (Ω), 25℃..... 143
Table 31: Battery Model Electrical Parameters - Resistor R1 (Ω), 25℃..... 143
Table 31: Battery Model Electrical Parameters - Resistor R2 (Ω), 25℃..... 144
Table 31: Battery Model Electrical Parameters - Resistor R3 (Ω), 25℃..... 144

Nomenclature & Acronyms

Variable	Units	Variable Description	Variable	Units	Variable Description
A, B		Dimensionless Constant	**k_A**	s^{-1}	Rate of Reaction
BEV		Battery Electric Vehicle	**k_B**	$J\ K^{-1}$	Boltzmann constant
C	F	Capacitance	**k_p**		Peukert Coefficient
C_0	F	Primary Capacitance	**k_T**		Thermal Conductivity
$C_{Branch\ x}$	F	Capacitance of Branch 'x'	**LCO**		$LiCoO_2$
C_{B1},C_{B2}	F	Capacitance of RC Branch 1,2	**LFP**		$LiFePO_4$
$C_{measured}$	F	Measured Capacitance	**Li^+**		Lithium ion
C_p	Ah	Peukert capacity	**LIB**		Lithium-ion Battery
c_p	$kJ\ kg^{-1}\ °C^{-1}$	Specific Heat Capacity	**Li-C**		Lithium Capacitor
C_R	F	Re-distribution Capacitance	**LiMO2**		Lithium Metal Oxide
$C_{RC\ Branch}$	F	RC Branch Capacitance	**LTO**		$LiTi_5O_{12}$
$C_{Transmission_Line}$	F	Transmission Line Capacitance	**mHEV**		micro Hybrid Electric Vehicle
C_V	V^{-1}	Voltage proportionality of Capacitance	**N**		Number of branches
CC		Current Collector	**NCA**		$LiNi_{0.8}Co_{0.15}Al_{0.05}O2$
D		Dimensionless Constant	**NCM**		$LiNi_{0.33}Co_{0.33}Mn_{0.33}O_2$
D	$m^2\ s^{-1}$	Diffusion coefficient	**Ni-Mh**		Nickel Metal Hydride
e	C	Electron charge	**OCV**		Open Circuit Voltage
E_a	$J\ mol^{-1}$	Activation Energy	**PB-A**		Lead-Acid
ECM		Equivalent Circuit Model	**PC**		Propylene Carbonate
ESW		Electrochemical Stability Window	**PE**		Polyethylene
F	$C\ mol^{-1}$	Faradays constant	**PHEV**		Plug-in Hybrid Electric Vehicle
F		Dimensionless Constant	**PP**		Polypropylene
HEB		High Energy battery	**PTC**		Pressure Temperature Current
HESS		Hybridised Energy Storage System	**R_u**	$JK^{-1}\ mol^{-1}$	Universal Gas Constant
HEV		Hybrid Electric Vehicle	**R**	Ω	Resistance
HPB		High Power Battery	**$R_{Branch\ x}$**	Ω	Resistance of branch 'x'
I	A	Current	**$R_{Contact}$**	Ω	Contact resistance
k		Transition speed	R_{leak}	Ω	Leakage resistance

Variable	Units	Variable Description	Variable Subscript	Variable Description
R_{ionic}	Ω	Ionic resistance		
R_{series}	Ω	Series resistance	Ch	Charge
S	$J\ K^{-1}$	Entropy	CC_Thick	Current Collector Thickness
SC		Supercapacitor	Dis	Discharge
SEI		Solid Electrolyte Interphase	El_Axial	Electrode in the y-direction
SEM		Scanning Electron Microscope	El_Spiral	Electrode in the x-direction
SoC		State of Charge	El_Thick	Electrode Thickness
T	°C	Temperature	i	species
t	s	Time	I	Denotes the turn number within the spiral of the jelly-roll
τ	s	Time Constant	irr	Irreversible
Th_{cc}	$J\ kg^{-1}\ °C^{-1}$	Thermal Mass of current collector	J	Denotes the discretisation unit number in the y-direction
Th_{el}	$J\ kg^{-1}\ °C^{-1}$	Thermal Mass of electrode	M	Denotes the number of discretisation units in the y-direction
Th_{sep}	$J\ kg^{-1}\ °C^{-1}$	Thermal Mass of separator	n	Denotes the number of turns of the spiral of the jelly-roll
S_{dl}	$J\ °C^{-1}$	Entropy of double layer	0	Initial condition
V	V	Voltage	OCV	Open Circuit Voltage
v_0	m^{-3}	Volume occupied by the electrolyte in the uncharged state	rev	Reversible
v_H	m^{-3}	Volume occupied by the electrolyte in the charged state	Sep_Thick	Separator Thickness
x		RC Branch Number	terminal	Measured at cell terminal
V	V	Cell potential	X	Denotes RC branch number
Q	J	Heat Generated	X	'x' direction
Q_R		Reaction Quotient	Z	'z' direction
V^0	V	Standard Cell Potential	+	In relation to the positive ion
z		Number of Moles of Electrons	-	In relation the negative ion
α	$°C^{-1}$	Temperature coefficient		
μ		Mobility		
η	V	Over-potential		

1.0 Introduction

1.1 The need for alternate energy storage systems in automotive powertrains

Increasingly stringent CO_2 legislation, the introduction of emissions free zones and customer demand has led to every major automobile manufacturer adopting powertrain electrification to varying degrees across their vehicle portfolio. Electrification reduces or eliminates the power demand placed upon the internal combustion engine by using electric motors to assist or provide vehicle propulsion and/or recapture energy. Different vehicle types pose significantly different demands on an Energy Storage System (ESS); the typical requirements for each vehicle type are summarised in Figure 1.

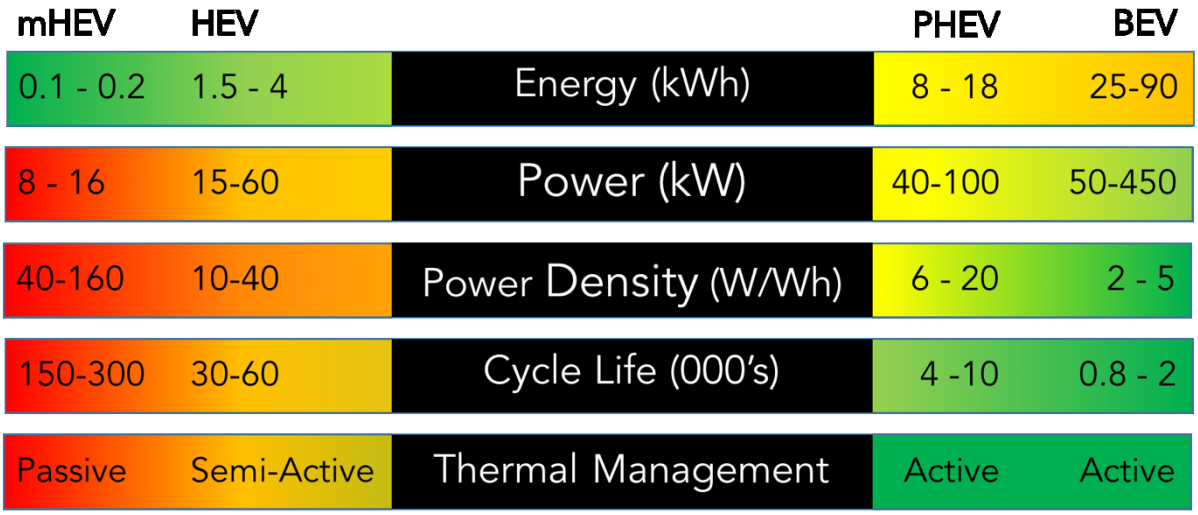


Figure 1: Energy storage system requirements for electrified vehicles which fall under the broad categories of mHEV, HEV, PHEV and BEV. In addition to a numerical quantification of the requirement, a colour scale is used to indicate the most challenging factors in the design of an energy storage system for the particular application. The scale passes from green to red, with green requirements proving the least challenging for traditional battery technology, and red requirements the most challenging. Sources - [1–14]

Vehicles classified as micro Hybrid Electric Vehicles (mHEVs) typically utilise a low voltage (48V) energy storage module to enable high power functions, such as electronic Power Assisted Steering (ePAS) and electric turbocharging (e-turbo), and limited vehicle propulsion assistance. Additionally, the system is used to reduce CO_2 emissions by recapturing waste kinetic energy from the engine, and enabling the engine to be switched off for extended periods of time. The ESS in a mHEV must provide or accept very high power for short time periods with minimal thermal management, therefore it must have the attributes of high power, low energy, large thermal operating window, and high cycle life.

Hybrid Electric Vehicles (HEVs) can be electrically propelled for moderate distances, and whilst the power demand is similar to that of mHEVs, the energy demand is larger, therefore HEVs typically utilise high voltage ESSs (200-450V). The thermal operating window need not be as wide as that of a mHEV as system availability can be actively managed through usage, i.e. electrical power can be limited if the cells are too hot or cold. Additionally, the usage profile dictates a lower cycle requirement than a mHEV as the larger energy capacity ESS is subject to fewer cycles of equal SoC change for a given driving distance. Plug-in Hybrid Electric Vehicles (PHEV) have a similar use-case to HEVs, however they must electrically propel the vehicle for longer distances and therefore require more energy. It is easier to justify thermal management for larger battery packs, therefore the required thermal operating window can be smaller.

Battery Electric Vehicles (BEVs) require significantly more energy and power than PHEVs, consequently larger ESSs are used. As with PHEVs, in a large ESS it is useful to add active thermal management therefore a large thermal operating window is not required. Further, a shorter cycle life is required in order to meet the vehicle life requirements; the greater ESS energy capacity reduces the number of cycles expected during vehicle lifetime.

Figure 2 shows the specific energy and power capability of a range of electrochemical devices and indicates the USABC targets for electrified vehicles. As is evident from the figure, whilst the individual power and energy requirements of each vehicle type can be met by lithium-ion batteries (LIBs), for some vehicle types they cannot be met simultaneously. Consequently, battery packs are typically oversized to meet either the power or energy requirement.

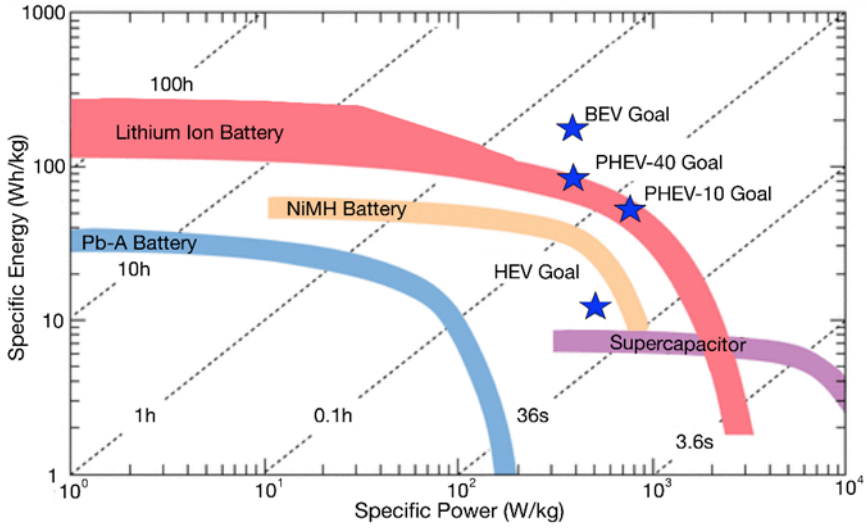


Figure 2: Ragone plot showing the power and energy capability of electrochemical devices. Markers show requirements for electrified vehicle targets as defined by USABC – adapted from [15]

For a HEV, the battery pack can be oversized to meet the power requirement; alternatively, power can be added to the battery pack though the addition of Supercapacitors (SC). An ESS consisting of a combination of LIBs and SCs is commonly referred to as a Hybridised Energy Storage System (HESS). In a HESS, the power and energy capability can be largely decoupled as the batteries provide the majority of the energy capability of the system, whilst the SCs provide the majority of the power capability. It is hypothesised that a combination of high-energy density LIBs combined with SCs will result in an ESS with a higher power density for a targeted energy density than a LIB-only ESS.

Power density in this context is defined as the power capability of an ESS relative to its energy storage capability; power density is a useful metric by which the compare the normalised power capability of different cells, and hence is a key metric in ESS sizing. The term 'C-rate' is often used interchangeably with power density, and defines the rate at which the battery can be charged or discharged relative to the rate which would result in the ESS being fully charged or discharged in a one hour time period.

Whilst this study is limited to intercalation chemistries, it is conducted with consideration of its applicability to conversion chemistries such as Lithium Sulphur (Li-S) and Lithium Air (Li-O_2). Whilst the state-of-the-art intercalation chemistries possess an energy capacity of up to 240Wh/kg, Li-S has achieved 350Wh/kg and is expected to reach 500Wh/kg in the near future, [16]. Conversion cathode chemistries possess poor power capability, therefore are not directly suitable for use in automotive applications, however ESS hybridisation may enable their use.

1.2 Thesis Aims

The performance of electrochemical devices is typically non-linear and highly variable as a function of operating conditions such as SoC and temperature. For instance, the resistance of batteries can increase by two orders of magnitude over the typical range of temperatures experienced in automotive applications, and the capacitance of a SC can vary by 50% as a function of SoC. An understanding of the phenomena which cause these changes enable actions to be taken to promote favourable changes in attributes and supress undesired behaviour. Furthermore, this knowledge can be used to generate models to accurately predict the performance of electrochemical devices over a range of operating conditions. Consequently, the research conducted in this thesis aims to combine the fundamental science involved with the operation of electrochemical devices and the engineering required for practical implementation of an ESS into an automotive environment. The aims of this thesis can be summarised as follows:

- Develop a physical understanding of device operation and degradation
- Create models that can be used to understand HESS performance over a variety of operating conditions
- Quantify the benefits of using a HESS in comparison to a battery-only system

It is intended that the novel contributions of this work to the academic community will include, but not be limited to advancements to SC modelling for engineering applications, quantification of the benefits of realistic HESSs in automotive environments, and a toolset enabling engineers to determine the suitability of HESSs for their application.

1.2.1 Research Questions and Working Hypothesis

The specific research questions motivating this work are:

- Can a HESS consisting of batteries and supercapacitors provide superior performance to battery only systems?
- Which automotive powertrain applications are most suited to the characteristics of a HESS?
- What are the performance limitations of HESSs in automotive applications?

A series of working hypothesis relating to the research questions are outlined below, and at relevant points throughout the thesis, they will be updated to reflect the findings of the author. It is hypothesised that:

- A combination of supercapacitors and high energy batteries can provide superior specific energy and power to a high power battery typically used in automotive applications.
- A HESS will generate less heat and therefore require less thermal management than a battery only system.
- Battery degradation in a HESS will be lower than in a comparable battery only system.
- Automotive OEMs can adopt a modular approach whereby the quantities of a particular SC and battery cells can be scaled for different types of vehicles to meet the requirements.

1.2.2 Scope of Work

Given the diversity of electrochemical devices available, the number of possible combinations of devices and the complexities involved in the operation of each, the following limitations have been applied to the scope of this study:

- Applications of the energy storage system are limited to direct or indirect vehicle propulsion in an electrified powertrain

- The electrochemical devices under consideration for this study are limited to lithium-ion batteries and supercapacitors.
- The developed models must be easily parameterised for a range of cells, and applicable over the typical operating conditions of the vehicles produced by the project sponsor.
- The development of a novel, high-fidelity battery model is beyond the scope of this study; existing knowledge and models should be used to maximise the time available for study of the hybridised energy storage system.
- The conducted degradation activities should enable qualitative comparative analysis – quantitative degradation analysis using a statistically significant number of cells is beyond the scope of the study.
- A single example of a HESS is to be studied – the developed toolset should enable analysis of a range of HESS topologies, using a range of cells, post-project.

1.3 Thesis Structure

To address the research questions, this thesis starts with a comprehensive literature review to explore the state-of-the-art knowledge, and identify the knowledge gaps. Once the knowledge gaps that prevent the research questions being answered have been identified, both experiments and modelling tools are designed to acquire the desired knowledge. The thesis consists of six chapters, and is structured as follows:

- **Chapter 1** – Introduction
  This chapter sets the scene for the context in which the work is to be complete, and explains why the research is valuable.

- **Chapter 2** – Experimental Methodology
  Experimental results are used extensively for model validation and to answer research questions. This chapter describes the techniques used to ensure the experimental results are appropriately controlled, repeatable and accurate. Furthermore, this chapter describes best practise for testing of electrochemical devices.

- **Chapter 3** – Supercapacitors
  A detailed literature review is conducted to describe the principle of operation of a SC, its electrical and thermal performance, and factors which affect degradation. Existing SC modelling is reviewed, and a novel electro-thermal model is created to predict electrical performance and temperature distribution within a cell. Model validation is conducted, and the model is subsequently used to investigate the prevalence of thermal gradients within SC cells during high current operation.

- **Chapter 4** – Lithium Ion Batteries
  A detailed literature review is conducted to describe the principle of operation of LIBs, the differences between high-energy and high-power batteries, the factors which affect their performance, and the physical origins of changes. A comprehensive review of degradation mechanisms is complete. The amassed knowledge is used to generate an electro-thermal model that is capable of predicting electrical performance during a drive cycle and the internal temperature distribution within the battery. The model is validated using experimental data.

- **Chapter 5** – Hybridised Energy Storage Systems

A literature review is conducted of the available HESS topologies and an appropriate topology is selected. The SC and LIB models are combined to create a HESS model, and validation is complete. The HESS model is used alongside experimental analysis to answer the research questions and explain whether the working hypothesis were correct or incorrect.

- **Chapter 6** – Conclusions and Future Outlook
  In this chapter, the findings pertaining specifically to the aims of the thesis are clearly laid out, and future work is discussed.

2.0 Experimental Methodology & Modelling Requirements

2.1 Experimental Methodology

Experimental results are used for system performance analysis, derivation of equations to describe electrochemical phenomena, model parameterisation and model validation, therefore it is imperative that the obtained results are of known accuracy, are repeatable and precise. This section discusses the methodology used to implement different experimental techniques; discussion will include boundary condition control, data acquisition best practise and requirements, and suitability of different experimental techniques for particular applications.

2.1.1 Cell Setup

2.1.1.1 Electrical connections

Electrical connections to the cell are made using the four-terminal sensing or remote sensing method, where a pair of cables are used to carry current whilst a second pair are used to measure voltage. The delivered voltage to the cell is measured through the sense wires; knowledge of the voltage at the desired source enables the cell cycler to compensate for the inevitable losses in cabling and connections. An illustration of the connections for the remote-sensing method are shown in Figure 3.

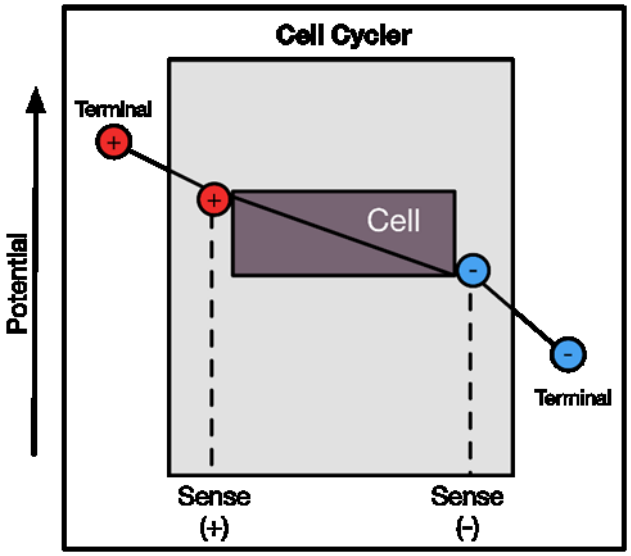


Figure 3: Schematic of cell connection using four-terminal sensing, with the potential drop between the terminals of the cell cycler indicated

The current carrying cables must be of sufficient gauge to not significantly heat up during operating; temperature change of the cable can be estimated analytically using Equation 1-Equation 3. Equation 1 determines the resistance of the cable, and the equation gives insight into good cable design for low resistance, and hence low heat generation. The electrically conductive region of the cable should possess low resistivity and have a large cross sectional area, whilst the cable itself should be short. The resistance of the connectors to the cable is assumed to be small for high quality connectors which have been correctly crimped to the cable. The rate of heat generation is defined by Equation 2, and the resultant temperature change of the cable is given by Equation 3.

$$R = {}^{\rho L}/_{A} \qquad \text{Equation 1}$$

$$\dot{Q} = I^2 R \qquad \text{Equation 2}$$

$$\Delta T = {}^{m c_p}/_{Q} \qquad \text{Equation 3}$$

To measure voltage, the sense cables are connected to a very high resistance circuit, thus very little current runs through these cables enabling the use of low gauge cabling. To minimize errors arising from the magnetic fields produced by cables and noise from electromagnetic interference, these cables should be twisted together, and the distance between the current carrying and voltage sense cables as well as the voltage sense connections should be maximized. The current carrying and sense cables should be connected at different points to include compensation for contact resistances. The connection method used for 18650 battery cells, which a named as such because they are 18mm in diameter, and 65 mm in length, is shown in Figure 4, where each connection is labelled.

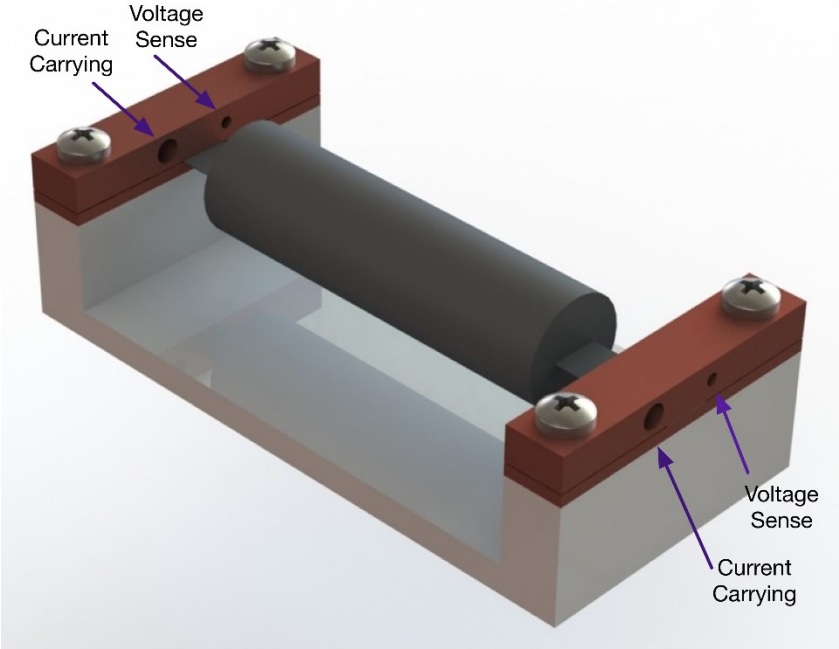


Figure 4: Render of test rig used for 18650 cell testing – Image credit: Timothy Engstrom

For low ESR cells, poorly controlled contact resistances between the cell terminals and external connections can be larger than the cell resistance. The contact resistance is increased by the presence of surface films, high surface roughness and low tightening torque. Figure 5 shows the influence of tightening torque and surface preparation on contact resistance where brass blocks identical to those shown in Figure 4 are used to clamp the terminals of a lithium ion battery pouch cell. Very minor discolouration due to the presence of a surface film is observed on the non-treated brass blocks, whereas the fully treated blocks provided a near mirror finish following polishing with fine grade sandpaper, and cleaning with isopropanol. Figure 5 shows that a fully-treated contact with a tightening torque of 2.5Nm results in a contact resistance below the minimum measureable value of the experimental setup ($2 \times 10^{-6}\,\Omega$), [17].

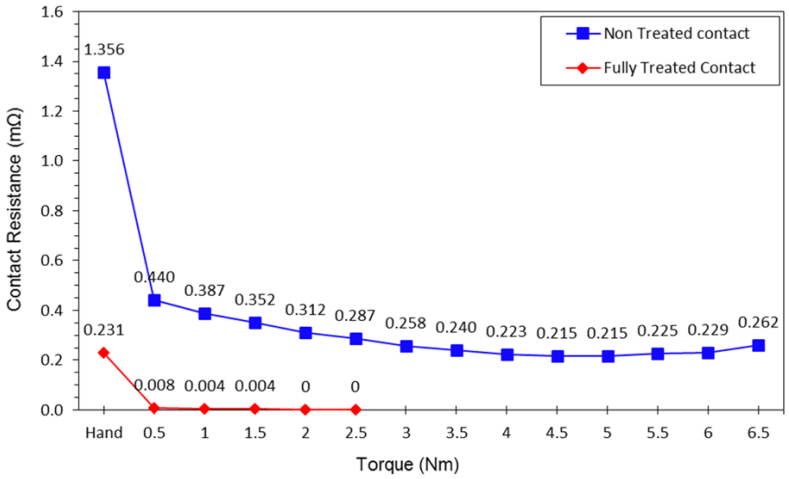


Figure 5: Variation of contact resistance of pouch cell with surface treatment and tightening torque - [17]

2.1.1.2 Thermocouple Connection

Thermocouples utilise the Seebeck effect, in which a potential difference occurs between dissimilar electrically conductive materials at a given temperature. The potential difference generated is a characteristic of the materials involved, enabling a potential difference for given materials to be correlated to a measured temperature. As the temperature measurement is based upon a voltage reading, it is necessary to electrically isolate the thermocouple from the electrical activity of the cell. Therefore, thermocouples are connected to the cell using a thin film of electrically insulating, yet thermally conductive epoxy, using the product TC-2810 from 3M.

According to IEC standard 60584 (Thermocouples – EMF specifications and tolerances) [18], the thermocouple of highest absolute accuracy within the range appropriate for batteries is a 'Class 1 - Type T'. The absolute accuracy of this thermocouple is +/- 0.5^0C over the range of -40 – 350^0C. Relative error however is much smaller; it is dominated by measurement device sensitivity [19]. The resolution of the device used (NI9213 Module with NI Compact DaQ) is 0.02^0C [20], therefore relative temperatures are always used in this study.

2.1.1.3 Thermal Boundary Conditions

Control of thermal boundary conditions is of great importance, and can significantly affect experimental results, [21]. Where low currents are used, and it is intended that the test be conducted under iso-thermal conditions, it is sufficient to place the cell in a thermally controlled chamber ensuring the rate of convection is consistent and a free thermocouple is used to measure the temperature of the thermally controlled environment independently. If the test is not intended to be iso-thermal or is not low current, additional considerations are required.

Heat transfer to the environment occurs as a result of conduction at the electrical interconnects, and convection at the surfaces exposed to the environment. Radiative heat transfer at room temperature for cylindrical cells is negligible. Insulating materials and thermo-electric devices may be used to enable control of thermal boundary conditions; their use is particularly useful during model parameterisation. Convective heat transfer can be largely eliminated through the use of insulating materials such as 'Rockwool' or glass foam. Their use replaces convective heat transfer with conductive heat transfer into the insulating material, though this is at a low and known rate, (<0.5 W/mK). Conductive heat transfer via the electrical connections can be controlled using Peltier elements to either maintain the cell at the desired temperature, maintain the electrical connections at a desired temperature or mimic cell temperature to minimize heat transfer. A detailed description is provided in instances where advanced thermal boundary conditions have been used.

2.1.1.4 Cell Equilibration

For repeatability, typically it is important for the cell to be at equilibrium prior to conducting a test, though this is not universally true. Barai et al [22] demonstrate that the results of Electrochemical Impedance Spectroscopy (EIS) varies significantly as a function of relaxation time. To aid repeatability, all testing conducted in this study utilised a rest time of 4 hours. This was reduced in cases where this was known to be excessive, such as for Cyclic Voltammetry (CV).

Equilibrium must be considered in the both the electrochemical and thermal domains. The cell is at electrochemical equilibrium when the lithium concentration at the particle surface and core have equalised. Thermal equilibrium requires the entire cell to be at the same temperature. The required rest time can be determined through knowledge of the thermal time constant, τ, as calculated in Equation 4, and its use in Newton's law of cooling as per Equation 5. These equations show that the thermal time constant is increased with increasing density (ρ), heat capacity (c_p) and volume (v), and decreased with an increase in heat transfer coefficient (h) and surface area (A_s).

$$\tau = \frac{\rho c_p v}{h A_s} \qquad \text{Equation 4}$$

$$\Delta T(t) = \Delta T_0 e^{-t/\tau} \qquad \text{Equation 5}$$

2.1.2 Experimental Techniques

This section describes the common electrochemical techniques used for data acquisition in this thesis. The typical applications of each technique are discussed as well as the confidence in results produced.

2.1.2.1 Cyclic voltammetry

Cyclic Voltammetry (CV) is a technique commonly used to determine the capacitance and electrochemical stability window of SCs and phase transitions in batteries. CV is a test in which the potential is varied at a defined rate between pre-defined limits and the required current is measured. The voltage (V) varies linearly with the voltage scan rate, v_s, for the forward scan as per Equation 6 and the reverse scan as per Equation 7.

$$V = V_i + v_s t \qquad \text{Equation 6}$$

$$V = V_i - v_s t \qquad \text{Equation 7}$$

In SCs, CV can be used to determine the maximum operating voltage, determine capacitance as a function of voltage and examine kinetic limitations. The CV profile of an ideal capacitor is rectangular, however in SCs where capacitance is a function of voltage, a gradual increase of current is expected during a sweep; current peaks indicate the presence of redox reaction [23]. Figure 6 (Left) shows typical SC voltammograms as the cell is cycled within its Electrochemical Stability Window (ESW). The ESW is defined as the voltage region within which undesired irreversible reactions do not occur, thus for acceptable lifetime, it is necessary to operate within this region. Figure 6 (Right) shows how the introduction of redox peaks as the electrode potential is increased enables determination of the ESW of a SC. The scan rate is related to cell capacitance (C) as per Equation 8.

$$C = \frac{I}{v_s} \qquad \text{Equation 8}$$

CV does not require the use of an extended rest period to obtain repeatable results, however the results of the first cycle should typically be disregarded to enable dynamic equilibrium to be reached.

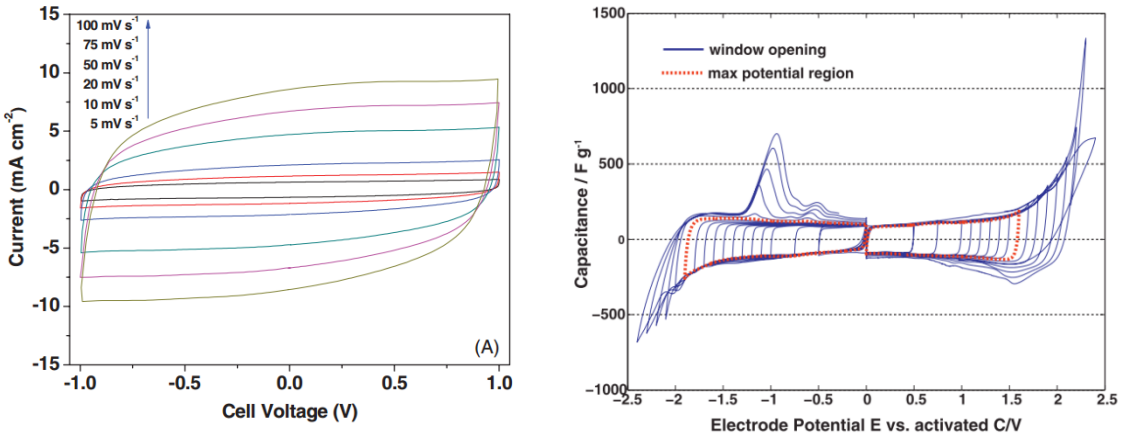


Figure 6: (Left) SC voltammogram as scan rate is varied within cell ESW - [24]**, (Right) Variation of electrode potential limit to determine stability window -** [25]

2.1.2.2 Electrochemical Impedance Spectroscopy

Electrochemical Impedance Spectroscopy (EIS) is a powerful technique that enables individual phenomena, such as ionic diffusion, to be separated from bulk activity, enabling a deeper understanding of cell behaviour as a function of operating conditions. EIS is a technique in which an oscillating current or potential is applied, and the magnitude and phase of the resultant potential or current response is measured. In galvanostatic mode, the applied current is given as Equation 9, and the resultant voltage is given as Equation 10, therefore the system impedance, Z, can be given as per Equation 11, where I_0 & V_0 refer to the steady state amplitude of the current and voltage, ω is the angular frequency, and θ is the phase.

For batteries and supercapacitors, it is best practise to operate in galvanostatic mode and hence oscillate the current and measure the voltage response, as very large currents may be required to rapidly change voltage. The applied current should be minimized as to not overly perturb the cell from equilibrium, not cause significant cell heating and limit SoC changes, however it must be sufficiently large for an acceptable signal-noise ratio.

$$\mathrm{I(t)} = I_0 \sin(\omega t) \qquad \textbf{Equation 9}$$

$$\mathrm{V(t)} = V_0 \sin(\omega t + \theta) \qquad \textbf{Equation 10}$$

$$\mathrm{Z}(\omega) = \frac{V(\omega)}{I(\omega)} \qquad \textbf{Equation 11}$$

A typical impedance spectra for a lithium ion battery is shown in Figure 7a, and notable regions are indicated, and below will be denoted regions 1-4 from left to right. The series resistance is shown on the plot at the intersection of the x axis; this occurs at high frequency as insufficient time is available for charging and discharging, thus the only contribution to the resistance is that from the electrical conductors. The shape of the curve in region two is commonly attributed to the resistance of the SEI layer at the anode, whilst region three is attributed to the charge transfer resistance and region four to diffusion processes.

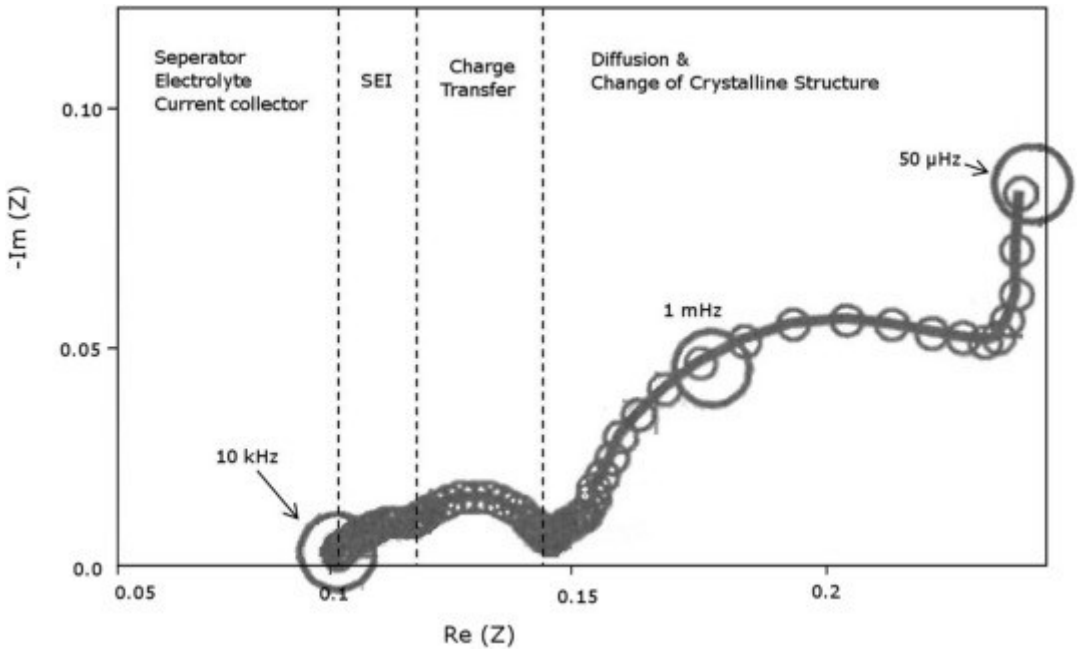


Figure 7: Typical EIS plot of a lithium-ion battery- [22,26]

Whilst it is possible to complete a qualitative comparative analysis through observation of changes in each of these areas for differing operating conditions, it is useful to numerically quantify the attributes of interest. Numerical determination of physical attributes such as double-layer capacitance and charge-transfer resistance has been the subject of an extensive field of literature [27–33]. Some information can be extracted using relative simple formula, such as Equation 12 for the calculation of SC capacitance, where Z' is the real component of the resistance and Z'' is the imaginary component. However, the complex nature of typical systems prevents them from being described analytically using ideal capacitances ($Z = (1/j\omega\, C)$), resistances ($Z = R$) and inductances $\left(Z = (j\omega L)\right)$. Therefore fitting to equivalent circuit models is typically required, with the use of a combination of capacitors, resistors, inductors and distributed elements which combine resistive, capacitive and inductive behaviour such as Warburg and Constant Phase Elements (CPE).

$$C = -\frac{Z''\,.|Z|^2}{\omega} - \frac{Z'}{\omega\,.|Z|^2} \qquad \text{Equation 12}$$

A Warburg element is often used to describe unrestricted diffusion into an electrode in electrochemical systems; the impedance of a Warburg element, Z_w, is defined as per Equation 13, where σ is the Warburg coefficient. A CPE is often used to replace capacitors in an equivalent circuit and the cause of the deviation between a CPE and a capacitor is often interpreted physically as being due to electrode/electrolyte interface roughness and irregularities; a CPE is defined as per Equation 14. The typical equivalent circuit used for fitting of results of LIBs is shown in Figure 8.

$$Z_w = \frac{1}{\sigma\sqrt{j\omega}} \qquad \text{Equation 13}$$

$$Z_{CPE} = \frac{1}{Q(j\omega)^n} \qquad \text{Equation 14}$$

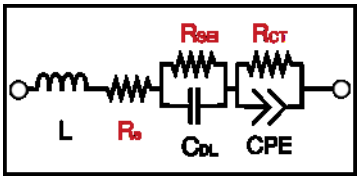


Figure 8: Typical equivalent circuit used for fitting of LIB EIS data

Whilst EIS has undoubtedly been proven to be an extremely powerful technique, great care must be taken both to control experimental conditions when generating the data and the manner in which the data is interpreted. The findings of Barai et al [22] show that the values produced by EIS continue to change when rest time is in excess of 10 hours. Whilst consistent rest times can be used for a qualitative comparison, EIS is not suitable for use as a quantitative technique.

2.1.2.3 IEC DC-ESR

SC resistance measurement during degradation testing was conducted using the methods defined in IEC62576 [34] to prevent subjective interpretations of the results. Resistance is determined by discharging the cell from its maximum rated voltage at a rate of 100 mA/F. The discharge curve (from a Voltage vs. time plot) between 1-3 seconds is extrapolated back to the Y-intercept. The difference between the maximum rated voltage and the y-intercept is taken as ΔV, and the resistance is calculated using ohm's law (ΔV/I=R).

2.2 Modelling Targets and Requirements

The modelling targets as defined by the project sponsor are summarised in Table 1 below.

Target	Min Value	Max Value
Usable SoC	10%	90%
Voltage Error (No load)	-50mV	+50mV
Voltage Error (Transient Loads)	-3% (-126mV)	+3% (+126mV)
Temperature Error	-1.5℃	+1.5℃

Table 1: Modelling Targets

The stipulated modelling requirements are:

- Developed models should run in an environment available to the project sponsor
- Parameterisation for a range of cells should be neither difficult nor highly time consuming
- Parameterisation should not require proprietary knowledge from a battery manufacturer
- Computation in a reasonable time period should be possible on a typical desktop computer

3.0 Supercapacitors

Motivation & Applicability to Research Questions

The purpose of this chapter is to explore the electrochemical and thermal characteristics of SCs and explore how they vary with operating conditions for latter comparison with LIBs. Particular focus has been placed upon the attributes of SCs which affect their performance in a HESS, namely capacity and resistance variation with operating conditions, heat generation during operation, low temperature performance and performance degradation following extended use.

An understanding of these factors is used to develop a model capable of predicting SC performance over an array of operating conditions, enabling latter combination with a lithium ion battery model to predict HESS behaviour in both cell-level and high voltage systems. An emphasis was placed upon the development of a high fidelity thermal model as the academic literature provided a limited understanding of thermal management and the effect of thermal gradients within SCs. The development of a high fidelity thermal model led to novel findings with respect to heat generation with SCs during operation.

3.1 Introduction

A number of variations of supercapacitor technology exist, and these can broadly be categorised as Electric Double Layer Capacitors (EDLCs), pseudocapacitors and hybrid capacitors. EDLCs utilise non-faradaic ion adsorption to store energy, whereas pseudocapacitors utilise fast, reversible, surface redox reactions. Hybrid capacitors combine an EDLC electrode with a pseudocapacitor electrode. Unless expressly stated otherwise, this review will limit discussion to EDLCs consisting of symmetric activated carbon electrodes (identical anode and cathode) utilising an electrolyte with an organic salt. Herein, EDLCs will simply be referred to as supercapacitors (SCs).

SCs possess a number of beneficial attributes in comparison to lithium-ion batteries (LIBs) for use in automotive traction applications. SCs utilise non-faradaic ion adsorption at electrode surfaces to store energy, as opposed to LIBs which store energy in the bulk of the electrode via chemical reactions, [35]. Consequently, SCs are capable of outputting far higher specific power than LIBs, [23]; high power output is desirable for electrified vehicles as the power output of the energy storage system is typically the limiting factor in drivetrain performance [36]. However, the direct ramification of the energy storage method in SCs is that they possess poor specific energy storage capabilities in comparison to LIBs, typically 5-10Wh/kg vs 150-200 Wh/kg, [14,37]. Other benefits of SCs for automotive applications include excellent cycle life [37,38], very low and stable resistance over a broad array of operating conditions [39], significantly lower heat generation than LIBs and consequently excellent efficiency, [23,35,40].

Whilst SCs have some very desirable attributes for automotive applications, their limited energy storage capability and voltage profile prevent their usage as a direct substitute for batteries, [41,42]. As this study aims to understand whether it is possible combine the discussed benefits of SCs with the high energy density and more favourable voltage profile of LIBs, it is necessary to understand the electrochemical and thermal characteristics of both SCs and LIBs to enable an understanding of their combined operation.

This chapter examines and relates the performance capability of SCs to their electrochemistry. The generated knowledge is subsequently used to create a model to estimate SC performance over an

array of operating conditions; this model can be used to understand SC performance when cells are combined to create modules, or when combined with batteries. Whilst degradation modelling is beyond the scope of this study, the causes of degradation in SCs are investigated to provide insight into the working hypothesis that an energy storage system combining LIBs and SCs will experience less degradation than a battery only system.

3.2 Operating Principle & Factors Affecting Performance

3.2.1 Operating Principle

SCs store electrical energy as potential energy between charged electrodes and ions at the electrode/electrolyte interface; energy is stored electrostatically, and electrons are not exchanged between the solid and liquid phase. Starting with a discharged cell, upon the application of a potential difference between the positive and negative terminals of the cell, the electrodes become either electron rich or electron deficient. This gives rise to the formation of electric fields around the electrodes that attract counter-ions available in the electrolyte and repel co-ions. Counter ions accumulate at the electrode surfaces to balance that charge. The electrons from the electrode, and the ions from the electrolyte are now held in position by a strong electric field between their opposing charges. The electrical energy applied to the cell is thus converted into potential energy in the form of electrostatic attraction. The structure of ions at the electrode/electrolyte interface which is opposing the excess charge of the electrodes in known as the Electric Double Layer (EDL).

The average distance between the regions of electronic and ionic charge of the electrode and electrolyte, known as the charge separation distance, dictates the energy stored within a SC. A smaller charge separation distance increases the strength of the electric field between the ions and electrode, thereby increasing the potential energy at the electrode/electrolyte interface and increasing the energy stored. A simplified schematic of a SC in its charged and uncharged state is shown in Figure 9.

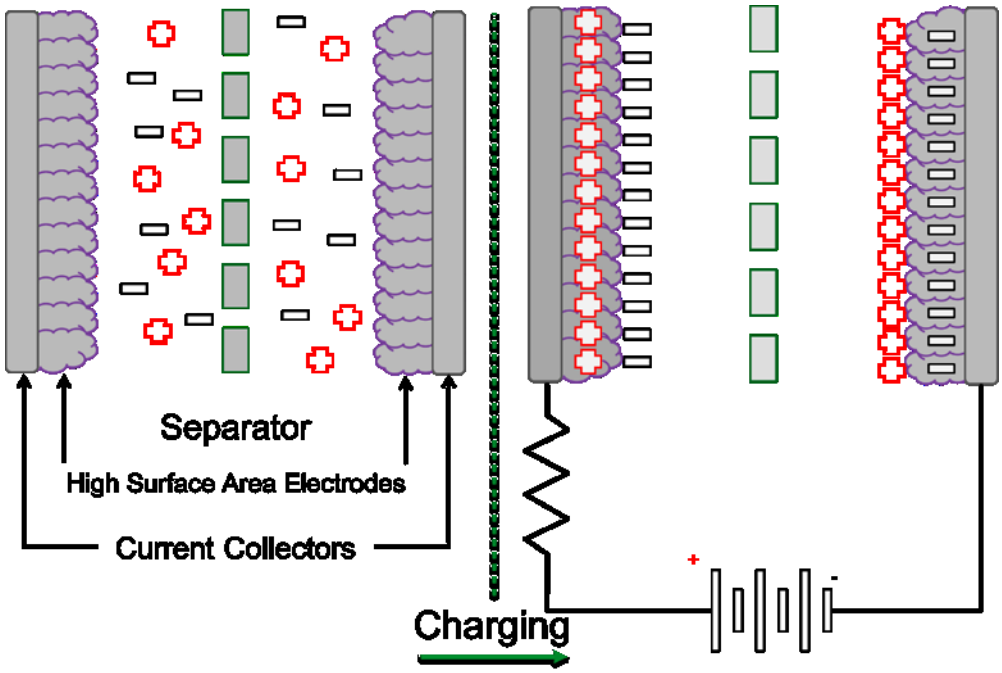


Figure 9: Simplified illustration of the charging mechanism of a SC. Positive (+) and negative (-) signs indicate regions of charge of opposing polarity.

Equation 15 and Equation 16 define the specific energy stored, E (Wh kg^{-1}), and the available pulse power, P (W kg^{-1}), [23]. The specific energy stored is a function of the capacitance, C (F), cell voltage,

V (V) and cell mass, m (kg). The specific power is a function of both cell voltage and resistance (Ω), and is often expressed as $P = V^2/4mR$. This however assumes an efficiency of 50%, therefore Burke et al incorporate an efficiency factor, EF into this equation as expressed in equation 2, where EF is the desired efficiency between 0→1.

$$E = \frac{{}^1/_2 CV^2}{3600\ m} \qquad \text{Equation 15}$$

$$P = \frac{9}{16}(1 - EF)\frac{V^2}{m\ R} \qquad \text{Equation 16}$$

3.2.2 Cell Constituents and Internal Structure

Cylindrical SC cells comprise a wound jelly-roll within an aluminium can, where the positive current collectors are welded to one side, and the negative to the other. The jelly-roll consists of sheets of porous carbon electrodes, aluminium current collectors and paper based separators which are wound in a spiral; these are arranged as depicted below in Figure 10. In this particular cell, (Maxwell K2 Series 650F), the jelly-roll is measured to be 5m long and is wound into a spiral consisting of 42 turns, with an outer diameter of 56mm.

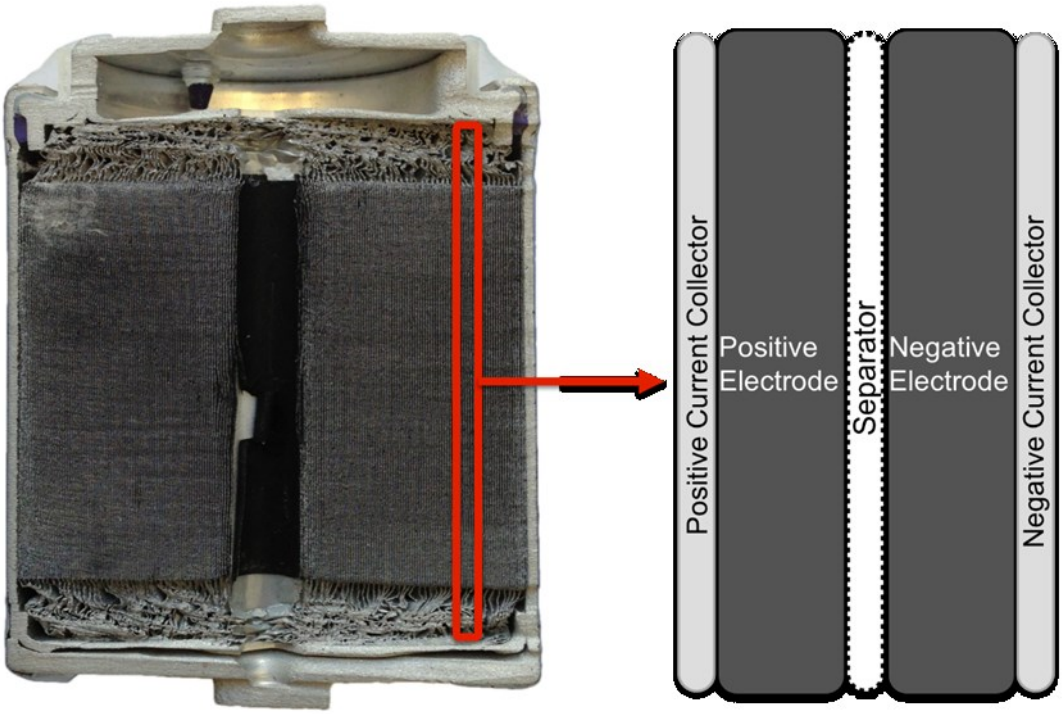


Figure 10: Image of cross section of a Maxwell 650F cell, including an illustration (not to scale) of the repeating element within the jelly roll

3.2.2.1 Electrodes

Supercapacitors utilise highly porous, activated carbon electrodes, with exceptionally high surface area to maximize their energy storage potential. Carbon is the ideal electrode material due to its high conductivity, high surface area, low cost, and established manufacturing process, [23,35,43]. The physical and chemical properties of the carbon significantly affect the performance of the supercapacitor.

An increase in the accessible surface area of the device leads to an increase in capacitance, up to a limit defined by the availability of free electrons within the carbon, [44]. The accessible surface area is increased by increasing electrode porosity, and the optimal pore size for energy storage is a function of the Electrochemical Stability Window (ESW) of the device [45]. Generally small pores (<1.5nm) will maximize the available energy, however the higher degree of confinement will reduce the power capability. Linking of pores improves electrical conductivity and reduces diffusion resistance, thus increasing power at the detriment of specific cell capacitance, [46]. Whilst it is possible to improve performance for a specific application by maintaining a very narrow distribution of pore size, this may result in detrimental effects with changes in operating frequency, [47].

Pore shape directly impacts the ability of ions to enter and exit the pore, thus also affects the frequency response of the device, [43]. Impurities within the carbon cause undesirable redox reactions; these reactions are typically observed as leakage current, and result in capacity loss or resistance rise [23,35,48].

3.2.2.2 Electrolyte

The electrolytes used in supercapacitors typically fall into three categories: aqueous, organic and ionic liquids. Although aqueous electrolytes are very low cost, their limited *practical* ESW (0→1V) limits their uses and energy storage capability, [23]. Room Temperature Ionic Liquids (RTILs) offer a high practical *ESW* of 0→6V, however it should be noted that early results with glassy carbon have been shown to have limited applicability to activated carbon, [25,49]. In addition, RTILs are hindered by high viscosity at low temperatures and high cost, [23]. Organic electrolytes possess a useful ESW of 0→3V [25], possess good conductivity, low viscosity changes with temperature, have a wide thermal operating range and acceptable cost and therefore have been adopted by the majority of the industry, [37,38,50].

Organic electrolytes typically take the form of a tetra-ethyl-ammonium tetra-fluouro-borate (TEATFB) salt in a Propylene Carbonate (PC) or Acetonitrile (AN) solvent. TEATFB yields a cation of tetra-ethyl-ammonium (Et_4N^+) and anion tetra-fluouro-borate ($BF_4{}^-$); the anion has a smaller physical size (0.48nm vs 0.67nm), [43], and a lower solvation free energy (-45.1 kcal mol^{-1} vs 51.2 kcal mol^{-1}) [51]. The practical ESW is significantly affected by operating temperature, and at elevated temperatures, PC generally exhibits higher stability than AN, [25]. Whilst PC solvents can offer superior capacity and lifetime at elevated temperatures, viscosity increases significantly at low temperatures resulting in a large rise in resistance due to reduced ion mobility and thus severely degraded low temperature performance, [23,25,52]. AN has a stable operating range of $-40 \rightarrow 65℃$; the upper limit is in place to prevent electrolyte decomposition and carbon oxidation, however this limit can be expanded with the use of additives, [53]. AN is the preferred salt in commercially available cells due to the greater stability of capacitance and resistance with temperature, and its higher conductivity, [43,52].

3.2.2.3 Internal Design

Whilst SCs are available in pouch and prismatic form factors, the cylindrical form factor is typically preferred. Whilst cylindrical cells have a lower packing density in a module than pouch or prismatic cells, they have lower manufacturing costs due to a low jelly-roll winding time, and typically possess a lower ESR as the larger area over which the current collectors can be connected results in a lower series resistance.

Cells can be designed to prioritise energy or power; high energy cells will have electrodes of greater porosity and thickness to maximize the surface area available for energy storage, [43]. Conversely,

electrodes for high power cells will possess less surface area, and be thinner to reduce tortuosity and minimize ionic resistance, [23].

Some cells utilise identical electrodes for the anode and cathode to minimize cell cost, though it is common to use a thicker positive electrode to reduce positive electrode potential and hence achieve higher cell voltages without major positive electrode degradation, [25,54]. This effect will be discussed in more detail in section 3.4). Higher voltage cells also require electrodes of greater purity (fewer functional groups following the activation process), [55], low separator water content [35] and selection of an electrolyte with an appropriate ESW [23].

3.2.3 The Electric Double Layer

In order to understand the factors affecting the ability of a SC to store charge, it is necessary to understand the formation and structure of the Electric Double Layer (EDL). Traditionally in electrochemistry the EDL is described by the theories of Helmholtz or Gouy-Chapman-Stern [23,35,56], however these theories do not account for many factors which have a significant effect upon capacitance, such as pore shape, pore size distribution and ion properties, [43]. Consequently, whilst these theories can provide indicative values of capacitance, they do not enable a deeper understanding of the formation or structure of the EDL in SCs. All further discussion of the EDL concerns SCs consisting of carbon electrodes with organic electrolytes as is typical of commercial SCs; it should be noted that the behaviour of ionic liquids can differ greatly from that described below, [57–59].

The work of Chmiola et al [60] challenged a long held belief in the electrochemistry community that the optimal pore size in SC electrodes was twice that of the solvated ion diameter, [61]. Chmiola et al suggested that the normalised capacitance of SCs could be dramatically increased by reducing electrode pore size to just above the diameter of a de-solvated ion. Studies exist from other research groups which both agree [62] and disagree [63] with the findings of Chmiola; Centeno et al suggest that the finding is a result of overestimation of surface area at pore diameters of <1nm due to the use of the Brunauer–Emmett–Teller (BET) theory for surface area determination, which is an estimate of surface area derived from gas adsorption.

Jiang et al [47] use density functional theory (DFT) to examine these conflicting claims and suggest that both a dramatic increase in capacitance and a very minor change in capacitance is possible for sub-nano-meter pores, with results varying with small changes in pore size distribution (where pore size distribution is statistical distribution of pore diameter). Through the use of Molecular Dynaimcs (MD) simulations, Feng et al [64] suggest that the confinement of ions in sub-nano-meter pores provides 40% more capacitance than a planar surface. The systems studied employ a $TEABF_4$ salt, and therefore consist of a TEA^+ cation and $BF_4{}^-$anion, both of which have a low solvation free energy in acetonitrile thus readily partially de-solvating for adsorption to a carbon surface in a pore which is smaller than the solvated ion, [64].

Whilst sub nano-meter pores provide the greatest capacitance at low potentials, the optimal pore size for energy storage increases with potential. Small pores reach charge saturation sooner than large pores, i.e. a greater number of counter-ions cannot be inserted to balance a larger electronic charge, [45].

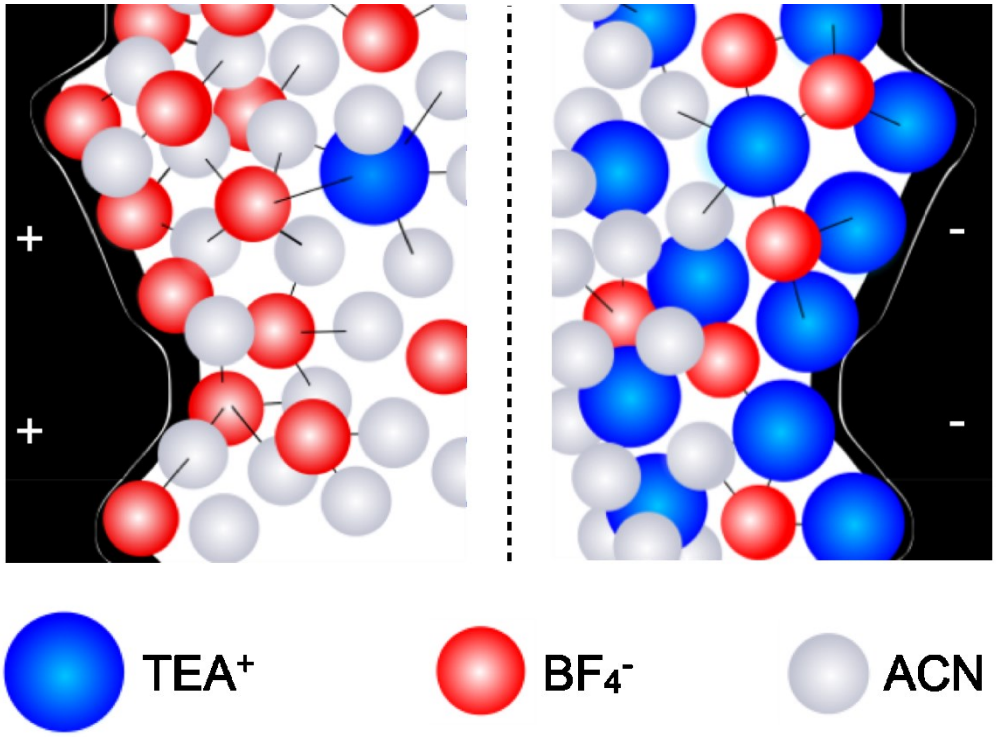


Figure 11: Schematic of EDL for a quasi-planar electrode – Created using the findings from [47,51,65,66]

The structure of the EDL varies with pore size [64], electrode potential [67] and polarity [68]. Where the pore size is much larger than the size of ion, the electrode can be described as quasi-planar; a schematic of the structure of the EDL for a quasi-planar electrode is drawn in Figure 11 based upon the findings discussed below. Feng et al suggests the presence of over-screening at the negative electrode due to the strong ion-ion affinity of TEA^+ and $BF_4{}^-$. The NMR studies of Deschamps et al [66] suggest that the over-screening effect is stronger at the negative electrode than at the positive electrode.

Additionally, Deschamps et al find that at the positive electrode the concentration of the solvent is virtually unchanged with potential, whereas at elevated potential the solvent is driven away from the negative electrode. It is likely that this difference is due to the much higher non-electrostatic ion-electrode potential of the TEA^+ ions [51], which lead to the favouring of a different mechanism to increase ionic charge density, [67]. The works of Wu et al [67] state that the preferred method of charging (to minimize free energy) at the negative electrode differs with electrode potential. At low potentials, ion exchange is favoured, at moderate potentials co-ion repulsion is favoured, and at high potentials, where all co-ions have been repelled, counter-ion attraction is favoured. Multiple NMR studies [66,68] confirm that the EDL structure differs with polarity.

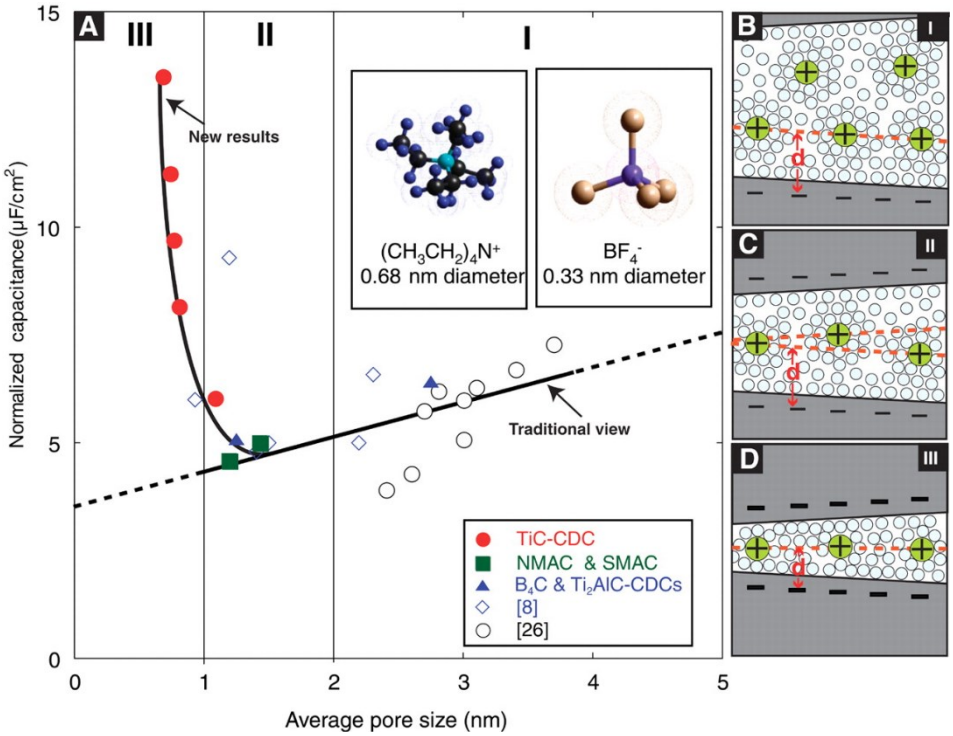


Figure 12: (A) Variation of normalised capacitance with average pore size, schematic of ion (green) and solvent (blue) arrangement for ions of (B) 2-5nm, (C) 1-2nm, (D) 0.7-1nm – Source [60]

Figure 12 contains schematics of the differing EDL structures in a negative electrode with pore sizes between 0→5nm. In comparison to region I (2-5nm), in region III (0.7-1nm), the ions experience greater confinement, must partially de-solvate to occupy the space and are packed closer together. Capacitance is lower in region II than in both regions I and III because the charge separation distance is greatest as indicated by the size of 'd' in Figure 12B-D.

Figure 13 shows how the EDL of a negatively charged sub-nano-meter pore changes with increasing charge. In the uncharged state, the strong ion-ion affinity will result in the presence of pairs of positive and negative ions, surrounded by solvent molecules in a distorted or partially de-solvated manner. As charge is applied, counter-ions are attracted and both co-ions and solvent molecules are repelled. Surface charge density is increased by increasing counter-ion packing, decreasing the average ionic and electronic charge separation distance and eliminating co-ions and solvent molecules from the pore.

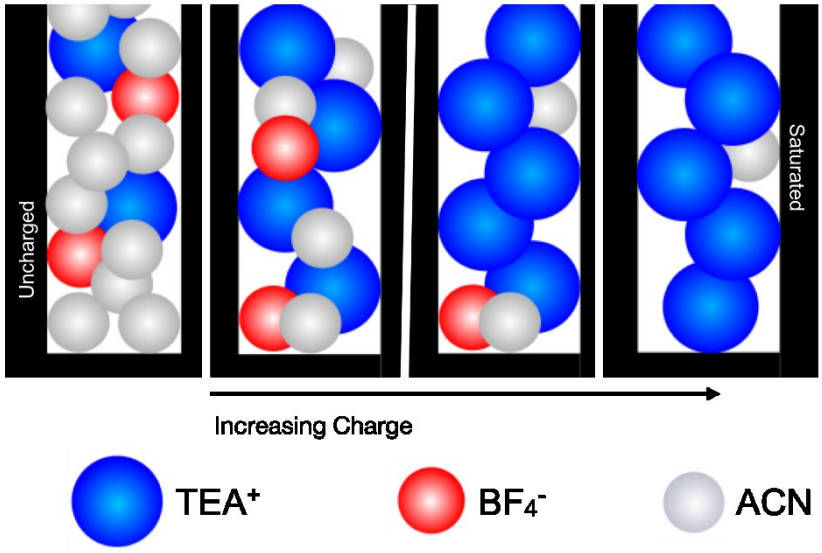


Figure 13: Schematic of evolution of the EDL for a sub-nano-meter porous electrode – Created using the findings from [47,51,65,66]

3.3 Factors Influencing Supercapacitor Performance

The resistance and capacitance of SCs are affected significantly by cell voltage, operating temperature, charge/discharge frequency and operating current, [35].

3.3.1 Variation with Voltage

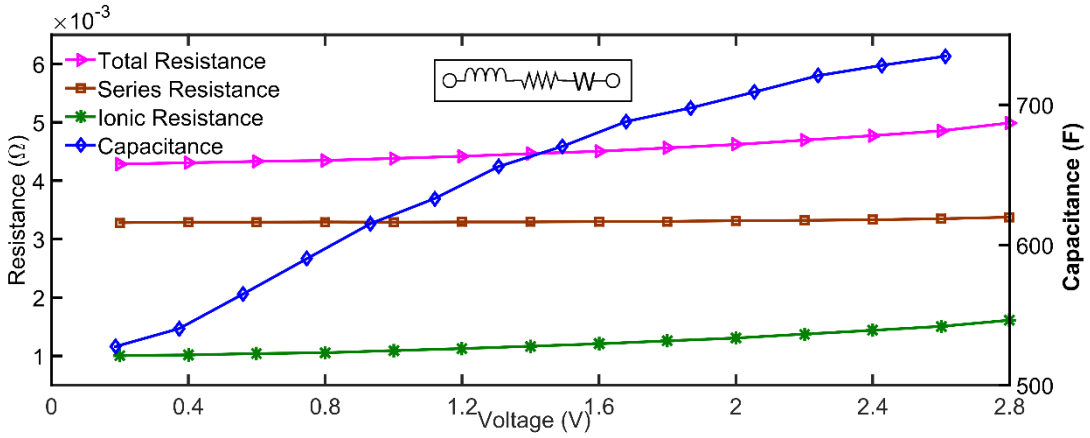


Figure 14: Capacitance & resistance variation of a Maxwell BCAP0650 cell with voltage

A change in the cell voltage results in an increase of both the capacitance and resistance of the cell as shown in Figure 14. The capacitance of the cell increases significantly and non-linearly with voltage, typically by 50-80% for a change in voltage of 2.7V. An increase in the cell voltage results in a decrease in the charge separation distance at the electrode/electrolyte interface, thereby increasing the electrostatic force of attraction. Consequently, the potential energy that can be stored in the double layer is increased, as is the cell's ability to store charge. This effect can be approximated with a linear increase in capacitance with voltage, [43].

It is possible to distinguish the series and ionic resistance of a supercapacitor through fitting of EIS data to a simple equivalent circuit, as seen in the inset of Figure 14, consisting of a series string of an inductance, a series resistance and Warburg element, [69]. The series resistance represents all of the bulk material and interface resistances hindering electron flow, whilst the ionic resistance (resistive element of the Warburg element) relates to the restriction of ion movement as a result of

separator and electrode porosity, electrolyte resistivity and concentration dependent tortuosity. Consequently, the series resistance does not vary with voltage, however the ionic resistance increases because the diffusion resistance increases due to larger ion path tortuosity, [23].

3.3.2 Variation with Temperature

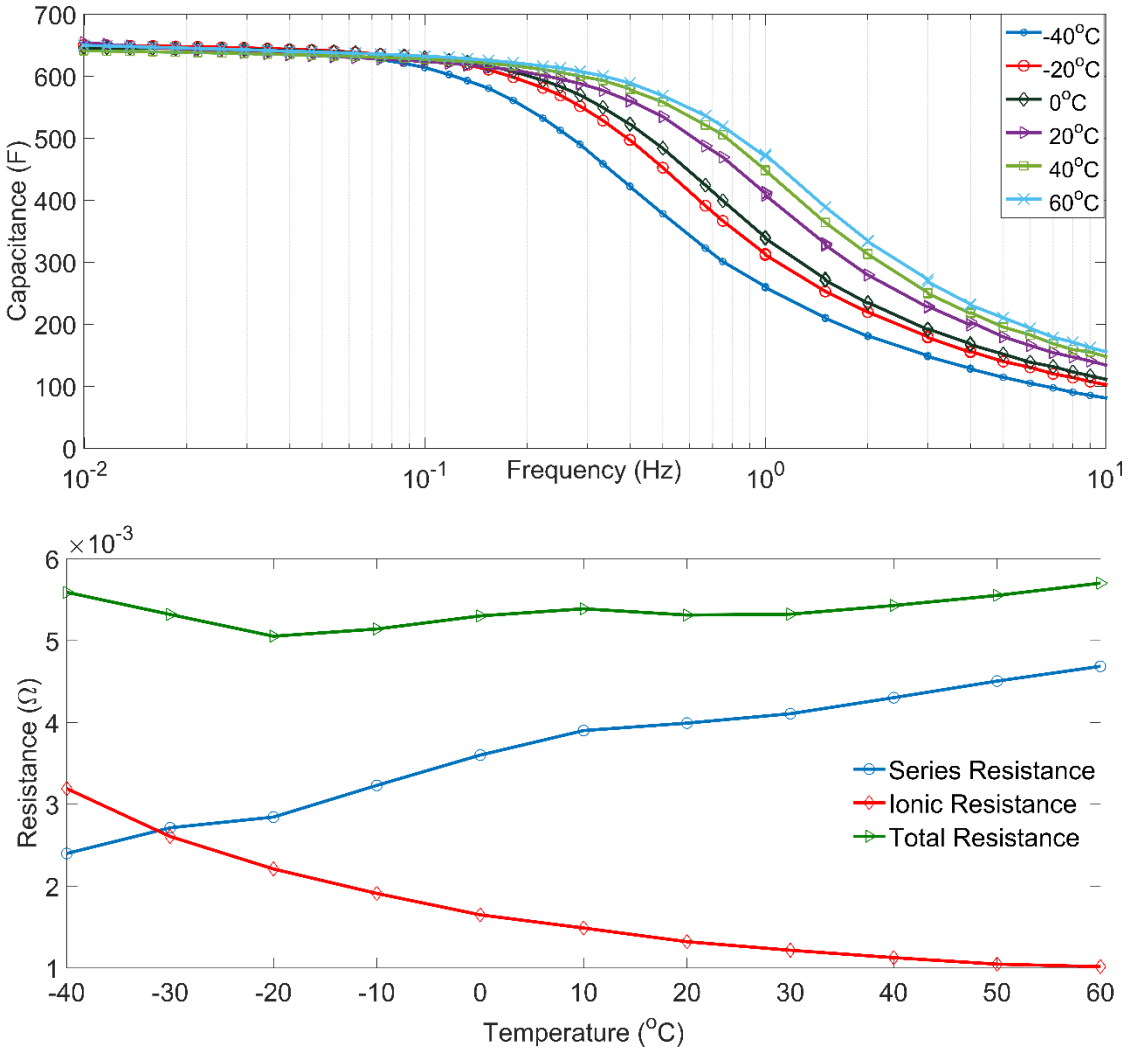


Figure 15: Measured capacitance & resistance variation of a Maxwell BCAP0650 cell with temperature

Whilst the capacitance of a cell is independent of temperature at very low frequencies, it is highly temperature dependent at higher frequencies where capacitance is diffusion limited. The capacitance at low temperatures is lower due to the reduced mobility of ions. At 1Hz, the capacitance is 80% greater at $60°C$ compared with $-40°C$. Higher temperatures assist ion diffusion and reduce electrolyte viscosity, and hence effectively increase the accessible surface area when capacitance is diffusion limited. This is evident from the higher capacitance and lower ionic resistance at higher temperatures, as shown in Figure 15.

For this particular cell, the total resistance varies little with temperature, however both the series and ionic resistance vary significantly. It is worth noting that larger capacitance cells which retain the same form factor, (simply increase in length between the terminals), have a larger ionic to series resistance ratio. The series resistance, which is made up of electrical conductors, increases linearly with temperature. Conversely, the ionic resistance follows an Arrhenius relation and decreases with an increase in temperature due to an increase in electrolyte conductivity, and thus reduced diffusion resistance, [35].

3.3.3 Variation with Current

The variation of capacitance with current can be calculated by using the below formula with a constant current and consistent voltage limits,

$$C = \frac{I.dt}{V_{max} - V_{min}} \qquad \text{Equation 17}$$

where C is the capacitance (F), I is the current (A), V is the voltage (V) and t is the time (s).

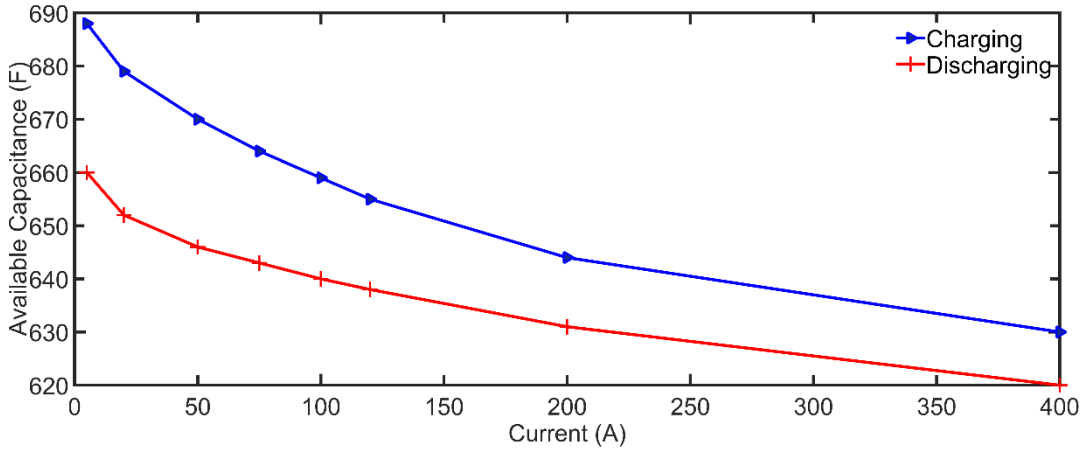


Figure 16: Available capacitance variation with applied current, measured during both a charge and discharge

The accessible capacitance of the cell changes with current, as less of the electrode surface area can be utilised over a shorter time period. Additionally, we observe a difference in the measured capacitance over a charge and a discharge. This occurs as the calculation is based upon measured cell voltage, and the measured voltage is not necessarily the voltage at all points within the cell. The easily accessible electrode surfaces will charge or discharge first; the more difficult to access surfaces will initially lag behind and eventually balance with the remainder of the cell. This phenomenon has been termed the residual charge effect [70,71], and is the cause of charge re-distribution. When charging, the measured cell voltage is slightly greater than the real voltage, whilst when discharging, the measured voltage is slightly lower than the real voltage. The true or equilibrium charge and discharge capacitance are almost identical.

The steady state and dynamic capacitance of the cell are not equal; the dynamic capacitance (due to the residual charge effect) will tend to the highest applied current.

3.4 Self Discharge & Degradation

When in a charged state, a SC has a higher Gibbs free energy than the discharged state, therefore as voltage is increased the driving force for spontaneous discharge to occur through any available mechanism is also increased, [35]. Self-discharge is well understood empirically [70,72–75], and has been shown to fit well an equation consisting of two exponential terms in the general form of Equation 18, [73–75].

$$V(t) = a_1.\exp\left(-\frac{t}{\tau_1}\right) + a_2.\exp\left(-\frac{t}{\tau_2}\right) \qquad \text{Equation 18}$$

It is well established that the first term is attributable to the effect of charge re-distribution [73,74,76,77], and it is widely theorised that the second term is attributed to leakage current as a result of faradaic reactions which result in degradation [72,74,75,78,79], however the number of

evidence based studies are limited [80,81]. Charge re-distribution differs from self-discharge in that it does not cause a loss of charge carriers from the EDL, whereas self-discharge does, [73,82].

3.4.1 Charge redistribution

Following a charging event, the voltage of the SC will decay over time. This decay is often incorrectly attributed to self-discharge. However, over short time periods this voltage decay is almost exclusively attributable to charge-redistribution [83]. Charge re-distribution can act over a period of many tens and up to hundreds of hours, particularly for very small pores where the diffusion coefficient can be greater than four orders of magnitude lower than the bulk, [70,76,83,84]. Charge-redistribution will cause the voltage of a SC to decay towards its equilibrium value following either a charging or discharging event, and thus can be distinguished from self-discharge as the voltage will increase following a discharge. Charge re-distribution differs from self-discharge in that it does not cause a loss of electrons or ions from the EDL, whereas self-discharge does.

In porous electrodes, the limited conductance of the electrolyte will result in a voltage drop across a pore, [85], which alongside differing ionic path lengths and the localised effect of electrode geometry will result in different areas of the electrode charging at different rates, [70]. A simplified example is provided in Figure 17 where the entrance to the pore becomes charged first due to a lower voltage drop, and shortest ionic path length due to its proximity to the bulk electrolyte. A concentration gradient is formed with a significantly larger ionic concentration at the entrance of the pore. A longer time period is required to access the full depth of the pore; as the ions diffuse to eliminate the concentration gradient, a greater surface area is accessed, thereby increasing the effective capacitance and reducing the voltage, [77,83].

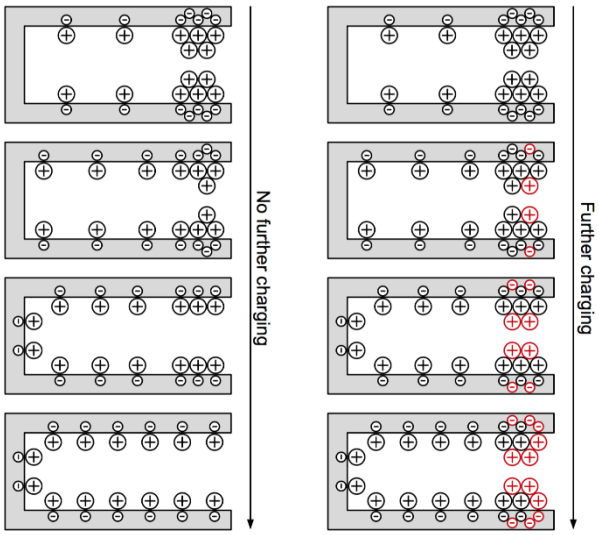


Figure 17: Illustration of charge redistribution as no further charge is applied (left), when additional charge is applied (right) - [86]

The extent of charge re-distribution is affected by tortuosity, pore size distribution, temperature, current, voltage, usage history and level of charge saturation, [35,70,73,77,83,84]. The tortuosity of a typical porous carbon electrode decreases the diffusivity from the bulk by 4-5 orders of magnitude, and sub-nano-meter pores can cause this value to drop by an additional 3-4 orders of magnitude during the ion exchange phase of a charge or discharge, [83]. Consequently, the time period required to partially or fully access these pores may require many hours and therefore not contribute in a useful manner for transient loads.

Higher temperatures result in faster re-distribution as electrolyte viscosity is reduced and the ions have greater energy, resulting in greater ion mobility, [70]. In instances where higher currents are used, less time for ion diffusion into the porous structure is available, therefore the imbalance of charge and subsequent re-distribution is increased, [76]. Constant-voltage charging can be used to saturate the cell at a given voltage; the greater the saturation time, the lower the charge re-distribution as shown in Figure 18.

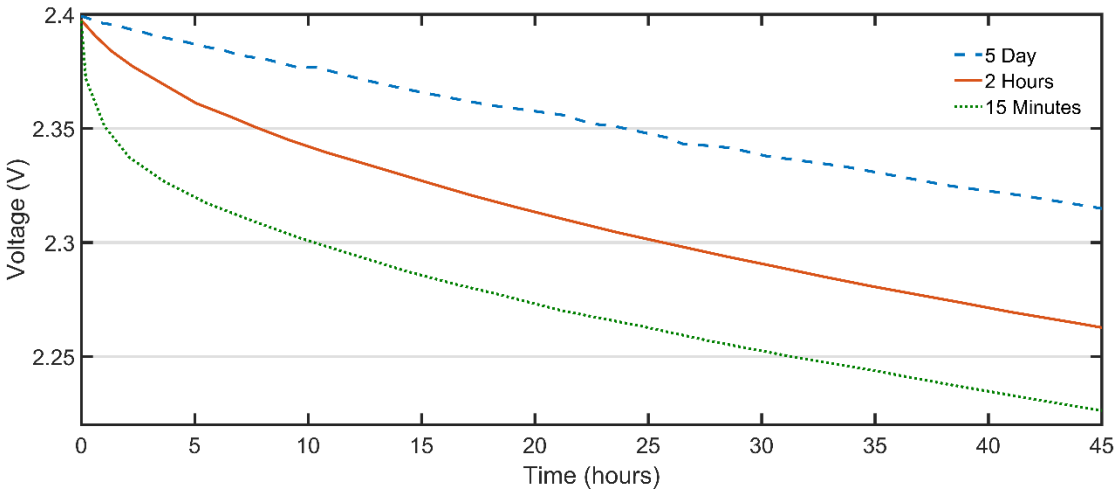


Figure 18: Voltage decay of SC cells charged to 2.4V and held at constant voltage for varying time periods - [70]

3.4.2 Causes of Self-discharge

Self-discharge is characterised as a voltage decay due to a loss of charge carriers from the EDL, and is widely theorised to be a result of faradaic reactions which result in degradation [72,74,75,78,79], however the number of evidence based studies are limited [80,81]. The rate of self-discharge is strongly affected by voltage and temperature [72,73,87], as they affect the rate of electron transfer rate, k, at the electrode/electrolyte interface as per Equation 19, [81], where K^0 is the rate constant at zero over-potential, α is the charge transfer coefficient, η is the overpotential defined as the difference between the double layer voltage and the redox potential of reaction, F is Faradays constant and T is the absolute temperature.

$$\mathrm{k} = k^0 \exp(-\alpha\eta F/RT) \qquad \textbf{Equation 19}$$

$$\frac{\mathrm{dV}}{dt} = -\mathrm{kV} \qquad \textbf{Equation 20}$$

The voltage loss as a result of degradation inducing faradaic reactions is given as Equation 20 by Tevi et al [81], whilst however this is yet to be demonstrated with commercial cells. Niu et al [78] propose different degradation mechanisms, providing associated equations to describe the rate of self-discharge. However, the works of Niu et al suggest that a linear voltage decay with log t is the result of activation controlled faradaic reactions, however Black et al [77] show that a linear voltage decay with log t is due to charge re-distribution in a porous electrode. The lack of evidence based analysis leads the author to conclude that greater analysis is required by the scientific community before a deeper understanding better than empirical relationships can be referred to with confidence.

3.4.3 Degradation Literature Review

Numerous sources report that the cycle life of SCs is far superior to that of LIBs [23,35,43,88], however given the differences in energy storage capability, this is somewhat of a meaningless metric when considering a HESS. A more useful comparison is energy throughput; a study by Du Pasquier et al [41] finds that the energy throughput before the capacity of a SC drops to 80% of the initial capacity is significantly greater than 5 times that of a lithium ion battery.

Degradation in SCs typically manifests itself as pore blockage through the development of surface films, gas evolution or physical separation of the electrode and current collector films; a summary is provided in Table 2. The user experiences degradation as an increase in resistance and a loss of capacitance; manufacturers typically define end of life of a cell as a 20% loss of capacitance and a 100% rise in resistance, [37]. The rate of degradation is affected by temperature and the voltage of the anode and cathode. Some authors suggest that operating current [89,90], frequency [91] and thermal cycling [92] affect degradation, however the number of published studies in these areas is limited, the number of cells used is not statistically significant, and in the case of operating current and frequency, the authors have not adequately controlled temperature to decouple these causes. In typical SC systems mechanical stress is thought to contribute little to degradation in comparison to faradaic reactions, [93].

Cause	Effect	Leads to	Enhanced by	Reduced by
Electrolyte decomposition as [local] potential exceeds ESW	Reduced ionic concentration Gas Generation Electrode exfoliation and cracking	Capacity loss	High SoC High Temperature High rate at high SoC	Controlling maximum voltage as a function of temperature Electrolyte additives
Surface film growth due to charge transfer at electrode/electrolyte interface	Increase charge separation distance Pore blockage	Capacity loss Resistance rise	High temperature High SoC	Electrolyte additives Component purity Control voltage as a function of temperature
Binder decomposition	Reduced mechanical stability	Capacity loss	Correct binder choice	High temperature
Separation of CC and Electrode	Inhomogeneous distribution of voltage and current	Resistance rise	High rate operation	Application of pressure to jelly-roll

Table 2: Summary of causes of SC degradation – Sources: [54,80,94–96]

Negligible degradation is observed when operating the cell within its ESW, [93,94], however elevated voltages result in electrolyte decomposition and the reaction of the electrolyte with electrode surface functionalities results in the development of surface films, which cause pore blockages, [87,93,97]. Figure 19 shows how cell capacitance varies as the floating voltage is varied from 2.75-4.0V. The capacity loss is similar below 3.25V, but increases significantly above this value. Weingarth et al [25] demonstrate that the stability limit of the anion and cation with the electrode differ, and with an AN solvent, the stability limit of the positive electrode is 1.3V vs carbon, whilst

the stability limit of the negative electrode is (-)1.7V vs carbon. Consequently, as illustrated in Figure 20, the degradation of the positive electrode dominates system degradation.

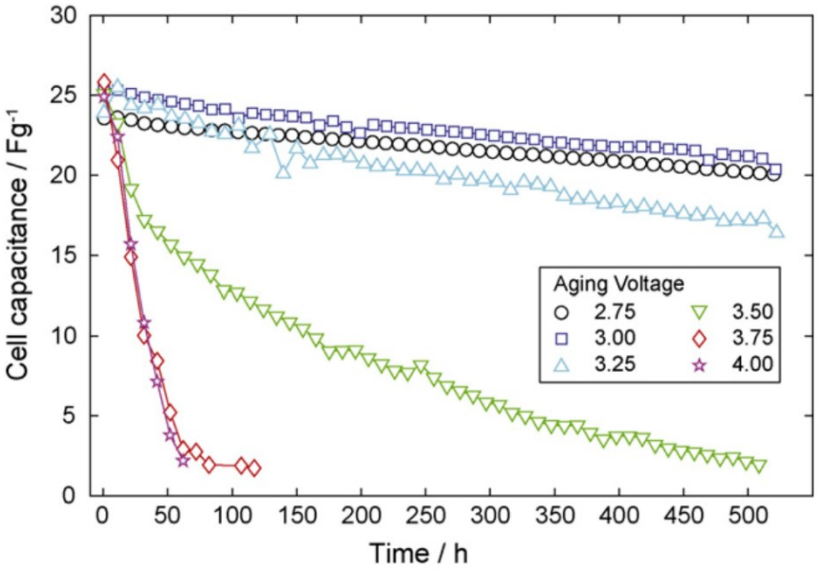


Figure 19: Change of cell capacitance over time as cells are aged via holding at voltages from 2.75-4V - [93]

To prevent the positive electrode dominating degradation, its thickness can be increased, thereby increasing capacitance and reducing electrode voltage for a given charge. Differing electrode thicknesses enables the use of higher cell voltages by maintaining both electrodes within their stable region, [98]. The stable potential of each electrode varies significantly as a function of temperature [25], therefore it should be mentioned that the above discussion is for 25°C. It is thought that the solvent plays a major role in the dominant degradation mechanisms as the majority of degradation is shifted to the negative electrode when using a PC solvent rather than an AN solvent, [54].

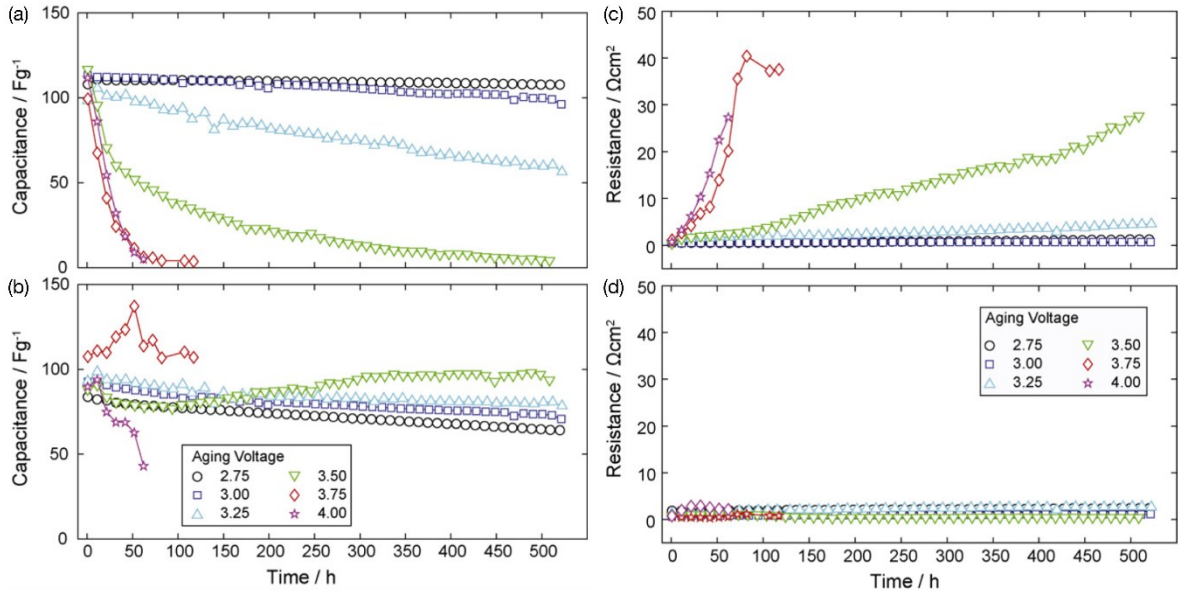


Figure 20:Change of capacitance and resistance of positive (a & c) and negative (b & d) electrodes as a result of holding cell at voltages between 2.75-4V, measured using three electrode setup - [93]

Temperature increases degradation via an Arrhenius relation [99] as more energetic particles increase the rate at which redox reactions occur, however as discussed previously, temperature and

voltage are inextricably linked, as demonstrated by Kovaltchouk et al [100]. The lack of understanding of the physical reactions occurring which result in voltage and temperature dependent degradation is highlighted by El Mejdoubi et al [101] who demonstrate the shortcomings of simple, yet commonly used voltage and temperature based degradation models.

3.4.4 Independent Degradation Testing

Given a lack of reliable literature on the topic of degradation of commercial SC cells a series of independent tests were conducted in an attempt to verify the findings of existing literature. Given the limitation of facilities directly available to the author, data generation and acquisition assistance was provided by Dr George Lane and Mr Alex Patsos of Ioxus Inc. Whilst a comparative analysis of all operating conditions was not possible, 16 cells were tested to examine the effect of voltage, temperature and cycling. Details of the conducted tests can be found in Table 3.

Capacitance and resistance were measured using the method defined by IEC62576, and all measurements were completed following a four-hour rest at 25℃. Floating tests consisted of holding the cells at a specified and fixed voltage and temperature, thus mimicking calendar ageing, whilst the cycling test charged and discharged between the upper and lower voltage limits specified at 120A with a 5 second rest following the completion of each half-cycle. Whilst the internal temperature of the cycled cells is not known, the surface temperature stabilised at a value of approximately 40℃; it is assumed that the internal temperature was greater than this value.

Test Type	Cell Type	Voltage (V)	Temperature (℃)	Number of Cells
Floating	Ioxus 3000F	2.70	65	3
Floating	Ioxus 3000F	2.70	85	3
Floating	Ioxus 3000F	2.85	65	2
Floating	Ioxus 3000F	2.90	65	2
Floating	Ioxus 3000F	2.95	65	2
Cycling	Ioxus 3000F	1.35 - 2.70	40*	2
Cycling	Ioxus 3000F	1.42 – 2.85	40*	2

Table 3: List of tests complete to evaluate degradation, *surface temperature, internal temperature is assumed to be higher

The results of the floating tests at 65℃ for the 3000F cells are presented alongside the results for the cycling tests in Figure 21. As floating voltage increases, capacitance loss increases, however at 2000h the difference is modest, the capacitance loss increasing from 8.3% for the 2.7V test to 11.7% for the 2.95V test. However, significant differences are observed in the resistance, with all tested float voltages showing a progressive and meaningful increase. The limited capacity loss with significant resistance rise would suggest the build-up of surface films, which in turn are reducing pore size, [94].

Given the findings of Weingarth et al [102] it is surprising to find that for commercial cells, cycling cells up to a given voltage results in higher capacity loss than floating at that voltage; for both 2.7V and 2.85V cycling producing approximately 0.5% more capacity loss after 2000h than floating. The resistance rise for the 2.7V float test and cycling test is almost identical, however significantly more resistance rise is observed at 2.85V during the floating test. The comparable capacitance loss and modest resistance rise during cycling suggests that cycling promotes a degradation mechanism which is less prevalent or absent during the floating tests. The author hypothesises that mechanical degradation, such as island formation in the electrodes plays an important role in the degradation of SCs via cycling at high currents.

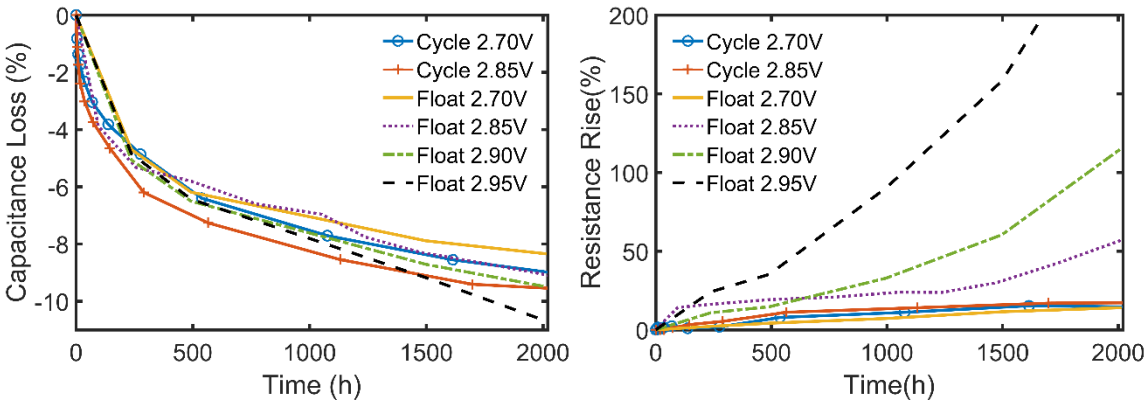


Figure 21: Capacitance loss (left) and resistance rise (right) following floating testing over a range of voltages at 65℃ presented alongside 120A cycling with 40℃ cell surface temperature for an Ioxus 3000F cell

The resistance rise as a result of increasing voltage generally follows the behaviour described in literature; when the resistance rise is fitted to an exponential equation, setting the initial value to the initial ESR enables the exponent to rise linearly with voltage upto 2.90V. Above this value, the exponent is increased, suggesting the onset of other degradation phenomena. Similarly, the capacitance loss with voltage can be fitted well to an exponential equation up to a limit of 2.9V, above this value capacitance loss is greatly increased.

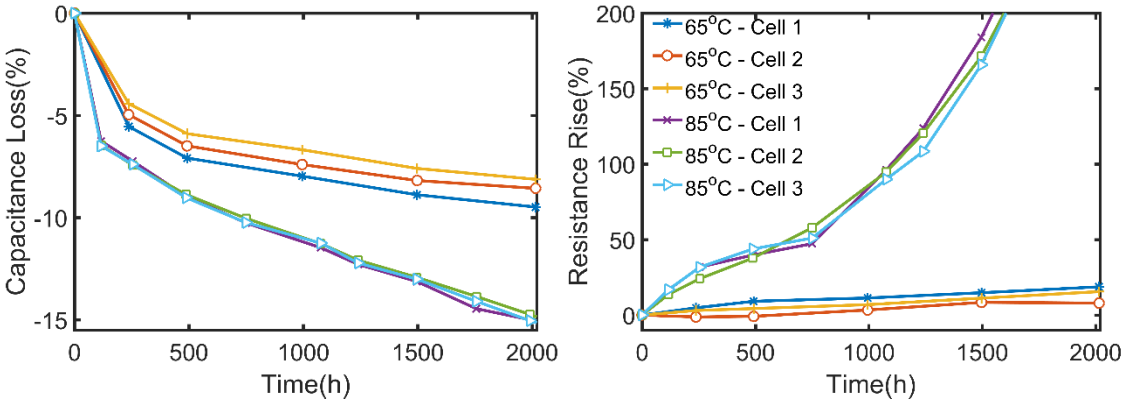


Figure 22: Comparison of capacitance loss (left) and resistance rise (rise) during floating test at 65℃ and 85℃ conducted on an Ioxus 3000F cell

Although it was not practically possible to conduct degradation testing over a range of temperatures, Figure 22 shows that capacitance loss and resistance rise are significantly increased when temperatures exceed 65℃. The development of a degradation model requires additional testing and analysis to determine relationships which can be extrapolated to typical operating conditions with confidence. Comprehensive degradation testing for the generation of a degradation model is beyond the scope of this study.

3.5 Interim Conclusion

The conducted electrochemical and thermal analysis has enabled the author to draw pertinent conclusions relating to the research questions and working hypothesis which have been defined in the introduction. The key conclusions are:

- The energy stored and power available is proportional to the square of voltage, therefore SC cell operating voltage should be maximized in the HESS to maximize SC performance.

- Capacitance is a strong function of SoC (typically varying by upto 50% within the operating voltage range), and a weak function of current (typically reducing by ~10% at the maximum rated continuous current). For the studied SC cells, capacitance is unaffected by temperature at frequencies of less than 0.1Hz, but strongly diminished above this frequency where capacitance is strongly diffusion limited.

  Series resistance increases with increasing temperature, however ionic resistance decreases. Ionic resistance increases substantially at sub-zero temperatures, and at -40°C is typically more than 100% larger than at 0°C. Resistance is largely independent of temperature for the studied cell due to the relative ratio of series to ionic resistance. Series resistance is largely independent of SoC, though ionic resistance can typically rise by upto 50% within the operating voltage of the cell. For the studied cell, resistance is largely independent of SoC.

- Charge re-distribution will have a major impact on cell voltage when SCs are meeting the power demand for an automotive drive cycle, and therefore must be accounted for during model development.

- SC degradation as a result of energy throughput is significantly lower than LIB degradation, therefore transitioning energy away from the battery to the SC should help reduce energy storage system degradation as hypothesised.

- The rate of SC degradation is rapidly increased when a voltage or temperature threshold is exceeded. The aforementioned voltage threshold is a strong function of temperature.

3.6 SC Model Development

3.6.1 Introduction

In a HESS SCs will be used for both high power, highly transient loads and low power steady loads. As the SCs will be required to meet high power demands, they will rise in temperature during operation. Repetitive high current charge and discharge pulses, as are common in the automotive environment, can lead to the formation of temperature gradients where the internal structure of the cell is hotter than the surface of the cell. The performance of SCs varies with temperature, particularly at low temperatures, [103]. Consequently, accurate electric modelling of SC performance for high currents over extended time periods requires knowledge of the temperature across the active material. In this section an electro-thermal model is developed in which the electrical model is temperature dependent and considers the temperature evolution of the active material.

3.6.2 Heat Transfer Model

3.6.2.1 Literature Review

To determine the temperature variation of a supercapacitor during operation, multiple authors have developed thermal models, which are suitable for a range of applications. For consideration of early cell design, d'Entremont et al [104] have calculated the reversible and irreversible heat generation during electrical operation using a continuum physical electrical model based on the Gouy-Chapman-Stern approximation of double layer. The model therefore defines the non-uniformity of heat generation throughout the active material. However, the study assumes the use of solid carbon planar electrodes rather than highly porous electrodes.

The majority of academic literature on this topic is concerned with the study of commercial SCs, and the heat diffusion equation is solved in one [105], two [106], or three dimensions [50] [107]. If solving the heat diffusion equation in one direction, heat transfer occurs through the material thickness of contacting materials, directly between the core of the cell and the outer surface of the can; axial temperature gradients (between the opposing terminals of a cylindrical cell) are not considered. If solving in two dimensions, axial temperature gradients can be considered, however the heat transfer around the spiral of the jelly-roll cannot. If solving in three dimensions, the aforementioned limitations are addressed, at the expense of computational cost. The full 3D model developed by Frivaldsky [107] in Comsol can be used to verify the thermal results of reduced order models, (if the temperature changes are not a result of electrical activity as the model of Frivaldsky has no electrical coupling).

The works of Gualous et al [106] experimentally measure the difference in temperature between the core and the surface of a cell during operation, and latterly model the thermal behaviour using a simplified two dimensional heat diffusion equation. These results demonstrate that the core of the cell is hotter than the surface during operation. It must be considered however that the insertion of (non-calibrated) thermocouples into the jelly-roll increases resistance, reduces axial thermal conductivity (some contact welds are missing), reduces radial thermal conductivity (looser winding), and increases the radial temperature gradient between the core and surface of the cell, (via elimination of the air gap between the jelly-roll and can).

The few authors [105,108] who have combined electrical and thermal models to produce electro-thermal models have used lumped thermal models only. The models are capable of providing reasonable estimations of electrical performance and temperature change over a range of electrical and thermal conditions. Berrueta et al [108] develop a temperature dependent electrical model, but ignore thermal gradients. The works of Parvini et al [105] do not constrain parameters within logical

limits as their electrical model has a capacitance value 10-15 times greater than the capacitance of the cell. The thermal model is lumped with an assumption of a fourth order polynomial cooling rate radially between the core and can, which does not account for the discontinuity of the air gap between the jelly-roll and can.

Given that SCs will be used for high power, highly transient loads in HESSs, it is necessary to develop a high fidelity thermal model capable of predicting axial and radial thermal gradients to investigate their magnitude and effect upon electrical performance. The works of Gualous et al [106] suggest a thermal gradient between the core and surface of the cell in excess of 6°C when cycling a cell at 95% efficiency (as defined by Equation 16), which could result in significant differences in electrical properties at low temperatures.

Knowledge of cell resistance and hence temperature of the active material immediately after a high current pulse is of interest in a HESS as it will influence the rate of current transfer between a SC and battery. Heat transfer between the active material and the surface takes time, therefore a lumped model which perfectly predicts cell surface temperature would under predict temperature change at low time periods, causing issues with resistance estimation.

3.6.2.2 Model description

To predict the temperature distribution across a cylindrical SC cell, a pseudo-3D heat transfer model is developed. Whilst it is desirable to have a thermal model capable of predicting axial and radial thermal gradients, the computational time associated with a 3D model is undesirable given that the model will be further slowed down by coupling with an electrical model. Therefore, a series of 1D thermal models are combined in a manner similar to that employed by Damay et al for LIBs, [109]. Axis-symmetry is used to reduce model complexity. The cell is divided into unit areas, and the geometric and thermal properties are defined using an equivalent thermal circuit analogy.

Each material has a defined thermal capacity and thermal resistance determined from literature in the *x*, *y* and *z* directions; Figure 23 graphically illustrates the manner in which this is distributed across the jelly-roll. The nomenclature for directional heat-transfer in this paper is defined as:

- *X*-direction: Heat transfer around the spiral in a given material.
- *Y*-direction: Axially lengthwise between the terminals of the cell in a given material.
- *Z*-direction: Radially across the thickness of the jelly-roll, between different materials.

Each turn of the spiral is discretised individually, and further split into ‘n’ segments along the Y-direction of the jelly-roll. As shown in Figure 23, each unit cell of the jelly-roll can conduct in the *x* and/or *y* directions to adjacent unit cells, or in the case of current collectors at the ends of the cell, into the terminal materials. Each unit cell can also conduct heat in the *z* direction, through the intermediate layers, which can be represented as a thermal short-circuit through the jelly-roll rather than around it. Heat-transfer in the *z*-direction through different materials is treaded as per the *x* and *y* direction, with varying material geometry and properties for each layer. This is graphically illustrated in the lower portion of Figure 23. It is assumed that the interface between materials does not introduce an additional thermal resistance; the model was found to be insensitive to the use of this assumption as the heat transfer in the *z*-direction is dominated by the low thermal conductivity of porous carbon.

Unit cells increase in width in the *x*-direction from the core to the edge of the jelly-roll because each x-direction discretisation consists of one turn of the spiral, and each turn of the spiral results in a progressively larger diameter. For the outer turns of the jelly-roll, where the unit cells are relatively long in the *x*-direction, heat transfer across the layers (in the *z*-direction), can be appreciable relative

to heat transfer around the jelly roll (in the *x*-direction) despite the higher thermal conductivity of the materials in the *x and y* directions. For the inner turns of the jelly-roll, heat transfer in the *x, y* direction around the jelly roll is dominant compared to through the layers, as the unit cells are now relatively short in the *x* direction. By discretizing with unit cells with variable *x* length and thermal short-circuits representing heat transfer between layers it is possible to model 3D temperature gradients in a straightforward way. Unlike the thermal model developed by Gualous et al, [110], heat transfer is considered in each direction, the heat transfer rate is dependent upon the geometric and thermal properties of each material, and crucially the air-gap between the jelly-roll and aluminium can is accounted for. This approach makes use of spiral symmetry to prevent the high computational cost associated with a fully discretised 3D model.

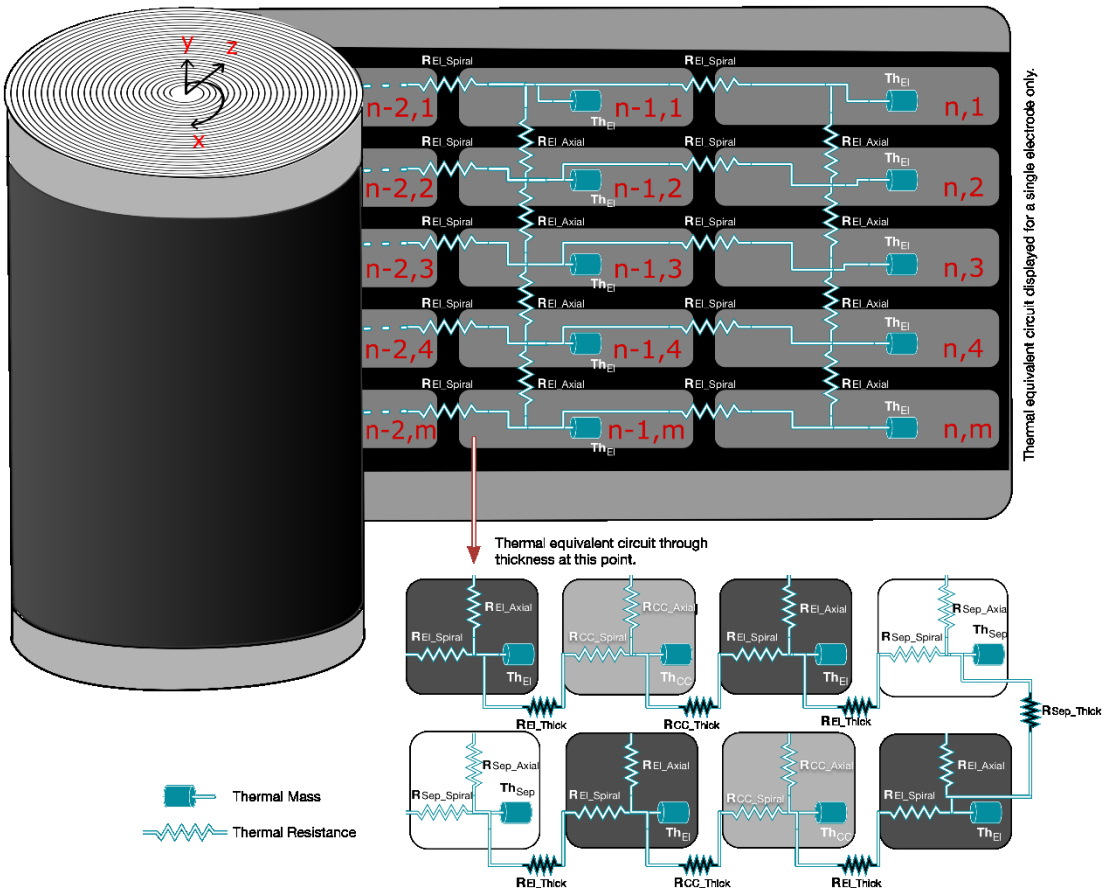


Figure 23: Illustration of the structure and discretisation of the jelly-roll in the developed pseudo-3D thermal model – [Top] Partially unwound jelly-roll with grey blocks illustrating the thermal model discretisation [for 'n' x 'm' elements] and a thermal equivalent circuit showing the thermal resistance and capacitance through a single electrode only, [Bottom] Illustration of the thermal connection between material layers, (heat transfer in the Z direction), in the jelly roll at discretisation segment (n-1,m) via a thermal equivalent circuit

There are two mechanisms for heat transfer between the system and the surroundings: conduction from the jelly-roll through the current collectors and further to the cell terminals, and convection, across the air gaps at the centre and outer boundary of the jelly-roll.

The utilised model for the jelly roll, the structure of which is shown in Figure 23, contains 1,764 thermal mass elements, 1640 conductive heat transfer elements in the *x* direction, 1344 in the *y* direction and 1470 in the *z* direction.

3.6.3 Electrical Model

Numerous authors have constructed models to predict the electrical behaviour of EDLCs that can broadly be categorised as either physical models [111–113] or equivalent circuit models, [71,76,77,104,114–116] . Although the physical models provide us with more information about the phenomena occurring within the cell, these models remain relatively immature, and to date, no model has provided validated results over a complex drive cycle. Lajnef et al, [115], developed a generic equivalent circuit model for an EDLC as shown in Figure 24a, and demonstrated that it reproduced EDLC behaviour reasonably well over long time periods whilst at a constant temperature. Devillers et al, [116], compares the accuracy of multiple electrical models over a period of 700 seconds at different temperatures, and confirms the findings of Lajnef et al. For this study, good reproduction of electrical behaviour over complex drive cycles is necessary, therefore an equivalent circuit model is favoured over a physical model.

The generic model in Figure 24a can be simplified to the very basic form seen in Figure 24b for frequencies between 1mHz-10Hz and time periods <500s. The author found that a single transmission line and a single RC branch can provide good voltage matching over transient loads and provide a good estimate for charge-redistribution for a particular time period, whilst being relatively simple to parameterise. A cell utilising porous electrodes has many time constants, thus for longer model operational time it is necessary to utilise additional RC and transmission line branches.

The transmission line branches model the available capacitance for a given resistance to adsorption, which is analogous to the ion adsorption path tortuosity, [85]. Each RC branch has a time constant that relates to the re-arrangement of ions; charge re-distribution is a non-linear process, hence the greater the number of RC branches utilised, the lower this discrepancy will be, at the trade-off of greater complexity. A detailed description of the correlation between electrical circuit elements and the physical processes occurring within the cell during operation has been complete by numerous authors, [35,108,117]. The following works study the effect of transmission line length, [35], and the number of RC branches, [118].

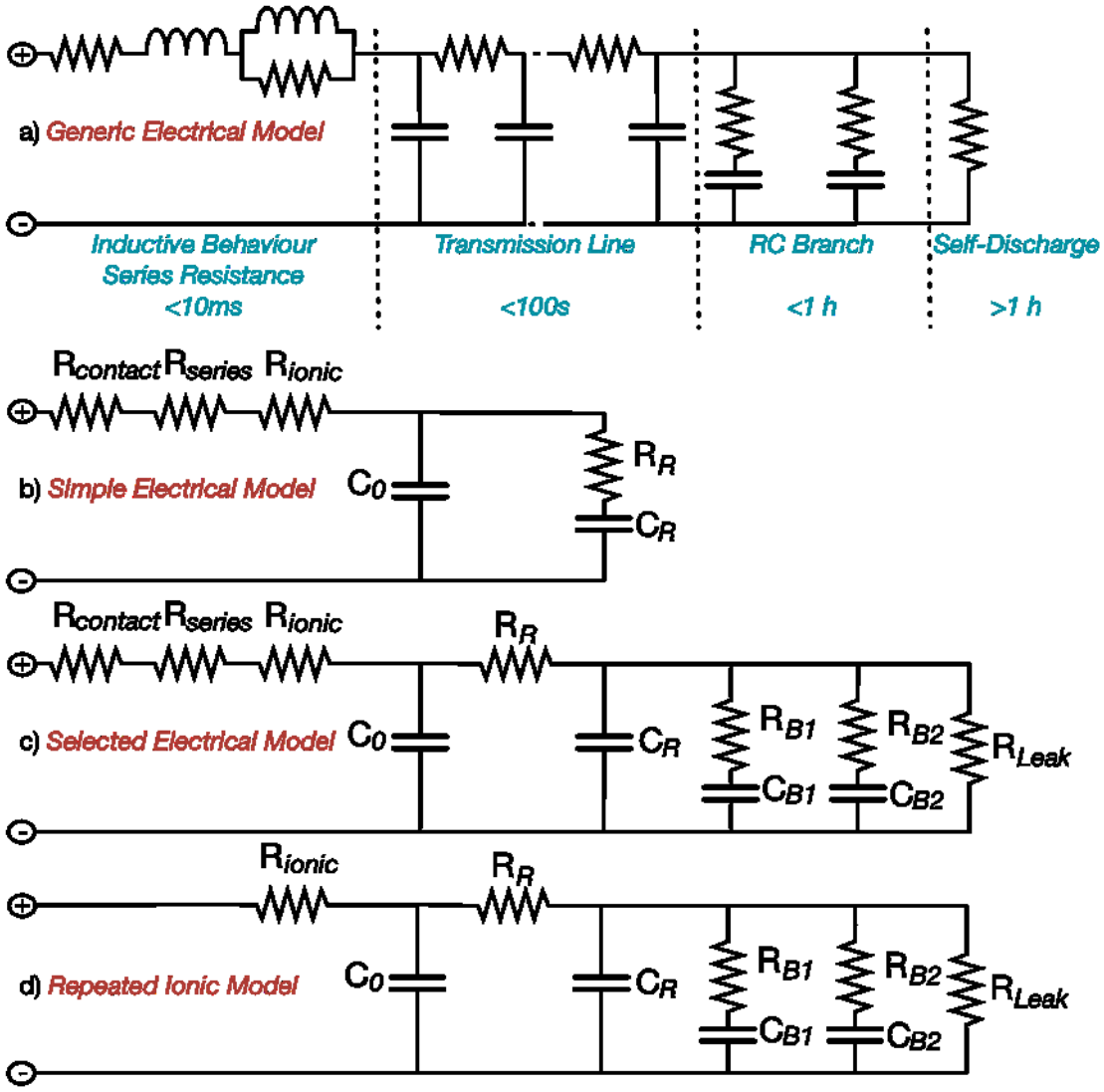


Figure 24: [a] A generic electrical equivalent circuit model which has been discretised by time domain for the electrical modelling of an EDLC - adapted from Lajnef [117] [b] Highly simplified electrical equivalent circuit model, [c] Selected model to be used during electrical parameterisation, [d] Repeated ionic unit used within semi-physical high fidelity model.

Figure 25 shows the evolution of the constituents of a pore within the electrode from an uncharged state to a fully charged state, and their representation in the model. Following the elapse of time period T_1, the initial charge of the transmission line is complete, however counter-ions and solvent molecules remain trapped within the pore. Given continuation of charging, the charge saturation of the pore will increase, with different stages of charge saturation being associated with increasing time constants of an RC branch.

The number of RC branches required to re-produce cell behaviour depends upon the time period of interest, and the accuracy required. Additionally, it is desirable to minimise the number of model parameters for consistency and reproducibility. The model shown in Figure 24c provides sufficient accuracy for the scope of this study over a broad range of conditions upto an operation time of 1500s, as shown in the model validation section.

Although electrical equivalent circuit models are capable of predicting the voltage response of EDLCs very accurately, the existing electrical cell models are empirical models and therefore cannot spatially define electrical activity and hence heat generation. Therefore, the use of a single electrical

equivalent circuit model with lumped resistances, such as that seen in Figure 24c, with a highly detailed thermal model necessitates the assumption of uniform volumetric heat generation. However, due to differing current paths and internal temperature gradients, the electrical activity, and hence rate of heat generation could vary throughout the cell. Consequently, it is necessary to create an electrical model that accounts for localised electrical activity throughout the cell, which can be used to determine whether the heat generation model must be distributed or lumped.

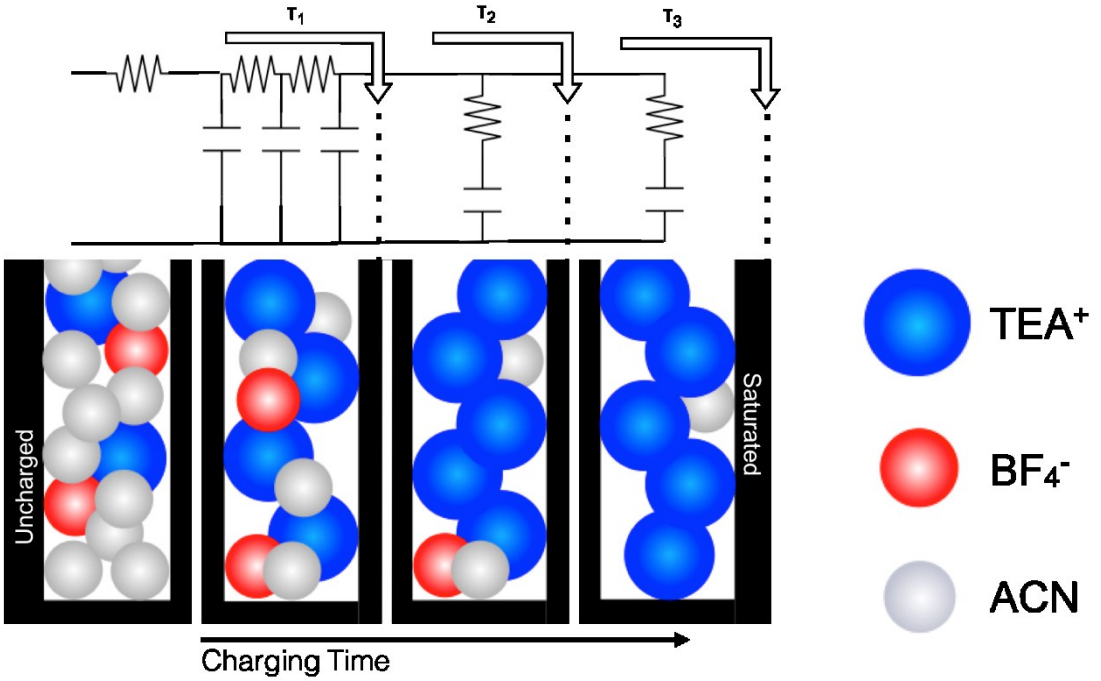


Figure 25: Illustration aligning the transmission line ($\tau 1$) and the RC Branches ($\tau 2$ & $\tau 3$) with different degrees of charge saturation within a carbon pore. Illustrations depecit findings of [51,65,66]

The equivalent circuit model in Figure 24c can very accurately recreate the voltage response of an EDLC, as shown in the model validation section. Therefore it is adapted to create a semi-physical high fidelity EDLC electrical model, illustrated in Figure 26. The model describes the electrical resistance path and spatial ionic activity of the cell using resistor networks and repeated equivalent circuits. The connections between the electrodes mimic ionic activity; each connection is via the repeated ionic circuit illustrated in Figure 24d. The electrodes are discretised into *'m'* axial segments, (between the electrodes/*y*-direction), and *'n'* radial segments, (each turn of the spiral jelly roll/*x*-direction).

A reduced schematic of the electrode resistor networks used to model the current collectors and electrodes is shown in Figure 26. Electrical resistances for the current collector and carbon are given as a function of the material resistivity and geometry. In the rolled jelly-roll, the matching node co-ordinates marked on the electrodes will form a locally flat electrode pair between which ionic movement can take place. The positions of nodes for ionic connection are shown on the resistor networks and the ionic connection between the resistor networks are illustrated in Figure 26. Each node is marked with co-ordinates (*i*,*j*), where *i* denotes the number of the turn within the spiral of the jelly roll, and *j* denotes the distance in element numbers away from the positive terminal, where each element is an equal fraction of the distance between the positive and negative terminals. Each ionic connection is made via the electrical circuit shown in Figure 24d, where its positive connection connects to (x,y) on the positive electrode, and its negative terminal connects to (x,y) on the negative terminal.

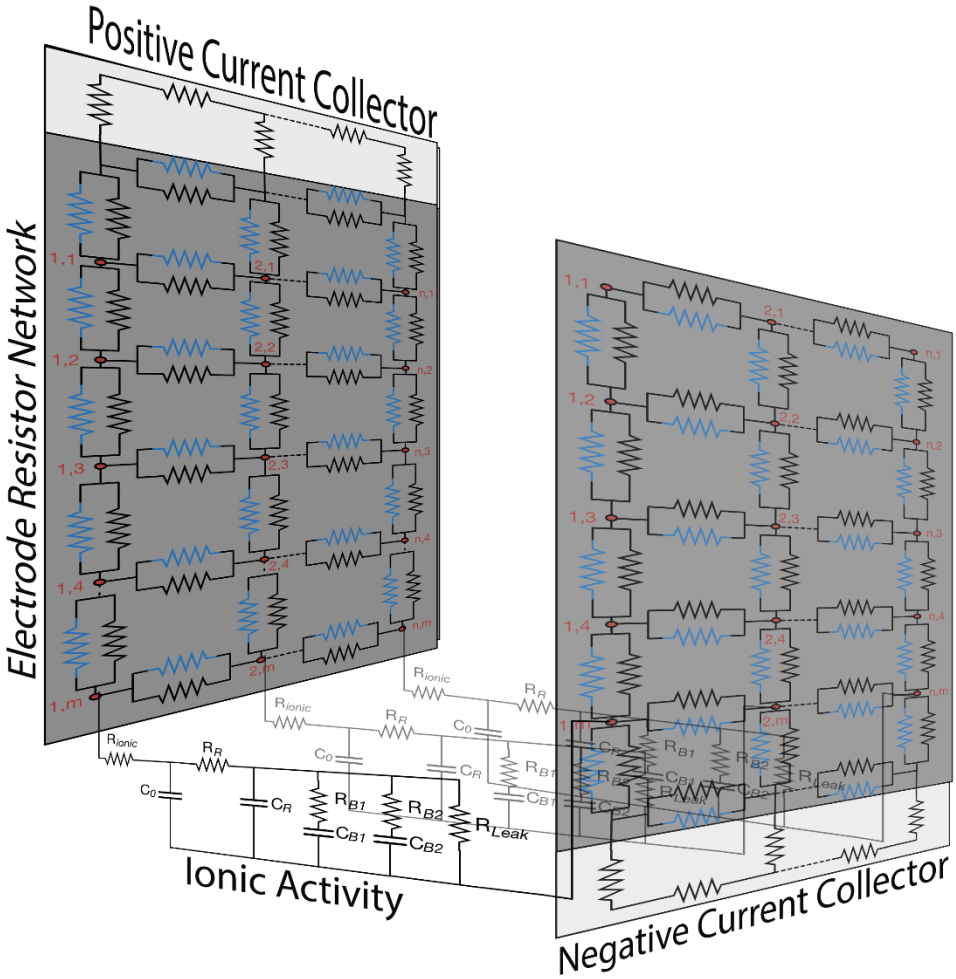


Figure 26: Reduced schematic of high fidelity semi-physical electrical model. The positive and negative electrode resistor networks are connected at nodes via a repeated electrical circuit which is shown to connect co-ordinates (1,5) and (2,5) on the positive and negative electrodes

3.6.4 Heat Generation Model

3.6.4.1 Heat Quantification

The heat generated within a supercapacitor can be categorised as either reversible or irreversible. The 'reversible heat' is due to changes in the arrangement of ions between the charged and uncharged states, and hence, changes in entropy. Schiffer et al [119] define the entropy of each double-layer for a monovalent electrolyte within the cell as:

$$S_{dl} = \frac{kCV}{e} \, ln\left(\frac{v_H}{v_0}\right) \qquad \text{Equation 21}$$

Where S_{dl} denotes the entropy of the double layer (J/K), v_H is the volume of the Helmholtz layer (m^{-3}), v_0 is the electrolyte volume, (m^{-3}), k is the Boltzmann constant $(m^2 kg s^{-2} K^{-1})$, and e is electron charge (C).

The underlying assumption is that the double layer is solely formed of a Helmholtz layer; a single layer of ions perfectly balances the charge on the electrode, the thickness of the double layer does not vary and is equal for both electrodes. The work of Schiffer et al [119] and Gualous et al [106] demonstrate that these assumptions remain valid for a highly microporous cell when assuming homogenous heating within the cell. Whilst the works of d'Entremont et al [104] indicate that the entropy at the positive and negative electrodes differs when the electrolyte contains dissimilar ions,

to the best knowledge of the author, no works have shown the difference in the entropic heat generated at the positive and negative electrodes. The entropy at each electrode is calculated in order to assess the heat generation within the cell.

Assuming the size of the double layer does not change with time, the entropy change with respect to time is:

$$\frac{dS_{\mathrm{dl}}}{d\mathrm{t}} = \frac{k_B \mathrm{C}}{\mathrm{e}}\, ln\left(\frac{\mathrm{v_H}}{\mathrm{v_0}}\right) \frac{d\mathrm{V}}{d\mathrm{t}} \qquad \text{Equation 22}$$

And the corresponding generation heat rate:

$$\frac{dQ_{\mathrm{reversible}}}{d\mathrm{t}} = -\mathrm{T}\,\frac{dS_{\mathrm{dl}}}{d\mathrm{t}} \qquad \text{Equation 23}$$

Substituting Equation 22 into Equation 23, and using, $\frac{\mathrm{d}V}{\mathrm{d}t} = \frac{I(t)}{C}$, an expression for the reversible heat generated at the positive and negative electrodes can be obtained:

$$\frac{dQ_{\mathrm{reversible_+}}}{d\mathrm{t}} = -\frac{\mathrm{Tk}}{\mathrm{e}}\, ln\left(\frac{\mathrm{v_{H_-}}}{\mathrm{v_0}}\right) \mathrm{I(t)} \qquad \text{Equation 24}$$

$$\frac{dQ_{\mathrm{reversible_-}}}{d\mathrm{t}} = -\frac{\mathrm{Tk}}{\mathrm{e}}\, ln\left(\frac{\mathrm{v_{H_+}}}{\mathrm{v_0}}\right) \mathrm{I(t)} \qquad \text{Equation 25}$$

The electrolyte typically utilised within commercial supercapacitors is Tetraethylammonium terafluoroborate, ($TEABF_4$), where the de-solvated positive ion (TEA^+) is 42% larger than the negative ion ($BF_4{}^-$), (0.68nm vs 0.48nm). Consequently, inserting values into Equation 24 and Equation 25, it is calculated that approximately 40% more entropic heat is generated at the positive electrode.

'Irreversible heat' generated within the cell is a result of losses due to electronic resistances within the solid phase and ionic resistances in the liquid phase. The irreversible heat generated is expressed as:

$$\frac{dQ_{\mathrm{irreversible}}}{d\mathrm{t}} = \sum_{\mathrm{j=1}}^{\mathrm{n}} \mathrm{R_x(T)\,I(t)^2} + \mathrm{I(t)^2 R_{contact}(T)} \qquad \text{Equation 26}$$

where R_x is the resistance of branch 'x' (Ω).

It is assumed that chemical reaction heat, i.e. that attributable to degradation via faradaic reactions, can be neglected when operating the cell within the manufacturer's defined operating conditions.

3.6.4.2 Heat Location

As described in the experimental methodology section, significant efforts were made to ensure contact resistances are consistent, therefore the heat generated across the contact resistances is equally applied to the positive and negative terminals.

The heat generated as a result of the series resistance within the cell is split between the carbon electrodes and aluminium current collectors as it is attributed to resistance in the solid phase. The electrical resistance of the carbon is two orders of magnitude greater than the resistance of the

aluminium [120,121], therefore heat generated as a result of the series resistance is allocated proportionally using a ratio of 99:1.

Ionic resistance is attributed to diffusion through the porous electrodes and separator. Ideally the distribution of heat should reflect the relative tortuosity of the electrode and separator, however this information is unavailable, therefore the heat is split gravimetrically.

System entropy and the disorder of ions within the electrolyte is at its maximum when the cell is fully discharged and ions can occupy the entire volume of the electrolyte. Charging the cell and ordering the ions at the electrodes results in a state of minimum ion disorder and entropy. Ion movement results in a local entropy change, thus the entropic heat is distributed over the volume occupied by the electrolyte, thus as per the ionic resistance it is distributed gravimetrically across the electrodes and separator.

3.7 Model Parameterisation

3.7.1 Electrical Model

The electrical model parameters are estimated using data acquired from Electrochemical Impedance Spectroscopy (EIS), and constant current charge and discharge curves. These parameter values are subsequently refined within tight boundaries using the Simulink parameter estimation toolbox. The parameters used in this model can be found in Table 4.

3.7.1.1 Capacitance

The measured capacitance is defined in the model as:

$$\mathrm{C_{measured}} = \mathrm{C_{Transmission_Line}} + \mathrm{C_{RC\ Branch}} \qquad \text{Equation 27}$$

where the transmission line capacitance, $C_{Transmission\ Line}$, is analogous to the capacitance of the easily accessible part of the porous structure, whereas the capacitance of the RC branches, $C_{RC\ Branch}$, is analogous to the capacitance of the difficult to access regions of the porous structure. The ease of access to the porous structure and the required adsorption energy vary based upon the tortuosity of the ions path to adsorption.

The transmission line capacitance is equal to the measured capacitance at the highest current of interest. Further, the transmission line capacitance is split into two capacitances, C_0, and C_R each of which has a voltage proportionality, C_v.

$$\mathrm{C_{Transmission_Line}} = (\mathrm{C_0} + (\mathrm{C_0}.\mathrm{C_v}.\mathrm{V})) + (\mathrm{C_R} + (\mathrm{C_R}.\mathrm{C_v}.\mathrm{V})) \qquad \text{Equation 28}$$

Where C_0 is the primary capacitance and is the capacitance measured at zero volts, which can be determined by backwards extrapolation of the capacitance curve in Figure 14, and inspection of the y-intercept. C_v is the capacitance voltage proportionality factor, and C_R is the re-distribution capacitance, which is typically 10% of C_0.

Given Equation 27 and Equation 28, it is possible to determine the RC branch capacitance from experimental data. However, the capacitance of each branch depends upon the number of branches, and the time period of interest. As an initial estimate, it is therefore suitable to distribute this capacitance equally between the branches. The optimisation algorithm refines the value.

3.7.1.2 Resistance

The measured resistance is implemented in the model as:

$$\mathrm{R_{measured}} = \mathrm{R_{series}} + \mathrm{R_{ionic}} \qquad \text{Equation 29}$$

The series resistance varies linearly with temperature as shown in Figure 14, hence can be given by:

$$\Delta R_{series} = R_{series_0}(1 + \alpha(T - T_0)) \quad \text{Equation 30}$$

where ΔR_{series} is the temperature dependent change of series resistance (Ω), R_{series_0} is the resistance at the initial temperature (Ω), α denotes the temperature coefficient of terminal material ($^{\circ}C^{-1}$) , T is the temperature of terminal (°C) and T_0 is the starting temperature of terminal (°C). The ionic resistance varies with an Arrhenius relation with temperature, and also varies with SOC, hence is given by:

$$R_{ionic} = (AV^2 + BV + D)exp(F/T) \quad \text{Equation 31}$$

Where A, B, D and F are dimensionless experimentally derived constants from EIS.

The RC branch resistance, $R_{RC\ Branch}$, is the resistance associated with the adsorption occurring in the high-energy/difficult to access adsorption areas. The resistance to ion flow in these areas is significantly higher than that of easily accessible areas, however the former contributes little to the measured resistance of the cell as there is little activity in these regions. As such, Equation 29 should include $R_{RC\ Branch}$ with a weighting factor determining its contribution to R_{ionic} as a function of the current through the RC branches. In reality, the current passing through the RC branches is difficult to quantify without a model, hence the calculated values of R_{series} and R_{ionic} are over-estimates and are used in the parameter optimisation as maximum values. The time constant of the redistribution branch, $\tau_R = C_R.R_R$, must correspond to the time required to discharge the cell from its maximum SOC, to minimum SOC at the maximum current that the model is valid for.

The resistance of the RC branches is determined by:

$$R_{Branch\ x} = \frac{(x/N).t_{Limit}}{C_{Branch\ x}} \quad \text{Equation 32}$$

where $R_{Branch\ x}$ is the resistance of branch *x*, N is the number of branches and t_{Limit} (s) is the period of model validity, upto a maximum of one hour.

Parameter	Value (F)	Parameter	Value (Ω)
C_0	500	$R_{contact}$	3.76e-5
C_v	0.105	R_{ionic}	3.84e-4
C_R	47.0	R_{series}	2.41e-4
C_{B1}	21.8	R_R	2.43e-2
C_{B2}	12.3	R_{B1}	6.32e-1
		R_{B2}	49.86
		$R_{leakage}$	9.47e+5

Table 4: Parameter values used in electrical model for Maxwell 650F Cell at 25°C

3.7.2 Thermal Model

The parameters for the thermal model were taken from literature, and are shown in Table 5.

Material	Specific Heat Capacity $(J\ kg^{-1}K^{-1})$	Thermal Conductivity $(W\ K^{-1}m^{-1})$	References
Aluminium Can	898	205	[122]
Aluminium Current Collector	898	205	[122]
Carbon Electrode (wet)	700	0.47	[123]
Separator (Paper Based) (wet)	1340	0.22	[124]
Polypropylene	1700	0.12	[124]
Air	1005	0.02	[122]

Table 5: Material properties for the parameterisation of the thermal model

3.7.3 Electro-thermal Model Configuration

The constructed electro-thermal model consists of a heat transfer model, a heat generation model and an electrical model. Above, multiple electrical models are presented in Figure 24 and Figure 26. The semi-physical high-fidelity electrical model presented in Figure 26 enables the heat generation model to locally define heat generation at each discretisation of the thermal model. However, it is significantly more computationally expensive than the use of the model presented in Figure 24c, which uses an assumption of uniform volumetric heat generation within a given material. Therefore, it would be highly desirable to make this assumption if possible.

To determine whether this assumption is valid, the spatial current density variation through the jelly-roll was examined with the use of the semi-physical high-fidelity electrical model. Figure 27 shows that dissimilar current paths through the jelly-roll lead to a variation in the current density, which will subsequently lead to spatial variations of the heat generated within the jelly-roll. However, the difference is small; for a 75A discharge starting at a uniform temperature of 20°C the total charge delivered between 0-14 seconds shows a maximum spatial difference of 1.4%, (with the greatest current density toward the radial core and axial extremities, i.e. (1,1) & (1,5)). These regions have the highest current density because they have the shortest resistance paths.

However, given that active material resistance will change with temperature, it is known that an existent temperature gradient enhances current density imbalance; this is shown in Figure 27b. Artificially imposing a constant temperature gradient of 6°C from the core to the edge of the jelly roll yields a maximum spatial difference in charge delivered of 3%.

Gualous et al [106] measured the radial temperature variation through a cell, and for an applied current of 15A found a temperature gradient of approximately 6°C between the can and the core of the jelly-roll, though the thermal gradient within the jelly-roll did not exceed 2°C. The thermal gradient found by Gualous et al is likely to be an overestimate due to the elimination of the air-gap between the jelly-roll and can during the insertion of thermocouples. The cell used by Gualous et al for these measurements has a volume of approximately a third and resistance 7 times greater than the cell used in this study, (Maxwell 650F). This study is interested in higher currents, therefore a value of a maximum temperature gradient of 6°C across the jelly-roll was assumed to be a reasonable test.

Given the small deviations in charge delivered by different regions of the jelly-roll, and hence small differences in heat generation, it was determined that it was reasonable to assume uniform volumetric heat generation in a given material. Consequently, the electrical equivalent circuit model in Figure 24c is utilised in conjunction with the heat transfer model in Figure 23 and the described heat generation model to form the electro-thermal model.

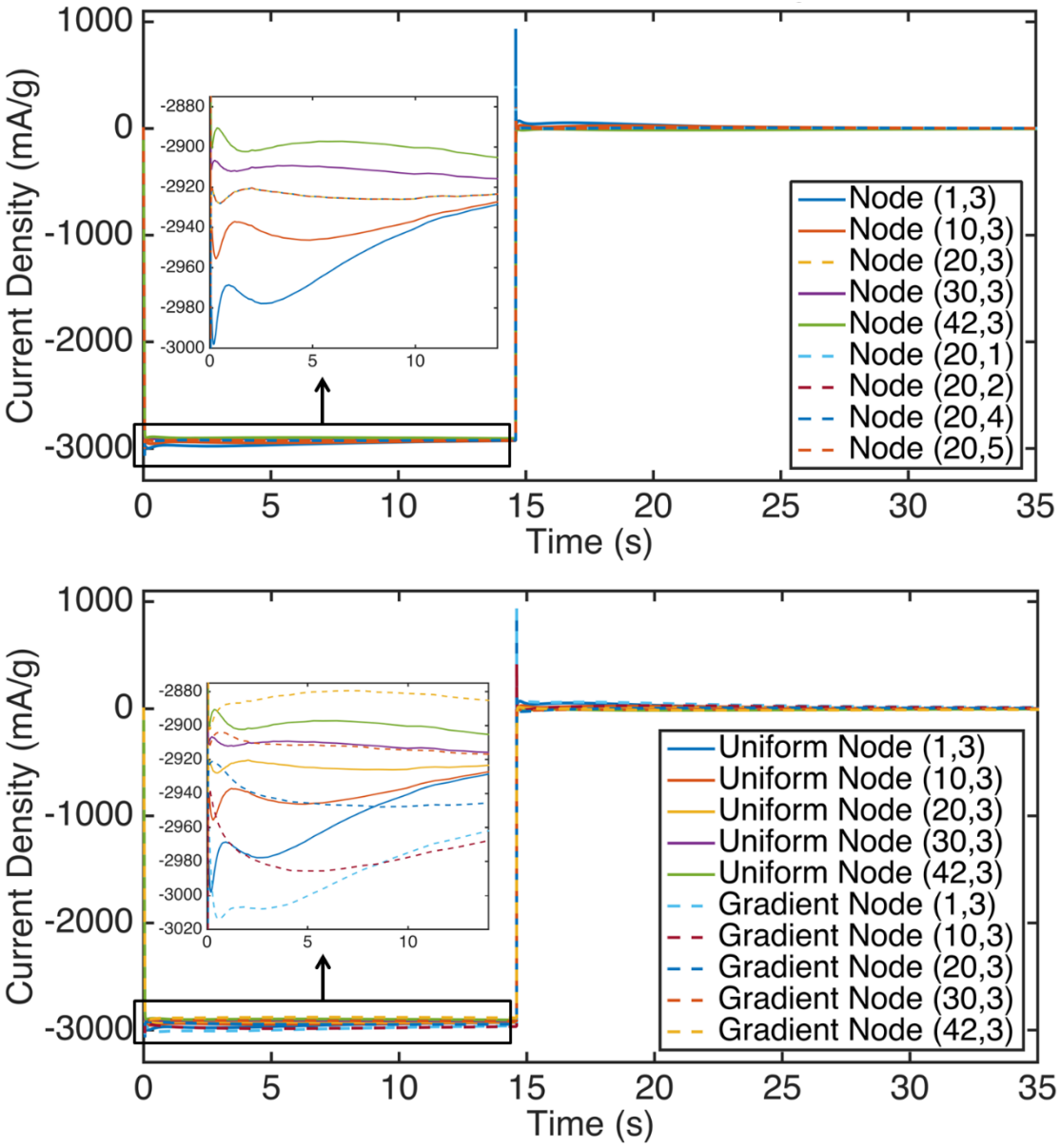


Figure 27: [a] Spatial current density variation through the jelly-roll whilst at a uniform temperature of 20℃ during a 15 second 75A discharge - Top. [b] Radial current density variation through jelly-roll of non-uniform temperature during a 15 second 75A discharge. An artificial radial temperature gradient of 6K between the core and edge of the jelly-roll was applied - Bottom.

3.7.4 Experimental Conditions for Validation

Charging and discharging of the cell is conducted using a Biologic HCP-1005 potentiostat with a 100A booster for currents upto 100A, and a Bitrode MCV for currents above this. EIS was conducted in galvanostatic mode with current amplitude of 3A using a Biologic BCS-815 potentiostat. For uniform temperature testing, an ESPEC BPL-3 thermal chamber was used.

Precise and accurate data was required for the thermal validation of the electro-thermal model. The best practise for cell preparation described in the experimental methodology section was utilised. Measures were taken to control the thermal boundary conditions; to prevent convection to the environment the cells were wrapped in an insulating material (Rockwool) with a thermal conductivity of 0.4W/mK. To control conduction to the environment, heating elements were attached to the cables of the cell-cycler, and a PID controller maintained the cables at the same temperature as the cell, thus minimizing heat transfer by minimizing the temperature difference.

3.8 Model Results, Validation & Discussion

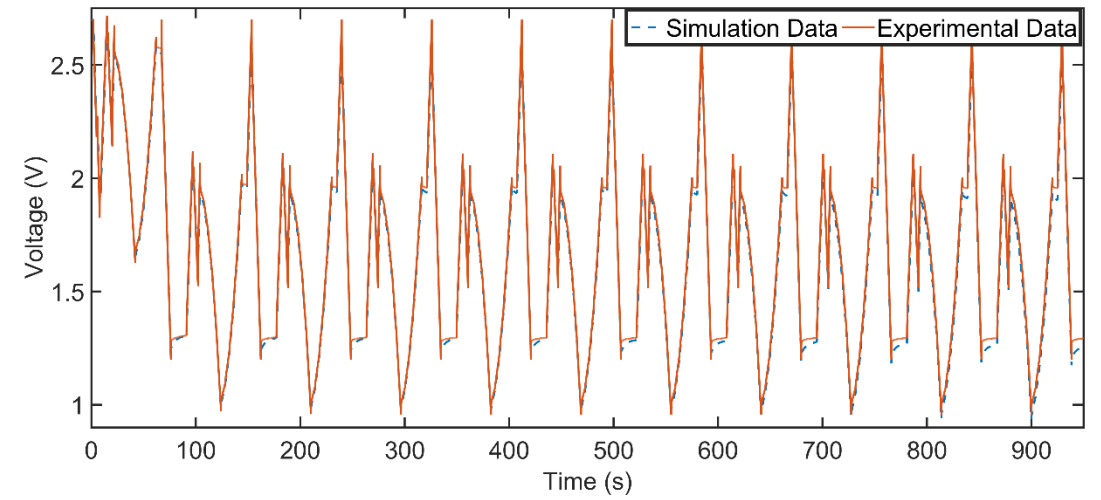
3.8.1 Electrical Model Validation

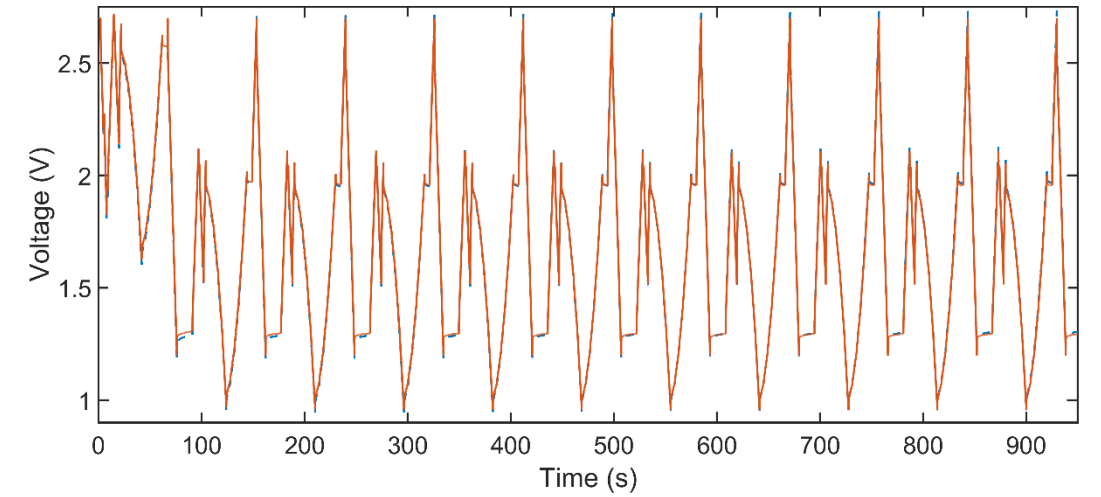
A current profile was developed to test the quality of the voltage estimation of the simple electrical model as seen in Figure 24b. A very good fit was achieved, with the maximum error occurring during the charge re-distribution process, most notably a short duration after a high current charge or discharge. The maximum error in the estimated voltage is 2%.

At times greater than 200 seconds, the voltage error of the simple model (Figure 24b) increases to 12% on the drive cycle seen in Figure 28c, therefore the model of increased complexity (Figure 24c) is used for all subsequent work in this paper.

For validation of the electrical element of the electro-thermal model, a transient drive cycle, seen in Figure 28c, is used to test the performance of the electrical model. This validation cycle has been developed to incorporate high and low currents, charges and discharges, different rates of change of current and different switching frequencies to test the model over an array of conditions. Figure 28a shows the voltage response of the complex electrical model (seen in Figure 24c) when operated at a constant temperature, whilst Figure 28b shows the voltage response when the electro-thermal model accounts for temperature changes because of electrical activity. The surface temperature rise over this cycle is 5℃, and thus resistance decreases with time.

If a constant temperature is input into the electrical model, as seen in Figure 28a, the model will not account for the decreasing resistance, and thus the error will increase with time and temperature rise. The maximum error at a time of less than 200 seconds is 2%. This error increases with time and by the end of the simulation at 950 seconds, the maximum error has increased to 4.3%. Figure 28b shows the voltage response where temperature change is accounted for. The resistance now changes with time, therefore the error does not increase with simulation time. The maximum error is stable at 2% and does not increase with time or temperature difference.





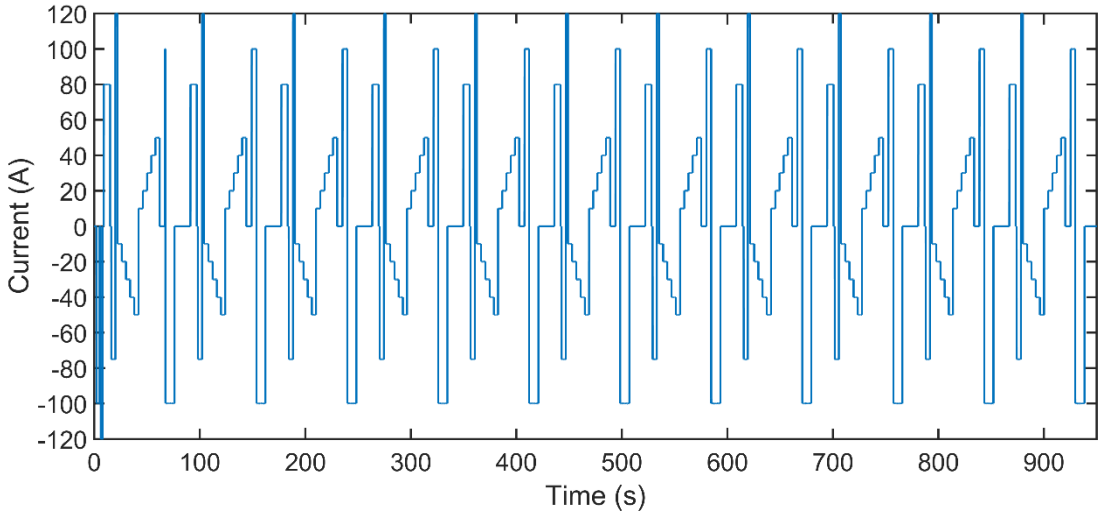


Figure 28a (Top) - Comparison of measured and simulated voltage of a Maxwell 650F EDLC over a highly transient load-cycle, using the complex model seen in Figure 24c with a constant temperature

Figure 28b (Middle) - Comparison of measured and simulated voltage of a Maxwell 650F EDLC over a highly transient load-cycle, using the complex model seen in Figure 24c with an updating jelly-roll temperature

Figure 28c (Bottom) – Current profile used for simulation in Figure 28a and Figure 28b

3.8.2 Thermal Model Validation

In real systems, temperature can only be measured at the surface of a cell, however it is mostly the temperature of the jelly roll which affects the performance and degradation of the cell. Therefore, it is desirable to understand the relationship between the surface temperature and the jelly-roll temperature. It is however useful to validate the model by examining the temperature change whilst charging and discharging over a range of conditions by examining surface locations. Initially, it is useful to examine the temperature change at a single surface location over a range of loading conditions, and latterly, to include other locations into the analysis.

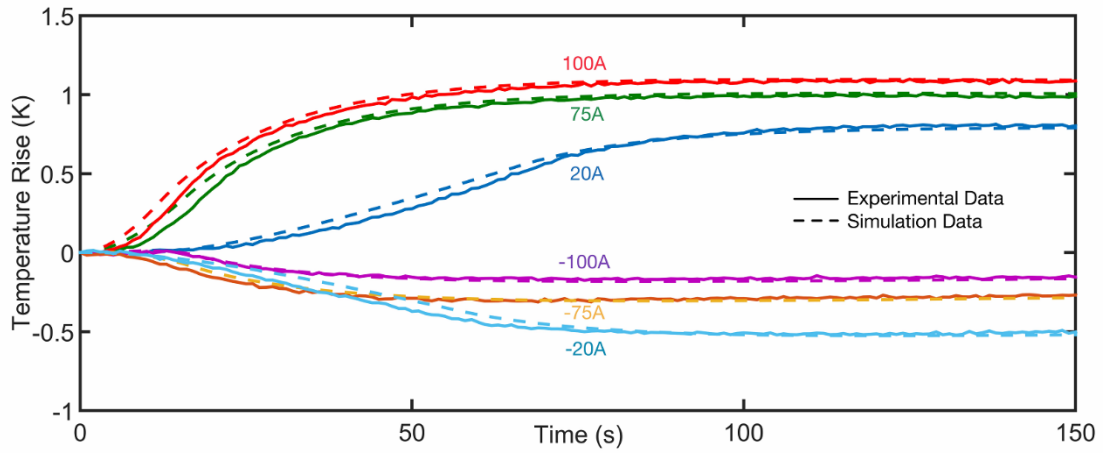


Figure 29: Temperature rise at the positive terminal for charge and discharge events from 20-100A

Figure 29 compares the simulated and experimentally derived temperature change at the positive terminal when the cell is charged or discharged between 0.1-2.7V. It demonstrates that the model provides a very good estimate for the total temperature evolution at the positive terminal for each charge or discharge event tested. Small discrepancies exist for up to 20 seconds for large current charges, and for up to 60 seconds for the small current discharges. The quality of fit, and location of maximum error in the simulated result is very similar at the negative terminal.

3.8.3 Predicted Internal Temperature

The thermal model allows the study of the coupling between the thermal and electrical properties of the cell, and its impact upon performance. For example, a detailed internal temperature map can be obtained for any electrical load.

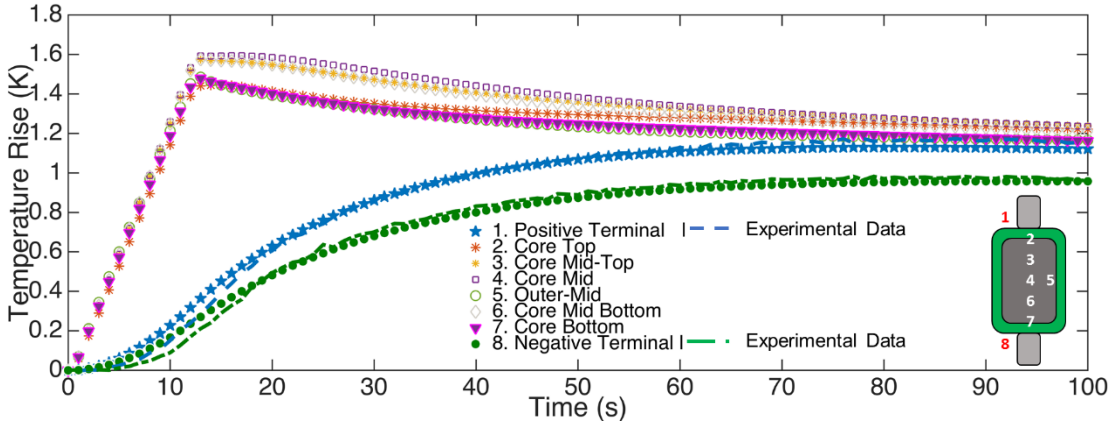


Figure 30: Predicted temperature distribution within a cell during and following a 100A charge from 0.1-2.7V

Figure 30 shows the model predictions of temperature evolution for various positions in the y-direction between the terminals, (during a constant current charge at 100A from 0.1-2.7V). Surface temperature measurements are shown for the positive and negative terminal; as in Figure 29 an excellent fit is achieved with the maximum error occurring at time periods of <20s. The maximum instantaneous temperature difference between the core of the jelly-roll and the surface of the cell is 1.23K, indicating that meaningful temperature gradients can be observed between the jelly-roll and surface of the cell during short duration pulse applications. The maximum temperature reached by the centre of the jelly-roll is 0.5K (46%) higher than the maximum temperature reached by the surface. The maximum temperature difference between the centre and outer edge of the jelly-roll is 0.1K, (6.2% cooler than the core). Table 6 shows the surface and core temperature differences for a range of currents. Following a 400A charge, the temperature gradient between the core and surface of the cell is in excess of 3.5K. Taking the surface temperature rather than the core temperature will induce an error of up to 6% in the resistance value, and up to 15% in the capacitance value. Whilst the duration of this error is limited to the period during which a thermal gradient is present, the errors will accumulate over time.

Charging Current	Maximum Predicted Temperature (K)		Maximum Predicted Temperature Difference (K)
	Surface	Jelly Roll	
75A	0.97	1.36	0.99
100A	1.09	1.59	1.23
400A	2.91	4.01	3.89

Table 6: Maximum cell temperature and maximum temperature difference for charging currents from 75-400A

Following periods of activity, thermal gradients form within the jelly-roll. Figure 31 shows the radial and axial thermal gradients between the core and the surface of the cell following the charge event at 1700s in Figure 32. There is little temperature variation (3%) in the radial direction due to the air gap between the outer surface of the jelly-roll (radial distance of 28mm from core) and the inner surface of the aluminium can (radial distance of 30mm from core). The axial temperature gradient (5%) is only slightly larger than the radial temperature gradient; however the axial temperature gradient is expected to be larger for longer cells, typically higher capacity cells within a product range, [37,38]. The core is 16% hotter than the surface in this particular test.

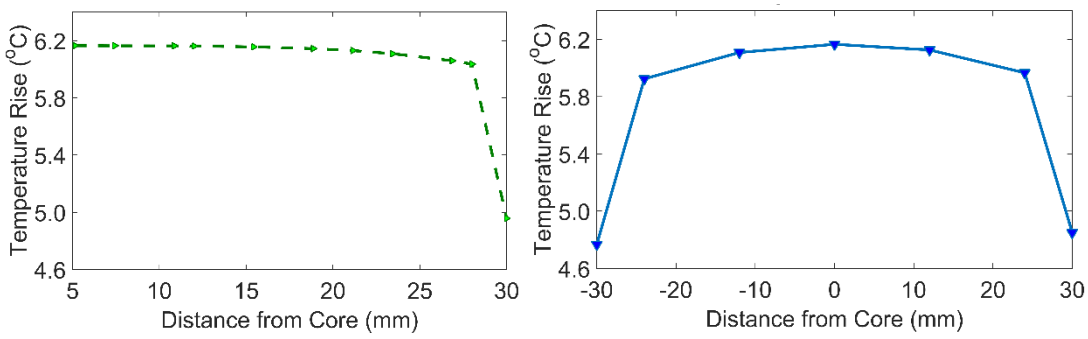


Figure 31: Predicted radial (left) and axial (right) temperature distributions in the cell from the core to the surface – Presented data taken following 1700s of continuous charging and discharging at 50A with natural convective cooling

It is shown in Figure 32 that following a period of continuously charging and discharging the cell at 50A between 1.2-2.7V, the predicted temperature at the positive and negative terminals of the cell matches the experimental data very well. The maximum error (0.3K) is seen at time periods between

600s and 1200s is equal for both the positive and negative terminals. The temperature of the positive and negative terminals diverges slightly over time; this divergence is predicted by the model and is a direct result of Equation 24 and Equation 25 derived above in section 3.6.4. As a result, this is the first model to predict this behaviour.

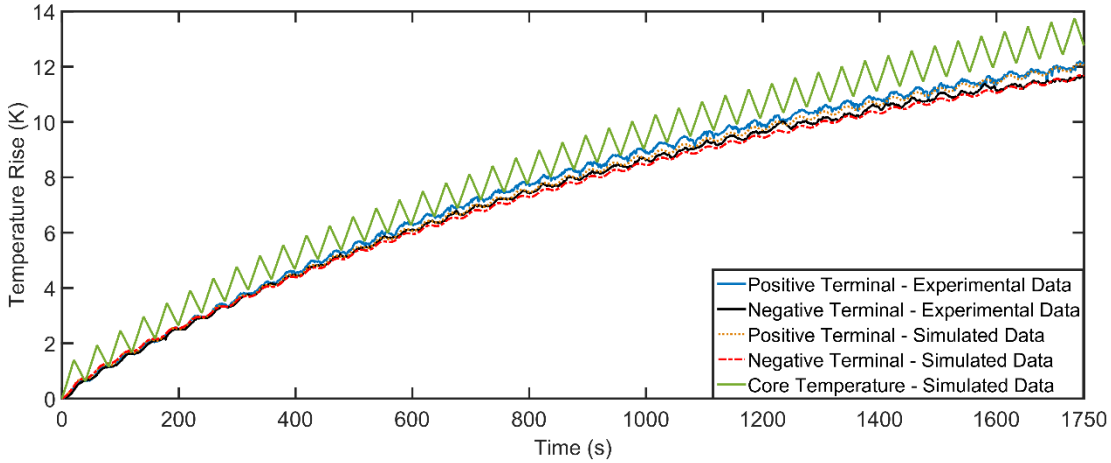


Figure 32: Comparison of temperature rise at the surface and core of the cell when in constant operation, i.e. continuous charge and discharge at 50A between 1.2-2.7V at 25℃

The model predicts that the temperature at the core of the cell is consistently higher than at the surface of the cell. Figure 32 shows the increasing divergence between the temperature at the core and at the surface of the cell.

The temperature gradient between the core and surface of the cell does not increase significantly over time because of good thermal conductivity between the current collectors and aluminium can. For heat generated within the carbon electrodes to conduct into the current collectors and subsequently the aluminium can, thermal gradients must exist, however these thermal gradients are supressed when the cell is discharged. Entropic heat generation causes heating on charge and cooling on discharge, and in the cell under study the combination of the ohmic and entropic heat caused by a 50A discharge results in a net cooling of the electrodes.

3.8.4 Comparison with Existing Works

3.8.4.1 Comparison with Experimental Data

Gualous et al [106] have inserted thermocouples into a cell and report measurements which show a much larger thermal gradients than predicted by this study; a comparison can be seen in Table 7. This result is expected as inserting thermocouples altered the physical structure of the device, and hence altered its thermal characteristics. The results of Gualous et al have been recreated in the model developed by this study to determine the physical changes necessary to account for the differences in thermal characteristics of the cell modified via thermocouple insertion.

Temperature Gradient Location	Measurements of Gualous et al (°C)	Predictions of this study (°C)
Core to radial edge of jelly-roll	1	0.1
Core of jelly roll to cell surface	Upto 5.4	Upto 1.2

Table 7: Comparison of temperature gradients predicted by this study with experimental works conducted by Gualous et al [106]

The thermal gradient between the radial edge and core of the jelly-roll can be re-created though elimination of the air-gap between the outer edge of the jelly-roll and the aluminium can. Gualous acknowledges that the jell-roll has been wound manually and that the 'mechanical tension is much smaller', which suggests that the aforementioned air-gap is not present in the cell with thermocouples inserted.

The thermal gradient between the surface and core of the cell can be re-created by greatly reducing the area of connections of the current collector with the terminals. Gualous et al acknowledge that 'current collector contacting is incomplete'. As a result, the thermal resistance for some parts of the jelly-roll is greatly increased as heat must conduct through a greater radial distance (in the *x*-direction) or through additional layers (in the *z*-direction) of aluminium, carbon and separator material to reach an area of current collector which is directly connected to a terminal.

3.8.4.2 Comparison with Existing Models

A lumped thermal model as utilised by numerous authors, [106,108,125,126], typically provides a good estimate of the overall temperature rise, however it cannot account for the time taken for heat to conduct from the core of the cell to the surface. As a result, the lumped model produces undamped results. A lumped model was generated using identical parameters for heat generation and heat transfer to the environment as the pseudo-3D model. A comparison between the results produced by the lumped thermal model and pseduo-3D model are shown below in Figure 33.

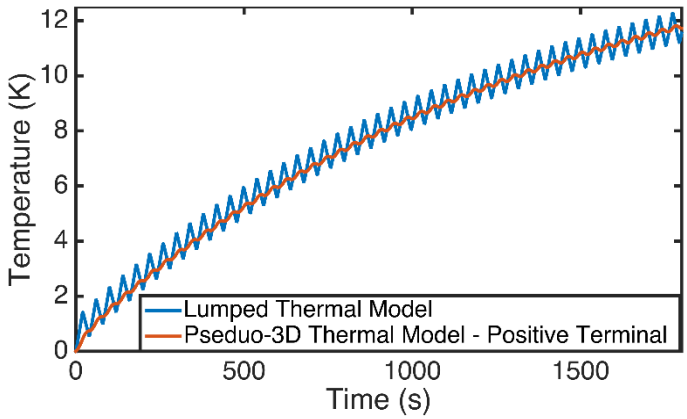


Figure 33: Comparison of temperature rise predicted by the lumped model and pseudo-3D model (positive terminal) when in constant operation, i.e. continuous charge and discharge at 50A between 1.2-2.7V at 25℃

A lumped thermal model is suitable if only the overall temperature rise is of interest. It cannot predict the temperature of the jelly-roll, and hence will introduce errors into the electrical model. Furthermore, over a single charge event (approximately 20 seconds) the maximum error is in excess of 200% (1℃ error). The use of a lumped thermal model in a capacitor management system would therefore lead to an overestimate of the rate of temperature change as a result of a pulse load.

Gualous et al [110] created a thermal model which considers heat transfer in the axial and radial directions (*y* and *z* directions), but does not consider heat transfer around the spiral of the jelly-roll (*x*-direction). Their model validation is complete using both a self-generated dataset and one provided by the Paul Scherrer Institute. The internal temperature measurements used for validation are of the central airgap of a Maxwell BCAP010 and a Maxwell BCAP0350 cell. The internal temperature measurements in this study clearly do not show the effects of entropy, which are shown very clearly in a latter study (2011) by the same author [106]. Consequently, the model also does not consider entropic thermal effects. Gualous et al do not show plots that show axial or radial

temperature distributions, and the pseudo-3D model developed in this study does not model the central air-gap, hence a meaningful comparison of findings is not possible.

Frivaldsky et al [107] created a 3D thermal model and evaluated the steady-state results to examine the temperature gradients which form. The axial and radial temperature distribution results shown in [107] are very similar to the results produced by the pseudo 3-D model which are shown in Figure 31. The model has no electrical coupling.

3.9 Modelling Conclusion

An electro-thermal model for a SC has been developed to predict the internal temperature of a cell whilst applying pulse loads. The electro-thermal model consists of a coupled electrical model, heat generation model and heat transfer model.

The electrical model is adapted from a generic physically meaningful equivalent circuit model of a SC. It is shown that the current density and hence rate of heat generation does not vary significantly throughout the jelly-roll. Therefore, it is suitable to assume uniform spatial heat generation within the jelly-roll although the temperature differs. The heat generation model considers both irreversible (ohmic) and reversible (entropic) heat generation. Typically, entropic heat generation is defined as a bulk value, however in this study entropy was independently calculated for the positive and negative electrodes. It is shown that the entropic heat generated at the positive electrode of a typical commercial SC is approximately 40% greater than that at the negative electrode. Consideration of entropy independently at each electrode was necessary to predict the temperature divergence of the positive and negative electrodes.

A physical pseudo-3D heat transfer model was developed to take advantage of the axisymmetric nature of cylindrical cells and avoid the high computational cost of a true 3D heat transfer model. Unlike other non-truly 3D thermal models, heat transfer is considered in each direction and the rate of heat transfer is governed by the geometric and thermal properties of the materials rather than bulk values. Consequently, the predicted radial temperature variation of the developed model shows a greater non-linearity than the other non-truly 3D thermal models, which is in line with the predictions of existing 3D thermal models.

The model indicates that under pulse load conditions, a temperature difference in excess of 3.5℃ can form between the surface of the positive terminal and the jelly-roll, however the temperature gradient across the jelly-roll is small. Therefore, it is important for electrical models to consider the temperature of the active material and not simply the surface of the cell when considering a high current pulse load condition. This is of particular importance in high capacity cells where the ionic resistance is greater than the series resistance. At very low temperatures, an increase of 3.5℃ can yield a change in resistance of up to 6% in the resistance value, and up to 15% in the capacitance value.

Greater knowledge of active material temperature of the SC enables a more accurate prediction of SC resistance and capacitance, which in turn enables a more accurate prediction of HESS performance when LIB and SC models are combined.

4.0 Lithium-ion Batteries

Motivation & Applicability to Research Questions

An understanding of the performance and characteristics of Lithium Ion Batteries (LIBs) is necessary for the development of an understanding of Hybridised Energy Storage Systems (HESSs) consisting of LIBs and SCs. This chapter briefly explains why LIBs are the dominant form of energy storage in electrified passenger vehicles, and subsequently discusses how LIBs function. The relationship between each component within the LIB and its performance is reviewed, and common internal design trade-offs such as material selection and thicknesses are explained. LIB performance variation as a function of operating conditions is subsequently presented and described analytically. This knowledge is used to generate a model to predict battery performance over a range of operating conditions, with a particular focus placed upon performance over an automotive drive-cycle. The causes of long term performance degradation are examined and a summary of degradation methods and their causes is provided.

4.1 Why use Lithium-ion Batteries in Automotive Applications

LIBs are the preferred form of energy storage for the automotive industry as it transitions to electrified passenger vehicles, [3,9,10,14,127]. Battery energy storage has a substantially higher well-wheel energy efficiency than hydrogen [128] or compressed air storage [129], and requires significantly less capital investment for energy supply infrastructure [130–133]. Furthermore, the lower volumetric requirements of battery energy storage enable automakers to produce a range of electrified vehicles with varying degrees of electrification using existing vehicle platforms, thereby reducing cost, time to market and risk. LIBs are preferred to other battery technologies largely due to their superior volumetric and gravimetric energy density as is evident from Figure 2 which graphically compares the energy density of LIBs to other forms of electrochemical energy storage.

Figure 1 summarises the requirements of energy storage systems for automotive applications; knowledge of these requirements enables a high-level configuration comparison of different electrochemical energy storage devices for a particular powertrain design. Telling benefits are revealed when the mass and volume required for other technologies are compared to a baseline LIB system.

The baseline used for comparison is a micro hybrid (mHEV) system from Audi, with a usable energy capacity of 0.24 kWh and power capability of 12kW. The minimum mass and volume of cells required to meet the requirements, whilst satisfying standard IEC 60038 [134] (which defines the required operating voltage range of 48V mHEV systems) is calculated and the results are displayed in Table 8, where it can be seen that the LIB ESS is by far the smallest and lightest.

To comply with increasingly stringent legislation and simultaneously increase the competitiveness of hybrid vehicles in the marketplace, a significant demand exists for batteries with higher energy density, [3,5,135–137]. An improved energy density should enable battery pack downsizing, however advancements in energy density are not typically accompanied by a corresponding rise in power density, and often power capability is reduced, [127,138,139]. This study aims to develop an understanding and predictive capability of HESS operation in automotive environments to evaluate whether the addition of the power capability of SCs enables the use of advancements in highly energy dense batteries in applications which typically require high power, such as HEVs.

	SC	Li-C	Pb-A	Ni-Mh	Li-ion
Suitable Cell	Maxwell BCAP 3400F	JSR Micro 3300F	East Penn Lead-Carbon	Panasonic Ni-Mh Prismatic	LG Ni-Rich NMC Pouch
Cell Configuration	20S5P	16S4P	4S1P (12V Modules)	50s3p	12S3P
Mass (kg)	51.0	22.4	31.1	25.0	11.9
Volume (L)	39.0	13.9	22.0	14.2	6.0

Table 8: Cell mass and volume required to replicate the performance of mHEV with a usable energy of 240Wh and power of 12kW that satisfies IEC standard 60038

4.2 Principle of Operation

A lithium-ion battery consists of a pair of porous electrodes which sandwich an ionically conductive yet electrically insulating separator, are adhered to current collectors, and immersed in an ionically conductive electrolyte. The electrodes serve as host materials into which lithium-ions can be intercalated (inserted into the bulk of the electrode) or extracted from/to the electrolyte. A schematic of the internal structure of a cell is shown below in Figure 34.

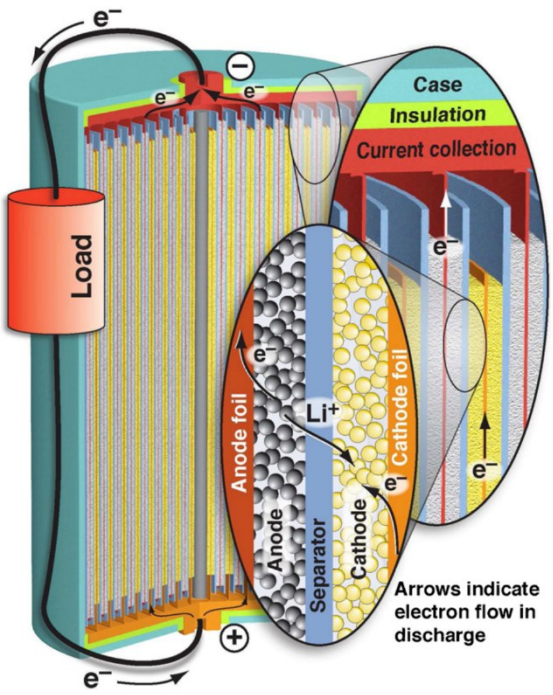


Figure 34: Illustration of the internal structure of a cylindrical battery cell at cell and particle scale -[140]

The cell is fully charged when the maximum permitted quantity of lithium is intercalated into the anode. When a load is applied to instigate a discharge, 'n' lithium ion (Li^+) are liberated from the interstitial space between atomic layers of the anode at the electrode/electrolyte interface via oxidation resulting in the release of lithium-ions and electrons. For a typical lithiated graphite electrode:

$$Li_{n+m}C_6 \Leftrightarrow^{Discharge}_{Charge} nLi^+ + ne^- + Li_mC_6 \qquad \text{Equation 33}$$

Simultaneous to the anode half-reaction, lithium ions intercalate into the cathode as this is the lowest available energy state. The lithium ions from the anode half-reaction are released into the

electrolyte where they diffuse to the cathode through the separator due to concentration gradients. The electrons are unable to pass through the separator, therefore they travel through the external circuit or load, via the electrodes and current collectors.

At the cathode electrode/electrolyte interface, a reduction reaction occurs between the lithium-ions and available electrons to intercalate lithium into the Lithium based Metal Oxide ($LiMO_2$) cathode in the form:

$$Li_xMO_2 + nLi^+ + ne^- \Leftrightarrow^{Discharge}_{Charge} Li_{x+n}MO_2 \qquad \text{Equation 34}$$

The depletion of lithium from the surface of the anode leads to a concentration imbalance between the surface and bulk. The concentration gradient gives rise to diffusion of lithium from the bulk of the particles to the surface. Similarly, at the cathode, the surface lithium concentration is higher than the bulk concentration leading to diffusion into the particle. The rate of lithium diffusion into and out of the bulk of the particle is a major factor in the power capability of the battery, and depends upon numerous factors including temperature and C-rate. A full charge or discharge is indicated by a rapid rise or decay in voltage when the anode/cathode become saturated or depleted of lithium or the electrolyte is depleted of lithium. The charging and discharging process is summarised in Figure 35.

The electrode at which an oxidation reaction is occurring should be denoted the anode and a reduction reaction denotes the cathode, therefore during a discharge the anode is the negative electrode, and the cathode is the positive electrode. Whilst the electrode at which oxidation/reduction occurs is reversed when charging, by unofficial convention this denomination remains unchanged. LIBs are designed to ensure that the anode always possesses more chemical potential than the cathode, therefore when the circuit is closed, a spontaneous discharge occurs.

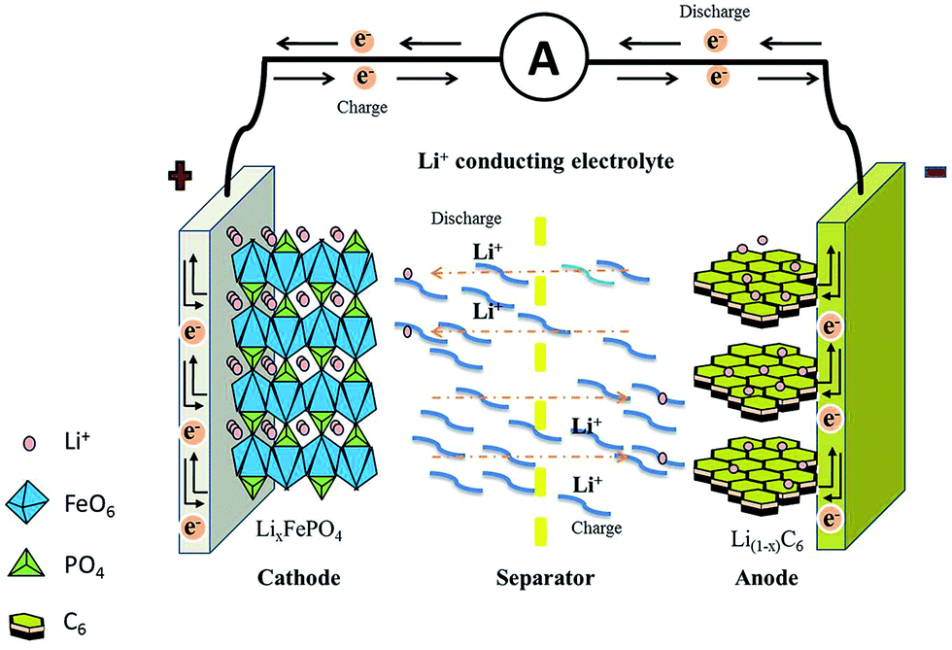


Figure 35: Illustration of the internal structure within a lithium ion battery with ion and electron motion indicated for a discharge process – [141]

4.3 Battery Design

Battery cells typically come in three form factors; cylindrical, prismatic and pouch. Cylindrical cells comprise a jelly roll wound around a mandrel, which is this inserted into a can typically made of aluminium. Pouch cells utilise a stacked jelly-roll contained within an aluminium laminate, and prismatic cells utilise either wound or stacked jelly-rolls within a cuboid aluminium can.

Cylindrical cells are the lowest cost due to the reduced number of processes required during their construction and as a result also benefit from a highly optimised production process given their widespread use in portable electronics. Further, they are fully mechanically contained thereby easing the process of correctly integrating them into a battery module. When integrating cylindrical cells into a module a relatively large drop in volumetric energy density will be observed due to the inherent packing density limitations of cylinders. To maximise energy density within the cell, current collectors typically have a low contact area with the cell terminals, resulting in a poor internal electrical and thermal path. As a consequence of these characteristics, cylindrical cells are typically ill-suited to small battery packs with a high power demand, and are more productively used in larger and lower power battery packs.

Prismatic cells incorporate large terminals and high current collector contact areas, and thus when considered in combination with their external aluminium can, they have a low resistance and high heat rejection. These attributes reduce the severity of some failure modes in prismatic cells which arise from over-charge or nail penetration. However, these features increase the inactive material content, thus prismatic cells typically possess comparatively poor cell level gravimetric and volumetric energy density. Prismatic cells are typically well suited to applications with high power requirements.

Pouch cells minimize inactive content, and offer the greatest module level design flexibility, however electrode stacking increases cell processing costs, and thereby pushing users to maximize cell capacity to control costs. Large pouch cells however pose challenges when attempting to satisfy abuse legislation, as a single cell failure will release a large amount of energy, and the heat transfer path is relatively poor in comparison to a prismatic cell. Pouch cells simultaneously offer the greatest level of design flexibility and design complexity.

The major constituents of a lithium-ion battery are discussed below; the desired characteristics of these constituents are largely (but not entirely) independent of the cell form factor.

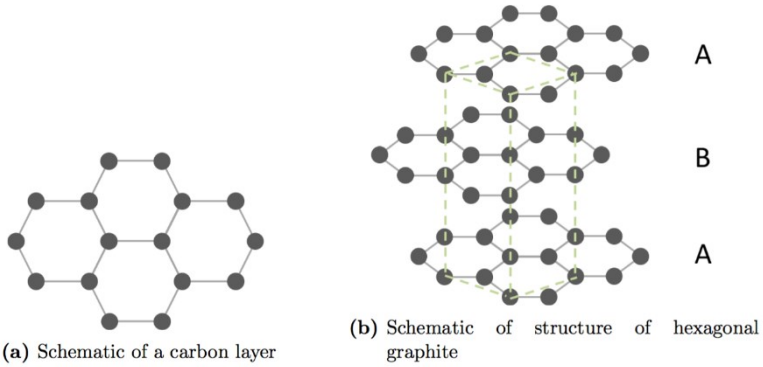
4.3.1 Anode

An ideal anode possesses high specific capacity, low potential [vs Li], high electrical conductivity, a high diffusion coefficient and is stable in electrolyte. The structure should be mechanically stable during operation with little volumetric change as the electrode undergoes lithiation and de-lithiation. During operation over an extended time period, irreversible capacity loss should be low, thus thermal, mechanical and chemical stability should be high throughout the expected range of operation.

Early lithium batteries possessed lithium metal anodes due to their very high (3860 mAh/g) specific capacity, low density and lowest potential [vs Li]. However, due to uncontrollable lithium dendrite formation and poor coulombic efficiency, a transition was made to intercalation materials, [142]. Graphite is currently the anode material of choice due to its high theoretical specific capacity (372 mAh/g), low potential [vs Li], high electrical conductivity, and low cost, [143]. Graphite anodes suffer from high capacity loss during the first cycle, when the Solid Electrolyte Interphase (SEI) is formed (further details about SEI formation are provided in section 4.5), however following the formation of

this passivating layer, capacity loss slows considerably, [144]. During lithiation, graphite experiences a modest volumetric expansion that is typically 13.5%, [145].

The structure of graphite impacts its lithium ion intercalation capacity, rate of degradation and potential [vs Li]. Graphite is formed of sheets of graphene; a single sheet of graphene consists of a 2-d hexagonal array of atoms, and is illustrated in Figure 36a. Sheets of graphene can be combined in parallel layers with a horizontal displacement; an illustration is provided in Figure 36b and this is commonly known as ABAB stacking or 2H graphite.



(a) Schematic of a carbon layer

(b) Schematic of structure of hexagonal graphite

Figure 36: (a) Graphene sheet structure (b) ABAB stacking of graphene sheets –Source: [146]

When lithium ions intercalate into ABAB stacked graphene sheets, it transforms into AAAA stacked graphene sheets (Stage 1), however structural transformations between ABAB, ABCA and AAAA stacking result in distinctive plateaus of the anode potential. Each plateau corresponds with transitions between distinct phases of structural change due to lithiation. The graphic in Figure 37 (Top) shows how structural changes affect the vacancies occupied by lithium ions as a function of stoichiometry, and in Figure 37 (Bottom), the transitions between voltage plateaus which correspond the stages 1-4 can be seen.

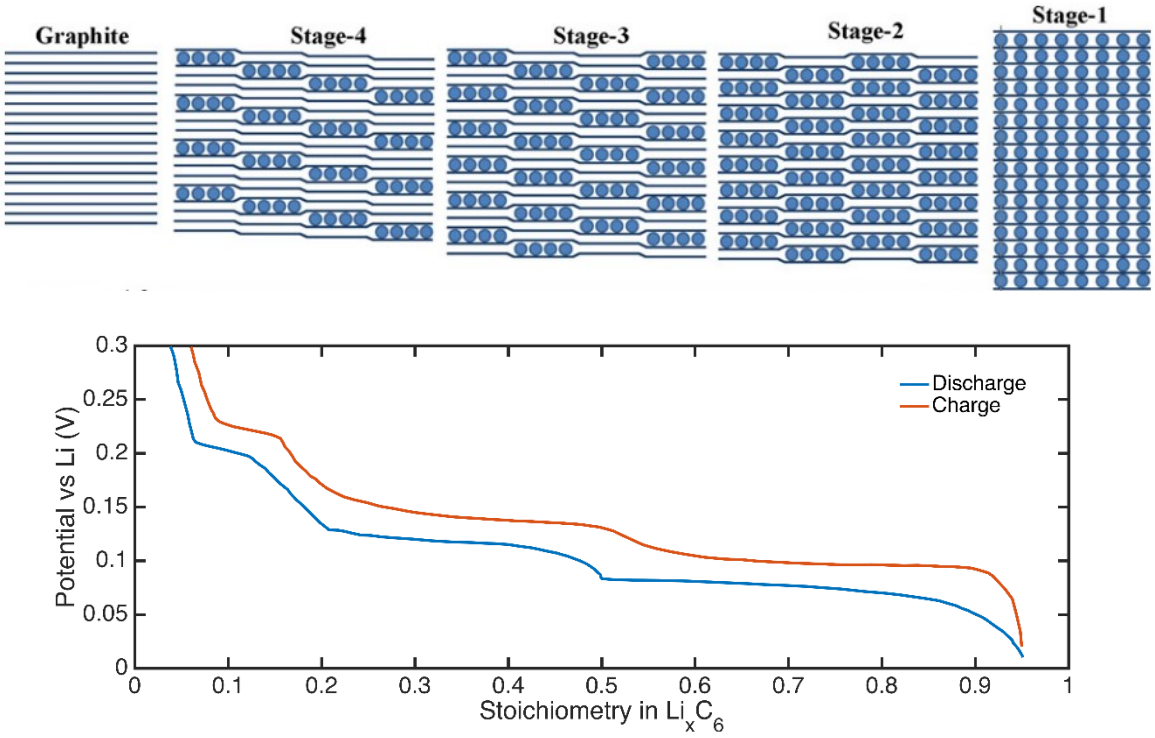


Figure 37: Plot of graphite anode potential vs Li as a function of stoichiometry, with a graphic illustrating – Adapted from [144,147]

$LiTi_5O_{12}$ (LTO) has also been used as an anode material because it is safe, thermally stable, and offers high cycle life during high current operation due to a very small (<0.5%) volume change during operation, [143]. However LTO has a high potential [1.55V vs Li], low energy capacity (175 mAh/g), moderate lithium diffusivity and electrical conductivity [143]. Whilst the high potential of LTO limits cell voltage, at a potential of 1.55V vs Li, lithium dendrites cannot form, increasing safety during low temperature charging. Additionally, LTO is chemically stable with the electrolyte preventing the formation of a SEI layer, which would slow lithium diffusion, increase resistance, and consume lithium thereby reducing capacity. Furthermore, the low volume change prevents particle cracking at high currents. LTO is a good anode choice for high power LIBs requiring high safety, low degradation and a wide thermal operating window.

Significant interest has been shown in the use of silicon as an anode material due to its very high theoretical capacity (4200 mAh/g), however lithiation and de-lithiation causes very large volumetric changes (300% vs the 13.5% of graphite), [145] [148]. Consequently, significant particle and SEI cracking occurs, resulting in very poor cycle life. Graphite and silicon have been blended in an attempt to produce an anode which has a higher specific capacity, yet is structurally stable. The addition of 10% silicon content to a graphite anode was shown to increase the reversible capacity of the electrode to 590 mAh/g (from 372 mAh/g) without significantly increasing capacity loss, [149].

4.3.2 Cathode

An ideal cathode should possess a high average potential [vs Li] to maximize cell voltage, a high lithium storage capability for good energy storage capability, and high diffusivity and electrical conductivity to minimise resistance. For long life, the structure should be mechanically stable during operation and insoluble in the electrolyte. Additionally, it should be inexpensive and only undergo exothermic decomposition at a high temperature or not at all to prevent thermal runaway.

Early LIBs used Lithium Cobalt Oxide (LiCoO2) as a cathode material due to its good specific capacity

(155 mAh/g) and high average potential [vs Li] (3.9V). Although $LiCoO_2$ remains popular, a great desire exists to transition to other cathode materials as Cobalt is a very expensive material, as shown in Figure 38, is carcinogenic accompanied by environmental issues [150]. Additionally, instability under thermal abuse conditions can result in thermal runaway and fire, meaning it is not suitable for all applications.

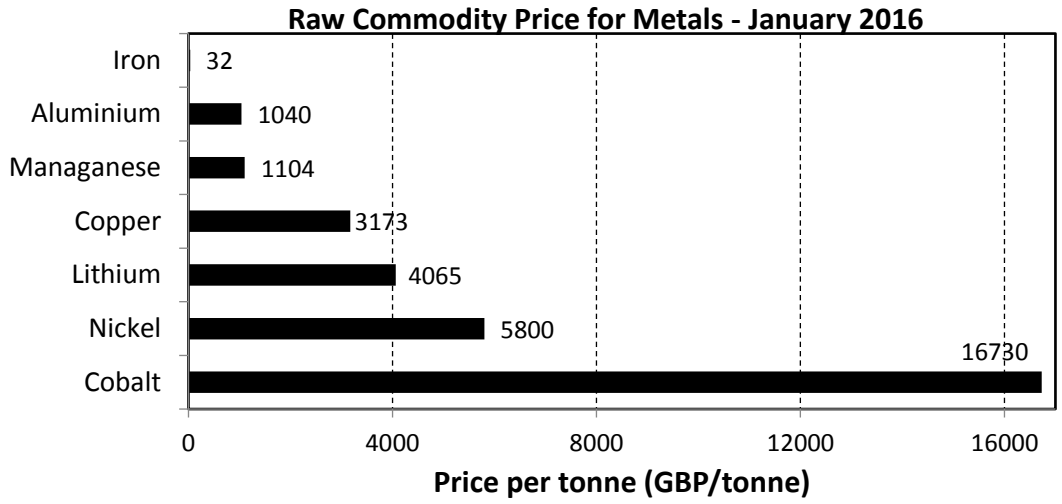


Figure 38: Raw commodity prices for metals as of January 2016 – Source: [151]

$LiNiO_2$ was developed as a lower cost alternative, however the lattice structure is less stable with cycling as the Ni is oxidized from the Ni^{2+} to the Ni^{3+} or Ni^{4+} state during de-intercalation, and the reverse during intercalation, [152]. This structural change causes significant degradation with cycling. Furthermore, the formation of NiO and O_2 leads to safety concerns. Doping $LiNiO_2$ with a small amount of Cobalt improves structural stability as its oxidation state does not change with cycling [152,153][154].

Doping $LiNi_{0.8}Co_{0.2}O_2$ with a small amount of Aluminium ($\leq 5\%$) to $LiNi_{0.8}Co_{0.15}Al_{0.05}O_2$ (NCA) significantly reduces impedance rise by preventing the build-up of a surface layer on the cathode. When charging to high SoC, Ni^{4+} is generated, and when this is subsequently reduced, a NiO film forms on the cathode surface, [153]. Aluminium is inactive and therefore reduces the specific capacity of the cathode, however morphology changes (to more spherical and dense particles) slightly reduce the impedance though these changes are small, [155].

Alternatively, $LiNi_{0.8}Co_{0.2}O_2$ can be doped with Managanese to $LiNi_{0.33}Co_{0.33}Mn_{0.33}O_2$ (NMC) to reduce the Nickel content, and hence limit issues with structural changes and surface films. The increased structural stability improves the stability at high potentials relative to both $LiNi_{0.8}Co_{0.2}O_2$ and NCA, [156]. It should be noted that at low SoC and elevated temperatures Manganese can dissolve into the electrolyte, [157]. Under thermal abuse conditions, the onset of exothermic reactions is at a higher temperature in NCM than NCA (325℃ vs 250℃), and approximately 50% less heat is generated, [158]. Furthermore, under these thermal abuse conditions, NCM also releases less oxygen than NCA, [158]. Consequently, NMC is typically favoured for high capacity cells with the use of NCA restricted to low capacity cells for safety reasons.

$LiFePO_4$ (LFP) has an olivine structure, therefore its thermodynamic potential is largely independent of intercalated Li^+ concentration. The material is thermally stable and does not generate O_2, therefore is less of a fire risk. The stability of the structure results in excellent cycle life, and the material is abundant, cheap and non-toxic, [150]. Whilst the raw materials for LFP are low cost, its

synthesis requires an inert environment, [144]. LFP particles are typically coated with carbon to increase their electronic conductivity, and the degree of graphitisation highly influences the electronic conductivity and hence the rate capability of the material. Furthermore, the carbon coating acts as a nucleating agent to reduce the particle size, and helps avoid the formation of ferric impurities which block channels of the olivine structure, [150]. However, LFP has low specific energy density (160mAh/g) and potential (3.45V vs Li), and has poor low temperature performance but is suitable for applications requiring high levels of safety and non-toxicity.

Whilst $LiCoO_2$ remains a popular cathode choice, the use of NCA and NMC is growing rapidly given their lower cost, and higher capacity. Owing to their relative attributes, NCA and NCM are gaining popularity, however the use of both technologies is controlled by patents, [15]. The properties of the discussed cathode materials are summarised below in Table 9.

Material	Structure	Specific Capacity (mAh/g)	Volumetric Capacity (mAh/cm^3)	Midpoint V Vs Li at C/20	Comments
$LiCoO_2$	Layered	148	550	3.9	Remains very common, Co is very expensive.
$LiNi_{0.33}Mn_{0.33}Co_{0.33}O_2$ - (NMC)	Layered	160-170	600	3.8	Safer and less expensive than $LiCoO_2$. Capacity dependent upon upper voltage limit.
$LiNi_{0.8}Co_{0.15}Al_{0.05}O_2$ - (NCA)	Layered	180-200	700	3.8	Similar safety to $LiCoO_2$, higher capacity.
$LiMn_2O_4$	Spinel	100-120	596	4.05	Inexpensive, safer than $LiCoO_2$, poor high temperature stability.
$LiFePO_4$ - (LFP)	Olivine	160	589	3.45	Very safe. Low volumetric energy.

Table 9: Overview of cathode material attributes for commercialised technologies – adapted from [144] ,[15] **and** [143]

4.3.3 Electrolyte

The purpose of an electrolyte is to carry lithium ions between the cathode and anode. An ideal electrolyte has high ionic conductivity to maximize ion transport, yet is a poor electronic conductor. It should have a wide electrochemical stability window, have high lithium salt solubility, and remain within the same state throughout the thermal operating region. It should be unreactive with other components within the battery, have a high flashpoint, be available at a reasonable cost and be non-toxic.

The electrolyte typically consists of multiple aprotic solvents and a lithium based salt; solvents are typically combined to take advantage of complementary characteristics to develop a solvent which is more suited for use as a battery electrolyte. Ethylene Carbonate (EC) is a commonly used electrolyte, however it must be mixed with another solvent such as Dimethyl Carbonate (DMC), Diethyl Carbonate (DEC), Ethyl Methyl Carbonate (EMC) or 1,2-Dimethoxyether (DME) to achieve suitable characteristics. For example, EC has a melting point of 36℃, therefore is unusable below this temperature, however by combining EC with EMC, the melting point can be reduced to -43℃, [159].

EC forms a relatively stable passivating layer on a graphite anode, thus supressing degradation from the electrolyte reacting with the electrode materials. The most highly researched lithium salts are $LiClO_4$, $LiAsF_6$, $LiBF_4$ and $LiPF_6$, however $LiPF_6$ is almost universally used in commercial applications [160,161]; these salts are typically not mixed due to limited choice of anions. The electrochemical stability window of the electrolyte should be considered with respect to a battery cathode; whilst a number of electrolytes appear to possess impressive electrochemical stability windows, the highly oxidising nature of transition-metal containing cathode materials reduces this, [162,163].

4.3.4 Separator

The purpose of the separator is to prevent physical contact between the anode and cathode to impede internal short circuits, and to allow lithium ions to diffuse through. Hence, good separators must be excellent electrical insulators, whilst simultaneously being good ionic conductors to minimize ionic resistance contributions. Additionally, to assist with manufacturability, safety and performance degradation, the separator should have good mechanical properties, be chemically stable and have controllable thermal properties.

Separators are typically made of Polyethylene (PE), Polypropylene (PP) or a tri-layered combination of the two, (PP-PE-PP), [144]. In a tri-layered separator, PE undergoes an irreversible structural change (melting) at approximately 130℃, preventing ion transfer through the separator and hence acting as a safety device to prevent thermal runaway. The PP has a higher melting point, and therefore maintains better mechanical integrity at these elevated temperatures, [164]. Further,

4.3.5 Current Collectors

Current collectors facilitate electron transfer between the electrodes and terminals of the cell. As such, current collectors should have a very high electronic conductivity, be resistant to corrosion in the typical potential range of the anode or cathode, and given that it is inactive, it should be of minimum mass, volume and cost.

Typically, current collectors are made of dissimilar materials for the anode and cathode; copper has excellent properties for use as a current collector, however corrosion occurs ready at potentials of > 2V [vs Li+] [157], therefore it is only suitable for use at the anode. Aluminium is commonly used for the positive current collector due to its stability up to 4.5V [vs Li+] (with an electrolyte consisting of EC-DMC and $LiPF_6$ or $LiBF_4$), and a good trade-off between volume, mass and cost, [165].

4.3.6 Internal Design

4.3.6.1 Electrode Selection

Complementary anodes and cathodes are selected to meet the targets of a particular cell design. Generally, it is desirable to maximise cell potential, create a relatively flat voltage curve and have little capacity fade and resistance rise as a result of usage. Different anode and cathode materials can be combined to achieve the desired attributes of the battery cell, however trade-offs are inherent in battery design. For instance, the specific energy storage capabilities of the anode and cathode will differ, therefore a differing active mass is required. Changing the electrode mass will result in changes to the minimum and maximum electrode stoichiometry (lithiation normalised against maximum lithiation), which in turn will affect average cell voltage and the shape of the OCV curve. Additionally, a change in electrode stoichiometry can have a significant impact upon cell resistance, and degradation.

Figure 39 shows the potential of the anode, cathode and full cell between 0-100% SoC for a Panasonic 18650 cell. Given that during a discharge, lithium ions are removed from the anode and

intercalated into the cathode causing a rise in the anode potential, and a decay of the cathode potential, it is evident that the anode is fully utilised. At 100% SoC the anode is almost entirely filled with lithium, therefore the potential [vs Li+] is very close to zero, and at 0% SoC the anode is highly devoid of lithium, hence the potential rises dramatically.

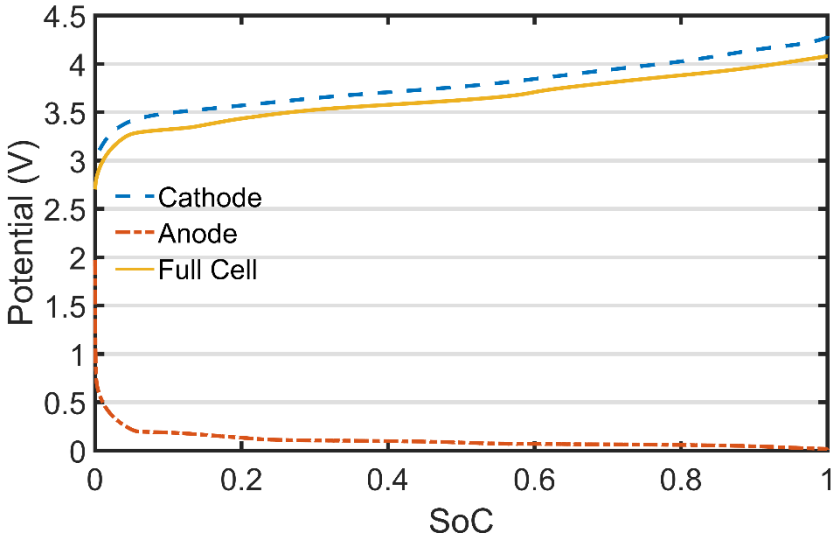


Figure 39: Potential of anode, cathode and full cell (Panasonic 18650) where potential of anode and cathode is against a lithium reference, and full cell potential difference is between the anode and cathode. Data acquired experimentally by author through creation of half-cells and discharge at a C/40 rate and 25℃

To maximise the cell potential, the maximum usable cathode potential should be matched to the lowest usable anode potential. However, the maximum potential of the cathode is limited by side-reactions and material stability, whilst the maximum potential of the anode is limited by copper corrosion, and the minimum potential is limited by lithium plating at low temperatures.

4.3.6.2 High Power & High Energy Cells

The suitability of a battery for a particular application is often largely defined by its specific energy and power per unit of mass and per unit of volume. Although particular cell chemistries may be more or less suited to use in high energy or high power battery cells, the same materials can be used to produce cells with dramatically different characteristics.

The energy density of a cell can be improved by increasing the electrode thickness and density, and decreasing the quantity of inactive materials such as binder, conductive agents and metallic electrode dopants, [144,166]. These changes maximize the quantity of active material within the cell and therefore increase the quantity of active lithium and intercalation sites, thereby increasing the energy which can be stored. However, these changes decrease the electrode surface area, increase the distance of solid state lithium diffusion, and reduce the structural stability and conductivity of the electrode. Therefore, it is apparent that internal design considerations to achieve high energy storage and high power output are largely mutually exclusive.

	High Energy Cell Panasonic 18650BD	High Power Cell Saft VL6P
Energy Density	235 Wh/kg 163 Wh/L	73.5 Wh/kg 37.8 Wh/L
Power Density (Peak) – Discharge	2461 W/kg 1822 W/L	3,470 W/kg 7,375 W/L
Power Density (Peak) - Charge	1227 W/kg 908.75W/L	2,295 W/kg 4,875 W/L
Operating Temperature (within 75% of peak performance)	-10°C → 45°C	-25°C → 55°C
Cost – (Estimated)	260 $/kWh 33.6 $/kW	1429 $/kWh 19.9 - $/kW

Table 10: A comparison of the attributes of high power and high energy NCA lithium-ion battery cells – Data Sources: Manufacturer supplied datasheets

High energy battery cells with modest power capability are far more abundant than high power cells due to the requirements of the portable electronics segment, which is the dominant battery market, [167]. High power battery cells are typically 30% more expensive than high energy batteries, with the price differential increasing as higher power is demanded, [168]. This difference can partially be attributed to economies of scale, and partially to the higher safety requirements of cells designed for the automotive market rather than the consumer electronics market, [168]. When considering future automotive cells, high power-cells remain more expensive per kWh as more non-active material and labour is required; this is reflected in the estimates shown in Figure 40.

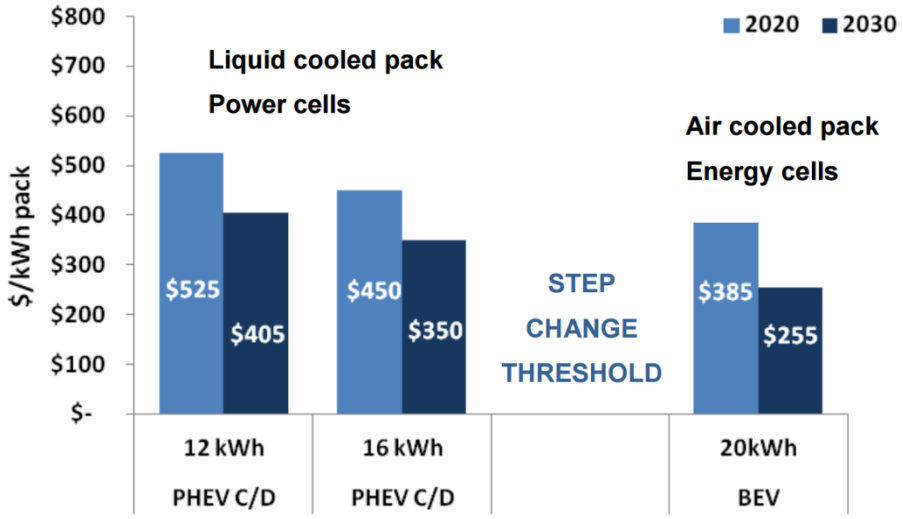


Figure 40: Estimated cost of high-power and high-energy cells in 2020 and 2030 - [168]

4.4 Capability variation with operating conditions

This chapter examines how typical operating conditions affect battery capability, with particular emphasis on energy capability and power availability, and the physical origin of these changes are explored. The available capacity and effective resistance of a battery cell is a function of temperature and current, and the effect, normalised around a point of 25°C and C/40, is shown in Figure 41. It can be seen that as current is varied, so too is the available energy capacity. The

available capacity during a constant current discharge can be described by the Peukert effect [169], which is defined in Equation 35 where C_p is the Peukert capacity, I is the applied current, k_p is the Peukert coefficient and t is the time in hours. The capacity of a battery with a Peukert coefficient of 1 does not vary with current; a typical coefficient for a high power LIB is approximately 1.01, whilst a high energy LIB can have Peukert coefficient of up to 1.1, [166].

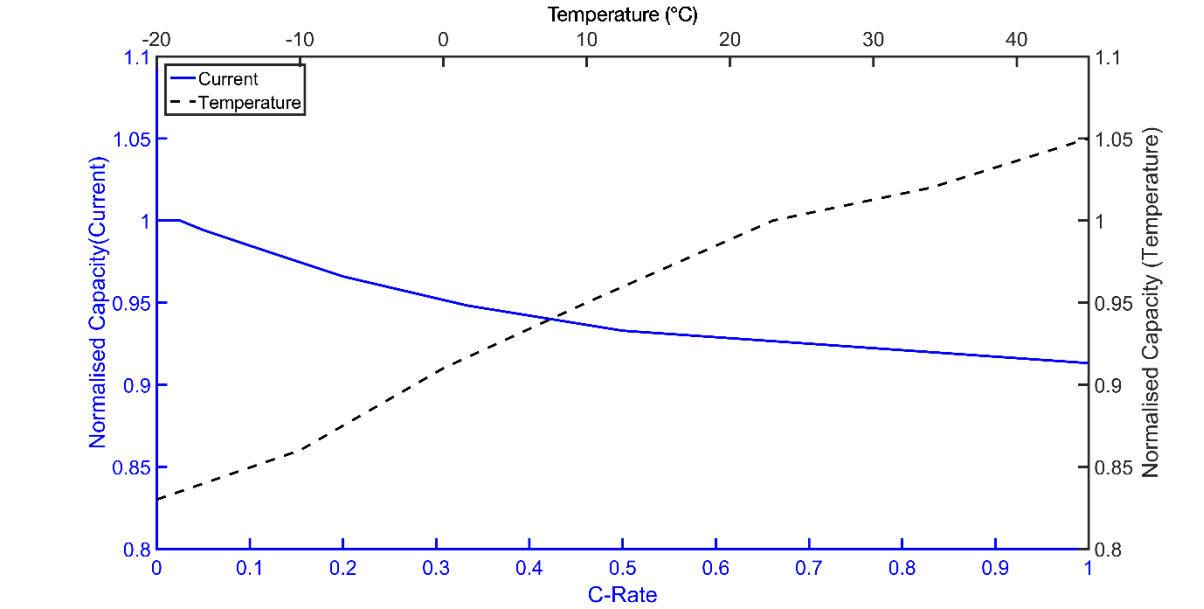


Figure 41: Capacity variation as a function of temperature and current where temperature is normalised around 25℃ and current is normalised against a C/120 discharge – Presented data acquired experimentally from a Panasonic 18650BD cell

$$C_p = I^{k_p} t \qquad \text{Equation 35}$$

The available capacity is reduced as current increases because of the increase in diffusion resistance which causes a greater IR drop or voltage-sag, that triggers the low voltage cut-off signifying the end of discharge earlier [169,170].

Resistance is related to SoC via a parabolic relation; resistance rises at high and low SoC due to a rise in diffusion resistance and charge transfer resistance, as one electrode has a high stoichiometry, whilst the other has a low stoichiometry leading to increased resistance to lithium ion exchange, [171]. Temperature strongly influences resistance, and in turn affects the available cell capacity in the same way. Resistance decreases as temperature increases because the rate at which chemical reactions occur increases [56], as does diffusivity [172,173] and electrolyte conductivity [174].

The relationship between the chemical reaction rate and temperature is described by the Arrhenius equation [56] as per Equation 36, and this relation can also be used to describe the effect upon electrolyte conductivity, [175]. The diffusivity variation with temperature can be given by the Nernst-Einstein relation [176] as per Equation 37.

$$k_A = Ae^{-E_a/RT} \qquad \text{Equation 36}$$

$$D_i = \frac{\mu_i R_U T}{zF} \qquad \text{Equation 37}$$

In the above equations, k (s^{-1}) is the rate constant of chemical reactions, A (s^{-1}) is an experimentally derived constant, E_a is the activation energy (J mol^{-1}), R_u is the universal gas constant (J mol^{-1} K^{-1}), T is

the absolute temperature (K), *i* is the species, D (m^2s^{-1}) is the diffusion coefficient, and μ (m^2Vs^{-1}) is the mobility.

Temperature also has an effect on the OCV and is defined by the Nernst equation as:

$$V = V^0 - \frac{RT}{zF} \ln Q_R \qquad \text{Equation 38}$$

where V is the cell potential (V), V^0 is the standard cell potential, z is the number of moles of electrons transferred per reaction, F is Faraday's constant (C mol^{-1}) and Q_R is the reaction quotient. The effect of temperature on OCV is shown in Figure 42, and highlights the requirement to consider temperature when estimating SoC from OCV.

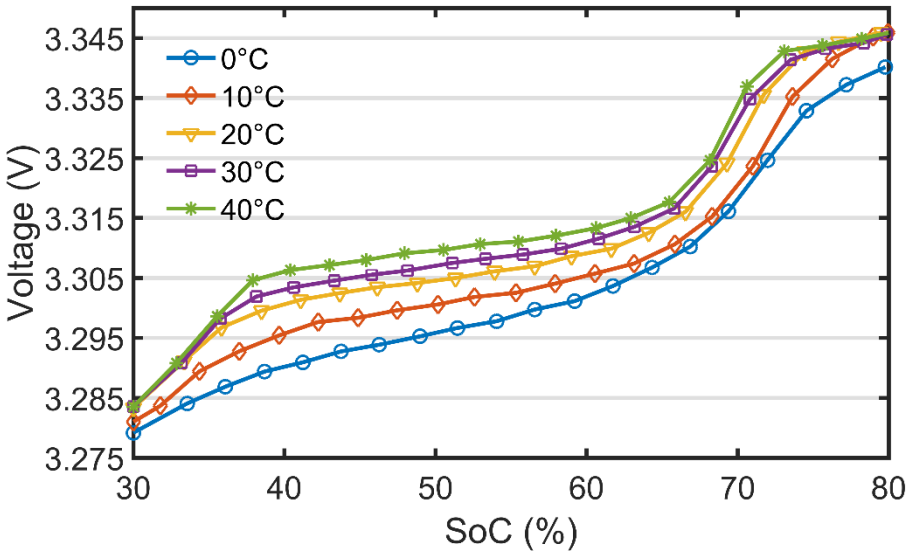


Figure 42: OCV variation with temperature - adapted from [177]

4.5 Degradation

A multitude of factors can cause capacity loss, impedance rise and catastrophic failure in lithium ion batteries. The causes of degradation can broadly be categorised as; electro-chemical stability, structural distortion and mechanical stress. Figure 43 provides a graphical overview of the degradation mechanisms in lithium ion batteries. The causes and effect of each of these degradation mechanisms are discussed below.

4.5.1 Anode Degradation

The operating potential of graphitic anodes in the charged state (below 0.3 V versus Li) is below the electrochemical stability window of the electrolyte, resulting in reductive electrolyte decomposition at the electrode/electrolyte interface, [144]. The decomposition products form a passivating film on the anode surface known as the Solid Electrolyte Interphase (SEI), which prevents further reduction of the electrolyte. The formation and stability of the SEI has a major impact upon degradation at the anode, and consequently, the degradation of graphitic anodes has been the subject of extensive study, [144,157,161,178–180]. Figure 44 graphically illustrates the main degradation phenomena which occur at the anode.

The SEI, which is typically 10-100Å thick, physically separates the electrode and the electrolyte, but remains ionically conductive, [157]. The SEI is heterogeneous, and formed of different chemical compounds which vary with the electrolyte constituents, [181]. The SEI is formed of both inorganic (LiF, Li_2O, Li_2CO_3) and organic (Li_2EDC), polymeric and oligomeric compounds [182,183].

The presence of an SEI layer increases the impedance of the battery due to the increased resistance to ion diffusion. The formation of the SEI results in an irreversible capacity loss and consumption of lithium from the electrolyte. The surface area of the anode is directly related to the irreversible capacity loss as a result of the creation of the SEI during the first cycle of the cell, [178]. However, it is not practical to simply minimize the surface area of the anode, as this would reduce the rate capability of the battery due to diffusion limitations. Spherical particles were found to be the ideal morphology as they minimized particle surface area and lithium ion diffusion path lengths, [144].

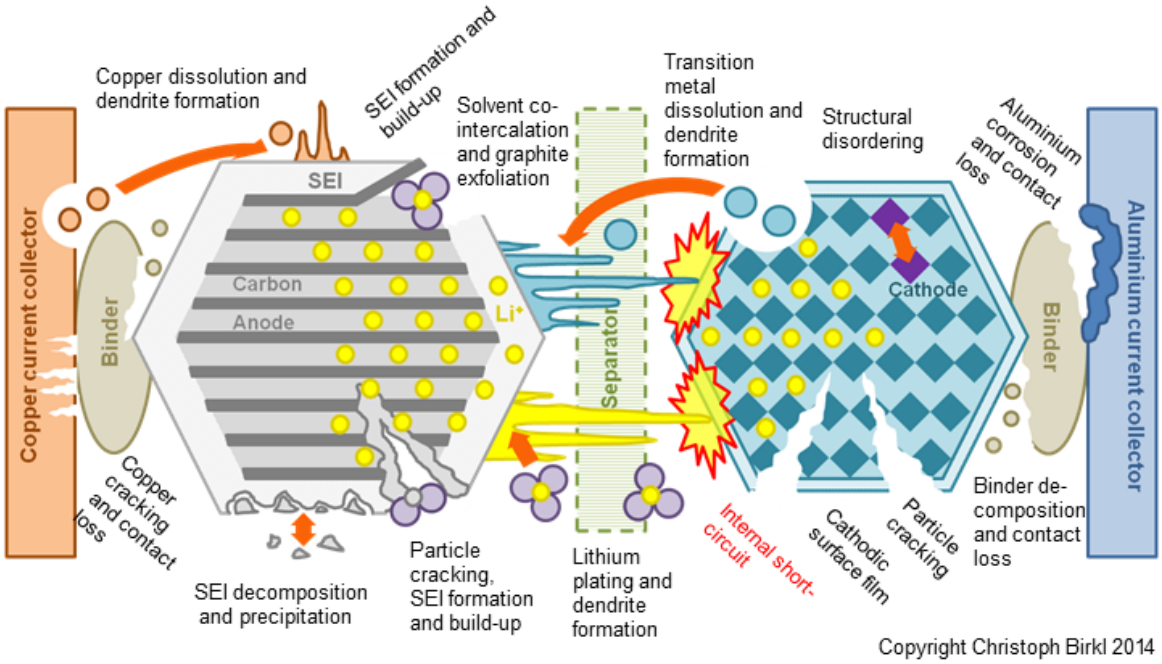


Figure 43: Illustration of the degradation mechanisms which can occur within a lithium-ion battery - [184]

With some electrolytes, typically Propylene Carbonate (PC) based, the formed SEI layer is incomplete or does not adequately passivate the anode. Incomplete passivation enables the intercalation of lithium-ions and their solvation shell between graphene sheets in a process known as graphite exfoliation. This results in the distortion of the structure and particle cracking due to gas evolution as the electrolyte undergoes reductive decomposition. Initially, this will result in increased SEI build up and hence increased capacity loss and impedance rise, and eventually this will lead to the formation of inactive islands of the anode as electrical contact is lost, [178].

The SEI thickness will continue to grow after the initial cycle as the SEI is mostly, but not entirely passivating, and constituents of the SEI can also be electrochemically unstable. Some solvent molecules can diffuse through the SEI to the graphite-SEI interface, where they will be reduced, [185]. Radicals produced during the initial growth of the SEI will decompose organic products such as the solvent, salt or unstable SEI products, and form additional radicals, causing further electrolyte and unstable SEI product decomposition, [182]. In addition, expansion and contraction of the anode during intercalation/delintercalation will cause the SEI to become unstable and crack, creating additional surfaces for SEI growth, [186]. Further, cathode materials that have dissolved into the electrolyte, such as Fe, Mn or Co, can precipitate and cause dendrite growth, [15,186].

It should be noted that the composition, porosity and thickness of the SEI can vary considerably on a single particle, [183]. The presence of the SEI increases charge transfer resistance, as it inhibits diffusion, [185]. Whilst higher temperatures improve the rate of lithium ion diffusion into and out of the anode, elevated temperatures can also result in a change of the morphology and composition of

the SEI, [144,187]. A change in morphology may result in graphite with no passivating film being exposed to the electrolyte, causing additional SEI growth. The structure also becomes less ordered, however this is not thought to cause significant degradation, [186]. Elevated temperatures can also cause the SEI to dissolve and subsequently re-precipitate causing a growth in the SEI thickness, [157].

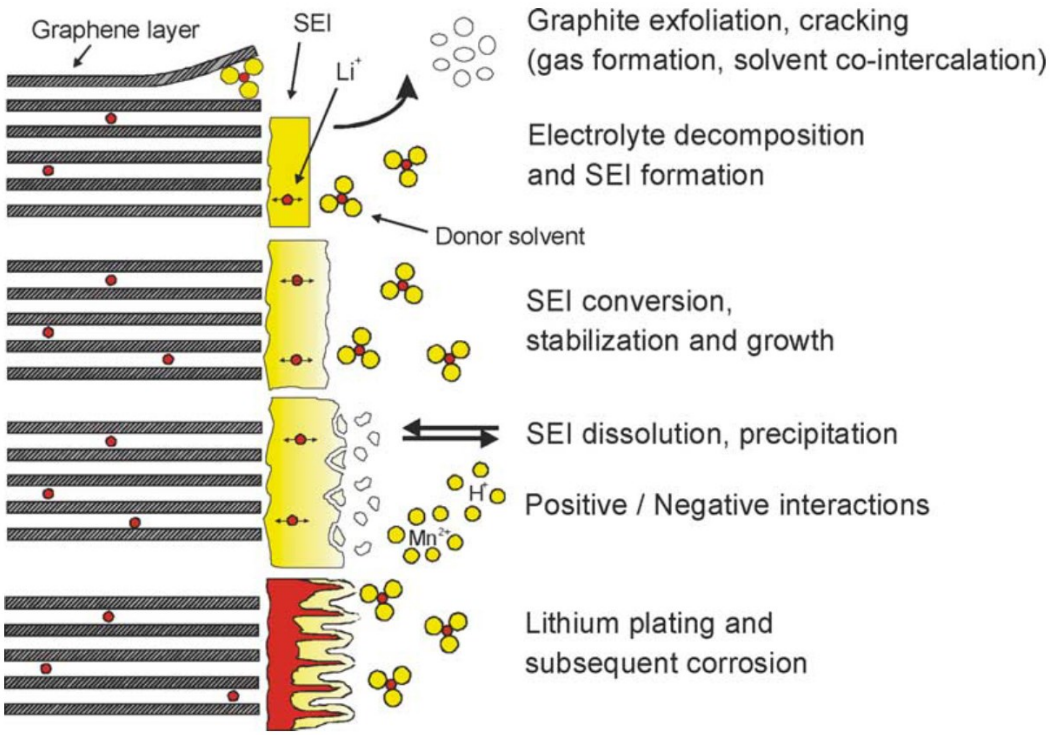


Figure 44: Anode degradation mechanisms - [157]

The intercalation potential of a carbon based anode is close to the potential of lithium metal. At low temperatures, where the rate of solid-phase and liquid phase diffusion is severely degraded, lithium may plate onto the surface of the anode, [157]. Whilst this is reversible, and plated lithium oxidises at a potential of 100mV, if the plating is not completely reversed, over time dendrites will grow, and it is possible for dendrites to puncture the separator and cause an internal short circuit which would result in catastrophic failure, [186].

The degradation mechanisms occurring at the anode are summarised in Table 11 below:

Cause	Effect	Leads to	Reduced by	Enhanced by
Electrolyte decomposition leading to SEI growth (Continuous side reaction at low rate)	Loss of Lithium Increased charge-transfer resistance	Capacity Fade Power Fade	Stable SEI (additives) Rate decrease with time	High Temperatures High SOC (low potential)
Solvent co-intercalation, gas evolution and subsequent cracking formation in particles	Loss of Active Material (Graphite Exfoliation) Loss of Lithium	Capacity Fade	Stable SEI (additives) Carbon pre-treatment	Overcharge
Decrease of accessible surface area due to continuous SEI growth	Impedance Rise	Power Fade	Stable SEI (additives)	High Temperatures High SOC (low potential)
Change in porosity due to volume changes, SEI formation and growth	Impedance Rise	Power Fade	External pressure Stable SEI (additives)	High cycling rate High SOC (low potential) High
Contact loss of active material particles due to volume changes during cycling	Loss of active material	Capacity Fade	External Pressure	High cycling rate High DOD High
Decomposition of Binder	Loss of lithium Loss of mechanical stability	Capacity Fade	Proper Binder Choice	High SOC High Temperature
Current Collector corrosion	Impedance rise Inhomogeneous distribution of current and potential	Power Fade Enhances other ageing mechanisms	Current collector pre-treatment and surface coating	Over-discharge Low SOC
Metallic lithium plating and subsequent electrolyte decomposition by metallic Li	Loss of Li (electrolyte)	Capacity fade Power fade	Narrow potential window	Low temperature High cycling rates Poor cell balance Geometric misfit

Table 11: Table summarising the causes of degradation at the anode, and factors affecting these causes – Adapted from [157]

4.5.2 Cathode Degradation

The degradation of the metal oxide cathode will depend upon its composition and structure. Generally capacity fade and impedance rise at the cathode is as a result of chemical dissolution or decomposition, structural changes during cycling and the modification of any surface film which may form, [144]. Figure 45 provides an illustration of the different degradation mechanisms occurring at the cathode.

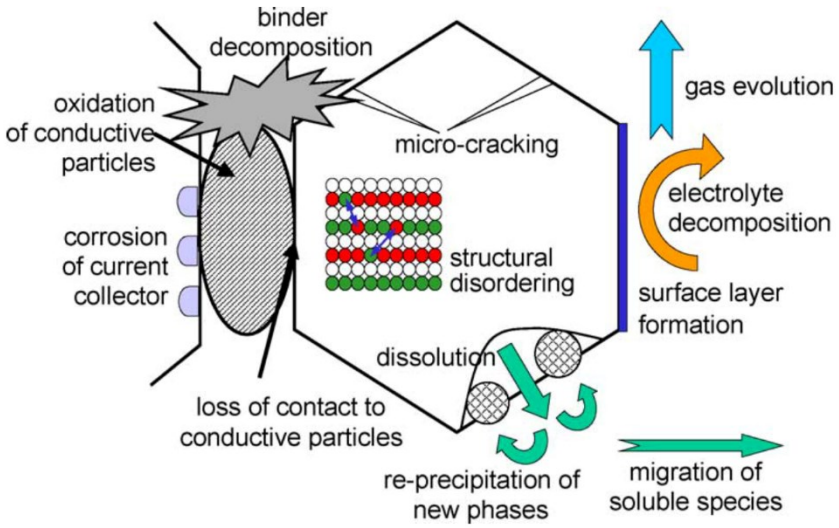


Figure 45: Summary of cathode degradation mechanisms – [157]

The cathode is subject to mechanical stress during operation due to the intercalation and removal of lithium ions, and phase transitions (if applicable) which will distort the structure. The resulting mechanical stress leads to particle cracking, structural disordering and could cause a loss of contact with conductive particles and the current collector. Structural disordering and a subsequent breakdown of the structure is a major degradation mechanism in spinel type cathodes, [188].

In $LiNiO_2$ based lithium ion batteries such as NCA and NCM, operation at elevated temperatures (>60°C) results in the formation of inactive Ni^{2+} and Ni^{3+} ions, where the proportion of inactive Ni increases with increasing temperature, [189]. Doping NCA with a small quantity of Mg increases the structural stability as it induces stronger and less distorted Ni-O bonds. Consequently, the formation of inactive divalent and trivalent Ni ions is supressed, [190].

When charging to high SoC, Ni^{4+} is generated, and when this is subsequently reduced, a NiO film forms on the cathode surface, [153]. The addition of Al in NCA helps to suppress this effect, however doping with Al is typically done in small quantities to prevent capacity loss as Al in an inactive cathode material, [153]. Consequently, surface films do form [191] and are a major cause of impedance rise at the cathode, [153,192].

The cathode operates within a voltage window (2.5-4.5V vs Li/Li+), which unlike the anode, is within the electrochemical stability window of the electrolyte, therefore the cathode does not typically cause electrolyte decomposition, [144]. At high cell SoC, the cathode will react with the electrolyte resulting in the formation of a surface film [157]; the rate of generation of this surface film increases with temperature, [193]. The thickness of the surface film has a strong effect on the impedance of the cathode, [153].

Elevated cathode potentials can cause corrosion of the aluminium current collector and the oxidation of conductive particles, [157]. The operation or storage of cells containing Mn at elevated temperatures (>50°C) results in significant degradation. Structural or chemical instability results in the dissolution of Mn into the electrolyte. Mn is transferred to the anode through diffusion, and reduces onto the surface, causing Mn plating and a significant increase in impedance at the anode, [194].

4.5.3 Degradation in Hybridised Energy Storage Systems

Hochgraf et al [195] conducted a study to compare battery degradation in a PHEV between a system consisting solely of LIBs, and one supported by SCs to form a HESS. The HESS consisted of the original LIB pack with the addition of a SC bank and a buck/boost bi-directional dc-dc converter. A control strategy was devised, and through simulation a modified power demand was generated for the battery in the HESS. Six LIB cells were tested in total; two using the original power demand, two using the derived modified power demand and two used to measure calendar ageing.

The study demonstrated a significant decrease in capacity loss and resistance rise. Given the above discussion, this is an entirely expected finding as the cell with the modified profile had a significantly reduced power demand, therefore experienced a lower current demand, lower energy throughput, and smaller SoC change. The described test is not directly relevant to the investigation of degradation in a HESS designed for automotive applications. In a real automotive application, the addition of a SC bank and DC-DC converter to an existing battery pack will result in an over-sized system that is prohibitive from a cost, volume and mass perspective. The beneficial attribute of high power availability from the SC is most effectively utilised by combining the SCs with high-energy LIBs to maximize the capabilities of the system; thus a more representative comparison would be between a high power LIB, and a high energy LIB combined with SCs.

Cause	Effect	Leads to	Reduced by	Enhanced by
Electrolyte decomposition at high potentials	Loss of Li Gas Evolution Increased charge-transfer resistance	Capacity Loss Power Fade	Increased electrolyte ESW Lower upper voltage limit	Overvoltage High Temperature
Structural disordering	Formation of inactive species Modified surface structure inhibits Li+ diffusion	Capacity Loss Power Fade	Cathode additives	High rate High Temperature
Particle Cracking due to intercalation and extraction of lithium ions	Reduced electrical contact Potential for active material loss	Power Fade Capacity Loss	Reduced rate Doping to stabilise structure	High Rate
Surface film formation	Impedance Rise	Power Fade	Electrolyte additives Cathode doping	High SoC High Temperature
Loss of contact to conductive particles	Inhomogeneous distribution of current and potential	Impedance Rise	Compression Improved binder	High rate cycling
Metal dissolution	Loss of active material Precipitation of electrically isolating species	Capacity Loss Impedance Rise Contributes to anode SEI	Doping to stabilise structure	Low SoC (low cathode potential) Elevated temperature
Oxidation of conductive particles	Reduction of electrical contact	Impedance Rise	Electrolyte additives	Overvoltage
Current collector corrosion	Impedance rise Inhomogeneous distribution of current and potential Reduction of electrical contact	Power Fade Enhances other ageing mechanisms	Current collector pre-treatment and surface coating	Overvoltage
Binder decomposition	Reduction of electrical contact Loss of mechanical stability	Impedance Rise	Appropriate binder choice	Overvoltage High Temperature

Table 12: Table summarising the causes of degradation at the cathode, and factors affecting these causes

4.6 Interim Conclusion

This chapter has thus far examined how LIBs function, and has used this knowledge to explain how and why different operating conditions affect performance and degradation. This knowledge is required to understand how best to manipulate the design of the HESS to achieve the potential performance benefits described in the working hypothesis.

High Power Batteries (HPBs) and High Energy Batteries (HEBs) can have significantly differing characteristics; their resistance can vary by an order of magnitude. Battery resistance will have a strong influence upon the most desirable HESS topology, as well as its performance, efficiency and value. An original working hypothesis of this study is that it is possible to achieve superior performance from a combination of high energy LIBs with supercapacitors than from high power LIBs alone. However, the characteristics of HEBs, which stem from higher diffusion resistance, draw doubts to this working hypothesis. HEBs have a larger resistance, which is more temperature dependent, and a larger Peukert coefficient, therefore are more affected by high currents. Their higher resistance results in less efficient energy storage, and greater heat generation. Whilst battery current will be reduced in a HESS, the higher resistance may result in greater heat generation, drawing doubts to the working hypothesis that a HESS will generate less heat. It should therefore also not be taken as given that a HESS will have higher energy efficiency than a HPB battery system; this will depend upon the specific cells used, the topology of the HESS and the drive cycle under consideration.

A HESS is also hypothesised to provide superior low temperature performance to a battery only system due to the large increase of LIB resistance at low temperatures. However, again, it should not be taken as given as HEBs will experience a greater rise in low temperature resistance than HPB. It is hypothesised that battery degradation will be reduced in a HESS, primarily due to reduced energy throughput and a lower peak and RMS power demand of the battery. However, the effect of transitioning from a HPB to a HEB must once again be considered. Whilst degradation mechanisms dependent upon energy throughput, such as low rate continuous electrolyte decomposition, are likely to be reduced, the effect upon degradation mechanisms dependent upon the magnitude of current are not straightforward to predict.

The magnitude of current that will result in degradation via structural disordering, particle cracking, and loss of contact with conductive particles will differ for HEBs and HPBs. In HEBs, for the application of a given current, larger concentration gradients and stresses will arise, and the binder and electrolyte additives are likely less suited to supressing these degradation mechanisms than those found in HPBs. However, the largest factor in determining whether battery degradation is reduced in a HESS is likely to be related to the temperature of the LIBs during operation, which is primarily related to cell selection and system design.

4.7 Battery Model Development

4.7.1 Models in Literature

Numerous battery models exist and they can broadly be categorised as empirical or black box models, equivalent circuit models and physics based models. Empirical models utilise extensive datasets in a black box approach to convert a given input to an output with no consideration of the processes occurring within the battery to cause these changes; whilst these models can be useful in some battery management system applications where the input conditions vary little and are known, they are unsuitable for predicting interactions between devices, and hence are unsuitable for prediction of HESS behaviour.

Equivalent Circuit Models (ECMs) use combinations of passive electrical components, such as capacitors and resistors to recreate the behaviour of a battery. The value assigned to the electrical components typically varies with operating conditions, such as SoC and temperature. The models are typically simple to build, and require little computational power, however they require a large amount of data for parameterisation. Furthermore, as these models do not directly compute the physical processes occurring within the battery, they are only valid within the operating conditions in which they were parameterised. For instance, a model parameterised using EIS, or low current charge/discharge data will not be valid for high current operation. Whilst the model will be capable of recreating the effect of the dominant physical processes at low currents, these differ at high currents. For instance, at high currents diffusion limitations will play an important role, and the charge transfer resistance will decrease with current according to an Arrhenius relation.

A typical schematic of an ECM is shown in Figure 46 below; different systems require different numbers of RC pairs to capture their dynamics, however three branches are not typically exceeded, [196]. Whilst a greater number of RC pairs can be used to improve the accuracy under a particular set of conditions, it is more difficult to assign a physical meaning to the components in question, therefore it is more difficult to ensure these remain within a valid range [197]. Consequently, whilst a greater set of RC pairs may provide improved accuracy for usage similar to that used for parameterisation, the range of conditions over which the model is valid is likely to be narrower. As ECMs do not model the specific processes occurring within a battery, and the parameters have limited physical meaning, their use as a diagnostic or prognostic tool is limited.

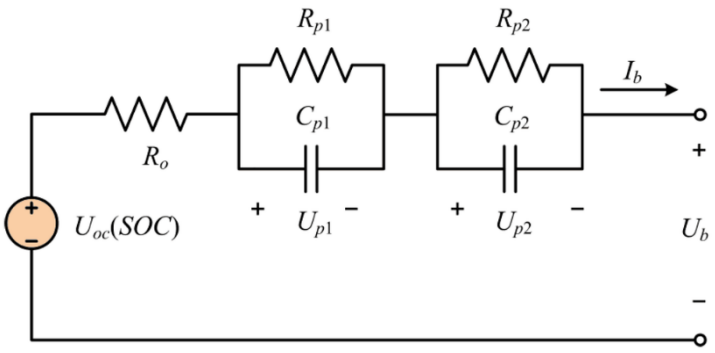


Figure 46: Typical battery equivalent circuit model –Source: [198]

Physics based models determine the response of a battery to a given input by mathematically modelling the processes occurring within the battery, such as redox reactions and diffusion. Consequently, physics based models can be operated over a very large range of conditions, and are easily adapted for use with different battery cells. Arguably, the largest challenge associated with physics-based models is parameterisation; some models have in excess of 80 individual parameters and some parameters may not have a physical meaning due to approximations and simplifications made in the mathematical description of physical processes, such as charge transfer.

The fundamental governing equations for physics based models were first set out by Fuller, Newman and Doyle for a 1D model, [199]. Many authors have subsequently added functionality to this model such as the addition of SEI layer growth [200–204], the effect of mechanical deformation as a result of electrochemical activity [205], and an expansion of the system to evaluate a 2D and 3D system [206–208]. These additions enable these models to be used to understand current flux in large form factor cells, track the effect of degradation as a result of SEI layer growth and evaluate the effect of different rates of cell compression.

4.7.2 Developed Model

A battery model is developed to run alongside a supercapacitor model to evaluate the performance of a HESS. The developed model is for a commercial Panasonic 18650BD cell, which has a cylindrical form factor, is a high-energy cell and consists of a NCA cathode mated to a graphite anode. The primary purpose of the model is to enable the author to simulate the performance of a HESS under a variety of conditions. Great efforts were dedicated to the development of a physics based model as it would enable identification of the factors limiting system performance, however, acceptable high-current performance could not be obtained for the desired cell. An ECM was therefore used to recreate the electrical and thermal performance of the battery cell, enabling prediction of electrical and thermal performance of a HESS and the ability to relate cell level behaviour to module level.

Given the use case for the model, it is necessary for the model to be able to recreate the behaviour of the cell at currents in excess of a 2C charge and 5C discharge. Consequently, a thermal model must be incorporated as high current operation will result in an appreciable temperature rise which will affect the electrical properties.

4.7.3 Model Structure

4.7.3.1 Electrical Model

The generic model developed by Chen et al [209] is adapted for use in the Matlab/Simulink environment as described by Jackey et al [210]. The model consists of a voltage source and three RC branches, each of which are a function of temperature, SoC and current. The RC branches must vary with current to capture the decrease of charge transfer resistance with increasing current. A schematic of the electrical circuit used in the ECM is shown in Figure 47.

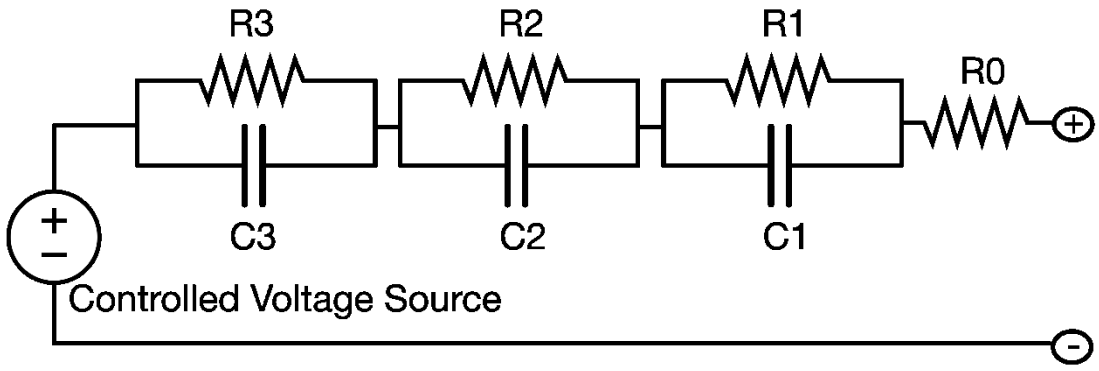


Figure 47: Schematic of utilised equivalent circuit model

The basis of the model is an SoC dependent voltage source which defines the open circuit voltage of the cell at a given SoC. The connected RC branches define the evolution of the over-potential of the cell following activity, i.e the difference between OCV and the actual cell voltage. During the application of current, the series resistance of the cell will cause an instantaneous change in voltage, which is defined by the resistance of R_0. The voltage drop across each RC branch is a function of time, and thus the modelled cell voltage can be given as,

$$V_{Cell}(t) = V_{OCV} - V_1(t) - V_2(t) - V_3(t) - IR_0 \quad \text{Equation 39}$$

where V_{OCV} is the open-circuit voltage, V_x is the voltage drop across RC branch x = 1→3.

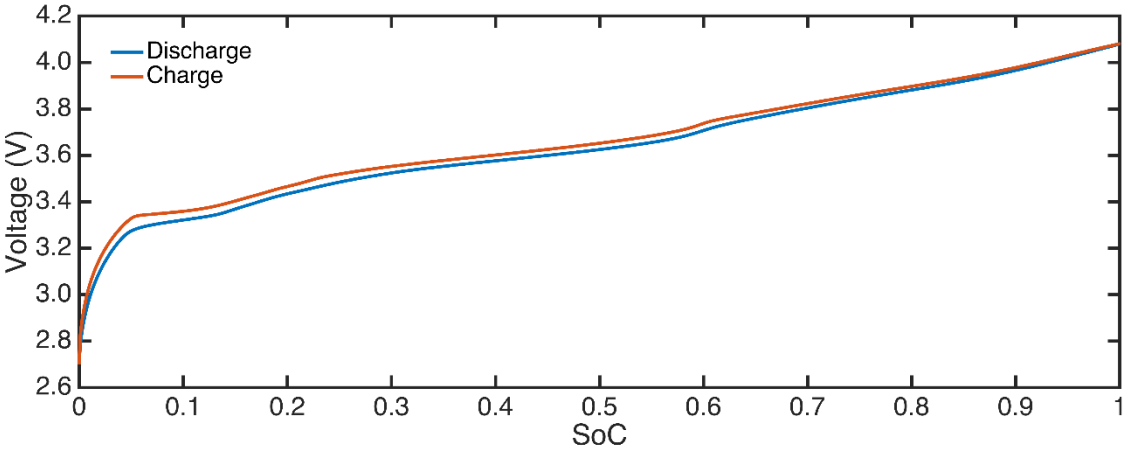


Figure 48: OCV as a function of state of charge at 25℃ determined through a constant current discharge at a rate of C/120

The pseudo-OCV was determined through a constant current charge and discharge at a rate of C/120, and the OCV was found to differ between the charging and discharging phase as shown in Figure 48. Between 10-60% SoC the mean difference between the charging and discharging phase is 35mV, and under 10% SoC the difference increases to a peak of 55mV. The modelling targets defined in section 2.2 require OCV voltage estimation to be accurate to 50mV, therefore it is necessary to use both a charging and discharging OCV lookup table.

$$\frac{dV_{OCV}(SoC)}{d\,SOC} = \begin{cases} \frac{dV_{OCV\,Ch}(SoC)}{d\,SOC} + k\left(V_{OCV\,Ch}(SoC) - V_{OCV}(SoC)\right), & \frac{dSoC}{dt} \geq 0 \\ \frac{dV_{OCV\,Dis}(SoC)}{d\,SOC} + k\left(V_{OCV\,Dis}(SoC) - V_{OCV}(SoC)\right), & \frac{dSoC}{dt} < 0 \end{cases} \quad \text{Equation 40}$$

An instantaneous change from OCV_{Dis} to OCV_{Ch} as the polarity of the applied current is changed would result in numerical inconsistencies, and would likely prevent the solver convergence. To prevent step changes in the OCV, a simple function as defined by Huria et al [197] in Equation 40, is used to transition between charge and discharge OCV as the model transitions between positive to negative currents. The transition speed, k, is a tuneable parameter and the effect of the function is shown in Figure 49.

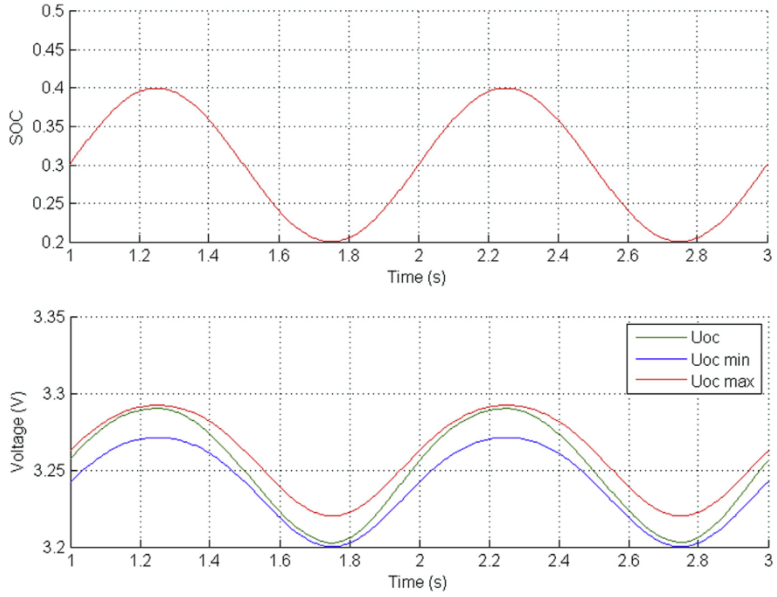


Figure 49: OCV transition between charge OCV and discharge OCV as SoC is varied - [197]

4.7.3.2 Thermal Model

A thermal model has two distinct functions; it must determine the rate of heat generation for given operating conditions and subsequently determine the resultant temperature change.

4.7.3.2.1 Heat Generation

There are multiple sources of heat within a lithium battery and they can broadly be categorised as electrical losses, entropic heating, species transport or mixing heat and degradation inducing reactions, [211]. The electrical losses are the combined losses attributable to interfacial kinetics and ohmic losses and can be described using the over-potential as per Equation 41, where I is the applied current (A), R is the resistance (Ω) and the over potential can be defined as $\eta = V_{OCV} - V_{terminal}$.

$$\dot{Q}_{irr}(t) = I^2 R(t) = I\eta(t) \quad \text{Equation 41}$$

The entropic heat is a result of structural changes of the electrodes as SoC varies, and under 1C operation can contribute more than 50% of the heat generated [212–214]. The heat generated as a result of entropy change can be defined as per Equation 42, where T is the absolute temperature (K), n is the number of electrons per reaction, F is Faradays constant, and ΔS is the entropy change ($Jmol^{-1}K^{-1}$). The term $\partial V_{OCV}/\partial T$ is commonly referred to as the entropic coefficient and varies strongly with battery chemistry and SoC, and weakly with temperature, [215–218].

$$\dot{Q}_{rev} = IT\frac{\Delta S}{nF} = IT\frac{\partial V_{OCV}}{\partial T} \quad \text{Equation 42}$$

The heating as a result of mixing, or more specifically the formation and breakdown of concentration gradients, is negative during operation, positive during relaxation and provides a net zero heating effect. This term is small in comparison to the electrical losses and entropy, [219,220]. Similarly, the heating caused by degradation inducing effects is very small in the operating range specified by the manufacturer, [211]. Consequently, the heat attributable to degradation and mixing is not considered in this model and the total heat generation within the model can be given as per Equation 43.

$$\dot{Q}_{Total} = \dot{Q}_{irr} + \dot{Q}_{rev} \quad \text{Equation 43}$$

4.7.3.2.2 Heat Transfer

Model Selection

The heat transfer model used to determine battery temperature change as a result of heat generation and thermal boundary conditions varies in fidelity from a simple lumped model [221,222], to a multi-lumped/pseudo 3D model [221,223,224] and a fully 3D model [175,225]. A multi-lumped model is adopted for this study as it enables evaluation of the temperature of segments of the jelly roll of the cell, without requiring the additional complexity of an electrochemical model. Given that the intended use of the model is pulse load applications, it is necessary to consider that a time delay which exists in heat reaching the cell surface from the location at which it was generated. During the pulse, the generated heat is likely to affect electrochemical performance due to a temperature change of the jelly roll, however the temperature of the jelly-roll will differ from the surface temperature, particularly at short time periods. Consequently, a lumped model that predicts surface temperature perfectly would under predict temperature rise, which in turn would result in poor electrical performance prediction.

When considering model fidelity, it is necessary to consider the limitations of the electrical model. An ECM is not capable of defining the generated heat attributable to the anode and cathode, nor is it capable of defining mixing heat. However, parallel networks of the ECMs can be used to determine current inhomogeneity when a thermal gradient is established within a cell, and hence estimate

spatial variations of heat generation within a cell. A thermal equivalent circuit was adapted for use with a Panasonic 18650 cylindrical battery cell. The heat transfer model considered each constituent of the battery separately and assigned geometric and thermal properties. The jelly roll was discretised into three segments radially, and 5 segments axially.

Model Description

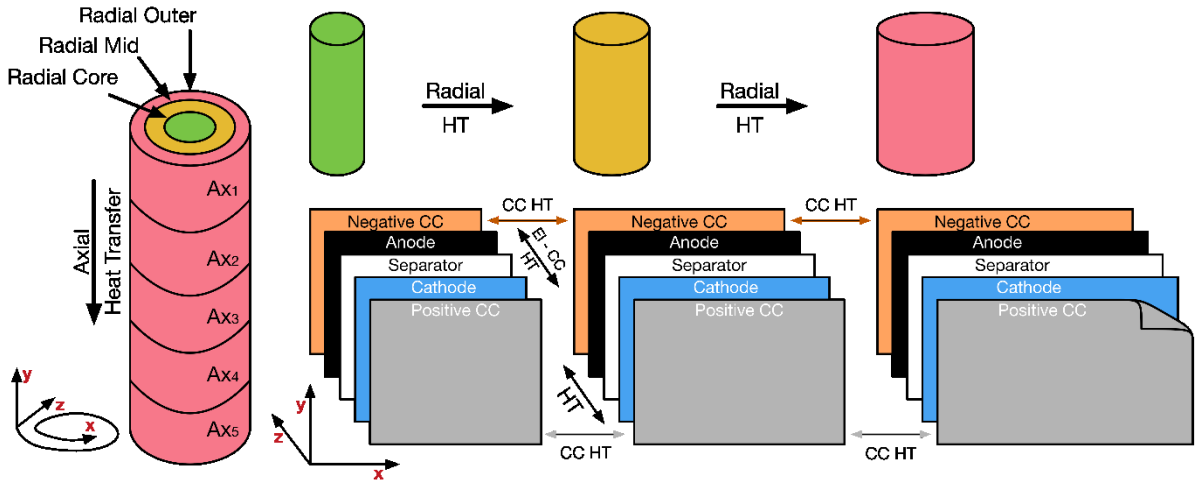


Figure 50: Graphical representation of heat transfer model showing the axial and radial discretisation and heat transfer paths

Figure 50 provides a graphical representation of discretisation of the jelly-roll in the thermal model, and the locations of heat transfer, as well as defining the *'x', 'y'* and *'z'* direction. Heat transfer within the jelly roll can occur radially through the thickness of the layers in the *z* direction, or around materials in the *x* direction. Whilst the thermal path is shortest in the *z*-direction, the thermal path in the *x* direction through the current collectors has the highest thermal conductivity.

The rate of radial heat transfer from the core to outer discretisation can be defined for heat transfer in the x direction and z direction using thermal resistance circuits. The rate of heat transfer in the x direction, $\dot{Q}_x$, is only considered for the current collectors as they possess a thermal conductivity that is two order of magnitude larger, and can be given as Equation 44, where the thermal resistance, R, is proportional to the length in the 'x' domain, and inversely proportional to the thermal conductivity, k_T, and the cross sectional area, A.

$$\dot{Q}_x = \frac{\Delta T}{R}, \qquad R = \frac{L}{kA}$$

$$\dot{Q}_x = \frac{\Delta T}{\left({}^{L_{CC}}/_{(k_{Cu} * A_{Cu}) + (k_{Al} * A_{Al})}\right)} \qquad \text{Equation 44}$$

The rate of heat transfer in the *z* direction, $\dot{Q}_z$, can be given as Equation 45, where r is the radius.

$$\dot{Q}_z = \frac{2\pi L k_z \Delta T}{\ln(r_{Mid}/r_{Core}) + \ln(r_{outer}/r_{Mid})} \qquad \text{Equation 45}$$

In each radial section, the separators and electrodes are lumped together as thermal masses, however the positive and negative CCs are considered individually to create nodes for modelling of

heat transfer in the *x*-direction. Axially (*y*-direction) within the jelly roll, heat conduction is considered individually for each thermal mass, namely, the electrode and separator bulk, the positive CC and the negative CC. Additionally, the conduction between the CC and pigtail is modelled, accounting for the differences of location, thermal mass and heat transfer area for the anode and cathode.

4.8 Model Parameterisation & Validation

4.8.1 Electrical Model

Model parameterisation is complete using the parameter estimation toolbox in Simulink via the layered approach as described by Jackey et al, [210]. EIS data is used to generate initial estimates for the value of each resistor and capacitor in the circuit. The following section describes the data required for model parameterisation and its acquisition. The use of the data in the parameter estimation toolbox to generate RC values is not discussed due to the comprehensive details provided by Jackey et al, [226].

4.8.1.1 OCV Data Generation

The basis for battery voltage estimation within the model is the OCV curve, and any errors in this data will directly apply to the results provided by the model. Whilst it is impractical to do a true OCV measurement as the SoC is changed in fine steps, a pseudo-OCV measurement can be obtained by completing a constant current charge or discharge between 0-100% SoC at a very low rate. Figure 51 shows the voltage variation over the SoC range as current is varied between a rate of C/40 and C/120, and the difference is quantified in Table 13. The rate was progressively decreased until negligible changes in the voltage profile and available capacity were observed.

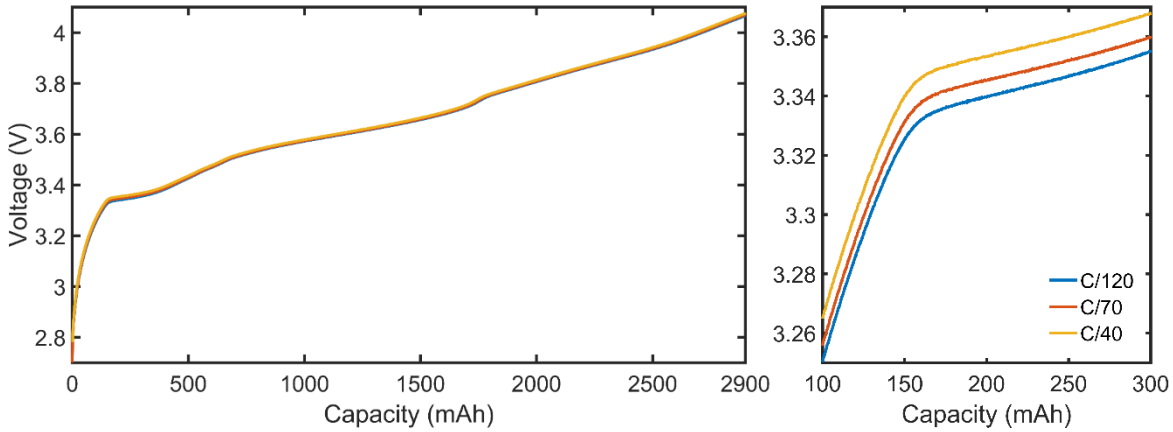


Figure 51: Charge curve with current of C/120, C/70 and C/40 between 0-100% SoC (left), and 3-10% SoC (right) where the greatest differences occur

As the OCV varies during charge and discharge as illustration in Figure 48, and varies with temperature, it is necessary to generate OCV data for a number of conditions. Given the targeted error as discussed in section 6.3.1, it was determined that a rate of C/70 would be most suitable as to minimize steady state error, whilst maintaining acceptable test time.

Rate	Maximum Difference (mV)	Average Difference (mV)
C/70	6	2.7
C/40	14	5.3

Table 13: Voltage difference as a result of varying current compared to a baseline of C/120

The Nernst equation (Equation 38) defines the variation of OCV as a function of temperature; for the cell in question, experimental results showed that the maximum variation of OCV in the parameterised temperature range was <1.5mV, therefore OCV measurements for charge and discharge at 25°C were used throughout.

4.8.1.2 Data for RC Initial Guess & Estimation

When using the parameter estimation toolbox, it is important to provide good initial estimates for the optimisation algorithm to find the global minima rather than local minima. GEIS is used at each SoC breakpoint, and the data is subsequently fit to an equivalent circuit that matches Figure 47. During fitting it is necessary to restrict the frequency to the low frequency region, (10mHz to 10Hz), and manually set R0 to the value equivalent to the x-axis intercept of a Nyquist plot of impedance.

For RC value estimation, experimental data is required where current pulses between SoC breakpoints are separated by sufficient rest times for the cell to reach OCV, an example of the resultant voltage profile is shown in Figure 52. As the required SoC range of validity of the model is 10-90%, 11 evenly spaced SoC breakpoints between 0 and 1 are used; whilst additional breakpoints improve model fidelity, the time required for experimental data acquisition is greatly increased. Ensuring the initial and final SoC of each pulse is concurrent with an SoC, current and temperature breakpoint greatly assists with the parameter estimation process.

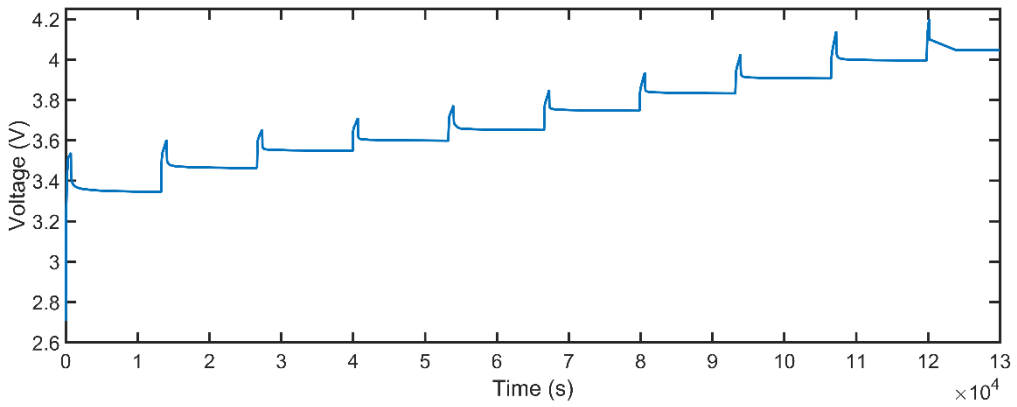


Figure 52: Voltage profile during 10% SoC constant current pulse charge profile between 0-100% SoC for RC value estimation

4.8.2 Thermal Model

The thermal model requires parameters describing the geometric features of the cell and material properties. The geometric properties are determined through cell disassembly, and the usage of an optical microscope and a Scanning Electron Microscope (SEM). Subsequently, all relevant surface areas, thermal masses and component masses are analytically determined; comprehensive details are provided in appendix A1. The parameters used in the model are measured where practical, and the remainder are taken from literature as presented in Table 14 and Table 15.

Parameter	Unit	-CC	Anode	Separator	Cathode	+CC	Source(s)
Thickness	μm	12	90	40	60	18	Measured
Density	$kg\ m^{-3}$	8933	1350	1009	3238	2770	[146,213,227]
Thermal Conductivity	$Wm^{-1}K^{-1}$	398	1.04	0.33	1.02	170	[146,213,227]
Heat Capacity	$JKg^{-1}K^{-1}$	385	1200	1978	975	875	[146,212,213,228]

Table 14: Jelly-roll parameters used for thermal model

Parameter	Unit	Value
Cell Mass	g	45.5
Can Thickness	mm	0.3
Can Mass	g	7.2
Pigtail Length (+ve)	mm	52
Pigtail Length (-ve)	mm	25
Pigtail Mass (+ve)	g	0.18
Pigtail Mass (-ve)	g	0.09

Table 15: Measured cell parameters

4.8.2.1 Cell Description

A cell was disassembled to determine the exact geometry and internal design; photographs of the cell during disassembly are shown in Figure 53. The cathode and anode materials are coated onto both sides of a Current Collector (CC) which is aluminium for the positive CC and copper for the negative CC. The electrode sheets are held apart by a pair of polymer separators sheets; the stacking arrangement is anode, separator, cathode and separator. The sheets of each material are approximately 700mm long and 60mm wide, and are spirally wound to form the jelly-roll. The separator sheets are slightly wider than the electrodes to prevent internal short circuits between the layers or between the cathode and the can, and the negative current collector is slightly longer to prevent electrode material being between the outer face of the jelly-roll and the can.

Two aluminium 'pig-tails' protrude from alternate ends of the jelly-roll and connect the CCs to the positive and negative terminals of the can. As shown in Figure 53, the negative pig-tail is connected to the negative CC at the outermost point of the jelly-roll whilst the positive pig-tail is connected approximately 400mm along the sheet from the core. The negative pig-tail is pressed against the base of the can, whilst the positive pigtail is physically connected to the positive terminal. The can is made of aluminium, and the majority of the case forms the negative terminal. The positive terminal which incorporates safety devices such as the Pressure Temperature Current (PTC) switch, is separated from the remainder of the can by a thin insulating material. Aluminium tabs are typically spot welded onto the positive and negative terminals for quick and convenient connection.

4.2.2 Heat Transfer Modes

$$\dot{Q}_x = \frac{\Delta T}{\left({}^{0.6547}/_{(398 * 7.2x10^{-7}) + (170 * 1.08x10^{-6})}\right)} = 7.2\ x\ 10^{-4}\Delta T \qquad \text{Equation 46}$$

$$\dot{Q}_z = \frac{2\pi(6x10^{-2})(41.9)\Delta T}{\ln(6.1x10^{-3}/3.4x10^{-3}) + \ln(8.8x10^{-3}/6.1x10^{-3})} = 16.8\Delta T \qquad \text{Equation 47}$$

Equation 46 and Equation 47 demonstrate that radial heat transfer is dominated by heat transfer in the *z* direction. Radial heat transfer in both the *x* and *z* directions has been implemented in the model for completeness, and flexibility for use with cells of differing geometry and finer discretisation where heat transfer in x-direction may play a larger role.

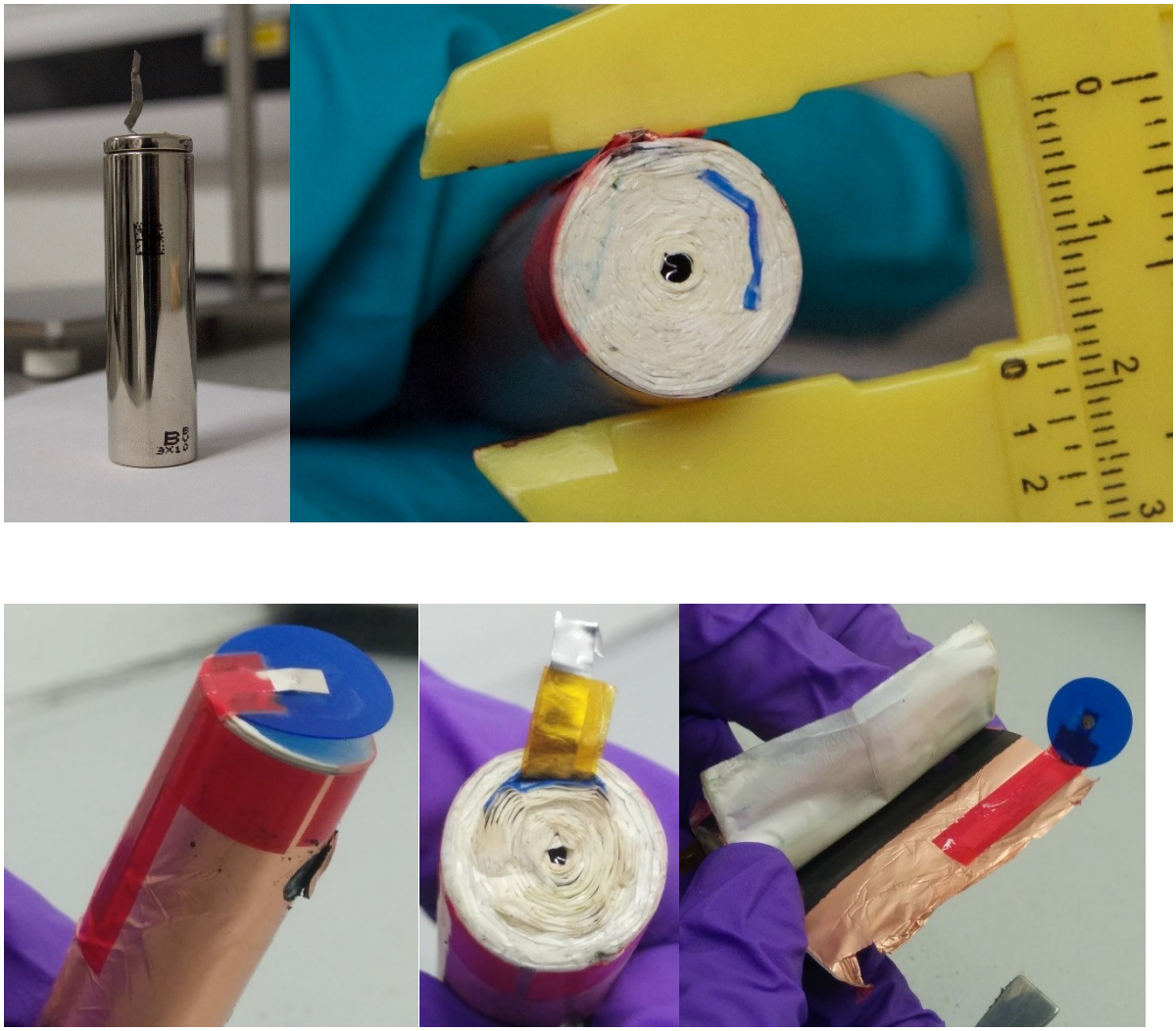


Figure 53: Photographs of Panasonic 18650BD cell during various stages of disassembly

4.8.3 Model Validation

Validation of the electrical parameters is complete against both similar data to that used for parameterisation, and automotive drive cycle data for differing ESS configurations. The parameters for the electrical model are a function of current, temperature and SoC, and therefore numerous; parameters are provided in full in appendix A2.

The plot in Figure 54 presents experimental data for a 2C pulse charge, which was used for parameterisation via the layered approach, with simulation data overlaid. A maximum voltage error of 52mV is observed when at an SoC above 10%; well within the target for pulsed loading of 3% (126mV). The parameters used for the creation of the plot are shown below in

SoC (%)	C1 (F)	C2 (F)	C3 (F)	R0 (Ω)	R1 (Ω)	R2 (Ω)	R3 (Ω)
0	1.25E+02	4.14E+04	6.52E+02	6.92E-02	1.20E-02	6.51E-03	2.35E-03
10	2.25E+03	1.38E+04	3.25E+02	5.20E-02	1.90E-02	2.12E-02	1.06E-02
20	2.55E+03	1.71E+04	4.28E+01	3.68E-02	6.94E-03	1.59E-02	1.59E-02
30	2.04E+03	3.19E+04	2.08E+02	3.86E-02	1.06E-02	4.87E-03	7.60E-03
40	2.59E+03	3.29E+04	2.41E+03	4.35E-02	6.08E-03	1.45E-02	7.92E-03

50	6.57E+03	2.01E+04	2.19E+03	4.56E-02	1.32E-03	4.94E-02	1.46E-02
60	4.13E+03	6.87E+04	1.06E+02	3.42E-02	9.81E-03	2.76E-02	1.38E-02
70	3.74E+03	4.21E+04	1.62E+02	2.94E-02	1.23E-02	1.36E-01	1.59E-02
80	5.62E+03	4.04E+04	4.03E+02	4.62E-02	1.57E-02	8.14E-02	6.15E-03
90	5.47E+03	3.55E+04	1.88E+01	1.86E-02	3.08E-02	1.45E-01	4.49E-02
100	3.68E+03	4.00E+04	2.13E+01	2.78E-02	1.82E-02	2.42E-01	7.75E-02

Table 16.

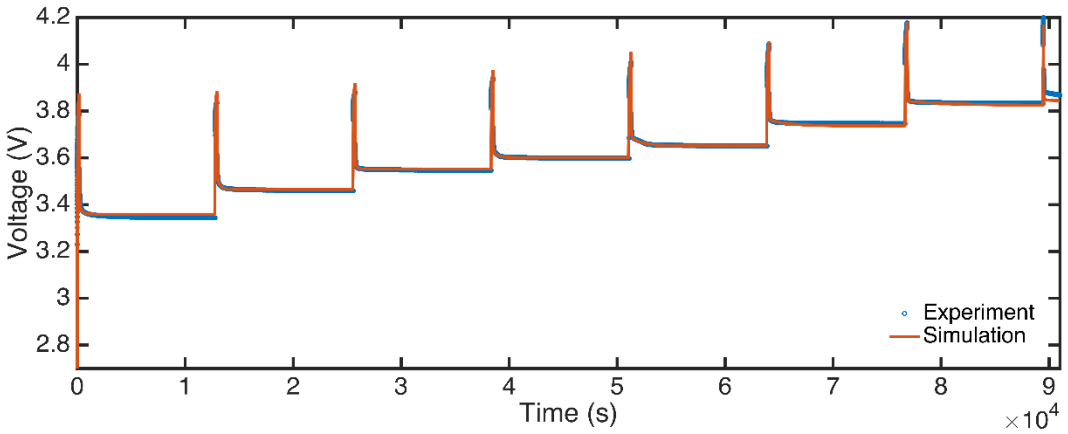


Figure 54: Comparison of experimental and simulated voltage for parameterised conditions - Experimental Conditions: Repeated application of 2C (6A) pulse load for 10% SoC (297mAh) at 25℃, Initial SoC – 0%

SoC (%)	C1 (F)	C2 (F)	C3 (F)	R0 (Ω)	R1 (Ω)	R2 (Ω)	R3 (Ω)
0	1.25E+02	4.14E+04	6.52E+02	6.92E-02	1.20E-02	6.51E-03	2.35E-03
10	2.25E+03	1.38E+04	3.25E+02	5.20E-02	1.90E-02	2.12E-02	1.06E-02
20	2.55E+03	1.71E+04	4.28E+01	3.68E-02	6.94E-03	1.59E-02	1.59E-02
30	2.04E+03	3.19E+04	2.08E+02	3.86E-02	1.06E-02	4.87E-03	7.60E-03
40	2.59E+03	3.29E+04	2.41E+03	4.35E-02	6.08E-03	1.45E-02	7.92E-03
50	6.57E+03	2.01E+04	2.19E+03	4.56E-02	1.32E-03	4.94E-02	1.46E-02
60	4.13E+03	6.87E+04	1.06E+02	3.42E-02	9.81E-03	2.76E-02	1.38E-02
70	3.74E+03	4.21E+04	1.62E+02	2.94E-02	1.23E-02	1.36E-01	1.59E-02
80	5.62E+03	4.04E+04	4.03E+02	4.62E-02	1.57E-02	8.14E-02	6.15E-03
90	5.47E+03	3.55E+04	1.88E+01	1.86E-02	3.08E-02	1.45E-01	4.49E-02
100	3.68E+03	4.00E+04	2.13E+01	2.78E-02	1.82E-02	2.42E-01	7.75E-02

Table 16: Table of parameters used for the generation of Figure 54

The intended use of the model is for the prediction of LIB performance during drive cycles both when operating independently (Cycle 1) and when combined with SCs (Cycle 2). The current for the two drive cycles used is shown in Figure 55 and Figure 56 (middle). Cycle 1 has higher discharge currents and a greater switching rate and has an initial SoC deliberately selected to test the voltage prediction during a pulse as it approaches the upper voltage limit, whilst Cycle 2 approaches the lower limit.

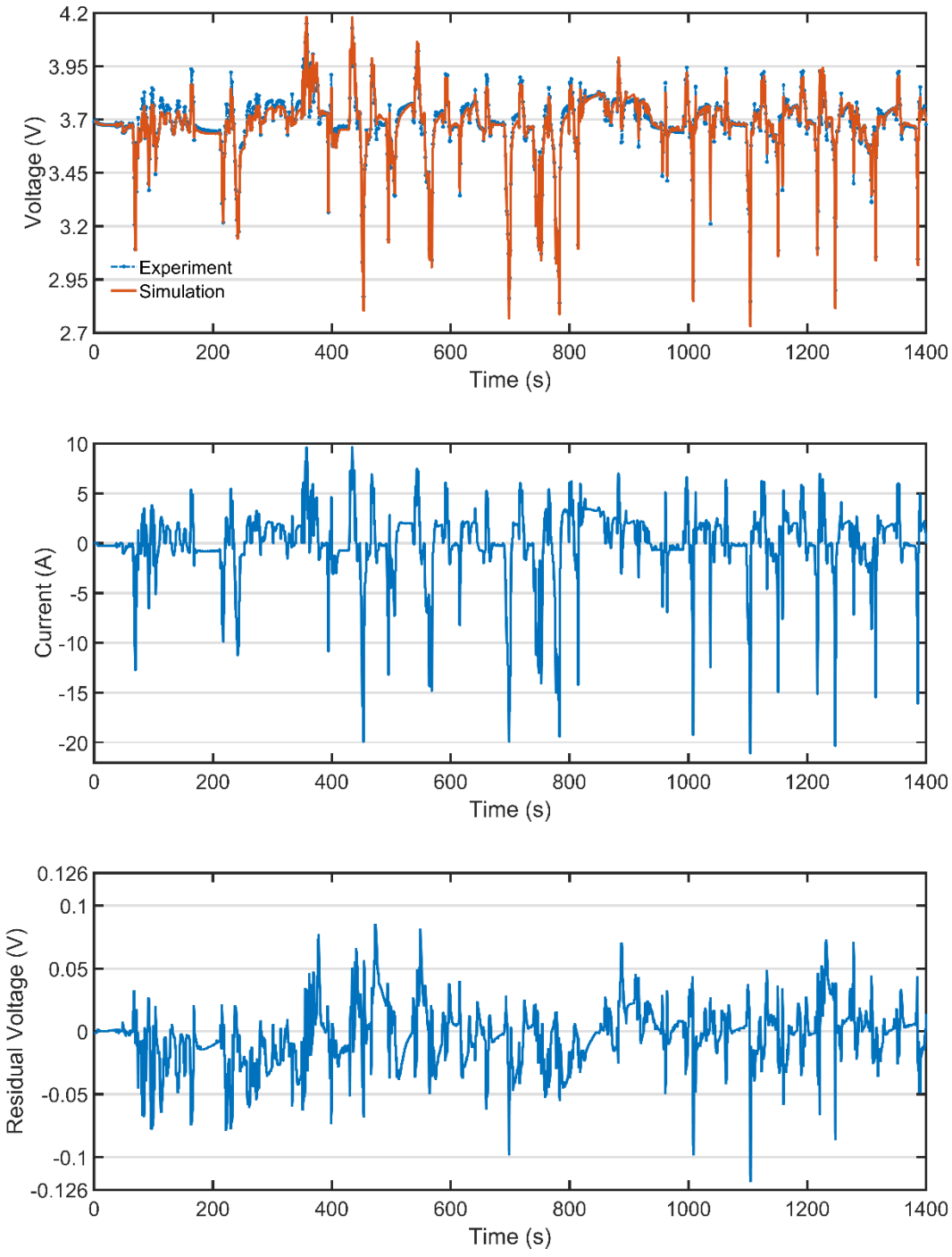


Figure 55: (Top) Comparison of experimental and simulated voltage for FTP drive cycle (Cycle 1), Initial SoC – 58%, Initial Temperature - 25℃, (Middle) Current profile of FTP drive cycle (Cycle 1), (Bottom) Residual between experimental and simulated voltage

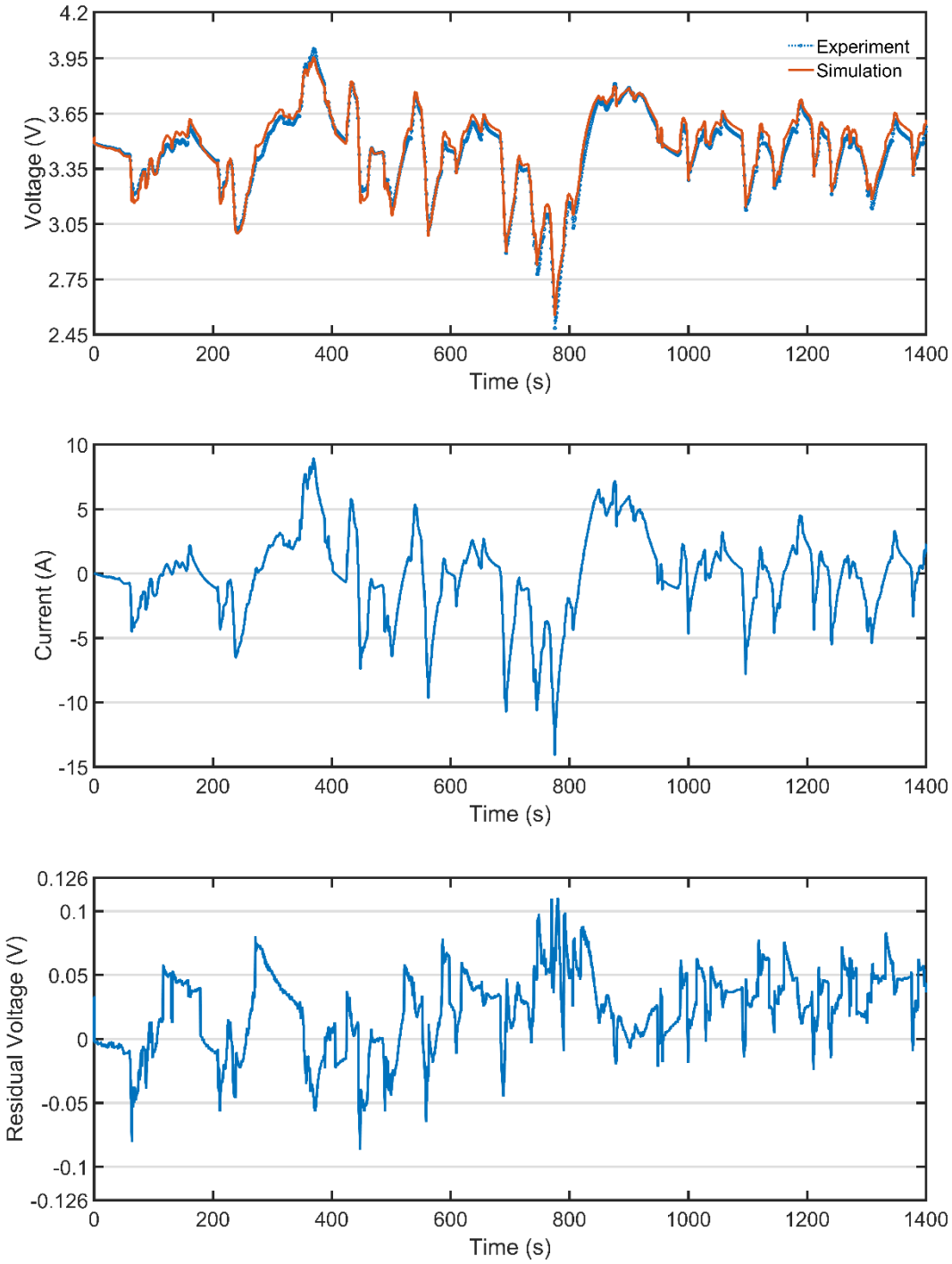


Figure 56: (Top) Comparison of experimental and simulated voltage for battery in a HESS over a drive cycle (Cycle 2), Initial SoC – 25%, Initial Temperature - 25℃, (Middle) Current profile of a battery in a HESS over the FTP drive cycle (Cycle 2), (Bottom) Residual between experimental and simulated voltage

Both Figure 55 and Figure 56 demonstrate that the model is capable of predicting the voltage response of the LIB during drive cycles within the target of a 3% voltage error up to the extremities of the voltage range. Modest changes to SoC to transition away from the limits of battery operation result in a greatly improved voltage prediction. Cycle 2 is used as a current demand for both Figure 56 and Figure 57, with Figure 57 having a 6% greater initial SoC; comparison of the residual plots clearly demonstrates this behaviour.

The predicted voltage, particularly at high currents, is highly dependent upon the temperature of the jelly-roll, thus a comparison of the predicted and experimentally measured temperature is shown in Figure 58. Terminal temperature is generally predicted well within the $\pm 1.5℃$ target, however the deviation briefly exceeds the target during high current charging events. This is likely to be attributable to a lack of complexity in the heat generation model which cannot independently predict heat generation at the anode and cathode.

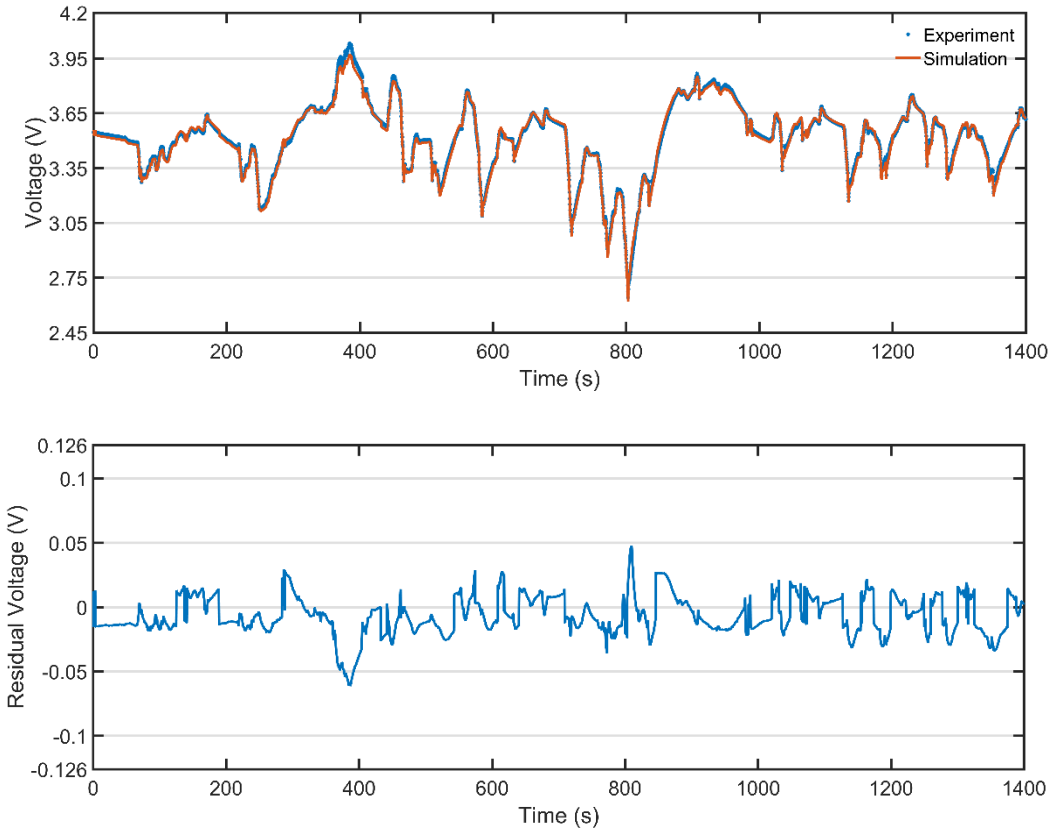


Figure 57: (Top) Comparison of experimental and simulated voltage for battery in a HESS over a drive cycle (Cycle 2), Initial SoC – 31%, Initial Temperature - 25℃, (Bottom) Residual between experimental and simulated voltage

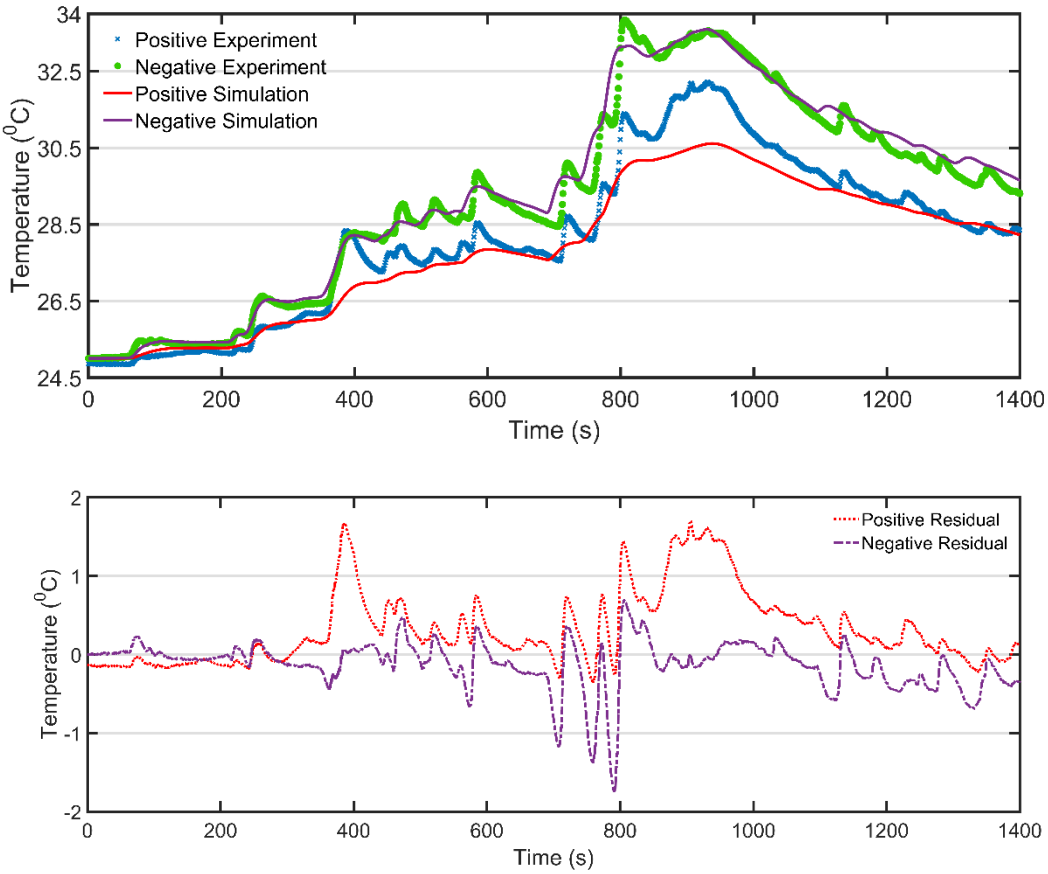


Figure 58: (a) Comparison of experimentally determined and simulated surface temperature for a battery in a HESS over a drive cycle (Cycle 2), Initial SoC – 25%, Initial Temperature - 25℃ (b) Residual of surface temperatures

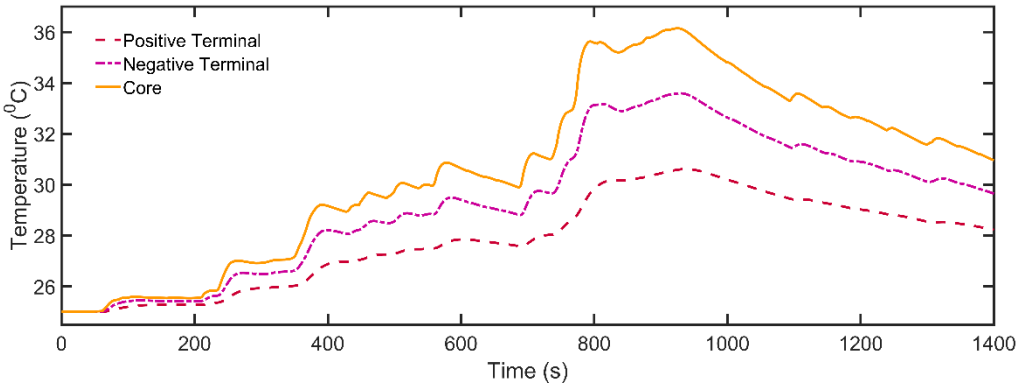


Figure 59: Plot of simulated temperature at the positive and negative terminal and at the core of the jelly-roll during cycle 2

The estimated temperature rise at the core is approximately 30% greater than the simulated temperature at the negative terminal, consistent with the findings of Forgez et al [223] who inserted a thermocouple into the core of an '18650' cylindrical cell. The estimated temperature gradient within the jelly-roll is small, with a peak of 0.15°C between the core and outer sections of the jelly-roll during Cycle 2. These findings are consistent with the high fidelity model of Somasundaram et al [225], albeit with a slight under-prediction of the peak thermal gradient due to reduced model fidelity; a comparison is shown in Figure 60, (note the small scale).

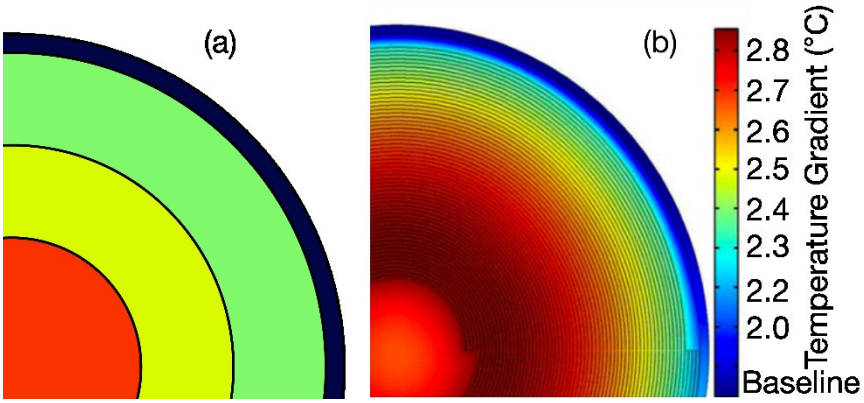


Figure 60: Temperature distribution across the radial cross section of a battery cell during a 5C discharge predicted by (a) the developed model, (b) Somasundaram model - [225]

4.9 Modelling Conclusion

An equivalent circuit electro-thermal battery model is developed to predict electrical and thermal performance of a LIB during automotive drive cycles both when operated alone and when in a HESS. It is necessary for the model to predict behaviour during high current operation during which significant heating will occur, therefore the electrical model, which accounts for variations in current, temperature and SoC is coupled to a thermal model which determines the heat generation and heat transfer.

The electrical model is parameterised using the 'layered approach' across the SoC range for currents ranging from a 2C charge to a 5C discharge. The initial estimate used for parameter estimated is generated through the use of EIS, and fitting is complete using the nonlinear least squares algorithm in the parameter estimation toolbox. Heat generation due to electrical losses and entropy changes is considered; heating as a result of chemical mixing and degradation inducing reactions is assumed to be negligible. Heat transfer is modelled through the use of thermal equivalent circuits to predict the internal temperature of the cell; high current pulse loads result in rapid heat generation, therefore it is necessary to predict electrical performance using the temperature of the active material.

It has been demonstrated that the model can predict terminal voltage during a drive cycle to within the target of a 3% voltage error over a range of SoC values and for drive cycles which exceed the maximum current for which the model is parameterised. The thermal model predicts temperature evolution at the positive and negative terminal well during a drive-cycle; the target of $\pm 1.5℃$ is briefly exceeded during high current charge, however the typical error is much lower than the target.

Heat generation is typically well predicted; however, the lumped resistance parameters limit the spatial discretisation of the heat generation model. Significant improvements to the thermal model are possible by decoupling both the constituents of the lumped series resistance parameter, and the anode/cathode resistance. This would enable the generated heat to be distributed more appropriately, and thus improve the prediction of the rate of change of temperature at the positive and negative terminals.

Internal temperature prediction is consistent with the findings of Forgez et al and Somasundaram et al. Internal thermal gradients during drive cycle operation are small for the cell under consideration, however a significant temperature difference exists between the cell surface and the core.

The developed electro-thermal model is parameterised in a time-efficient manner and is capable of predicting the electrical performance of a LIB over an automotive drive cycle to within the targeted error. A thermal model is used to predict the radial and axial temperature distribution within the cell. The error in predicted surface temperature is typically small, however it does exceed the targeted error briefly during high current charging. Internal temperature gradients are shown to be consistent with the findings of other studies.

5.0 Hybridised Energy Storage System

Motivation & Applicability to Research Questions

This chapter investigates whether it is possible to combine supercapacitors suitable for an mHEV with high-energy batteries suitable for use in a BEV to create a Hybridised Energy Storage System (HESS) suitable for use in a HEV. A passive HESS topology is investigated due to its low cost and complexity and therefore high reliability. A low cost HESS is found to be capable of meeting the electrical demands of a HEV during a drive cycle. The operating principles of HESSs are discussed and factors limiting system performance are explored. The performance of the HESS is found to be significantly less temperature dependent than battery-only systems, however the heat generated suggests a requirement for thermal management. A correctly sized HESS is shown to generate less heat than a specialised HPB ESS. The HESS degrades at a similar rate to a specialised HPB. In a HESS, battery resistance rises faster than supercapacitor resistance; as a result, the supercapacitor provides a greater current contribution over time, therefore the energy throughput, temperature rise and rate of degradation of the batteries is reduced.

5.1 Introduction

It is desirable for an automaker to create a modular electrified powertrain to enable the usage of the same base components across its portfolio of vehicles. The energy and power requirements of the Energy Storage System (ESS) vary significantly for different vehicle types; the requirements are summarised in Figure 1.

Vehicles classified as micro Hybrid Electric Vehicles (mHEVs) typically utilise a low voltage (48V) energy storage module to enable high power functions, such as electronic Power Assisted Steering (ePAS) and electric turbocharging (e-turbo). Additionally, the system is used to reduce CO_2 emissions by capturing regenerative energy from the vehicle, and enabling the engine to be switched off for extended periods of time. The ESS in a mHEV must provide or accept very high power for its size (commonly referred to as ‘C-Rate’) for short time periods with minimal thermal management, therefore it must have the attributes of high power, low energy, large thermal operating window, and high cycle life.

Hybrid Electric Vehicles (HEVs) can be electrically propelled for short distances and require significantly more power than a mHEV, therefore HEVs typically utilise high voltage ESSs (200-450V). The HEV is less cost sensitive than the mHEV, therefore semi-active thermal management can be used to improve system performance. Additionally, the usage profile dictates a lower cycle requirement than a mHEV as the larger energy capacity ESS is subject to fewer cycles for a given driving distance. Plug-in Hybrid Electric Vehicles (PHEV) have a similar use-case to HEVs, however they must electrically propel the vehicle for longer distances and therefore require more energy and consequently lower power density. Greater value exists in thermal management of larger battery packs, therefore the required thermal operating window is smaller.

Battery Electric Vehicles (BEVs) require significantly more energy and power than PHEVs, consequently larger ESSs are used. As with PHEVs, in a large ESS active thermal management provides good value, therefore a large thermal operating window is not required. Further, a comparatively shorter cycle life is sufficient in order to meet the vehicle life requirements.

As the requirements of the ESS for each vehicle configuration differ, it follows that a different battery or EDLC cell would be implemented in a module for each. However, the research and development required for the implementation of previously unused cells is costly, resource intensive and highly time consuming. It is therefore desirable to commonize cells across vehicle types.

SCs or High Power Battery (HPB) cells can be used to satisfy the requirements of an mHEV, and High Energy Battery (HEB) cells can fulfil the requirements of a BEV. Whilst it is not possible to use the same cells for a mHEV and BEV given the mutually exclusive attributes required, it is postulated that the cells for the mHEV and BEV could be combined to create a Hybridised Energy Storage System (HESS) for use in HEV and PHEV vehicles. This would enable automotive OEMs to adopt a modular approach whereby high energy and high power cells can be combined and their relative numbers scaled to meet the requirements of different vehicles.

Relatively few studies have analysed combinations of batteries and SCs for use in automotive applications [195,229–247], and a smaller number yet examine automotive traction applications, [237,239,243,244,247]. The studies that have considered traction applications do not consider practical requirements in hybrid vehicles, such as cost, volume, mass and reliability, and thus typically employ high cost and low reliability high power bi-directional DC-DC converters.

It is hypothesised that a combination of SCs and HEBs can reproduce the electrical capabilities of a HPB in automotive applications, whilst increasing energy efficiency, thereby reducing thermal management requirements and battery degradation. This study aims to quantify the electrical, thermal and degradation benefits of a HESS suitable for a HEV application against a specialised Energy Storage System (ESS).

5.2 Evaluation Conditions

5.2.1 Drive Cycle Selection

For meaningful and repeatable results, all comparisons were made using an automotive drive cycle. The NEDC drive cycle has a combination of very slow acceleration, constant velocity operation and long idle times compared to FTP-72, the drive cycle currently used for fuel economy and emissions certification in the US. Although the RMS current required for a HEV to meet the demand of the NEDC and FTP-72 drive cycles is similar (25 vs 28.5A), a comparison of Figure 61a and Figure 61b demonstrates that the current demand for the FTP drive cycle contains peaks of significantly larger amplitude and frequency. The FTP cycle was considered a better representation of real world usage.

Whilst both drive cycles are expected to be superseded by the WLTP drive cycle in the near future, at the time of writing, the details of this drive cycle are yet to be finalised. Therefore, the FTP-72 drive cycle is determined to be the most appropriate drive cycle to use.

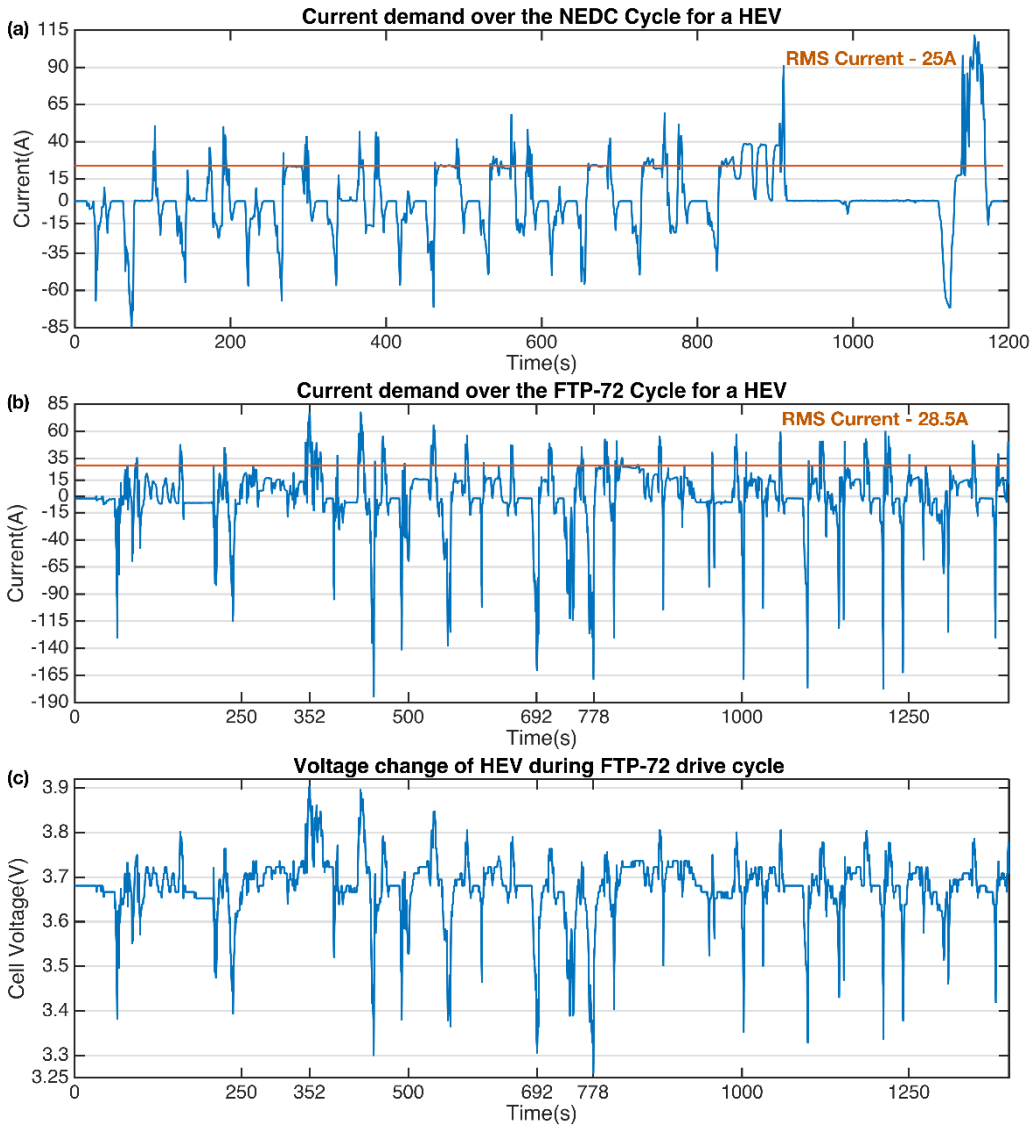


Figure 61: (a) Current request of a HEV during the NEDC drive cycle – orange line indicates the RMS current (25A), (b) Current request of a HEV during the FTP-72 drive cycle – orange line indicates the RMS current (28.5A), (c) Voltage evolution of a high power battery cell during the FTP drive cycle – Initial Conditions: 3.68V, 25℃

5.2.2 Drive Cycle Analysis

The Federal Test Procedure 75 (FTP-75) driving cycle is used by the Environmental Protection Agency (EPA) to determine the 'city driving' fuel efficiency for the US market. It is widely regarded as the most representative drive cycle of real world driving of the cycles currently used globally for emissions and fuel economy certification, [248,249]. The FTP-75 drive cycle consists of three distinct sections, the cold start phase (505s in duration), the stabilisation phase (866s in duration) and the hot start phase (505s in duration), which is a repetition of the cold start phase, [249]. Given that the objective of this work is capability analysis, the drive cycle was truncated by removing the hot-start phase to reduce cycle time without compromising the potential for performance analysis. The truncated version of the FTP-75 drive cycle is known as the FTP-72 drive cycle or the Urban Dynamometer Driving Schedule (UDDS).

The FTP-72 drive cycle is 1369s in duration, covering a distance of 12km at an average speed of 31.5km/h. The current demand and cell voltage shown in Figure 61b and Figure 61c was measured from a HEV and dynamically controlled by the Vehicle Supervisory Controller (VSC). It should therefore be noted that this value is dependent upon the vehicle specifications and control strategy,

therefore is designed around a particular ESS, and should only be used as an indicative requirement. This exact demand profile was utilised for all ESSs tested in this work to ensure they are comparable to a baseline.

The challenging aspects of the FTP drive cycle reside around the current peaks; the most challenging current pulses are those immediately preceded by additional current pulses of the same direction. It is possible to identify the most challenging parts of the drive cycle through examination of the peaks and troughs in the plot in Figure 61c showing the voltage change of a battery within the ESS during the drive cycle. The most severe/challenging charging event (350s), and discharging event (777s) are preceded by a period of charging or discharging respectively, and are not the instances of maximum charging/discharging current, suggesting that power availability is an important consideration when designing an ESS for this drive cycle. In this context, a challenging current demand is a high current pulse following activity which would lead to a reduced battery power availability.

5.3 System Configuration

A HESS consisting of SCs and batteries can adopt multiple topologies; these topologies can be categorised as active, semi-active or passive. Passive systems combine SCs and batteries in parallel and do not employ any direct control of the current provided by each device, [240,241,250–252]. Semi-active systems use a DC-DC converter to control the power contribution of either the SCs [245,253] or batteries [254,255]. A fully active system uses two DC-DC converters to independently control the power contribution of both the SCs and batteries, [256,257]. Multiple authors have worked to design bi-directional DC-DC converters specifically for the HESS application, [258–260]. A schematic of each configuration is provided in Figure 62.

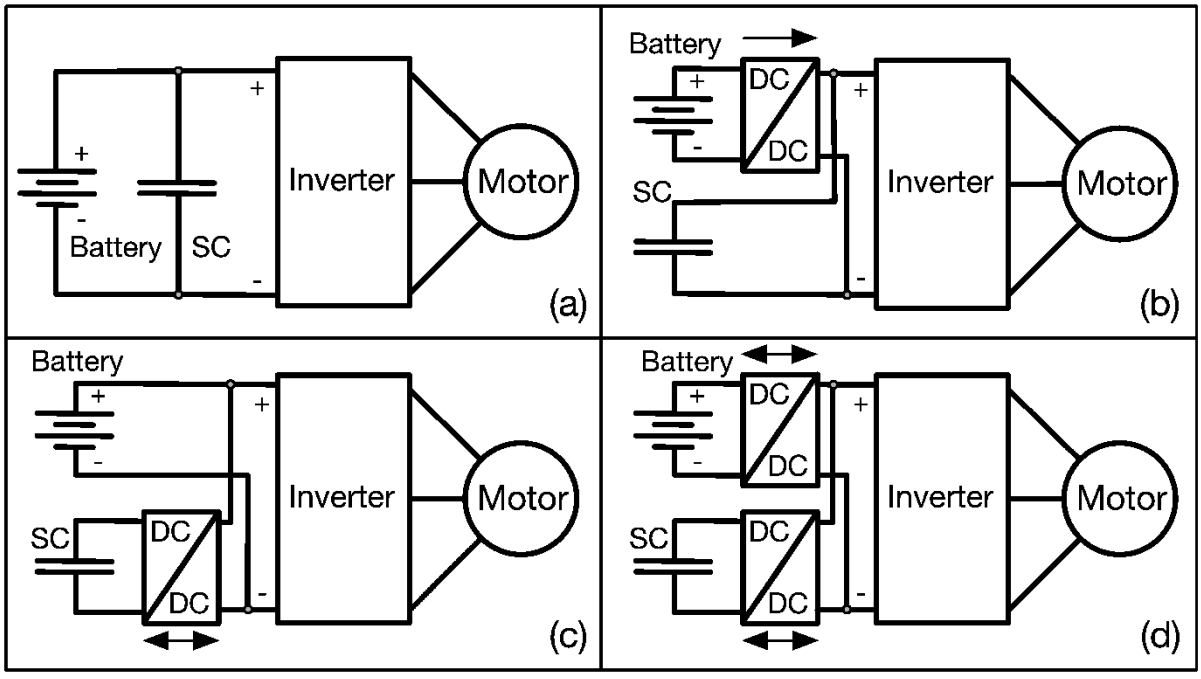


Figure 62: Schematic of (a) Passive HESS Topology (b) Battery semi-active HESS Topology (c) SC semi-active HESS Topology (d) Fully active HESS Topology – Adapted from [261,262]

5.3.1 Passive HESS

In passive systems, SCs and batteries are connected in parallel with one another, and the output of the parallel string is connected to the load. The current split between the battery and the SC is controlled by the relative resistance of each device, and cannot be actively controlled. The passive configuration does not require any control electronics unlike semi-active and fully active systems and is therefore in general the most robust, the cheapest, and requires the least package volume. Over a pulsed discharge, a passive HESS reduces battery current and voltage fluctuations thereby increasing energy efficiency and reducing battery degradation. However, the contribution of battery current to a current pulse does increase with pulse duration due to the SC voltage changing faster than the battery voltage when energy is added or removed. As a result, both the battery current rating and the SC energy capacity are factors that limit the maximum duration of a pulse that can be sustained. In this configuration, only a small fraction of the energy capacity of the SC is used. Whilst this system provides the fewest performance benefits, it is the cheapest, least complex and most reliable, [262].

5.3.2 Semi-active HESS

The most common semi-active HESS topologies are the battery semi-active HESS and SC semi-active HESS, where the DC-DC converter is placed on the battery pack and capacitor bank respectively. The SC semi-active HESS enables control over the power contribution or acceptance of the SCs, and decouples the battery and SC voltage. Given independent control over the utilisation of the SCs, a larger proportion of their energy capacity can be used, and the duration of pulse power output or acceptance becomes primarily dependent upon the energy storage capacity of the SC bank. Given that the output of the SC bank can be controlled, the battery output can be kept near constant, and the DC-DC converter does not need to be active under low current or steady state conditions. Additionally, the SC bank can be sized to the energy and power requirements, and not to the system voltage requirements. It has been shown by Miller et al [239] that the optimal configuration is up-converting of a lower voltage SC bank voltage to a higher DC-bus voltage.

However, the SC semi-active HESS requires a high-power buck-boost DC-DC converter that matches the required maximum power input and output. Further, this converter must be capable of accepting a wide lower voltage range to maximize the usable energy from the SC bank, at a relatively high efficiency for the HESS to maintain acceptable levels of energy efficiency, [263]. The DC-DC converter must also have a sufficiently fast response to meet the demands of a highly transient load, [239]. A uni-directional DC-DC converter would not allow the SC bank to be used for charge acceptance, and hence would rapidly become depleted.

A battery semi-active HESS enables control of battery current, and hence the load can be kept within those limits known to reduce battery degradation. Further, the required DC-DC converter power is limited to a region between the RMS power demand and peak battery output permitted, and hence is significantly lower than in the SC semi-active HESS topology, [262].

However, a fundamental issue with the battery semi-active HESS is that the SoC of the capacitor bank controls the DC-bus voltage which becomes highly dynamic, resulting in inverter control problems, [239]. Consequently, a small SoC window must be used to maintain an acceptable voltage output. In order to provide the required energy within the SoC window the SC pack must be oversized. In addition, in this configuration the converter must be active at all times, thereby decreasing energy efficiency, [263].

5.3.3 Fully-active HESS

Many topologies exist for a fully-active HESS, [260,264,265], however discussion in this work will be limited to a topology in which a bi-directional converter is placed upon both the battery and the SC. This configuration enables optimal usage of both the battery pack and the SC bank, and provides the performance benefits of both the SC semi-active HESS and the battery semi-active HESS.

Whilst this system may provide the greatest control, and the best theoretical performance, it does require two DC/DC converters, one of which must be bi-directional and high power, which increase significantly the financial and package volume cost, [246,258,259,263].

5.3.4 Topology Selection

For appropriate topology selection, it is necessary to consider the requirements of the application. The targeted application is a HEV which contains both an electrical powertrain and an internal combustion engine based powertrain, and therefore the primary considerations for topology selection for this application are cost, complexity, reliability and volume.

Very high power bidirectional DC-DC buck-boost converters (>60kW) with a wide input voltage range, such as those required for a SC semi-active and fully active HESS are typically large, very costly, require significant thermal management and suffer from low efficiency and reliability, [266,267]. Consequently, it is highly desirable to avoid the use of these devices in a HEV, thus the fully-active and SC semi-active topologies are not considered. The battery semi-active topology suffers from large DC-bus voltage fluctuations which will result in a requirement for a large input voltage range for the motor controller. Further, the fact that all energy is channelled through a DC-DC converter reduces efficiency and an oversized SC bank and DC-DC converter add cost and volume. For these reasons, a battery semi-active topology is not considered.

The passive HESS has performance benefits over a battery only system, does not substantially increase complexity and improves system reliability via a reduction of power fade. Depending upon system configuration, the passive HESS can be lower in cost or mass/volume than a battery only system. Consequently, the passive HESS is the topology selected and will hereafter simply be referred to as the HESS.

5.4 Experimental Setup

5.4.1 Cell Selection

It is the intention of this study to determine whether it is possible to replace a High Power Battery (HPB) specialised for use in a HEV with a HESS consisting of SCs suitable for use in a mHEV and High Energy Battery (HEB) cells suitable for use in a BEV. The Saft VL6P cell is a HPB commonly used in HEV applications, [268–270], and was selected to represent a specialised cell for HEV applications and provide a baseline for comparison for the HESS. The cell has an NCA cathode and a graphite anode, each of which are relatively thin to enable continuous high power operation.

An appropriate cell for a BEV possesses high energy-density, acceptable power density and is low cost, therefore the Panasonic 18650BD (P18650BD) cell was selected to represent the High-Energy Battery (HEB). The P18650BD also uses an NCA cathode and a graphite anode, however with much thicker electrodes. Given its highly successful use in the Tesla Model S, the P18650BD cell is proven to satisfy the performance requirements of a BEV, and the cost of a single cell is estimated to be under $2, [14]. Although the automotive industry is shifting toward large form factor high capacity cells, the P18650BD cells were selected to determine whether an ultra low-cost system was viable. The total commercial cost of the HESS using I3kF cells is estimated to be <40% of the cost of the HPB.

The Ioxus Titan 2000F (I2kF) SC cell was selected as the SC cell for use in the HESS; in addition to the characteristics required for use in a mHEV, namely high power-density, acceptable energy density and excellent cycle life, it possesses extremely low equivalent series resistance (ESR) which aids HESS performance. The selected cell has activated carbon electrodes of different thickness, and uses an electrolyte consisting a TEABF4 salt in an acetonitrile based solvent. Where discussed, this cell was substituted with the and 3000F variant of the same cell, hereafter referred to as I3kF.

The HESS combines two series connected I2kF cells, in parallel with two parallel connected P18650BD cells, as illustrated in Figure 63a. The performance of the HESS is to be compared with that of a specialised HPB, and HEBs in parallel strings to analyse the benefits of adding SCs a an ESS consisting of a particular battery cell. The HPB has a slightly higher energy capacity than the batteries in the HESS (7Ah vs 6.4Ah), however the maximum cumulative energy change during the FTP drive cycle is 0.08Ah, therefore this energy capacity difference is assumed to be inconsequential.

5.4.2 Equating Lab Scale Test to Module Level

In the lab-scale test, two SC cells are connected in series (2s1p), and subsequently connected in parallel with two batteries which themselves are connected in parallel (1s2p configuration), as per Figure 63a, because the SC cells have a lower maximum voltage. Therefore, the ratio of SC cells to batteries in series for the lab scale test was 2:1. At a module level, this ratio would be reduced to approximately 1.4:1. For example, a 300V module for a HEV must consist of approximately 69 cells in series to achieve the desired voltage, and 2 parallel strings to approximately match the energy capacity of the HPB. The maximum voltage is matched by 100 SC cells in series (assuming the use of 3V cells); the use of parallel strings of SC cells is unnecessary, as in instances where greater SC energy is required, it is best to use a larger SC cell.

At a module level the HESS will perform differently to the lab scale setup. Primarily, the relative resistance of the battery and SC will change, which in turn will affect the split of current between the SC and batteries. Additionally, given the smaller ratio of SC to battery cells, each SC cell will operate at a higher voltage for the SC bank and battery module voltage to match. The consequence of the SCs operating at a higher voltage is that they will exhibit a higher capacitance, as capacitance is a strong function of operating voltage, [39]. Therefore, smaller capacity SC cells are required in a module than in a lab scale test.

A simple function cannot be given to equate the capacitance or energy of a cell in the lab scale test to those of cells at the module level. The capacitance of the SC cells varies non-linearly with SoC, and a change in energy storage of the SC cells will impact both the voltage change during operation, and the energy contribution of the battery. The modelling tool developed in section 5.8 suggests that the performance of the 3000F HESS is matched at the module level by a 2475F capacitor. The determination of this value is discussed in section 5.8.3.

5.4.3 Experimental Setup

A test rig was created to enable the measurement of HESS and battery current, cell voltages and cell temperatures, whilst controlling thermal boundary conditions and maintaining low and repeatable contact resistances. The test rig for the HESS is pictured in Figure 63b.

Consistent values of contact resistances are important, as the ratio of resistance between the SCs and batteries largely dictate the current split between the two devices. In order to compare the performance of the system under different conditions, it is necessary that the contact resistance does not change when cells are removed and re-connected. To maintain consistency, each time the cells were reconnected the contact areas for the cells were polished with fine grain sand-paper and

cleaned with isopropanol to remove foreign objects, surface impurities and oxide layers, and the surface area and tightening torque of connections were controlled to consistent levels.

Thermocouples were connected to cell terminals using an electrically insulating, thermally conductive boron-nitride based epoxy, (3M TC-2810), and radially across cells using Kapton tape. Type K thermocouples with a precision of 0.1℃ were used alongside a NI CompactDAQ with an NI9213 module for data acquisition. Current measurements using a hall-effect sensor were found to produce very noisy results at low battery currents, therefore shunt resistors were used for this purpose. The shunt resistor used to measure battery current was placed between the SC and battery cells as shown in Figure 63a.

The insertion of a resistor into the circuit changes the distribution of current, however efforts were made to ensure that this effect was negligible. An oversized shunt resistor with a resistance of $1x10^{-4}\Omega$ was utilised alongside a high resolution (16-bit) voltage measurement device (NI CompactDAQ with an NI9206 module); this combination yielded a resolution of $5.8x10^{-2}$A per bit. At the maximum anticipated battery operating temperature of 50℃, the minimum resistance of each battery cell is 30 $\mathrm{m}\Omega$, reducing to $15\mathrm{m}\Omega$ in the 2P configuration; therefore the maximum reduction of battery current the $0.1\mathrm{m}\Omega$ shunt resistor should cause is estimated to be 0.66%.

The FTP drive cycle testing was conducted using a Maccor Series 4000 battery cycler, and measurements to track degradation were completed using a Biologic BC-815 potentiostat. Data for voltage, current and temperature was acquired via a National Instruments CompactDAQ connected to the Labview software package running on a standard desktop PC.

The system performance is strongly dependent on temperature; therefore, an Active Thermal Management (ATM) system is developed in order to maintain the desired test temperature, thereby largely decoupling the effect of heat generation during the test from the system performance. Peltier elements are used to cool the battery and SC terminals; the power supplies for the Peltier elements are controlled by Labview, which implements PID control to maintain either the cell or battery connector temperature at the desired level. The location of the Peltier elements is marked in Figure 63b; water cooling blocks placed directly atop the Peltier elements are required to maintain the cooling efficiency of the Peltier elements at acceptable levels. Peltier elements operate with efficiencies that are typically less than 15%, thus are not suited to commercial thermal management applications, however they useful devices for lab based testing.

The ATM system is reactive and not predictive. Whilst the temperatures do deviate from the desired level, the magnitude and duration of their deviation are greatly reduced in comparison to operation with the ATM switched off, as shown in Figure 63c. The maximum temperature rise at the negative terminal is reduced by 50%, and the rise of average temperature is reduced by 90%, (ATM on – 25.3℃ ATM off – 28.6℃). To enable the temperature of the system to quickly return to the desired level, a high proportional gain (K_p) value is required, however the rapidly varying rate of heat generation tends to lead to a cooling overshoot. To reduce the effect of the overshoot, the test rig is placed within a large thermal chamber which is held at the target temperature, and a series of fans are used to maintain a consistent level of forced convection, thus eliminating the need for bi-directional power supplies for the Peltier elements.

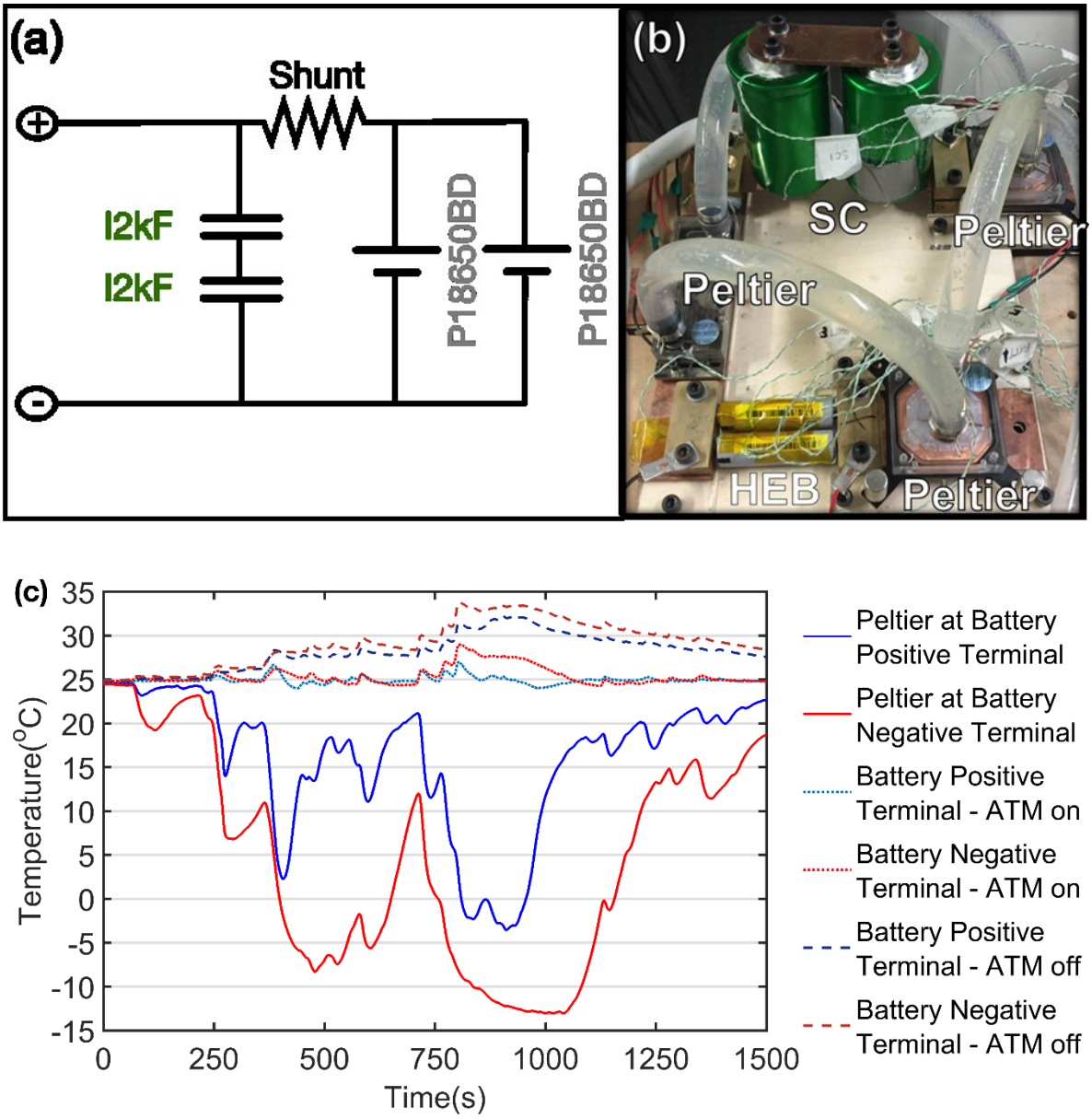


Figure 63: (a) Schematic of lab scale HESS (b) Photograph of lab scale HESS experimental setup (c) Comparative analysis of battery temperature in the HESS using I2KF SCs with and without the active thermal management system (ATM) operational

5.5 System Performance

5.5.1 HESS Performance Analysis

In a HESS, the current split between the EDLCs and batteries is a function of time, the relative resistance of each device, and the EDLC capacity. Figure 64 (top) shows the battery current evolution with time as a square wave current profile as applied to the HESS. Given our lab scale experimental configuration (SC 2s1p, battery 1s2p), the instantaneous current for each battery and SC cell can be determined by using circuit theory as:

$$I_{0_{\mathrm{Batt}}} = I_{\mathrm{T}}\left[1 - \left(\frac{{}^{R_{\mathrm{Batt}}}/_{n_{\mathrm{Batt}}}}{(R_{\mathrm{SC}} \cdot n_{\mathrm{SC}}) + ((R_{\mathrm{Batt}})^{-1} \cdot n_{\mathrm{Batt}})^{-1}}\right)\right] \quad \text{Equation 48}$$

$$I_{0_{SC}} = I_T\left[1 - \left(\frac{R_{SC}.n_{SC}}{(R_{SC}\cdot n_{SC}) + ((R_{Batt})^{-1}\cdot n_{Batt})^{-1}}\right)\right] \quad \text{Equation 49}$$

where I_0 (A) is the instantaneous current at the beginning of the applied step current, I_T (A) the total applied current, *R* (Ω) the equivalent series resistance and *n* the number of cells. The subscripts 'Batt' and 'SC' refer to the battery and SC cells respectively.

When the HESS begins at equilibrium, the battery current approximately obeys a simple quadratic relation as a function of time during the pulse:

$$I_{Batt}(t) = A\cdot I_T\cdot t^2 + B\cdot I_T\cdot t + I_{0_{Batt}} \quad \text{Equation 50}$$

where A, B are constants fitted to experimental data, and $I_{0_{Batt}}$ can be calculated for *t*=0 using Equation 48. Whilst the current of the system shown can be described using a linear function of time, the behaviour in HESSs using smaller SCs is best described used a quadratic function of time.

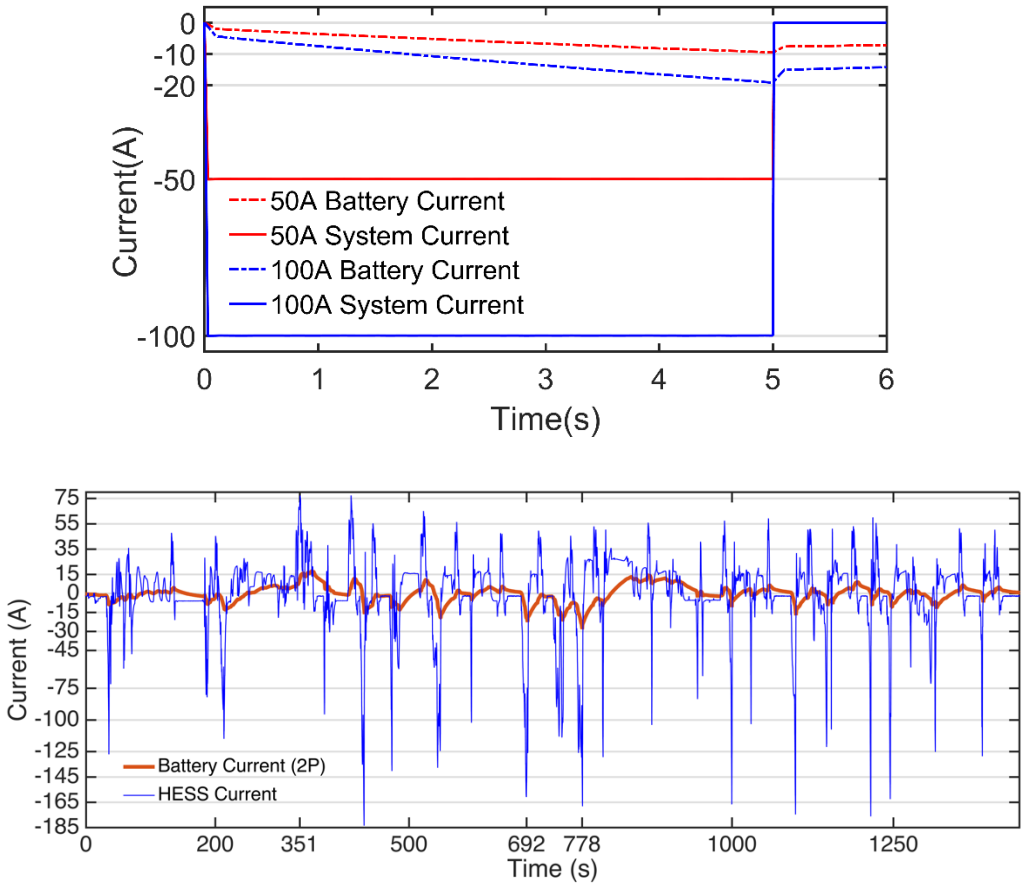


Figure 64: Comparison of HESS and battery current for 5 second square wave current pulses (top) and over the FTP drive-cycle (bottom). 'Battery current' denotes the total current provided by both cells. HESS uses I3kF SCs, operated at 25℃ with an initial voltage of 3.49V

Whilst the instantaneous current split between the batteries and SCs is determined by the relative resistance of each device, the battery current increases with time during the current pulse. The greatest benefits arise when the SC resistance is much smaller than the battery resistance; in this configuration, the SC ESR (0.17mΩ x 2) is two orders of magnitude lower than the ESR of the batteries (31.5mΩ / 2). Therefore, over a 5 second pulse 80-95% of the current is supplied by the SC.

As a result, the SC SoC and hence voltage will drop faster than the battery voltage. Given that the batteries and SC are connected in parallel in the HESS, they must remain at the same voltage. Therefore, the battery current contribution rises, simultaneously causing a decrease in the SC current contribution, such that the voltage of the two devices matches. The rate of increase of battery current therefore is highly dependent upon the capacity of the SCs used in the HESS. Given an equal energy discharge, a SC of lesser capacity decreases in voltage to a greater extent as $Energy = 0.5 \cdot Capacitance \cdot Voltage^2$, therefore a lower capacity SC induces a higher rate of battery current increase during a current pulse. Following the removal of the system load, a decaying current continues to flow from the batteries to the SC until the SC voltage matches the battery voltage.

The proportion of the total current demand over the FTP drive cycle provided by the batteries is shown in Figure 64 (bottom), and the peak and RMS values are provided in Table 17. The HESS with I3kF capacitors decreases the peak current of the batteries by 77% during charging and by 85% during discharge, while the RMS current is reduced by 80% in comparison to the system current (which is the same as the current of the HPB).

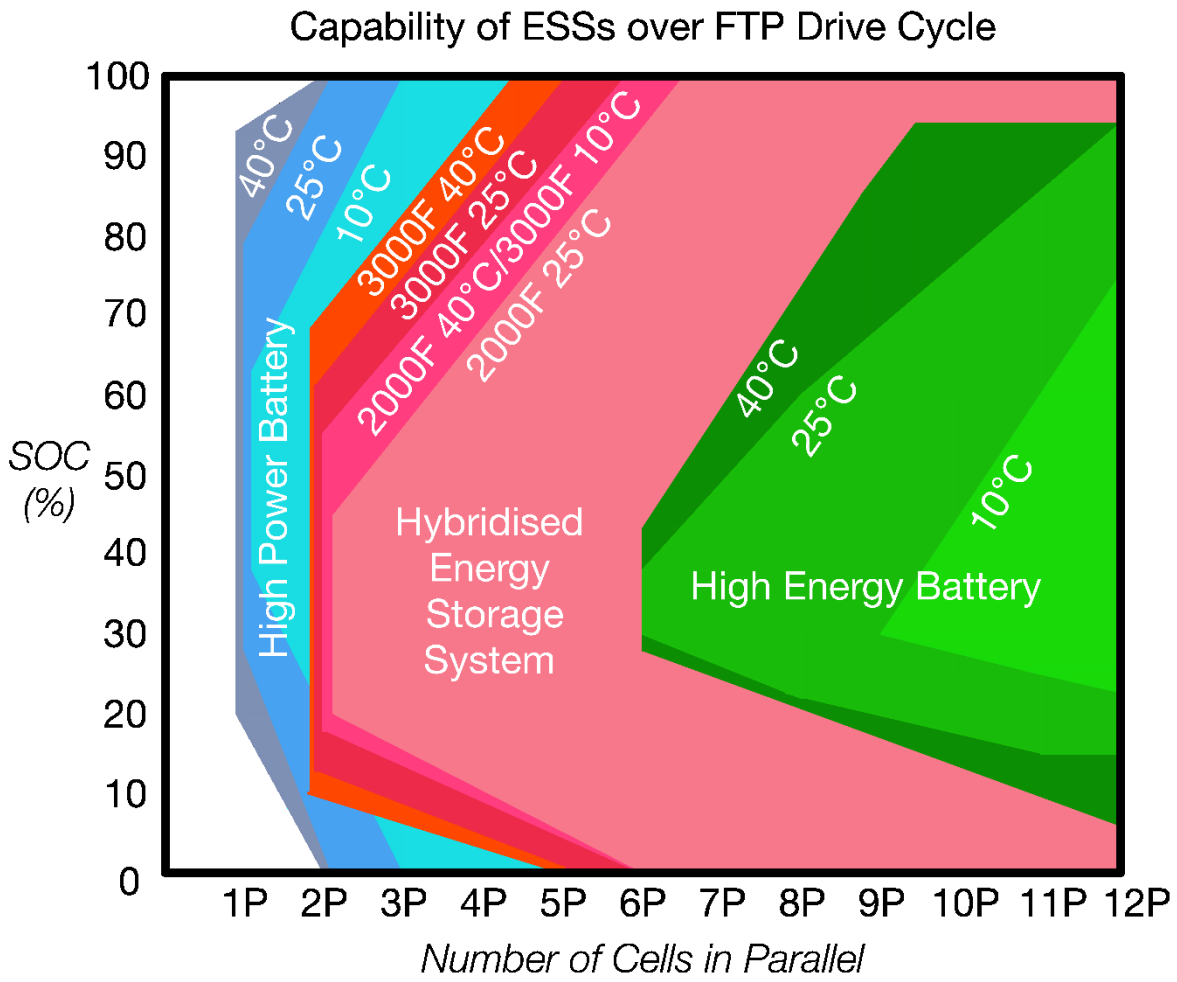
	Peak Current (A)		RMS Current (A)
	Charge	Discharge	
SAFT VL6P (HPB)	77.4	183.5	28.5
P18650BD (HEB - 8P)	9.6	23.0	3.73
HESS 2000F Battery	10.6	17.8	3.9
HESS 3000F Battery	8.9	14.1	2.8

Table 17: Comparison of peak and RMS battery current over the FTP cycle at 25℃ for each system under consideration

5.5.2 HESS Performance relative to other systems

The capability of HPBs, HEBs and HESSs to meet the current demand of the FTP drive cycle within their limits of operation is dependent upon the initial SoC, temperature, number of cells in parallel, and, in the case of the HESS, the size of the SCs. Figure 65 (Top) graphically demonstrates the capability of the different types of ESSs, showing the range of SoC that can be used without compromising power capability, at different temperatures. For example, it shows that at 10℃ an 8P HEB system will not work at any SOC, and at least 10 cells in parallel are required for a limited operating range at this temperature. In contrast, the 3000F HESS system with just 2 battery cells in parallel has an SOC window of 20-55% at 10℃.

The cycle is charge neutral, and the maximum charge deviation during the cycle is relatively small (peak of 0.08Ah discharge) in comparison to the capacity of the battery cells tested. The limiting factor is the ability of each ESS to supply current for the frequent and large current spikes whilst remaining within safe voltage limits. The high-current pulses pose a challenge for each of the ESSs under evaluation; the presence of a current spike leads to a temporary reduction of power availability due to slow diffusion within the battery cell electrodes. This solid state diffusion limitation manifests itself as an increase in resistance. Diffusion limitations can reduce the battery power availability enough to cause sufficient increase of the battery resistance such that their voltage reaches the safety limit before meeting the requirements of the drive cycle. In a HESS, as the battery resistance rises due to diffusion limitations, an increasing current demand is placed on the SC. Consequently, the SC capacity becomes an increasingly important factor in the terminal voltage of the HESS and in determining its capabilities within safe operating limits.



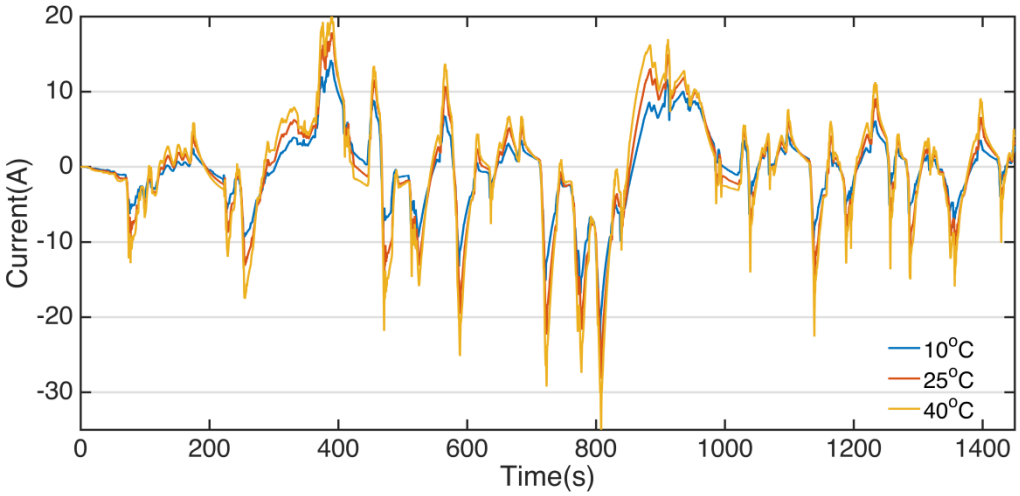


Figure 65: (Top) Experimentally determined performance map showing the ability of different energy storage systems to meet the requirements of the FTP drive cycle in a hybrid electric vehicle as a function of state of charge, number of cells in parallel, temperature, and in the case of the HESS, capacitor size. Different shades of blue show the performance of the high power battery, different shades of red show the performance of the HESS, and different shades of green show the performance of the high energy battery system. Active thermal management system is used. (Bottom) Total current provided by batteries in HESS over the FTP drive cycle at different operating temperatures

Additionally, solid state diffusion is strongly dependent on temperature, varying according to an Arrhenius relationship; therefore, temperature strongly affects system performance. The system

with the strongest temperature dependence is the HEB ESS; their thicker and denser electrodes which improve energy density simultaneously reduce diffusivity and increase the diffusion path length. In a 10P configuration, the window of operation for the high-energy cells is 80% smaller by capacity at 10°C than at 40°C. The high-power cells show a weaker temperature dependence with a window of operation that is 66% smaller; additional details are provided in Table 18.

	Usable SoC Range (%)			Capability at 10°C relative to 40°C (%)
	40°C	25°C	10°C	
SAFT VL6P (HPB – 1P)	21-94 (73)	28-78 (50)	38-63 (25)	34
P18650BD (HEB - 10P)	12-94 (82)	17-78 (61)	26-43 (17)	20
HESS 2000F (18650 – 2P)	17-55 (38)	20-45 (25)	-	-
HESS 3000F (18650 – 2P)	10-68 (58)	13-61 (48)	17-55 (37)	64

Table 18: Experimentally determined effect of temperature on usable SoC range to run the FTP drive – values in brackets show difference between minimum and maximum SoC

The HESS shows a weaker dependence upon temperature, with the system using I3kF capacitors exhibiting a usable SoC range that is 36% smaller by capacity at 10°C than at 40°C. At lower temperatures battery resistance increases significantly, whereas the SC resistance remains relatively constant, [39]. Consequently, the ratio of the relative resistance of the battery to the SCs increases, leading to a reduction of the battery current contribution to system current. The effect is significant, as the battery current is reduced by up to 55% when operated at 10°C compared with 40°C as shown in Figure 65 (bottom). Therefore, in the HESS the reduced power capability of the battery cells at low temperatures is offset by a significantly reduced battery current demand. At elevated temperatures, the resistance of the battery cells drops considerably, whilst the resistance of the SCs is relatively stable, thus the HESS performance increase at elevated temperatures is also less than that of the HEB and HPB.

The battery current demand might appear similar for the HEB system and the HESS using 2000F SCs, (similar RMS and peak values of current, shown in Table 17), however the current varies considerably when considered in the time domain. Figure 66a shows a comparison of the battery current over the FTP drive cycle for the HEB, HESS 2000F and HESS 3000F. The profile of the current demand for the HEB system is a downscaled version of the FTP-72 drive cycle, however in the HESS the SCs smoothen this load considerably, reducing the rate of current change. The histograms in Figure 66b show that the HEB system demands a wide range of battery currents with appreciable time spent above 10A. Comparatively, the HESS spends significantly less time providing a current of over 10A, and a greater period of time providing less than 10A. As the batteries in the HEB ESS and the HESS are utilised in a very different manner, the factors limiting performance differ.

The capability of the HEB system is limited by its power capability, and as discussed previously, the power availability is particularly poor when the HEB cell is not at equilibrium due to diffusion limitations. The HEB system is sized by adjusting the number of cells in parallel to reduce current demand to a level where each cell has sufficient power available to meet the requirements.

The capability of the HESS is limited by SC capacity and battery power availability, which are coupled, and by the SC ESR. Battery resistance increases as power availability is reduced, thus battery power availability impacts the current demand placed upon the SCs as the ratio of battery to SC resistance changes, resulting in a change in rate of SC SoC variation. Following the removal of a load, current transfer occurs between the SC and battery at a decaying rate as necessary to maintain the two

devices at an equal voltage. Thus, the greater the change of SC SoC, the greater the power demand on the battery, and thus the lower the battery power availability shortly after a charge/discharge event. A SC of greater capacity reduces SC SoC variations, improves battery power availability and reduces battery Energy Throughput (ET).

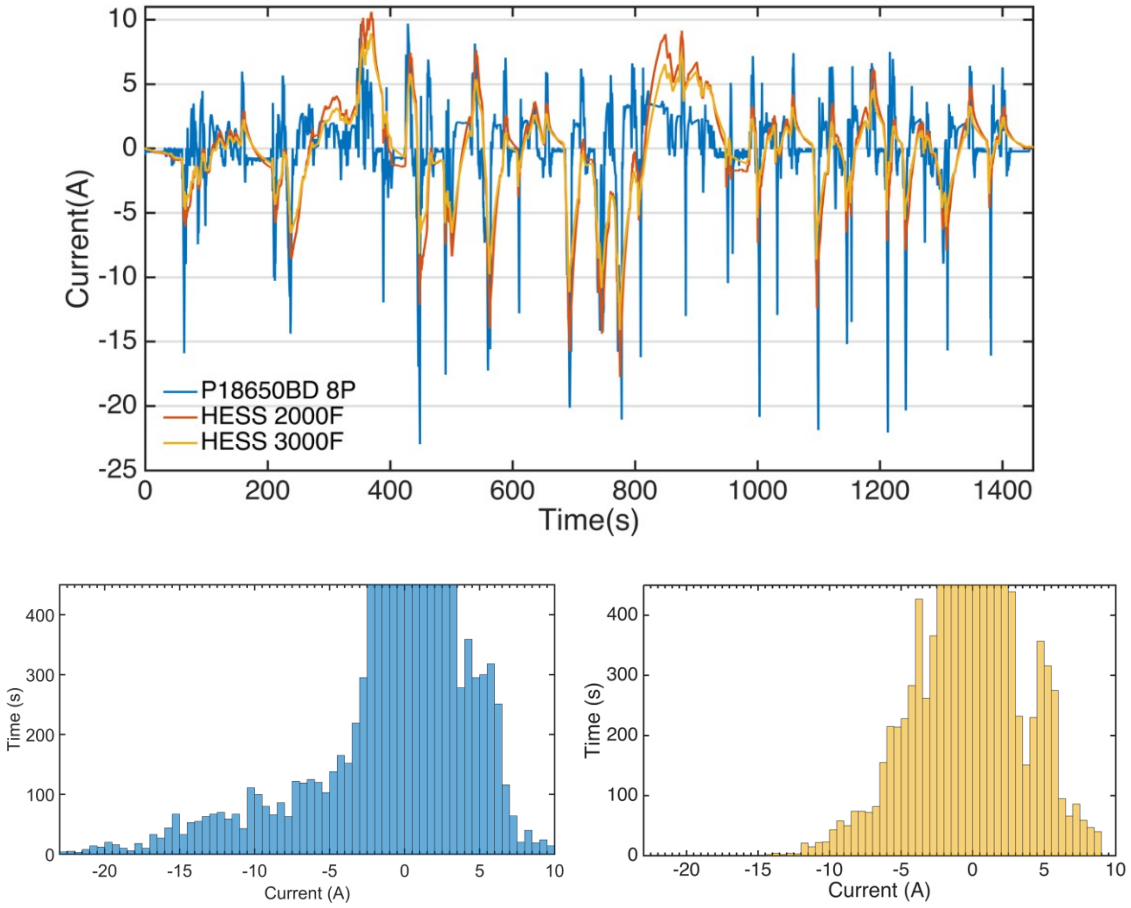


Figure 66: (a) Battery current comparison between HESS using 2000F and 3000F Capacitors and high-energy cells in 8P configuration – Initial Conditions: 3.49V, 25℃, ATM on (b) Histograms showing the current distribution from a single battery within the HEB ESS in the 8P configuration (left) and a single battery in the I3kF HESS (right)

The voltage change of the HESS mirrors the behaviour of the battery current; the voltage change during the FTP drive cycle is significantly greater (up to 60%) with the I2kF SCs than with the I3kF SCs. This is attributable to the increased demand placed upon the battery in the HESS using I2kF SCs due to the lower SC capacitance and higher SC resistance.

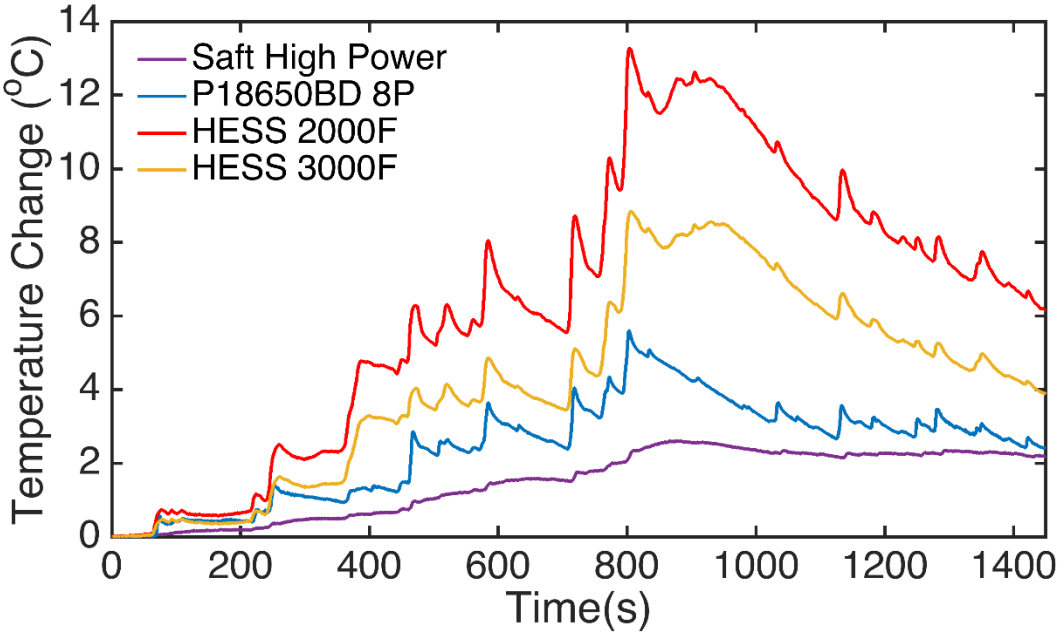


Figure 67: Battery temperatures at the negative terminal – Initial Conditions: HESS and HEB systems at 3.49V and HPB at 3.57V (corresponding to midpoint of usable SoC at 10℃), both systems at 25℃

It is necessary to consider heat generation alongside temperature change to compare thermal management requirements. There are multiple sources of heat within a lithium battery and they can broadly be categorised as electrical losses, entropic heating, species transport or mixing heat and degradation inducing reactions, [211]. In high current, pulse load applications, heat generation is dominated by electrical losses, [219,220], therefore other sources can be neglected. The electrical losses are the combined losses attributable to interfacial kinetics and ohmic losses and can be determined using the over-potential as per Equation 51, where I is the applied current (A), R is the resistance (Ω) and the over-potential can be defined as $\eta = |V_{terminal} - V_{OCV}|$. Cumulative heat generation over each cycled is calculated as the integral of Equation 51. The cumulative heat generation for each ESS over the FTP drive cycle is presented in Table 19, and the measured cell temperature is shown in Figure 67.

$$\dot{Q}_{El_Loss}(t) = I^2R(t) = I\eta(t) \qquad \text{Equation 51}$$

	Battery Heat (J)	SC Heat (J)	Module Configuration Battery | SC	HV Module Heat (J)
HPB	2549	-	72S1P	183,528
HEB	801	-	69S8P	442,152
HESS 2000F	1372	171	69S2P | 100S1P	206,453
HESS 3000F	906	158	69S2P | 100S1P	140,828

Table 19: Cumulative heat generation for each ESS over the FTP drive cycle - Initial Conditions: HESS and HEB systems at 3.49V and HPB at 3.57V (corresponding to midpoint of usable SoC at 10℃), both systems at 25℃

When each system is tested with the ATM system switched off, the HPB experiences the smallest temperature increase, whilst the batteries in the HESS using 2000F SCs experience the largest. Although the HPB generates the greatest amount of heat at the cell level, it increases in temperature the least as the Saft VL6P cell has a significantly greater thermal mass than the P18650BD cell. The batteries in the HESS using 2000F SCs increase in temperature the most; their ET (as presented in Table 20) and therefore heat generation is greater than the other ESSs using the P18650BD cell. The

temperature rise at the terminals of the SCs did not exceed 1℃ for either HESS, and the vast majority of heat generation occurs within the battery cells.

Whilst the cell level temperature rise is greatest in the HESS battery cells, at the module level the heat generated by the HESSs is significantly less than the HEB system, and comparable to the HPB system. The 2000F HESS configuration generates 12% more heat than the HPB ESS, whilst the 3000F system generates 23% less heat. It can therefore be concluded that an appropriately sized HESS will generate less heat than a HPB ESS, the bulk of the heat generation occurs within the battery cells and therefore is more localised, and passive thermal management should suffice for the SCs. A reduction of heat generated and increased localisation should enable thermal management system downsizing. Additionally, reduced thermal losses demonstrate improved energy efficiency.

The ET for each ESS is similar (within 1.5%), and is shown in Table 20. As current is controlled, differences in ET are a result of voltage change differences. In the HESSs, the ET for each battery cell is reduced by over 80% in comparison to the total ET of the HESS. However, for both of the HESSs the ET for each battery cell is greater than it is for the HEB system (assuming each parallel string in the HEB system is identical).

	Energy Throughput per Cycle (kJ)	Reduction of battery energy throughput (%)*
HPB System	86.0	-
HEB System	85.6	-
HEB Single Cell	10.7	88
HESS 2000F System	86.2	-
HESS 2000F Each HEB Cell	14.8	83
HESS 3000F System	86.8	-
HESS 3000F Each HEB Cell	11.9	87

Table 20: Energy throughput for each ESS during the FTP drive cycle - Initial Conditions: HESS and HEB systems at 3.49V and HPB at 3.57V, temperature of 25℃ with active thermal management system enabled. (* calculated with respect to the ET of each system)

5.5.3 System Specification & Cost

Whilst it has been shown that the HESS can perform comparably to the specialised HPB from the perspective of meeting the power demand of a certification drive-cycle, it is necessary to consider the additional factors important in system design. The cost, mass and volume of the ESS are key considerations in the adoption of HESSs in hybridised vehicles, as both an electrified and an internal combustion engine must be integrated into a single vehicle powertrain. The battery cells used in both tested HESSs were selected because they were highly advantageous from a cost perspective, however the high resistance of the battery cells requires large capacity SC cells. Consequently, the trade-off for low cost in this case is a significant increase in both mass and volume, as shown in Table 21. In the context of an executive saloon vehicle, such as a BMW 3 Series or Audi A4, implementation of the 3000F HESS would save £398 in cell cost per vehicle, however would require the sacrifice of 6% of the boot volume.

The cost of converting cells to modules is expected to be similar for both battery-only ESSs and HESSs; the HESS may enable slight thermal management system downsizing (depending upon system sizing), and the cost of additional sensors and a capacitor management system is expected to be small. As discussed in section 5.5, it should be noted that smaller capacity SCs can be used in a module than in the lab scale test. Additionally, it is not practical to implement the HEB ESS shown in Table 21 primarily due to its poor performance at low temperatures.

	HPB	HEB (8P)	HESS 2000F	HESS 3000F
Mass (kg)	24.9	25.0	45.0	54.6
Volume (L)	12.8	10.7	31.7	44.5
Energy (kWh)	1.68	6.45	1.61[1]	1.61[1]
Usable Energy (kWh) [2]	0.87	2.13	0.40	0.79
Cell Cost / Module (£)	1584	813	1063	1186

[1] Battery Energy Only, [2] Within SoC region where FTP cycle can be run

Table 21: Specification of modules consisting of HPB, HEB and HESSs using 2000F and 3000F SCs – Usable energy capacity at 25℃

Customers demand greater EV driving range from second generation HEVs, thus it would follow that a large form factor battery cell (as is the trend with EV battery selection) would be used in a HESS. In a HESS with a large form factor battery, a significantly smaller SC cell could be used owing to the lower battery ESR and high power capability. Cost, performance and weight/volume can be traded off against one another by using different cell types and configurations to create a HESS with the desired attributes.

Table 22 shows potential systems using large form factor battery cells with a target of >4.5kWh of usable energy. Based on the results of this study, it is predicted that a HESS consisting of large form factor battery cells and ultra-low resistance 600F SC cells provides performance that is competitive with the HPB ESS. This configuration was selected to demonstrate that for particular requirements, a HESS could provide a lighter and cheaper ESS than a battery only ESS.

	HPB	HEB	HESS 2000F	HESS – 600F
Configuration	72S 3P (Saft VL6P)	69S 2P (EIG 20Ah)	69S 1P (EIG 20Ah) & 96S 1P (I2kF SC)	69S 1P (EIG 20Ah) & 96S 1P (600F Low ESR SC)
Mass (kg)	74.5	62.1	59.8	53.1
Volume (L)	38.2	59.0	59.3	41.8
Energy (kWh)	5.0	10.6	5.3[1]	5.3[1]
Usable Energy (kWh) [2]	4.8	3.7	4.8	4.5
Cell Cost / Module (£)	4752	3179	2450	2142

[1] Battery Energy Only, [2] Within assumed SoC region where FTP cycle can be run

Table 22: Specification of modules consisting of HPB, HEB and HESSs using 2000F and 3000F SCs for higher energy capacity HEVs - Usable energy capacity at 25℃

5.6 Degradation

To evaluate the hypothesis that the HESS degrades at a similar rate to a specialised HPB, tests were conducted to determine the capacity loss and resistance rise following prolonged usage under typical automotive conditions. The FTP-72 drive cycle was run continuously for 1080 cycles, with degradation measured periodically via a C/20 discharge, a pulse discharge, Electrochemical Impedance Spectroscopy (EIS), and a high-rate discharge. All measurements were performed at 25℃, with forced convection but without active thermal management.

For each ESS, the thermal boundary conditions were controlled to mimic tab cooling at module level; the cells were subjected to forced convection in a temperature controlled environment, and the connections to the battery tabs and SC terminals were held at a constant temperature of 25℃. The initial SoC used for each ESS was the mid-point of the usable SoC range in which the FTP-72 cycle would run. Following each cycle, the cell was charged using a constant-voltage regime to the voltage corresponding to the initial SoC for a period of two minutes to prevent voltage drift during cycling.

In the following analysis the data provided for the HESS system is that describing the battery cells in a 3000F HESS, as SC degradation was found to be negligible. Additionally, all analysis should be considered qualitative rather than quantitative, as it was not performed on a statistically significant number of samples.

5.6.1 Capacity Loss & Resistance Rise

Cell	Capacity (mAh) 0 Cycles	Capacity (mAh) 528 Cycles	Capacity (mAh) 1080 Cycles	Capacity Loss (mAh)	Normalised Loss (%)
HPB	7660	7571	7410	250	3.3%
HEB (8P)	3020	2997	2970	50	1.7%
HESS Cell 1	3005	2897	2874	131	4.3%
HESS Cell 2	2963	2907	2884	79	2.7%

Table 23: Capacity loss during degradation testing determined via a C/20 discharge

Table 23 shows the capacity loss of batteries in each ESS during degradation testing; in each case, the capacity loss after 1080 runs of the FTP-72 cycle is modest. The capacity loss of the HPB is similar to the average between HESS losses (3.3% vs 3.6%) indicating that the HESS has a similar rate of degradation to the specialised HPB. As expected, the lowest capacity loss is seen in the HEB in the 8P configuration. Since the system is oversized to meet the pulse power requirements, the ET for a single cell was lower than that for a cell in the HESS.

Cell	Series Resistance	Fitting Error (%)	SEI Resistance	Fitting Error (%)	Charge Transfer Resistance	Fitting Error (%)
HPB						
New	0.00064	6.0	0.00257	3.9	0.0017	4.4
Aged	0.00066	7.0	0.00253	3.9	0.0020	1.1
Increase (%)	3.1%		-1.8%		15.5%	
HEB (8P)						
New	0.0239	1.0	0.00751	4.5	0.0191	3.9
Aged	0.0241	1.2	0.00780	3.1	0.0208	3.1
Increase (%)	0.0%		3.8%		8.5%	
HESS Cell 1						
New	0.0263	0.4%	0.00407	3.4%	0.0221	1.5%
Aged	0.0279	0.3%	0.00512	2.6%	0.0239	2.0%
Increase (%)	6.1%		25.9%		8.3%	
HESS Cell 2						
New	0.0259	0.48%	0.00419	5.99%	0.0219	2.10%
Aged	0.0276	0.33%	0.00499	2.59%	0.0236	1.96%
Increase (%)	6.9%		19.1%		7.2%	

Table 24: Series, SEI and Charge Transfer Resistance of new and aged cells, as determined through EIS

In order to distinguish different forms of degradation, the series, SEI and Charge Transfer Resistances (CTR) have been extracted from EIS measurements. The resistance values are listed in Table 24 and the equivalent circuit used for fitting is shown in Figure 68 (Top).

In the HPB the largest increase (of 15%) is that of the charge transfer resistance which is the resistance to intercalation/deintercalation at the electrode/electrolyte interface; the variations of series and SEI resistances are within fitting error. Given the presence of a significant capacity loss and limited changes in series and SEI resistances, it is hypothesised that the main degradation

mechanism is structural disordering, [157]. Lithium ions replace divalent Nickel atoms within the cathode, resulting in a consumption of lithium from the electrolyte, and the modified structure restricts lithium diffusion within the cathode; these lead to capacity fade and charge transfer resistance rise.

The HEB in the 8P configuration experiences little change in its series and SEI resistance, and a modest increase in CTR. In comparison, the battery cells in the HESS show a similar increase in CTR, but significantly greater rise of SEI and series resistances. This effect is expected, given that the average temperature of the cells is greater in the HESS than in the HEB system, causing faster reaction kinetics, and SEI growth.

EIS spectra of the new and aged cells from the HESS are shown in Figure 68 (Top). In the 'new' state, the cells show similar impedance spectra, with modest but notable differences. The greater depression of the first semi-circle for Cell 2 indicates a greater SEI resistance than Cell 1, additionally, there is notable difference in the radius of the second semi-circle which indicates a change of charge transfer resistance, [161]. It is clear however that, with the exception of series resistance, the spectra of both cells in the aged state are almost identical. As the cells aged, the parallel connection of the battery cells served to self-balance cell state-of-health and thus led to a convergence of the two EIS spectra.

As the battery cells degrade and their resistance increases, a greater proportion of the system resistance is attributable to the batteries, and hence the SCs provide a larger contribution to the total system current. As shown in Figure 68 (Bottom), the reduction in current provided by the batteries leads to a reduction in the temperature rise of the cells. This suggests that the thermal management system for the batteries in a HESS should be sized for start of life, and not end of life as per convention in systems with battery cells only. Furthermore, this effect should act to balance parallel strings in the battery pack, where lower resistance cells provide more power and naturally reduce the duty on the more degraded cells.

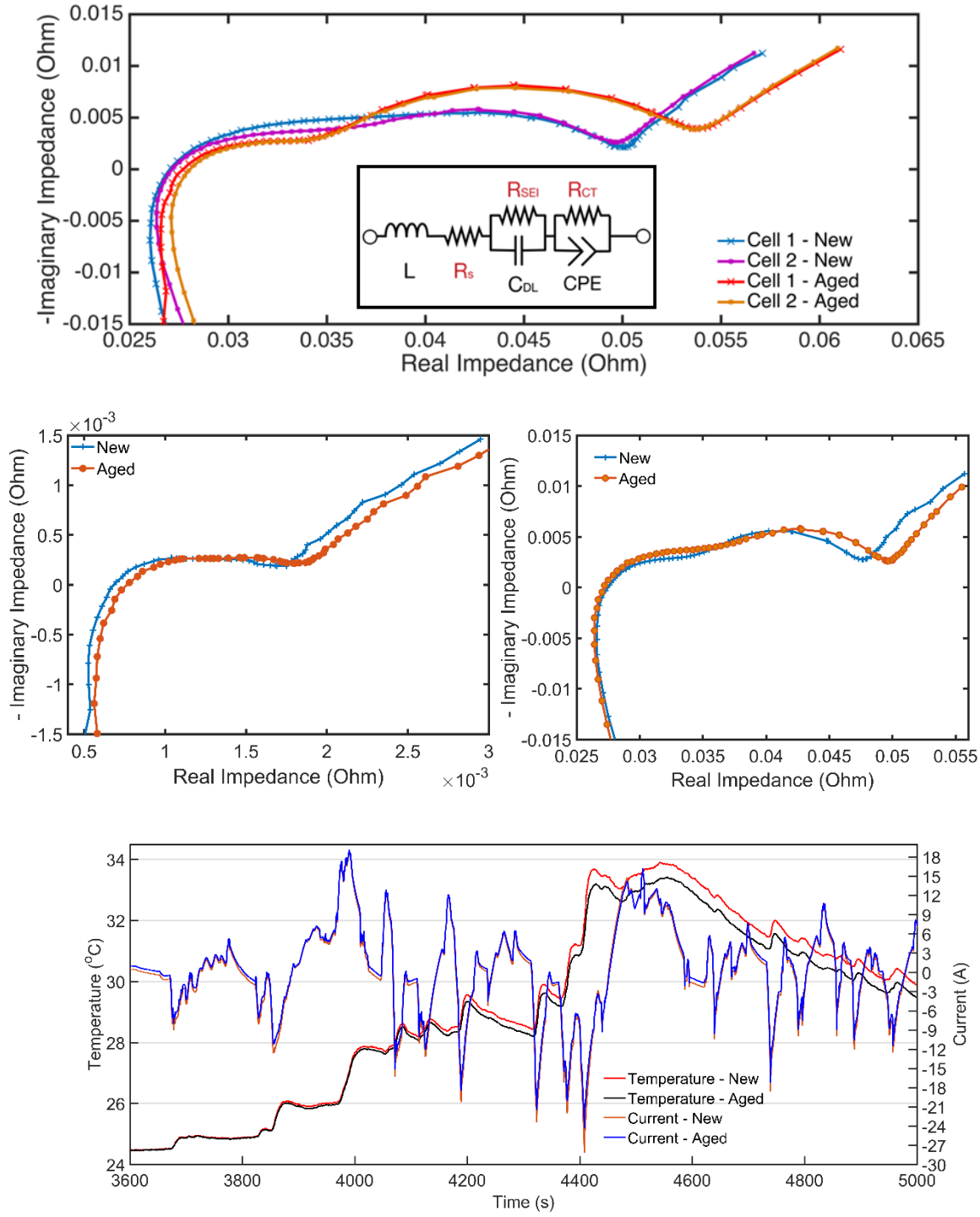


Figure 68: Comparison of new and aged cells through EIS: EIS Plots (Top) of HESS (inset shows the equivalent circuit to which data was fitted), (Mid-Left) HPB, (Mid-Right) HEB, (Bottom) Temperature and current over the FTP drive cycle at various stages of cell aging

5.7 Interim Conclusion

An investigation is carried out to determine whether High Energy Batteries (HEBs) suitable for use in a Battery Electric Vehicle (BEV) can be combined with Supercapacitors (SCs) in a Hybridised Energy Storage System (HESS) in order to replace a specialised High Power Battery (HPB) in a Hybrid Electric Vehicle (HEV). Multiple system topologies are evaluated which can be broadly categorised as passive, semi-active and fully-active, and a passive configuration, in which SCs are connected in parallel with HEBs, is preferred from cost and reliability perspective.

The electrical and thermal performance of the HESS is evaluated over an automotive drive cycle (FTP-72), using the current demand for a HEV, with appropriate thermal boundary conditions for the application. The SoC range over which the HESS is capable of satisfying the current demand is very similar to the specialised HPB at 25°C, (SoC Range of 48% vs 50%), and similar performance using HEBs would require the use of a 10P configuration. A considerable variation is found between the temperature sensitivities of the Energy Storage Systems (ESSs) considered; in comparison to system performance at 40°C, at 10°C the SoC region of operation is reduced by 80% for the HEB ESS, 66% for the HPB ESS, and 36% for the HESS. The performance is reduced at lower temperatures due to increased battery resistance, however in the HESS, this is partially offset by an increased SC contribution to the system energy throughput.

Of the ESSs considered, perhaps counterintuitively, the battery cells in the HESS experience the greatest temperature rise. Whilst the energy throughput of each battery cell in the HESS is reduced by over 80% with respect to the energy throughput of the HPB, the energy throughput of each cell is greater (by 11-38% depending on SC size) than through a HEB in an 8P configuration, thus more heat is generated per cell. However, when considering heat generation at a module level, significantly less heat is generated by the 3000F HESS than both the HEB and HPB ESSs, enabling downsizing of the thermal management system. Reduced thermal losses indicate that a correctly sized HESS is more efficient than a HPB ESS.

Degradation testing of the specialised HPB and the HESS is performed by running the FTP-72 drive cycle 1080 times. The SCs in the HESS do not degrade measurably. The capacity loss of the HPB and HEBs in the HESS is similar (3.3 vs 3.6%). All ESSs tested experience a statistically significant increase in charge transfer resistance, while the batteries in the HESS also experience a rise in series and SEI resistances. It is hypothesised that the main contributor to the rise in charge transfer resistance is structural disordering of the cathode. Given the higher temperature in the HESS cells during degradation testing, it is hypothesised that the notable series and SEI resistance increase in the HESS cells is a result of increased electrolyte decomposition and subsequent growth of the SEI layer.

As the batteries in the HESS degrade, their resistance increases while that of the SCs does not vary; as a result, the SC current contribution increases, resulting in a reduction of battery current. The temperature rise within the batteries is reduced, meaning the thermal management system for a HESS should be sized for beginning of life rather than end of life, as is the case for battery-only systems. Additionally, it is hypothesised that the rate of battery degradation in the HESS will continue to decrease as battery current demand drops.

The combination of battery cells and supercapacitors in a passive system is shown to be a promising solution for the very power demanding HEV. Based on the analysis presented here, further optimisation of this system can be performed to suit the particular application of interest.

5.8 HESS Modelling

5.8.1 Model Configuration

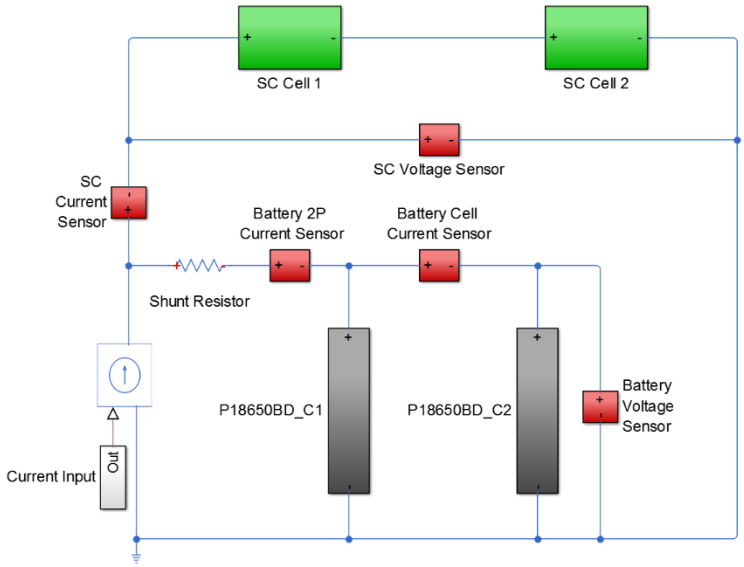


Figure 69: HESS model structure in Simulink

The developed HESS model combines the LIB and SC models developed in previous chapters, making simplifications where appropriate to reduce computational requirements. When simulating the capabilities of the lab scale system, the full fidelity battery model is used alongside the SC electrical model only; the model structure in Simulink is shown in Figure 69. Experimental analysis showed that SC surface temperature did not deviate by more than 1.5°C, thus the findings of the SC thermal modelling suggests that the SC internal temperature varies by < 10°C. In the temperature range of 10-50°C, the change of SC capacitance and resistance is small in comparison to LIB changes [39], therefore it is not necessary to implement a SC thermal model for this analysis. A resistor is added to mimic the shunt resistor in the experimental setup.

When simulating capabilities at a HV module level, the additional resistances associated with HV safety, such as contactors and module interconnect resistances are not considered. Consequently, current is distributed equally between parallel strings, and each cell in the series string contributes equally, therefore SoC and temperature is tracked for a single cell rather than computed independently.

5.8.2 Model Validation

For validation, the HESS model is run over the FTP drive cycle across a range of SoC points, and the predicted voltage, current split between the SCs and batteries and temperature is compared with experimental data. Results are compared with the modelling requirements outlined in section 2.2.

A comparison of simulated and experimentally measured HESS (3000F) voltage is shown in Figure 70 (Top) and a plot of the residual is shown in Figure 70 (Bottom). The largest error occurs during rapid transitions between high current charge and discharge, however the maximum error in the predicted voltage is 105mV, which satisfies the target of a 3% voltage error (126mV). Predicted and experimentally determined single battery cell current demand is shown in Figure 71, and a similar quality prediction is achieved.

It should be noted that '*medfilt1*' Matlab function is used to remove spikes from the residual voltage data which are caused by discrepancies in the time domain of the simulation and experimental data of under 100ms. To ensure the filter does not distort the true results, a manual comparison of

maximum and minimum system voltages was carried out. The error in the maximum predicted voltage is 69mV, (3.964 vs 4.033V), and 61mV for the minimum voltage (2.697 vs 2.636V); the maximum filtered residual is shown to be 105mV in Figure 70 (Bottom), and occurs just prior to the point at which the minimum voltage is reach due to a small time domain discrepancy. Therefore, it is reasonable to state that the application of the function 'medfilt1' does not reduce the true error between the calculated voltage difference between the predicted and experimentally determined voltage.

The minimum and maximum voltage predicted by the model is compared with values measured during experimentation in Table 25. The error in the voltage predicted by the simulation is within the target of 3% across a range of SoC points corresponding to the SoC range over which the HESS is capable of satisfying the demand of the FTP drive cycle whilst remaining within its voltage limits.

	Minimum Voltage			Maximum Voltage		
SoC (%)	Predicted	Measured	Error (%)	Predicted	Measured	Error (%)
16	2.172	2.192	0.5	3.816	3.887	1.7
25	2.526	2.432	2.2	3.905	3.982	1.8
31	2.696	2.636	1.4	3.964	4.033	1.6
47	2.795	2.700	2.4	4.042	4.102	1.5
57	2.865	2.765	2.4	4.092	4.156	1.5

Table 25: Comparison of HESS (3000F) simulated and experimentally measured minimum and maximum voltage during FTP drive cycle at multiple initial SoC points with an initial temperature of 25℃

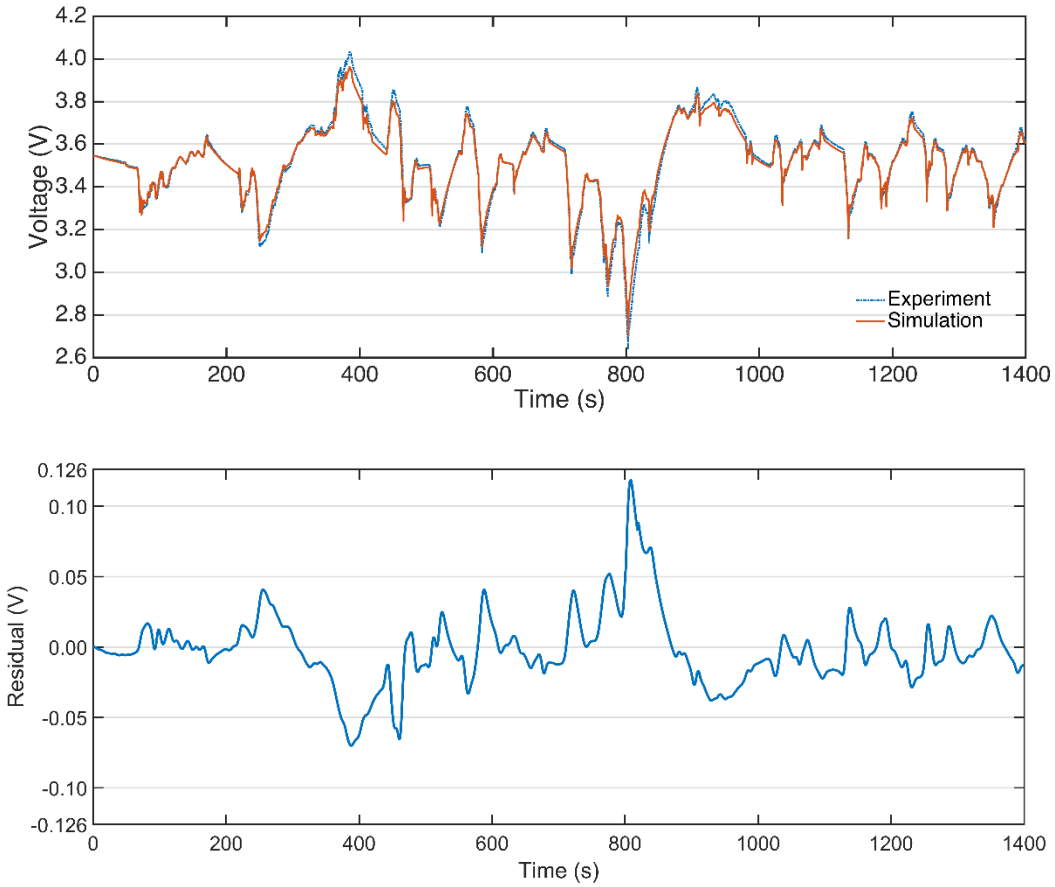


Figure 70: Comparison of simulated and experimentally determined HESS (3000F SCs) voltage (Top), with a plot of voltage error (Bottom), during FTP drive cycle following the current profile shown in Figure 61b – Initial Conditions: SoC – 31%, Temperature - 25℃

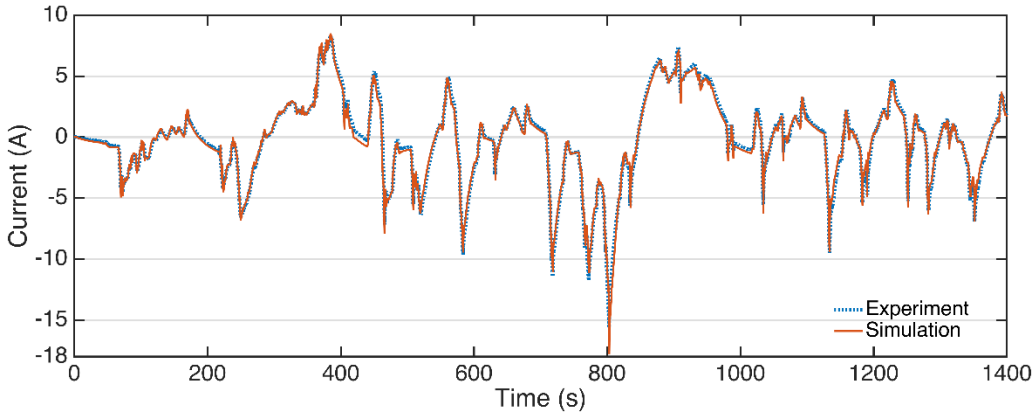


Figure 71: Comparison of simulated and experimentally determined battery current within the HESS (3000F SCs), during FTP drive cycle following the current profile shown in Figure 61b. – Initial Conditions: SoC – 31%, Temperature - 25℃

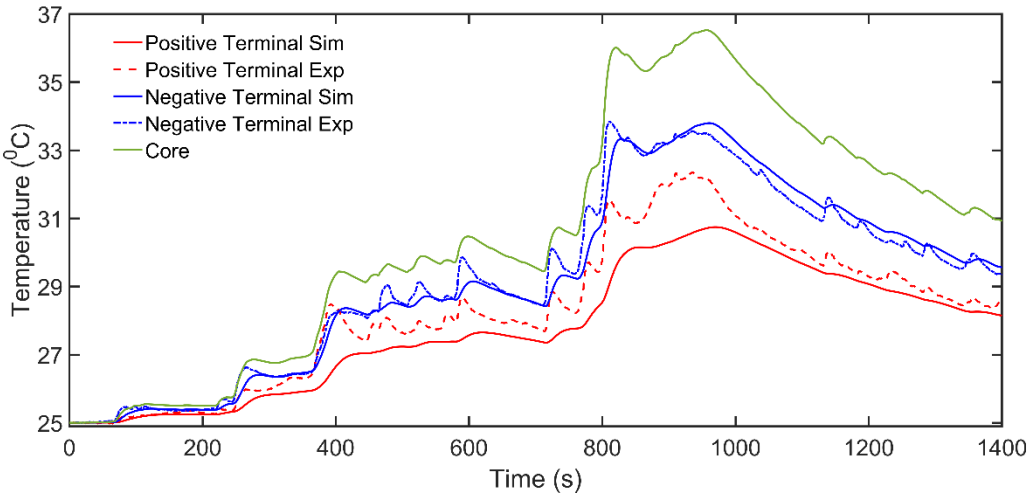


Figure 72: Comparison of simulated and experimentally determined battery temperature within the HESS (3000F SCs), during FTP drive cycle following the current profile shown in Figure 61b. – Initial Conditions: SoC – 31%, Temperature - 25℃

The predicted battery temperature at positive and negative terminals is compared against experimental data in Figure 72 and presented alongside the predicted temperature at the core of the battery. The error in temperature prediction at the negative terminal (0.9℃ max) is well within the target of ± 1.5℃; the steady state error is small, however the predicted rate of change of temperature is significantly lower than the experimentally determined value. This is likely attributable to using a lumped series resistance parameter, and hence not appropriately apportioning the resultant heat appropriately, in particular, the heat generated in the immediate vicinity of the terminal.

Similar behaviour is observed at the positive terminal, however a larger steady-state error contributes to a larger deviation between the predicted and measured temperature (1.8℃ max). The larger steady state error is likely attributable to a lack of model complexity which prevents independent prediction of heat generation at the positive and negative terminal, resulting in a working assumption that generated heat is equally distributed between the anode and cathode, which is known to be false [271]. The instances during which the targeted error is exceeded are very short, thus it is taken that the model provides estimates of sufficient quality to enable the author to use the model to answer the research questions.

The large temperature gradient between the terminals and the core are caused by poor heat transfer between the current collectors and terminals. The consequence of this large temperature gradient is that the electrodes will experience highly non-uniform utilisation which will result in reduced available capacity, increased resistance for a given average temperature and increase degradation.

5.8.3 System analysis through Simulation

5.8.3.1 Energy Capacity

Whilst the majority of the energy capacity of a HESS is provided by the batteries, the contribution of the SC should not be neglected; as shown by Figure 73 (Left), the contribution of SC energy to HESS energy capacity is approximately 20% for the 2000F HESS, and 30% for the 3000F HESS. The battery Peukert coefficient remains unchanged when operated in a HESS for a constant current discharge over a long time period. Therefore, HESS energy capacity can be determined by translating the battery capacity curve estimated by Peukert's law by the SC energy capacity between the upper and

lower voltage limit. The available energy capacity of the HESS in the HV configuration (69S2P P18650BD with 96S1P SC) is similar to the HPB.

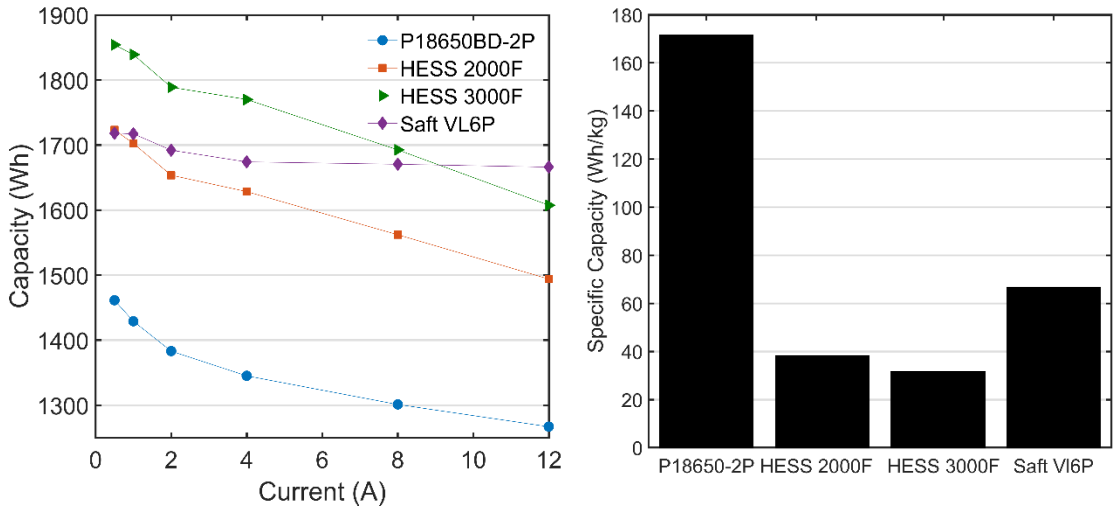


Figure 73: (Left) Available energy capacity between 281-186V, (Right) Gravimetric energy capacity with the application of a 12A load – Source: HESS and P18650BD data from simulation, Saft VL6P data acquired from experimentation

The gravimetric energy capacity of the HESS in the HV configuration is 40-50% lower than the HPB as shown graphically in Figure 73 (Right). The Gravimetric Energy Capacity (GEC) or the energy capacity per kg of a HESS will always be significantly lower than that of a HEB ESS as SCs have poor specific energy, however the combination of different cells, or a change to system requirements should enable a HESS to have a higher GEC than a HPB ESS. An improved HESS GEC can be achieved through an increase of battery GEC without a reduction of power capability, or via an increase of HEB power capability which would enable SC downsizing. Therefore, counter-intuitively it is possible to increase HESS SEC by reducing the energy capacity of the HEBs (albeit higher power) used alongside the SCs.

Additionally, the I2kF and I3kF SCs used in this study are poorly optimised for mass, with the can of the cell contributing 25-38% to the cell mass. Significant opportunities exist to improve HESS SEC through SC mass reduction via mechanical design optimisation. Increasing SC voltage is highly beneficial for HESS GEC as the energy capacity of the system is increased (and is accompanied by an increase of power capability), whilst the number of cells required and therefore mass is reduced.

5.8.3.2 Power Capability

The efficiency (EF) when a current pulse is applied can be given as Equation 52, as defined by Burke et al [272]. A current pulse of 5 seconds is of interest in automotive applications, therefore the maximum power capability, P_{max}, for a 5 second pulse and 80% minimum efficiency is calculated using ohm's law.

$$EF = \frac{P}{P + I^2R} = \frac{1}{1 + IR/V} = \frac{V}{V_{OCV}} \qquad \text{Equation 52}$$

Figure 74 shows the maximum power at which an EF of over 80% could be maintained during a 5 second pulse load. Data for the P18650BD system and HESS is determined using the developed modelling tools, whilst the capabilities of the Saft VL6P cell are determined experimentally. As desired, it is evident that the power capability of the HEB cells is boosted significantly by the addition of the SCs. It is interesting to note that the power capability of the HESS at 80% EF increases as SoC is

reduced because battery resistance rises, and therefore a greater proportion of the current is provided by the SCs which have a significantly lower resistance.

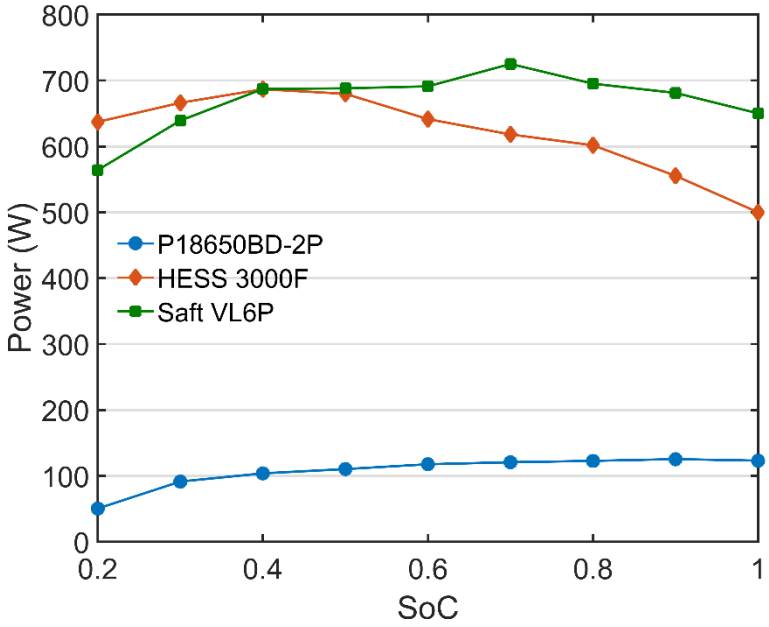


Figure 74: 5 second pulse power resulting in a minimum efficiency of 80% - HESS & P18650BD data from model, Saft data from experimental analysis – Initial conditions - 25℃

The power capability of the HESS is similar to that of the HPB at 25℃, however the power capability is SoC and temperature dependent. As shown in Figure 65, the HESS is less temperature sensitive than LIB only systems, therefore at lower temperatures HESS power capabilities decrease less than those of HPBs, and at elevated temperatures they increase less. The HPB is 33% of the mass of the 3000F HESS, therefore whilst the power capabilities are similar, the HPB retains a three times higher specific power capability.

5.8.3.3 Equating Lab Scale to Module Scale

As discussed in section 4.2, the HESS will perform differently at the module scale than the lab scale setup. The relative resistance of the battery and SC will change, resulting in a change to the current split between the SC and batteries. Furthermore, the reduced ratio of SC to LIB cells results in each SC operating at a higher voltage, SC capacitance is a strong function of voltage. Consequently, smaller capacity SC cells are required in a module than in a lab scale test.

SC cells of reduced capacity are accompanied by an increase in resistance, [37,38,273], therefore as the size of the cell that is equivalent to the I3kF cell at the lab-scale is estimated for the module level, capacitance and resistance are varied together to maintain this relationship. The capacitance and resistance of the equivalent cell that provided near identical module performance to the I3kF lab-scale system is determined using the model, and the results are shown in Table 26.

SC Cell	Capacitance (F)	Resistance (mΩ)	Mass (g)	Volume (mL)
I2kF	2000	0.28	390	308
I3kF	3000	0.26	510	410
Equivalent Cell	2471	0.2705	420	371

Table 26: Table of capacitance, resistance, mass and volume as specified by the manufacturer for I2kF and I3kF SC cells and estimated values for the cell that would provide the equivalent performance to the I3kF when the lab-scale test is up-scaled to the module level

The mass and volume of the cell can be estimated by independently estimating the change in length and hence mass of the Jelly-Roll (JR) and can of the cell assuming a constant diameter and terminal thickness. The volume of the JR is proportional to the capacitance therefore the estimated capacitance is used to calculate the length of the JR. The JR density is determined from the existing cells and used to calculate the mass of the JR of the equivalent cell. Knowledge of JR length enables determination of cell length, and hence volume, positive terminal mass and cell mass. A breakdown of the values is provided in Table 27.

SC Cell	JR Height (mm)	JR Mass (g)	Cell Height (mm)	Positive Terminal Mass (g)	Negative Terminal Mass (g)
I2kF	86.7	272.0	108.1	82.7	10.7
I3kF	133.6	378.5	155.0	96.2	10.7
Equivalent Cell	109.9	322.6	131.3	87.4	10.7

Table 27: Measured jelly-roll and can properties for the I2kF and I3kF cells, and estimated values for the cell that would provide the equivalent performance to the I3kF when the lab-scale test is up-scaled to the module level

Were the equivalent cell available, HESS mass and volume could be reduced by 12-14%, as shown in Table 28. Whilst this knowledge is helpful when considering the trade-offs of a HESS relative to a LIB ESS, the HESS remains substantially larger and heavier.

	Mass (kg)	Volume (L)
HESS 3000F	54.6	44.5
HESS Equivalent Cell	47.9	38.1
Percentage Change	-12.3%	-14.3%

Table 28: Comparison of mass and volume of HESS using the I3kF and equivalent cell SCs

5.8.4 Modelling Conclusions

The previously developed ECMs of a LIB and SC were combined to create a HESS model to enable electrical and thermal prediction of HESS performance both in a low-voltage lab scale configuration, and a high voltage module configuration. The developed HESS was shown to be capable of predicting voltage throughout the FTP drive cycle, to within the target of 3%, across the SoC range that the HESS is capable of meeting the current demand within safe voltage limits. Battery temperature is predicted well within the target of $\pm 1.5℃$ at the negative terminal, however this target is very briefly exceeded at the positive terminal where the maximum deviation is $1.8℃$.

The energy capacity and power capability of the HESS are comparable to that of the HPB, however the specific energy and specific power are considerably lower for the considered system configuration. For a HESS to possess superior specific energy capacity and specific power capability to a HPB, HEB and SC capabilities must be balanced; a HEB with a lower energy but higher power capability will likely improve HESS specific energy by enabling SC downsizing. SC downsizing is of particular interest because the SCs in the HESS have an energy density which is two orders of magnitude lower than the HEBs. Increasing SC voltage will increase both the specific energy and specific power.

As the lab-scale HESS is up-scaled to module level, the SCs can be downsized as they are operated at a higher SoC and hence possess higher capacitance, and the relative resistance between the SCs and LIBs is changed. The developed model predicted that the 3000F SCs used at a lab scale could be downsized to 2471F, which in turn would lead to a HESS mass reduction of 12% and a volume reduction of 14%.

5.9 Suitability for use in Automotive Applications

HESS design is a trade-off between cost, performance and mass/volume and can be expressed as a trade-off triangle following the philosophy of a Penrose triangle as per Figure 75; improving one attribute necessitates a compromise of at least one other. In the HESS considered, a low cost configuration was evaluated, and performance is matched to that of the HPB, therefore a compromise is made in terms of mass/volume. Whilst the characteristics of a HESS can be altered within specific bounds through the use of different combinations of cells, the findings within this chapter are sufficiently generic to consider applications across different automotive traction applications.

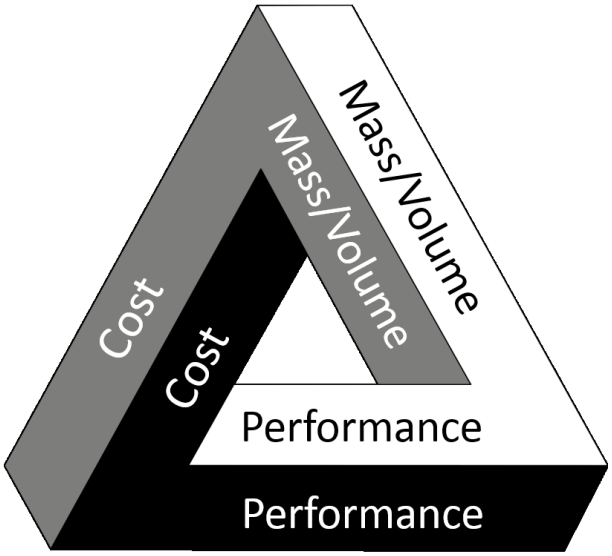


Figure 75: HESS configuration trade-off expressed as a Penrose triangle

This study demonstrated that a HESS is suitable for use in a HEV. The low cost system proposed matched the performance of a specialised HPB ESS, and offers significant cost savings of approximately £400. However, as per the trade-off triangle, this is accompanied by an increase in volume, that is equivalent to approximately 6% of the boot space of a typical executive saloon vehicle, though this may be partially offset by modified thermal management requirements. The use of a HESS in a HEV fits into a wider electrification strategy by enabling the use of a battery used in a BEV to be used in a HEV. Reducing the number of different battery cells used decreases cell purchase cost through economies of scale, reduces R&D costs and facilities/test equipment requirements and therefore potentially reduces time to market.

A HESS can likely be beneficial in a PHEV in a similar manner to that demonstrated for a HEV; a greater proportion of the ESS will consist of LIBs, therefore the effect of hybridisation should be considered in this context. The use of a HESS should decrease the rate of heat generation rise in the LIBs as the ESS degrades, and localise heat generation to a greater degree, thereby enabling downsizing of the thermal management system. However, charging time will be increased due to a lower continuous power rating.

The ESS in a mHEV is highly cost and volume sensitive, therefore the suitability of a HESS for this application will depend upon the comparative pricing of HEB, HPB and SC cells. Increased localisation of heat in the HEBs is likely to require semi-active thermal management to control battery degradation, increasing both system cost and volume. The use of a LIB with sufficiently high power capability to not require semi-active thermal management in the HESS would likely be prohibitive

from a cost perspective, but may be considered if the existing system is oversized due to degradation concerns.

The use of a passive HESS inevitably results in a significant reduction of specific energy capacity of the ESS, therefore HESSs are typically unsuitable for a BEV, where significant emphasis is placed upon meeting the energy storage requirements. An increasing demand exists for increased power capability in BEVs to enable fast charging [14,135,136,274,275], however whilst a HESS will increase pulse power capability, it has little effect upon the continuous power capability of the ESS. The use of a HESS may be beneficial in a BEV if it enables the use of conversion cathode batteries such as Li-S or Li-O_2.

6.0 Conclusion & Future Work

6.1 Conclusions

The overarching motivation for this study was to determine whether the use of a Hybridised Energy Storage System (HESS), consisting of Lithium Ion Batteries (LIBs) and Supercapacitors (SC), in automotive traction applications is beneficial in comparison to battery-only systems. Therefore, the aim of this thesis was to develop a physical understanding of the operating process of a SC, LIB and hence a HESS and subsequently use this knowledge to develop a HESS model to enable performance prediction. Further, this study aimed to understand the modes of performance degradation in a HESS and the differences in their rate and magnitude. The amassed knowledge was to be used to determine whether a HESS should be used in automotive traction applications by comparing its benefits and limitations against a LIB-only Energy Storage System (ESS).

Due to the large number of possible HESS topologies, efforts were focused on a passive HESS because it is the simplest, cheapest, most robust option and its performance benefits in an automotive context have not been previously examined in academic literature. An in-depth review of SC and LIB operation and degradation was conducted, and the differences highlighted. This knowledge was used to guide model development for the SC, LIBs and subsequently, the HESS. Additionally, an experimental analysis was conducted for model validation, and to investigate degradation, which is outside the scope of the model.

A physically meaningful Equivalent Circuit Model (ECM) is used to recreate SC electrical performance over a range of operating conditions. A pseudo-3D high fidelity thermal model is developed using thermal equivalent circuits to examine the occurrence of thermal gradients within SC cells, and their effect upon electrical performance. The development of the thermal model included the derivation of expressions to quantify differing rates of entropic heat generation in the positive and negative electrode. The electro-thermal SC model was shown to perform excellently in predicting electrical and thermal performance over time periods similar to those of typical automotive drive-cycles.

The high fidelity thermal model showed that thermal gradients within SCs are small, even at very high currents due to the excellent thermal conduction between the current collectors and cell terminals. The use of a high fidelity thermal model improved electrical performance predictions over extended time periods as a thermal gradient that forms between the jelly-roll and the can. The effect of temperature change upon electrical performance is greatest at very low temperatures, and diminishes greatly at temperatures of 10°C and above.

An ECM is combined with a thermal equivalent circuit to predict LIB electrical and thermal performance, over a range of operating conditions. The developed thermal model is capable of predicting the internal temperature of cylindrical cells as well as the temperature difference that occurs at the positive and negative terminals. The model was shown to predict electrical performance over a drive cycle to within the targeted error. Cell terminal temperature was typically predicted well, though the targeted error was exceeded briefly for high current charge events. The predicted radial thermal gradient within the cell was shown to be consistent with the experimental findings of other authors, and the model predictions of high fidelity models.

The developed SC and LIB models are combined to create a model of a passive HESS which mirrors the experimental setup used for HESS testing. To reduce computational time, the high fidelity SC thermal model is not used alongside the SC electrical model. Over the temperature range of the model, the heat generation, and effect of temperature rise and temperature gradients is much greater for LIBs than for SCs. The changes in SC capacitance and resistance are small in comparison

to LIB changes, and experimental validation showed SC temperature changes to be small for the test case of interest, the FTP drive cycle.

Experimental validation of the HESS showed that the model was capable of predicting electric performance of the system within the targeted error over the entire SoC range for which the cell voltage was within safe limits. As per the LIB model, temperature change was generally predicted well, with the targeted error briefly exceeded during high current charging. The model was used to correlate the performance of a low-voltage lab-scale setup to a high-voltage system as would be used in an automotive traction application.

A combination of experimental analysis and use of the developed modelling tools led to the following findings:

1. Whilst the HESS examined in this study possessed similar energy and power to the specialised LIB-only ESS, the gravimetric and volumetric energy and power are lower. Whilst it is possible for the HESS to possess greater energy and power density than the specialised LIB-only ESS, a trade-off is required between the attributes of cost, performance and mass/volume. A reduction in mass/volume for a particular level of performance would therefore increase HESS cost. The studies HESS was designed to be low cost; cell cost is estimated to be approximately £400 lower.

2. The performance of a HESS is less temperature sensitive than a LIB-only ESS; performance is reduced at lower temperatures due to increased battery resistance, however in the HESS, this is partially offset by an increased SC contribution to the system energy throughput.

3. A correctly sized HESS will generate less heat overall than a LIB-only ESS, and the heat will be more localised. As a result, it should be possible to downsize the thermal management system.

4. Performance degradation via capacity loss is similar for the HESS and LIB-only ESS, however battery resistance rise is greater in the HESS due to increased temperature rise in each battery cell. With appropriate thermal management, performance degradation is expected to be similar for both the HESS and LIB-only ESS. SC degradation is negligible in comparison to battery degradation.

5. The rate of degradation in a HESS reduces as battery resistance rises. A faster rise in resistance in the LIB than in the SC results in a larger SC current demand and a reduced LIB current demand. Consequently, heat generation and battery energy throughput is reduced, resulting in a reduced rate of degradation.

6. Whilst the pulse power of the HESS and LIB-only ESS is comparable, the continuous power rating of the HESS is lower. This is of particular importance during system sizing for a PHEV where customer demands for fast-charging and engine-off operation.

7. This study demonstrated that SC cells suitable for an mHEV can be combined with battery cells suitable for use in a BEV to create a HESS suitable for use in a HEV, thereby enabling manufacturers to use hybridisation to implement a modular ESS across their range of electrified vehicles.

6.2 Future Work

The presented work explores the effect of the implementation of the simplest HESS topology in automotive traction applications, and hence provides a foundation upon which further work may be conducted, and a baseline for comparison. The time limitations of a 3 year funded PhD require that a relatively narrow scope is adopted for investigation of this broad topic. Were more time available, the author feels significant value could be added to this work in the following areas:

Model Development

- Model Order Reduction of SC Thermal Model – The high-fidelity thermal model proved to be a useful tool for SC thermal investigations, however a reduced order model is required for practical use in a simulation of a high voltage HESS.

- Expanded LIB model parameterisation – Parameterisation using a finer and broader SoC and temperature discretisation will improve the range of model validity, enable low temperature studies and improve estimation accuracy.

- Improved Heat Generation Model - Decouple lumped series resistance parameter and anode/cathode resistance for improved estimation of rate of temperature change at battery terminals, and improved estimation during high current charging.

- HESS Topology comparison – Use the developed models to compare the capabilities of different topologies.

- Develop LIB degradation model – Examine effect of different HESS topologies on degradation and track HESS performance and efficiency changes with degradation.

- Create cost models – Enable estimation of the costs of the power electronics and thermal management system required for different HESS topologies and applications.

- Integration into full vehicle model – Determine vehicle level attribute changes where the vehicle supervisory control is optimised for the HESS.

Experimental Analysis

- Degradation study to failure – Track performance changes as HESS degrades to failure to determine whether the observed behaviour continues. Develop a guide for HESS sizing for end of life, with a particular focus upon SC capacity.

- Determine compatibility with Li-S in passive configuration – Polysulphide shuttle which leads to “infinite charging” may render Li-S incompatible for use in a passive HESS, however if developments in Li-S technology can overcome these issues, a HESS could make conversion chemistries viable for high power applications such as automotive applications.

Cell Analysis

Specialised SC for HESS applications – Existing SC cells are poorly suited for use in a HESS as their mechanical design is optimised for cost and very high current applications. A cell optimised for automotive HESS would likely have a different form factor, would be designed for a lower maximum current and would therefore have a reduced non-active mass and volume. The resistance would be

minimized and voltage maximized. Additional work is required to define the optimal SC design for use in HESSs.

References

[1] USABC, USABC Goals for Advanced Batteries for 48V Hybrid Electric Vehicle Applications USABC Requirements of Energy Storage Systems for 48V HEV's at EOL, 2014.

[2] U.D. of Energy, U .S. Department of Energy Vehicle Technologies Program Battery Test Manual For Plug-In Hybrid Electric Vehicles, 2014.

[3] D. Kok, S. Chorian, Designing The Right Battery For The Right Vehicle, in: Adv. Automot. Batter. Conf. 2015, 2015.

[4] R. Matthe, OEM perspective on battery support for lifetime: repair refurbishment re-use recycle, in: Adv. Automot. Batter. Conf. 2015, 2015.

[5] A. Oury, 2016 Chevrolet Malibu Hybrid Battery Pack, in: Adv. Automot. Batter. Conf. 2015, Detroit, 2015: pp. 1–20.

[6] USABC, USABC Goals for Advanced Batteries for PHEVs for FY 2018 to 2020 Commercialization, 2014.

[7] USCAR, USCAR: Energy Storage System Goals, 2015. http://www.uscar.org/guest/article_view.php?articles_id=85.

[8] W. Zhou, Thermal Design and Simulation of Traction Batteries in Vehicles, in: Adv. Automot. Batter. Conf. 2015, 2015: pp. 1–18.

[9] T. Glass, Lithium-Ion Battery Audi Q7 e-tron, in: Adv. Automot. Batter. Conf. 2016, Mainz, 2016: pp. 1–15.

[10] M. Schneider, Li-Ion battery for 48V application, in: Adv. Automot. Batter. Conf. 2016, Mainz, 2016: pp. 1–17.

[11] E. Karden, P. Shinn, P. Bostock, J. Cunningham, E. Schoultz, D. Kok, Requirements for future automotive batteries – a snapshot, J. Power Sources. 144 (2005) 505–512. doi:10.1016/j.jpowsour.2004.11.007.

[12] E. Karden, S. Ploumen, B. Fricke, T. Miller, K. Snyder, Energy storage devices for future hybrid electric vehicles, J. Power Sources. 168 (2007) 2–11. doi:10.1016/j.jpowsour.2006.10.090.

[13] S. Amjad, S. Neelakrishnan, R. Rudramoorthy, Review of design considerations and technological challenges for successful development and deployment of plug-in hybrid electric vehicles, Renew. Sustain. Energy Rev. 14 (2010) 1104–1110. doi:10.1016/j.rser.2009.11.001.

[14] M. Anderman, Tesla Motors, the Gigafactory, and their impact on the xEV Industry, in: Adv. Automot. Batter. Conf. 2015, 2015: pp. 1–22.

[15] M. Doeff, Cathodes, in: R.A. Meyers (Ed.), Encycl. Sustain. Sci. Technol., 2nd ed., Springer-Verlag New York, 2012.

[16] M. Wild, L. O'Neill, T. Zhang, R. Purkayastha, G. Minton, M. Marinescu, G.J. Offer, Lithium sulfur batteries, a mechanistic review, Energy Environ. Sci. 8 (2015) 3477–3494. doi:10.1039/C5EE01388G.

[17] A. Siddiq, Suitability of Lithium Titanate Batteries for Materials Handling Vehicles, Imperial College London, 2015.

[18] IEC, IEC 60584-1:2013 - Thermocouples - Part 1: EMF specifications and tolerances, 2013. https://webstore.iec.ch/publication/2521.

[19] A. Jackson, B. Shaw Norway, N.J. Mansfield, A. Kopystynski, B. Shaw Leith, U.A. Brzezinski, Reducing errors that lead to uncertainties in thermal conductivity measurements, 2006.

[20] National-Instruments, NI 9213 Datasheet, (2016). http://www.ni.com/pdf/manuals/374916a_02.pdf (accessed May 17, 2016).

[21] S.C. Chen, C.C. Wan, Y.Y. Wang, Thermal analysis of lithium-ion batteries, J. Power Sources. 140 (2005) 111–124. doi:10.1016/j.jpowsour.2004.05.064.

[22] A. Barai, G.H. Chouchelamane, Y. Guo, A. McGordon, P. Jennings, A study on the impact of lithium-ion cell relaxation on electrochemical impedance spectroscopy, J. Power Sources. 280 (2015) 74–80. doi:10.1016/j.jpowsour.2015.01.097.

[23] F. Beguin, E. Frackowiak, Supercapacitors: Materials, Systems and Applications, Wiley-VCH, 2011.

[24] G.P. Pandey, A.C. Rastogi, Solid-State Supercapacitors Based on Pulse Polymerized Poly(3,4-ethylenedioxythiophene) Electrodes and Ionic Liquid Gel Polymer Electrolyte, J. Electrochem. Soc. 159 (2012) A1664–A1671. doi:10.1149/2.047210jes.

[25] D. Weingarth, H. Noh, A. Foelske-Schmitz, A. Wokaun, R. Kötz, A reliable determination method of stability limits for electrochemical double layer capacitors, Electrochim. Acta. 103 (2013) 119–124. doi:10.1016/j.electacta.2013.04.057.

[26] D. Aurbach, B. Markovsky, M.. Levi, E. Levi, A. Schechter, M. Moshkovich, Y. Cohen, New insights into the interactions between electrode materials and electrolyte solutions for advanced nonaqueous batteries, J. Power Sources. 81 (1999) 95–111. doi:10.1016/S0378-7753(99)00187-1.

[27] B.A. Boukamp, Electrochemical impedance spectroscopy in solid state ionics: recent advances, Solid State Ionics. 169 (2004) 65–73. doi:10.1016/j.ssi.2003.07.002.

[28] M. Itagaki, N. Kobari, S. Yotsuda, K. Watanabe, S. Kinoshita, M. Ue, In situ electrochemical impedance spectroscopy to investigate negative electrode of lithium-ion rechargeable batteries, J. Power Sources. 135 (2004) 255–261. doi:10.1016/j.jpowsour.2004.04.004.

[29] Z. Deng, Z. Zhang, Y. Lai, J. Liu, J. Li, Y. Liu, Electrochemical Impedance Spectroscopy Study of a Lithium/Sulfur Battery: Modeling and Analysis of Capacity Fading, J. Electrochem. Soc. 160 (2013) A553–A558. doi:10.1149/2.026304jes.

[30] E. Barsoukov, J.R. Macdonald, Impedance spectroscopy: Theory, Experiment, and Applications, Wiley, 2005.

[31] A. Lasia, Electrochemical Impedance Spectroscopy and its Applications, Springer New York, New York, NY, 2014. doi:10.1007/978-1-4614-8933-7.

[32] A. Lasia, Impedance of Porous Electrodes, in: Electrochem. Impedance Spectrosc. Its Appl., Springer New York, New York, NY, 2014: pp. 203–250. doi:10.1007/978-1-4614-8933-7_9.

[33] M.E. Orazem, B. Tribollet, Electrochemical impedance spectroscopy, Wiley, 2008.

[34] IEC, IEC 62576:2009 - Electric double-layer capacitors for use in hybrid electric vehicles - Test methods for electrical characteristics, 2009. https://webstore.iec.ch/publication/7220.

[35] B.E. Conway, Electrochemical Supercapacitors, Springer; 1999 edition (April 30, 1999), 1999.

[36] B. Straubel, J, Tesla All Wheel Drive (Dual Motor) Power and Torque Specifications, Tesla Mot. Blog. (2015). https://www.teslamotors.com/en_GB/blog/tesla-all-wheel-drive-dual-motor-

power-and-torque-specifications (accessed April 18, 2016).

[37] Maxwell Technologies, Maxwell K2 Datasheet, n.d. http://www.maxwell.com/images/documents/K2Series_DS_1015370_5_20141104.pdf (accessed July 20, 2015).

[38] Ioxus Corp, Ioxus iCap Datasheet, New York, NY, 2015. http://www.ioxus.com/wp-content/uploads/2015/01/DataSheet_Ioxus_60mm_141207.pdf (accessed July 20, 2015).

[39] W. Sarwar, M. Marinescu, N. Green, N. Taylor, G. Offer, Electrochemical double layer capacitor electro-thermal modelling, J. Energy Storage. 5 (2016) 10–24. doi:10.1016/j.est.2015.11.001.

[40] J.M. Miller, Ultracapacitors for PHEV? Application and Systems Engineering Perspective, in: IEEE Southeast. Michigan Sect., 2008: pp. 1–43.

[41] A. Du Pasquier, I. Plitz, S. Menocal, G. Amatucci, A comparative study of Li-ion battery, supercapacitor and nonaqueous asymmetric hybrid devices for automotive applications, J. Power Sources. 115 (2003) 171–178. doi:10.1016/S0378-7753(02)00718-8.

[42] A. Chu, P. Braatz, Comparison of commercial supercapacitors and high-power lithium-ion batteries for power-assist applications in hybrid electric vehicles: I. Initial characterization, J. Power Sources. 112 (2002) 236–246. doi:10.1016/S0378-7753(02)00364-6.

[43] J.M. Miller, Ultracapacitor Appliations, Institution of Engineering and Technology, 2011. doi:10.1049/PBPO059E.

[44] M. Hahn, M. Baertschi, O. Barbieri, J.-C. Sauter, R. Kötz, R. Gallay, Interfacial Capacitance and Electronic Conductance of Activated Carbon Double-Layer Electrodes, Electrochem. Solid-State Lett. 7 (2004) A33. doi:10.1149/1.1635671.

[45] S. Kondrat, C.R. Pérez, V. Presser, Y. Gogotsi, A.A. Kornyshev, Effect of pore size and its dispersity on the energy storage in nanoporous supercapacitors, Energy Environ. Sci. 5 (2012) 6474. doi:10.1039/c2ee03092f.

[46] C. Portet, P.L. Taberna, P. Simon, E. Flahaut, C. Laberty-Robert, High power density electrodes for Carbon supercapacitor applications, Electrochim. Acta. 50 (2005) 4174–4181. doi:10.1016/j.electacta.2005.01.038.

[47] D.-E. Jiang, J. Wu, Microscopic Insights into the Electrochemical Behavior of Nonaqueous Electrolytes in Electric Double-Layer Capacitors., J. Phys. Chem. Lett. 4 (2013) 1260–7. doi:10.1021/jz4002967.

[48] P. Kurzweil, M. Chwistek, Electrochemical stability of organic electrolytes in supercapacitors : Spectroscopy and gas analysis of decomposition products, J. Power Sources. 176 (2008) 555–567. doi:10.1016/j.jpowsour.2007.08.070.

[49] M.P.S. Mousavi, A.J. Dittmer, B.E. Wilson, J. Hu, A. Stein, P. Bühlmann, Unbiased Quantification of the Electrochemical Stability Limits of Electrolytes and Ionic Liquids, J. Electrochem. Soc. 162 (2015) A2250–A2258. doi:10.1149/2.0271512jes.

[50] D.H. Lee, U.S. Kim, C.B. Shin, B.H. Lee, B.W. Kim, Y.-H. Kim, Modelling of the thermal behaviour of an ultracapacitor for a 42-V automotive electrical system, J. Power Sources. 175 (2008) 664–668. doi:10.1016/j.jpowsour.2007.09.081.

[51] G. Feng, J. Huang, B.G. Sumpter, V. Meunier, R. Qiao, Structure and dynamics of electrical double layers in organic electrolytes., Phys. Chem. Chem. Phys. 12 (2010) 5468–79. doi:10.1039/c000451k.

[52] R. Kötz, M. Hahn, R. Gallay, Temperature behavior and impedance fundamentals of supercapacitors, J. Power Sources. 154 (2006) 550–555. doi:10.1016/j.jpowsour.2005.10.048.

[53] P. Simon, Y. Gogotsi, Materials for electrochemical capacitors., Nat. Mater. 7 (2008) 845–54. doi:10.1038/nmat2297.

[54] P.W. Ruch, D. Cericola, A. Foelske, R. Kötz, A. Wokaun, A comparison of the aging of electrochemical double layer capacitors with acetonitrile and propylene carbonate-based electrolytes at elevated voltages, Electrochim. Acta. 55 (2010) 2352–2357. doi:10.1016/j.electacta.2009.11.098.

[55] U. Kumara, Activated Carbon for High Voltage EDLC, in: ECCAP Symp. - AABC, Mainz, 2016.

[56] A. Bard, L. Faulkner, Electrochemical Methods - Fundamentals and Applications, 1980. http://fora.aa.ufl.edu/docs/47/20Sept11/UCC_20Sept11_ABE5XXX.pdf (accessed December 4, 2013).

[57] G. Feng, S. Li, V. Presser, P.T. Cummings, Molecular Insights into Carbon Supercapacitors Based on Room-Temperature Ionic Liquids, J. Phys. Chem. Lett. 4 (2013) 3367–3376. doi:10.1021/jz4014163.

[58] M. V. Fedorov, A. a. Kornyshev, Towards understanding the structure and capacitance of electrical double layer in ionic liquids, Electrochim. Acta. 53 (2008) 6835–6840. doi:10.1016/j.electacta.2008.02.065.

[59] M.Z. Bazant, B.D. Storey, A. a. Kornyshev, Double Layer in Ionic Liquids: Overscreening versus Crowding, Phys. Rev. Lett. 106 (2011) 046102. doi:10.1103/PhysRevLett.106.046102.

[60] J. Chmiola, G. Yushin, Y. Gogotsi, C. Portet, P. Simon, P.L. Taberna, Anomalous increase in carbon capacitance at pore sizes less than 1 nanometer., Science. 313 (2006) 1760–3. doi:10.1126/science.1132195.

[61] P. Simon, Y. Gogotsi, Charge storage mechanism in nanoporous carbons and its consequence for electrical double layer capacitors, Philos. Trans. R. Soc. A Math. Phys. Eng. Sci. 368 (2010) 3457–3467. doi:10.1098/rsta.2010.0109.

[62] D. Aurbach, M.D. Levi, G. Salitra, N. Levy, E. Pollak, J. Muthu, Cation Trapping in Highly Porous Carbon Electrodes for EDLC Cells, J. Electrochem. Soc. 155 (2008) A745. doi:10.1149/1.2957911.

[63] T.A. Centeno, O. Sereda, F. Stoeckli, Capacitance in carbon pores of 0.7 to 15 nm: a regular pattern., Phys. Chem. Chem. Phys. 13 (2011) 12403–6. doi:10.1039/c1cp20748b.

[64] G. Feng, J. Huang, B.G. Sumpter, V. Meunier, R. Qiao, Structure and dynamics of electrical double layers in organic electrolytes., Phys. Chem. Chem. Phys. 12 (2010) 5468–79. doi:10.1039/c000451k.

[65] C. Merlet, B. Rotenberg, P. a Madden, P.-L. Taberna, P. Simon, Y. Gogotsi, M. Salanne, On the molecular origin of supercapacitance in nanoporous carbon electrodes., Nat. Mater. 11 (2012) 306–10. doi:10.1038/nmat3260.

[66] M. Deschamps, E. Gilbert, P. Azais, E. Raymundo-Piñero, M.R. Ammar, P. Simon, D. Massiot, F. Béguin, Exploring electrolyte organization in supercapacitor electrodes with solid-state NMR., Nat. Mater. 12 (2013) 351–8. doi:10.1038/nmat3567.

[67] P. Wu, J. Huang, V. Meunier, B.G. Sumpter, R. Qiao, Voltage Dependent Charge Storage Modes and Capacity in Subnanometer Pores., J. Phys. Chem. Lett. 3 (2012) 1732–7. doi:10.1021/jz300506j.

[68] J.M. Griffin, A.C. Forse, W.-Y. Tsai, P.-L. Taberna, P. Simon, C.P. Grey, In situ NMR and electrochemical quartz crystal microbalance techniques reveal the structure of the electrical double layer in supercapacitors., Nat. Mater. 14 (2015) 812–9. doi:10.1038/nmat4318.

[69] B. Wu, M.A. Parkes, V. Yufit, L. De Benedetti, S. Veismann, C. Wirsching, F. Vesper, R.F. Martinez-Botas, A.J. Marquis, G.J. Offer, N.P. Brandon, Design and testing of a 9.5 kWe proton exchange membrane fuel cell–supercapacitor passive hybrid system, Int. J. Hydrogen Energy. 39 (2014) 7885–7896. doi:10.1016/j.ijhydene.2014.03.083.

[70] M. Kaus, J. Kowal, D.U. Sauer, Modelling the effects of charge redistribution during self-discharge of supercapacitors, Electrochim. Acta. 55 (2010) 7516–7523. doi:10.1016/j.electacta.2010.01.002.

[71] D. Torregrossa, M. Bahramipanah, E. Namor, R. Cherkaoui, M. Paolone, Improvement of Dynamic Modeling of Supercapacitor by Residual Charge Effect Estimation, IEEE Trans. Ind. Electron. 61 (2014) 1345–1354. doi:10.1109/TIE.2013.2259780.

[72] Y. Diab, P. Venet, H. Gualous, G. Rojat, Self-Discharge Characterization and Modeling of Electrochemical Capacitor Used for Power Electronics Applications, IEEE Trans. Power Electron. 24 (2009) 510–517. doi:10.1109/TPEL.2008.2007116.

[73] J. Kowal, E. Avaroglu, F. Chamekh, A. Šenfelds, T. Thien, D. Wijaya, D.U. Sauer, Detailed analysis of the self-discharge of supercapacitors, J. Power Sources. 196 (2011) 573–579. doi:10.1016/j.jpowsour.2009.12.028.

[74] H. El Brouji, J.-M. Vinassa, O. Briat, N. Bertrand, E. Woirgard, Ultracapacitors self discharge modelling using a physical description of porous electrode impedance, 2008 IEEE Veh. Power Propuls. Conf. (2008) 1–6. doi:10.1109/VPPC.2008.4677493.

[75] Q. Zhang, J. Rong, D. Ma, B. Wei, The governing self-discharge processes in activated carbon fabric-based supercapacitors with different organic electrolytes, Energy Environ. Sci. 4 (2011) 2152. doi:10.1039/c0ee00773k.

[76] J. Black, H. a. Andreas, Effects of charge redistribution on self-discharge of electrochemical capacitors, Electrochim. Acta. 54 (2009) 3568–3574. doi:10.1016/j.electacta.2009.01.019.

[77] J. Black, H.A. Andreas, Prediction of the self-discharge profile of an electrochemical capacitor electrode in the presence of both activation-controlled discharge and charge redistribution, J. Power Sources. 195 (2010) 929–935. doi:10.1016/j.jpowsour.2009.08.040.

[78] J. Niu, B.E. Conway, W.G. Pell, Comparative studies of self-discharge by potential decay and float-current measurements at C double-layer capacitor and battery electrodes, J. Power Sources. 135 (2004) 332–343. doi:10.1016/j.jpowsour.2004.03.068.

[79] B.W. Ricketts, C. Ton-That, Self-discharge of carbon-based supercapacitors with organic electrolytes, J. Power Sources. 89 (2000) 64–69. doi:10.1016/S0378-7753(00)00387-6.

[80] Q. Zhang, C. Cai, J. Qin, B. Wei, Tunable self-discharge process of carbon nanotube based supercapacitors, Nano Energy. 4 (2014) 14–22. doi:10.1016/j.nanoen.2013.12.005.

[81] T. Tevi, A. Takshi, Modeling and simulation study of the self-discharge in supercapacitors in presence of a blocking layer, J. Power Sources. 273 (2015) 857–862. doi:10.1016/j.jpowsour.2014.09.133.

[82] P. Azaïs, L. Duclaux, P. Florian, D. Massiot, M.-A. Lillo-Rodenas, A. Linares-Solano, J.-P. Peres, C. Jehoulet, F. Béguin, Causes of supercapacitors ageing in organic electrolyte, J. Power Sources. 171 (2007) 1046–1053. doi:10.1016/j.jpowsour.2007.07.001.

[83] J.W. Graydon, M. Panjehshahi, D.W. Kirk, Charge redistribution and ionic mobility in the micropores of supercapacitors, J. Power Sources. 245 (2014) 822–829. doi:10.1016/j.jpowsour.2013.07.036.

[84] C. Hao, X. Wang, Y. Yin, Z. You, Analysis of Charge Redistribution During Self-discharge of Double-Layer Supercapacitors, J. Electron. Mater. 45 (2016) 2160–2171. doi:10.1007/s11664-016-4357-0.

[85] R. De Levie, On porous electrodes in electrolyte solutions—IV, Electrochim. Acta. 8 (1963). http://www.sciencedirect.com/science/article/pii/0013468664850155 (accessed February 20, 2014).

[86] B. Wu, Fuel Cell Hybrid Electric Vehicle Powertrain Modelling and Testing, Imperial College London, 2014.

[87] P. Azaïs, L. Duclaux, P. Florian, D. Massiot, M.-A. Lillo-Rodenas, A. Linares-Solano, J.-P. Peres, C. Jehoulet, F. Béguin, Causes of supercapacitors ageing in organic electrolyte, J. Power Sources. 171 (2007) 1046–1053. doi:10.1016/j.jpowsour.2007.07.001.

[88] A. Burke, M. Miller, E. Van Gelder, Ultracapacitors and Batteries for Hybrid Vehicle Applications, 2009.

[89] W. Lajnef, J.-M. Vinassa, O. Briat, H. El Brouji, S. Azzopardi, E. Woirgard, Quantification of ageing of ultracapacitors during cycling tests with current profile characteristics of hybrid and electric vehicles applications, IET Electr. Power Appl. 1 (2007) 683. doi:10.1049/iet-epa:20070066.

[90] P. Kreczanik, P. Venet, A. Hijazi, G. Clerc, Study of Supercapacitor Aging and Lifetime Estimation According to Voltage, Temperature, and RMS Current, IEEE Trans. Ind. Electron. 61 (2014) 4895–4902. doi:10.1109/TIE.2013.2293695.

[91] R. German, O. Briat, A. Sari, P. Venet, M. Ayadi, Y. Zitouni, J.M. Vinassa, Impact of high frequency current ripple on supercapacitors ageing through floating ageing tests, Microelectron. Reliab. 53 (2013) 1643–1647. doi:10.1016/j.microrel.2013.07.030.

[92] M. Ayadi, O. Briat, A. Eddahech, R. German, G. Coquery, J.M. Vinassa, Thermal cycling impacts on supercapacitor performances during calendar ageing, Microelectron. Reliab. 53 (2013) 1628–1631. doi:10.1016/j.microrel.2013.07.079.

[93] P.W. Ruch, D. Cericola, A. Foelske-Schmitz, R. Kötz, A. Wokaun, Aging of electrochemical double layer capacitors with acetonitrile-based electrolyte at elevated voltages, Electrochim. Acta. 55 (2010) 4412–4420. doi:10.1016/j.electacta.2010.02.064.

[94] S. Ishimoto, Y. Asakawa, M. Shinya, K. Naoi, Degradation Responses of Activated-Carbon-Based EDLCs for Higher Voltage Operation and Their Factors, J. Electrochem. Soc. 156 (2009) A563. doi:10.1149/1.3126423.

[95] P.W. Ruch, R. Kötz, A. Wokaun, Electrochemical characterization of single-walled carbon nanotubes for electrochemical double layer capacitors using non-aqueous electrolyte, Electrochim. Acta. 54 (2009) 4451–4458. doi:10.1016/j.electacta.2009.03.022.

[96] P. Kreczanik, P. Venet, A. Hijazi, G. Clerc, Study of Supercapacitor Aging and Lifetime Estimation According to Voltage, Temperature, and RMS Current, IEEE Trans. Ind. Electron. 61 (2014) 4895–4902. doi:10.1109/TIE.2013.2293695.

[97] M. Zhu, C. Weber, Y. Yang, M. Konuma, Chemical and electrochemical ageing of carbon materials used in supercapacitor electrodes, Carbon N. Y. 46 (2008) 1829–1840.

doi:10.1016/j.carbon.2008.07.025.

[98] D. Cericola, R. Kötz, A. Wokaun, Effect of electrode mass ratio on aging of activated carbon based supercapacitors utilizing organic electrolytes, J. Power Sources. 196 (2011) 3114–3118. doi:10.1016/j.jpowsour.2010.11.157.

[99] H. Gualous, R. Gallay, G. Alcicek, B. Tala-Ighil, A. Oukaour, B. Boudart, P. Makany, Supercapacitor ageing at constant temperature and constant voltage and thermal shock, Microelectron. Reliab. 50 (2010) 1783–1788. doi:10.1016/j.microrel.2010.07.144.

[100] T. Kovaltchouk, B. Multon, H. Ben Ahmed, J. Aubry, P. Venet, Enhanced Aging Model for Supercapacitors Taking Into Account Power Cycling: Application to the Sizing of an Energy Storage System in a Direct Wave Energy Converter, IEEE Trans. Ind. Appl. 51 (2015) 2405–2414. doi:10.1109/TIA.2014.2369817.

[101] A. EL MEJDOUBI, A. Oukaour, H. Chaoui, H. Gualous, jalal sabor, youssef slamani, Prediction Aging Model for Supercapacitor's Calendar Life in Vehicular Applications., IEEE Trans. Veh. Technol. (2016) 1–1. doi:10.1109/TVT.2016.2539681.

[102] D. Weingarth, A. Foelske-Schmitz, R. Kötz, Cycle versus voltage hold – Which is the better stability test for electrochemical double layer capacitors?, J. Power Sources. 225 (2013) 84–88. doi:10.1016/j.jpowsour.2012.10.019.

[103] R. Kötz, M. Hahn, R. Gallay, Temperature behavior and impedance fundamentals of supercapacitors, J. Power Sources. 154 (2006) 550–555. doi:10.1016/j.jpowsour.2005.10.048.

[104] A. d'Entremont, L. Pilon, First-order thermal model of commercial EDLCs, Appl. Therm. Eng. 67 (2014) 439–446. doi:10.1016/j.applthermaleng.2014.03.061.

[105] Y. Parvini, J.B. Siegel, A.G. Stefanopoulou, A. Vahidi, Preliminary results on identification of an electro-thermal model for low temperature and high power operation of cylindrical double layer ultracapacitors, in: 2014 Am. Control Conf., IEEE, 2014: pp. 242–247. doi:10.1109/ACC.2014.6859394.

[106] H. Gualous, H. Louahlia, R. Gallay, Supercapacitor Characterization and Thermal Modelling With Reversible and Irreversible Heat Effect, IEEE Trans. Power Electron. 26 (2011) 3402–3409. doi:10.1109/TPEL.2011.2145422.

[107] M. Frivaldsky, J. Cuntala, P. Spanik, Simple and accurate thermal simulation model of supercapacitor suitable for development of module solutions, Int. J. Therm. Sci. 84 (2014) 34–47. doi:10.1016/j.ijthermalsci.2014.04.005.

[108] A. Berrueta, I. San Martín, A. Hernández, A. Ursúa, P. Sanchis, Electro-thermal modelling of a supercapacitor and experimental validation, J. Power Sources. 259 (2014) 154–165. doi:10.1016/j.jpowsour.2014.02.089.

[109] N. Damay, C. Forgez, M.-P. Bichat, G. Friedrich, Thermal modeling of large prismatic LiFePO4/graphite battery. Coupled thermal and heat generation models for characterization and simulation, J. Power Sources. 283 (2015) 37–45. doi:10.1016/j.jpowsour.2015.02.091.

[110] H. Gualous, H. Louahlia-Gualous, R. Gallay, A. Miraoui, Supercapacitor Thermal Modeling and Characterization in Transient State for Industrial Applications, IEEE Trans. Ind. Appl. 45 (2009) 1035–1044. doi:10.1109/TIA.2009.2018879.

[111] M.W. Verbrugge, P. Liu, Microstructural Analysis and Mathematical Modeling of Electric Double-Layer Supercapacitors, J. Electrochem. Soc. 152 (2005) D79. doi:10.1149/1.1878052.

[112] S. Allu, B. Velamur Asokan, W.A. Shelton, B. Philip, S. Pannala, A generalized multi-

dimensional mathematical model for charging and discharging processes in a supercapacitor, J. Power Sources. 256 (2014) 369–382. doi:10.1016/j.jpowsour.2014.01.054.

[113] R. Drummond, D.A. Howey, S.R. Duncan, Low-order mathematical modelling of electric double layer supercapacitors using spectral methods, J. Power Sources. 277 (2015) 317–328. doi:10.1016/j.jpowsour.2014.11.116.

[114] S. Buller, E. Karden, D. Kok, R.W. De Doncker, Modeling the dynamic behavior of supercapacitors using impedance spectroscopy, Ind. Appl. IEEE Trans. 38 (2001) 1622–1626. http://ieeexplore.ieee.org/xpls/abs_all.jsp?arnumber=955972 (accessed December 5, 2013).

[115] W. Lajnef, J.-M. Vinassa, O. Briat, S. Azzopardi, E. Woirgard, Characterization methods and modelling of ultracapacitors for use as peak power sources, J. Power Sources. 168 (2007) 553–560. doi:10.1016/j.jpowsour.2007.02.049.

[116] N. Devillers, S. Jemei, M.-C. Péra, D. Bienaimé, F. Gustin, Review of characterization methods for supercapacitor modelling, J. Power Sources. 246 (2014) 596–608. doi:10.1016/j.jpowsour.2013.07.116.

[117] W. Lajnef, J.-M. Vinassa, O. Briat, S. Azzopardi, E. Woirgard, Characterization methods and modelling of ultracapacitors for use as peak power sources, J. Power Sources. 168 (2007) 553–560. doi:10.1016/j.jpowsour.2007.02.049.

[118] V. Musolino, L. Piegari, E. Tironi, New Full-Frequency-Range Supercapacitor Model With Easy Identification Procedure, IEEE Trans. Ind. Electron. 60 (2013) 112–120. doi:10.1109/TIE.2012.2187412.

[119] J. Schiffer, D. Linzen, D.U. Sauer, Heat generation in double layer capacitors, J. Power Sources. 160 (2006) 765–772. doi:10.1016/j.jpowsour.2005.12.070.

[120] M. Iwaida, E. Komazawa, M. Noguchi, K. Andou, Current collector for electric double-layer capacitor, (1999). https://www.google.com/patents/US5949637.

[121] A.G. Pandolfo, A.F. Hollenkamp, Carbon properties and their role in supercapacitors, J. Power Sources. 157 (2006) 11–27. doi:10.1016/j.jpowsour.2006.02.065.

[122] D.H. Lee, U.S. Kim, C.B. Shin, B.H. Lee, B.W. Kim, Y.-H. Kim, Modelling of the thermal behaviour of an ultracapacitor for a 42-V automotive electrical system, J. Power Sources. 175 (2008) 664–668. doi:10.1016/j.jpowsour.2007.09.081.

[123] O.S. Burheim, M. Aslan, J.S. Atchison, V. Presser, Thermal conductivity and temperature profiles in carbon electrodes for supercapacitors, J. Power Sources. 246 (2014) 160–166. doi:10.1016/j.jpowsour.2013.06.164.

[124] H.H. Hauge, V. Presser, O. Burheim, In-situ and ex-situ measurements of thermal conductivity of supercapacitors, Energy. 78 (2014) 373–383. doi:10.1016/j.energy.2014.10.022.

[125] M. Al Sakka, H. Gualous, J. Van Mierlo, H. Culcu, Thermal modeling and heat management of supercapacitor modules for vehicle applications, J. Power Sources. 194 (2009) 581–587. doi:10.1016/j.jpowsour.2009.06.038.

[126] A. Hijazi, P. Kreczanik, E. Bideaux, P. Venet, G. Clerc, M. Di Loreto, Thermal Network Model of Supercapacitors Stack, IEEE Trans. Ind. Electron. 59 (2012) 979–987. doi:10.1109/TIE.2011.2158769.

[127] J.M. Tarascon, Li-ion batteries and beyond: Recent advances, in: Adv. Automot. Batter. Conf. 2015, Mainz, 2015.

[128] S. Campanari, G. Manzolini, F. Garcia de la Iglesia, Energy analysis of electric vehicles using batteries or fuel cells through well-to-wheel driving cycle simulations, J. Power Sources. 186 (2009) 464–477. doi:10.1016/j.jpowsour.2008.09.115.

[129] F. Creutzig, A. Papson, L. Schipper, D.M. Kammen, Economic and environmental evaluation of compressed-air cars, Environ. Res. Lett. 4 (2009) 044011. doi:10.1088/1748-9326/4/4/044011.

[130] F. Mueller-Langer, E. Tzimas, M. Kaltschmitt, S. Peteves, Techno-economic assessment of hydrogen production processes for the hydrogen economy for the short and medium term, Int. J. Hydrogen Energy. 32 (2007) 3797–3810. doi:10.1016/j.ijhydene.2007.05.027.

[131] P. Doran, S. Robeson, D. Wright, J. Craven, Finance and the fuel cell industry: a review of the current financing climate, 2003. doi:10.1016/S0360-3199(02)00244-6.

[132] M.W. Melaina, Initiating hydrogen infrastructures: preliminary analysis of a sufficient number of initial hydrogen stations in the US, Int. J. Hydrogen Energy. 28 (2003) 743–755. doi:10.1016/S0360-3199(02)00240-9.

[133] J. Dong, C. Liu, Z. Lin, Charging infrastructure planning for promoting battery electric vehicles: An activity-based approach using multiday travel data, Transp. Res. Part C Emerg. Technol. 38 (2014) 44–55. doi:10.1016/j.trc.2013.11.001.

[134] IEC, IEC 60038:2009 - IEC standard voltages, 2009. https://webstore.iec.ch/publication/153.

[135] D. Howell, US DOE Electric Drive Vehicle Battery R&D Impacts, Progress, and Plans, in: Adv. Automot. Batter. Conf. 2015, Detroit, 2015: pp. 1–22. doi:10.1093/ajae/aat032.

[136] L.T. Nitz, Creating e-Motional EVs, in: Adv. Automot. Batter. Conf. 2015, Advanced Automotive Battery Conference 2015, Detroit, 2015: pp. 1–27.

[137] Chevrolet, 2016 Chevrolet Volt, in: Adv. Automot. Batter. Conf. 2015, Advanced Automotive Battery Conference 2015, Detroit, 2015: pp. 1–17.

[138] M.M. Thackeray, C. Wolverton, E.D. Isaacs, Electrical energy storage for transportation—approaching the limits of, and going beyond, lithium-ion batteries, Energy Environ. Sci. 5 (2012) 7854. doi:10.1039/c2ee21892e.

[139] P.G. Bruce, S.A. Freunberger, L.J. Hardwick, J.-M. Tarascon, Li–O2 and Li–S batteries with high energy storage, Nat. Mater. 11 (2011) 19–29. doi:10.1038/nmat3191.

[140] A.M. Colclasure, R.J. Kee, Thermodynamically consistent modeling of elementary electrochemistry in lithium-ion batteries, Electrochim. Acta. 55 (2010) 8960–8973. doi:10.1016/j.electacta.2010.08.018.

[141] H. Lee, M. Yanilmaz, O. Toprakci, K. Fu, X. Zhang, A review of recent developments in membrane separators for rechargeable lithium-ion batteries, Energy Environ. Sci. 7 (2014) 3857–3886. doi:10.1039/C4EE01432D.

[142] W. Xu, J. Wang, F. Ding, X. Chen, E. Nasybulin, Y. Zhang, J.-G. Zhang, Lithium metal anodes for rechargeable batteries, Energy Environ. Sci. 7 (2014) 513–537. doi:10.1039/C3EE40795K.

[143] N. Nitta, F. Wu, J.T. Lee, G. Yushin, Li-ion battery materials: present and future, Mater. Today. 18 (2014) 252–264. doi:10.1016/j.mattod.2014.10.040.

[144] J. Dahn, G. Ehrlich, Linden's Handbook of Batteries, 4th Edition, in: T. Reddy (Ed.), Linden's Handb. Batter., McGraw Hill Professional, n.d.: pp. 26.1–26.78.

[145] J. Christensen, Modeling Diffusion-Induced Stress in Li-Ion Cells with Porous Electrodes, J. Electrochem. Soc. 157 (2010) A366. doi:10.1149/1.3269995.

[146] N. Tanaka, Modeling and Simulation of Thermo-Electrochemistry of Thermal Runaway in Lithium-Ion Batteries, 2014.

[147] V.A. Sethuraman, L.J. Hardwick, V. Srinivasan, R. Kostecki, Surface structural disordering in graphite upon lithium intercalation/deintercalation, J. Power Sources. 195 (2010) 3655–3660. doi:10.1016/j.jpowsour.2009.12.034.

[148] J. Xiao, W. Xu, D. Wang, D. Choi, W. Wang, X. Li, G.L. Graff, J. Liu, J.-G. Zhang, Stabilization of Silicon Anode for Li-Ion Batteries, J. Electrochem. Soc. 157 (2010) A1047. doi:10.1149/1.3464767.

[149] V.G. Khomenko, V.Z. Barsukov, Characterization of silicon- and carbon-based composite anodes for lithium-ion batteries, Electrochim. Acta. 52 (2007) 2829–2840. doi:10.1016/j.electacta.2006.11.006.

[150] L.-X. Yuan, Z.-H. Wang, W.-X. Zhang, X.-L. Hu, J.-T. Chen, Y.-H. Huang, J.B. Goodenough, Development and challenges of LiFePO 4 cathode material for lithium-ion batteries, Energy Environ. Sci. 4 (2011) 269–284. doi:10.1039/C0EE00029A.

[151] InvestmentMine, Commodity and Metal Prices, (2016). http://www.infomine.com/investment/metal-prices/ (accessed March 10, 2016).

[152] W.-S. Yoon, K.Y. Chung, J. McBreen, D.A. Fischer, X.-Q. Yang, Electronic structural changes of the electrochemically Li-ion deintercalated LiNi0.8Co0.15Al0.05O2 cathode material investigated by X-ray absorption spectroscopy, J. Power Sources. 174 (2007) 1015–1020. doi:10.1016/j.jpowsour.2007.06.214.

[153] D.. Abraham, R.. Twesten, M. Balasubramanian, I. Petrov, J. McBreen, K. Amine, Surface changes on LiNi0.8Co0.2O2 particles during testing of high-power lithium-ion cells, Electrochem. Commun. 4 (2002) 620–625. doi:10.1016/S1388-2481(02)00388-0.

[154] C. Delmas, M. Ménétrier, L. Croguennec, I. Saadoune, A. Rougier, C. Pouillerie, G. Prado, M. Grüne, L. Fournès, An overview of the Li(Ni,M)O2 systems: syntheses, structures and properties, Electrochim. Acta. 45 (1999) 243–253. doi:10.1016/S0013-4686(99)00208-X.

[155] C.H. Chen, J. Liu, M.E. Stoll, G. Henriksen, D.R. Vissers, K. Amine, Aluminum-doped lithium nickel cobalt oxide electrodes for high-power lithium-ion batteries, J. Power Sources. 128 (2004) 278–285. doi:10.1016/j.jpowsour.2003.10.009.

[156] I. Belharouak, Y.-K. Sun, J. Liu, K. Amine, Li(Ni1/3Co1/3Mn1/3)O2 as a suitable cathode for high power applications, J. Power Sources. 123 (2003) 247–252. doi:10.1016/S0378-7753(03)00529-9.

[157] J. Vetter, P. Novák, M.R. Wagner, C. Veit, K.-C. Möller, J.O. Besenhard, M. Winter, M. Wohlfahrt-Mehrens, C. Vogler, A. Hammouche, Ageing mechanisms in lithium-ion batteries, J. Power Sources. 147 (2005) 269–281. doi:10.1016/j.jpowsour.2005.01.006.

[158] I. Belharouak, W. Lu, D. Vissers, K. Amine, Safety characteristics of Li(Ni0.8Co0.15Al0.05)O2 and Li(Ni1/3Co1/3Mn1/3)O2, Electrochem. Commun. 8 (2006) 329–335. doi:10.1016/j.elecom.2005.12.007.

[159] J.Z. Pei Kang Shen, Chao-Yang Wang, San Ping Jiang, Xueliang Sun, Electrochemical Energy: Advanced Materials and Technologies, 2015.

[160] D. Aurbach, Y. Talyosef, B. Markovsky, E. Markevich, E. Zinigrad, L. Asraf, J.S. Gnanaraj, H.-J.

Kim, Design of electrolyte solutions for Li and Li-ion batteries: a review, Electrochim. Acta. 50 (2004) 247–254. doi:10.1016/j.electacta.2004.01.090.

[161] D. Aurbach, Review of selected electrode–solution interactions which determine the performance of Li and Li ion batteries, J. Power Sources. 89 (2000) 206–218. doi:10.1016/S0378-7753(00)00431-6.

[162] K. Xu, Nonaqueous Liquid Electrolytes for Lithium-Based Rechargeable Batteries, Chem. Rev. 104 (2004) 4303–4418. doi:10.1021/cr030203g.

[163] J.-M. Tarascon, M. Armand, Issues and challenges facing rechargeable lithium batteries, Nature. 414 (2001) 359–367. doi:10.1038/35104644.

[164] G. Venugopal, Characterization of thermal cut-off mechanisms in prismatic lithium-ion batteries, J. Power Sources. 101 (2001) 231–237. doi:10.1016/S0378-7753(01)00782-0.

[165] A.H. Whitehead, M. Schreiber, Current Collectors for Positive Electrodes of Lithium-Based Batteries, J. Electrochem. Soc. 152 (2005) A2105. doi:10.1149/1.2039587.

[166] H. Zheng, J. Li, X. Song, G. Liu, V.S. Battaglia, A comprehensive understanding of electrode thickness effects on the electrochemical performances of Li-ion battery cathodes, Electrochim. Acta. 71 (2012) 258–265. doi:10.1016/j.electacta.2012.03.161.

[167] M. Lu, Current Situation Regarding xEV-Batteries in the Chinese Market and Future Outlook, in: Adv. Automot. Batter. Conf. 2016, 2016. https://www.advancedautobat.com/conferences/automotive-battery-conference-Europe-2016/battery-technology-market/track-1.html.

[168] P. Bruce, Cost and Performance of EV Batteries, Cambridge, 2012.

[169] D. Doerffel, S.A. Sharkh, A critical review of using the Peukert equation for determining the remaining capacity of lead-acid and lithium-ion batteries, J. Power Sources. 155 (2006) 395–400. doi:10.1016/j.jpowsour.2005.04.030.

[170] A. Hausmann, C. Depcik, Expanding the Peukert equation for battery capacity modeling through inclusion of a temperature dependency, J. Power Sources. 235 (2013) 148–158. doi:10.1016/j.jpowsour.2013.01.174.

[171] C.D. Rahn, C.-Y. Wang, Battery Systems Engineering, 2013. doi:10.1002/9781118517048.

[172] C.R. Pals, Thermal Modeling of the Lithium/Polymer Battery, J. Electrochem. Soc. 142 (1995) 3274. doi:10.1149/1.2049974.

[173] D.M. Bernardi, R. Chandrasekaran, J.Y. Go, Solid-State Transport of Lithium in Lithium-Ion-Battery Positive Electrodes, J. Electrochem. Soc. 160 (2013) A1430–A1441. doi:10.1149/2.042309jes.

[174] K. Smith, C.-Y. Wang, Power and thermal characterization of a lithium-ion battery pack for hybrid-electric vehicles, J. Power Sources. 160 (2006) 662–673. doi:10.1016/j.jpowsour.2006.01.038.

[175] W. Fang, P. Ramadass, Z. (John) Zhang, Study of internal short in a Li-ion cell-II. Numerical investigation using a 3D electrochemical-thermal model, J. Power Sources. 248 (2014) 1090–1098. doi:10.1016/j.jpowsour.2013.10.004.

[176] K. Becker-Steinberger, S. Funken, M. Landstorfer, K. Urban, K. Becker-Steinberger, S. Funken, M. Landstorfer, K. Urban, A Mathematical Model for All Solid-State Lithium-Ion Batteries, in: ECS Trans., 2010: pp. 285–296. doi:10.1149/1.3393864.

[177] Y. Xing, W. He, M. Pecht, K.L. Tsui, State of charge estimation of lithium-ion batteries using the open-circuit voltage at various ambient temperatures, Appl. Energy. 113 (2014) 106–115. doi:10.1016/j.apenergy.2013.07.008.

[178] D. Aurbach, H. Teller, M. Koltypin, E. Levi, On the behavior of different types of graphite anodes, J. Power Sources. 119-121 (2003) 2–7. doi:10.1016/S0378-7753(03)00115-0.

[179] Y. Zhang, C.-Y. Wang, X. Tang, Cycling degradation of an automotive LiFePO4 lithium-ion battery, J. Power Sources. 196 (2011) 1513–1520. doi:10.1016/j.jpowsour.2010.08.070.

[180] R.. Wright, J.. Christophersen, C.. Motloch, J.. Belt, C.. Ho, V.. Battaglia, J.. Barnes, T.. Duong, R.. Sutula, Power fade and capacity fade resulting from cycle-life testing of Advanced Technology Development Program lithium-ion batteries, J. Power Sources. 119-121 (2003) 865–869. doi:10.1016/S0378-7753(03)00190-3.

[181] E. Peled, D. Golodnitsky, G. Ardel, V. Eshkenazy, The Sei Model - Application to Lithium Polymer Electrolyte Batteries, Electrochim. Acta. 40 (1995) 2197–2204. doi:Doi 10.1016/0013-4686(95)00163-9.

[182] F.A. Soto, Y. Ma, J.M. Martinez de la Hoz, J.M. Seminario, P.B. Balbuena, Formation and Growth Mechanisms of Solid-Electrolyte Interphase Layers in Rechargeable Batteries, Chem. Mater. 27 (2015) acs.chemmater.5b03358. doi:10.1021/acs.chemmater.5b03358.

[183] K. Edström, M. Herstedt, D.P. Abraham, A new look at the solid electrolyte interphase on graphite anodes in Li-ion batteries, J. Power Sources. 153 (2006) 380–384. doi:10.1016/j.jpowsour.2005.05.062.

[184] C. Birkl, Degradation of Lithium Ion batteries, Energy Power Gr. - Oxford. (2014). http://epg.eng.ox.ac.uk/content/degradation-lithium-ion-batteries (accessed January 7, 2016).

[185] A.M. Colclasure, K.A. Smith, R.J. Kee, Modeling detailed chemistry and transport for solid-electrolyte-interface (SEI) films in Li–ion batteries, Electrochim. Acta. 58 (2011) 33–43. doi:10.1016/j.electacta.2011.08.067.

[186] V. Agubra, J. Fergus, Lithium Ion Batery Anode Aging Mechanisms, Materials (Basel). 6 (2013) 1310–1325. doi:10.3390/ma6041310.

[187] B.V. Ratnakumar, M.C. Smart, S. Surampudi, Effects of SEI on the kinetics of lithium intercalation, J. Power Sources. 97-98 (2001) 137–139. doi:10.1016/S0378-7753(01)00682-6.

[188] J.H. Lee, J.K. Hong, D.H. Jang, Y.-K. Sun, S.M. Oh, Degradation mechanisms in doped spinels of LiM0.05Mn1.95O4 (M=Li, B, Al, Co, and Ni) for Li secondary batteries, J. Power Sources. 89 (2000) 7–14. doi:10.1016/S0378-7753(00)00375-X.

[189] T. Sasaki, T. Nonaka, H. Oka, C. Okuda, Y. Itou, Y. Kondo, Y. Takeuchi, Y. Ukyo, K. Tatsumi, S. Muto, Capacity-Fading Mechanisms of LiNiO[sub 2]-Based Lithium-Ion Batteries, J. Electrochem. Soc. 156 (2009) A289. doi:10.1149/1.3076136.

[190] A.H. Tavakoli, H. Kondo, Y. Ukyo, A. Navrotsky, Stabilizing Effect of Mg on the Energetics of the Li(Ni,Co,Al)O2 Cathode Material for Lithium Ion Batteries, J. Electrochem. Soc. 160 (2012) A302–A305. doi:10.1149/2.059302jes.

[191] S. Muto, Y. Sasano, K. Tatsumi, T. Sasaki, K. Horibuchi, Y. Takeuchi, Y. Ukyo, Capacity-Fading Mechanisms of LiNiO[sub 2]-Based Lithium-Ion Batteries, J. Electrochem. Soc. 156 (2009) A371. doi:10.1149/1.3076137.

[192] D.P. Abraham, R.D. Twesten, M. Balasubramanian, J. Kropf, D. Fischer, J. McBreen, I. Petrov,

K. Amine, Microscopy and Spectroscopy of Lithium Nickel Oxide-Based Particles Used in High Power Lithium-Ion Cells, J. Electrochem. Soc. 150 (2003) A1450. doi:10.1149/1.1613291.

[193] M. Wohlfahrt-Mehrens, C. Vogler, J. Garche, Aging mechanisms of lithium cathode materials, J. Power Sources. 127 (2004) 58–64. doi:10.1016/j.jpowsour.2003.09.034.

[194] S. Komaba, N. Kumagai, Y. Kataoka, Influence of manganese(II), cobalt(II), and nickel(II) additives in electrolyte on performance of graphite anode for lithium-ion batteries, Electrochim. Acta. 47 (2002) 1229–1239. doi:10.1016/S0013-4686(01)00847-7.

[195] C.G. Hochgraf, J.K. Basco, T.P. Bohn, I. Bloom, Effect of ultracapacitor-modified PHEV protocol on performance degradation in lithium-ion cells, J. Power Sources. 246 (2014) 965–969. doi:10.1016/j.jpowsour.2012.09.038.

[196] H. He, R. Xiong, H. Guo, S. Li, Comparison study on the battery models used for the energy management of batteries in electric vehicles, Energy Convers. Manag. 64 (2012) 113–121. doi:10.1016/j.enconman.2012.04.014.

[197] T. Huria, G. Ludovici, G. Lutzemberger, State of charge estimation of high power lithium iron phosphate cells, J. Power Sources. 249 (2014) 92–102. doi:10.1016/j.jpowsour.2013.10.079.

[198] Y. Tian, C. Chen, B. Xia, W. Sun, Z. Xu, W. Zheng, An Adaptive Gain Nonlinear Observer for State of Charge Estimation of Lithium-Ion Batteries in Electric Vehicles, Energies. 7 (2014) 5995–6012. doi:10.3390/en7095995.

[199] M. Doyle, T.F. Fuller, J. Newman, Modeling of Galvanostatic Charge and Discharge of the Lithium/Polymer/Insertion Cell, J. Electrochem. Soc. 140 (1993) 1526. doi:10.1149/1.2221597.

[200] A.M. Colclasure, K.A. Smith, R.J. Kee, Modeling detailed chemistry and transport for solid-electrolyte-interface (SEI) films in Li–ion batteries, Electrochim. Acta. 58 (2011) 33–43. doi:10.1016/j.electacta.2011.08.067.

[201] H.J. Ploehn, P. Ramadass, R.E. White, Solvent Diffusion Model for Aging of Lithium-Ion Battery Cells, J. Electrochem. Soc. 151 (2004) A456. doi:10.1149/1.1644601.

[202] M.B. Pinson, M.Z. Bazant, Theory of SEI Formation in Rechargeable Batteries: Capacity Fade, Accelerated Aging and Lifetime Prediction, J. Electrochem. Soc. 160 (2012) A243–A250. doi:10.1149/2.044302jes.

[203] P. Ramadass, B. Haran, R. White, B.N. Popov, Mathematical modeling of the capacity fade of Li-ion cells, J. Power Sources. 123 (2003) 230–240. doi:10.1016/S0378-7753(03)00531-7.

[204] Q. Zhang, R.E. White, Capacity fade analysis of a lithium ion cell, 2008. doi:10.1016/j.jpowsour.2008.01.028.

[205] S. Golmon, K. Maute, M.L. Dunn, Numerical modeling of electrochemical–mechanical interactions in lithium polymer batteries, Comput. Struct. 87 (2009) 1567–1579. doi:10.1016/j.compstruc.2009.08.005.

[206] X. Xiao, W. Wu, X. Huang, A multi-scale approach for the stress analysis of polymeric separators in a lithium-ion battery, J. Power Sources. 195 (2010) 7649–7660. doi:10.1016/j.jpowsour.2010.06.020.

[207] M. Guo, G.-H. Kim, R.E. White, A three-dimensional multi-physics model for a Li-ion battery, J. Power Sources. 240 (2013) 80–94. doi:10.1016/j.jpowsour.2013.03.170.

[208] K.-J. Lee, K. Smith, A. Pesaran, G.-H. Kim, Three dimensional thermal-, electrical-, and

electrochemical-coupled model for cylindrical wound large format lithium-ion batteries, J. Power Sources. 241 (2013) 20–32. doi:10.1016/j.jpowsour.2013.03.007.

[209] M. Chen, G.A. Rincon-Mora, Accurate Electrical Battery Model Capable of Predicting Runtime and I–V Performance, IEEE Trans. Energy Convers. 21 (2006) 504–511. doi:10.1109/TEC.2006.874229.

[210] T. Huria, M. Ceraolo, J. Gazzarri, R. Jackey, High fidelity electrical model with thermal dependence for characterization and simulation of high power lithium battery cells, in: 2012 IEEE Int. Electr. Veh. Conf., IEEE, 2012: pp. 1–8. doi:10.1109/IEVC.2012.6183271.

[211] T.M. Bandhauer, S. Garimella, T.F. Fuller, A Critical Review of Thermal Issues in Lithium-Ion Batteries, J. Electrochem. Soc. 158 (2011) R1. doi:10.1149/1.3515880.

[212] S. Basu, R.S. Patil, S. Ramachandran, K.S. Hariharan, S.M. Kolake, T. Song, D. Oh, T. Yeo, S. Doo, Non-isothermal electrochemical model for lithium-ion cells with composite cathodes, J. Power Sources. 283 (2015) 132–150. doi:10.1016/j.jpowsour.2015.02.127.

[213] L.H. Saw, Y. Ye, A.A.O. Tay, Electrochemical–thermal analysis of 18650 Lithium Iron Phosphate cell, Energy Convers. Manag. 75 (2013) 162–174. doi:10.1016/j.enconman.2013.05.040.

[214] J.-S. Hong, Electrochemical-Calorimetric Studies of Lithium-Ion Cells, J. Electrochem. Soc. 145 (1998) 1489. doi:10.1149/1.1838509.

[215] H. Yang, J. Prakash, Determination of the Reversible and Irreversible Heats of a LiNi[sub 0.8]Co[sub 0.15]Al[sub 0.05]O[sub 2]/Natural Graphite Cell Using Electrochemical-Calorimetric Technique, J. Electrochem. Soc. 151 (2004) A1222. doi:10.1149/1.1765771.

[216] P.J. Osswald, M. del Rosario, J. Garche, A. Jossen, H.E. Hoster, Fast and Accurate Measurement of Entropy Profiles of Commercial Lithium-Ion Cells, Electrochim. Acta. 177 (2015) 270–276. doi:10.1016/j.electacta.2015.01.191.

[217] V. V. Viswanathan, D. Choi, D. Wang, W. Xu, S. Towne, R.E. Williford, J.-G. Zhang, J. Liu, Z. Yang, Effect of entropy change of lithium intercalation in cathodes and anodes on Li-ion battery thermal management, J. Power Sources. 195 (2010) 3720–3729. doi:10.1016/j.jpowsour.2009.11.103.

[218] J.P. Schmidt, A. Weber, E. Ivers-Tiffée, A novel and precise measuring method for the entropy of lithium-ion cells: ΔS via electrothermal impedance spectroscopy, Electrochim. Acta. 137 (2014) 311–319. doi:10.1016/j.electacta.2014.05.153.

[219] K.E. Thomas, J. Newman, Heats of mixing and of entropy in porous insertion electrodes, J. Power Sources. 119-121 (2003) 844–849. doi:10.1016/S0378-7753(03)00283-0.

[220] K. Chen, G. Unsworth, X. Li, Measurements of heat generation in prismatic Li-ion batteries, J. Power Sources. 261 (2014) 28–37. doi:10.1016/j.jpowsour.2014.03.037.

[221] E. Prada, D. Di Domenico, Y. Creff, J. Bernard, V. Sauvant-Moynot, F. Huet, Simplified Electrochemical and Thermal Model of LiFePO4-Graphite Li-Ion Batteries for Fast Charge Applications, J. Electrochem. Soc. 159 (2012) A1508–A1519. doi:10.1149/2.064209jes.

[222] Y. Ji, C.Y. Wang, Heating strategies for Li-ion batteries operated from subzero temperatures, Electrochim. Acta. 107 (2013) 664–674. doi:10.1016/j.electacta.2013.03.147.

[223] C. Forgez, D. Vinh Do, G. Friedrich, M. Morcrette, C. Delacourt, Thermal modeling of a cylindrical LiFePO4/graphite lithium-ion battery, J. Power Sources. 195 (2010) 2961–2968. doi:10.1016/j.jpowsour.2009.10.105.

[224] M. Xu, Z. Zhang, X. Wang, L. Jia, L. Yang, A pseudo three-dimensional electrochemical–thermal model of a prismatic LiFePO4 battery during discharge process, Energy. 80 (2015) 303–317. doi:10.1016/j.energy.2014.11.073.

[225] K. Somasundaram, E. Birgersson, A.S. Mujumdar, Thermal–electrochemical model for passive thermal management of a spiral-wound lithium-ion battery, J. Power Sources. 203 (2012) 84–96. doi:10.1016/j.jpowsour.2011.11.075.

[226] R. Jackey, Estimating Parameters of a Battery, Mathworks. (2009). http://www.mathworks.com/videos/estimating-parameters-of-a-battery-68957.html?refresh=true (accessed April 27, 2016).

[227] R.E. Williford, V. V. Viswanathan, J.-G. Zhang, Effects of entropy changes in anodes and cathodes on the thermal behavior of lithium ion batteries, J. Power Sources. 189 (2009) 101–107. doi:10.1016/j.jpowsour.2008.10.078.

[228] M. Shadman Rad, D.L. Danilov, M. Baghalha, M. Kazemeini, P.H.L. Notten, Adaptive thermal modeling of Li-ion batteries, Electrochim. Acta. 102 (2013) 183–195. doi:10.1016/j.electacta.2013.03.167.

[229] A.W. Stienecker, T. Stuart, C. Ashtiani, An ultracapacitor circuit for reducing sulfation in lead acid batteries for Mild Hybrid Electric Vehicles, J. Power Sources. 156 (2006) 755–762. doi:10.1016/j.jpowsour.2005.06.014.

[230] J.N. Marie-Francoise, H. Gualous, R. Outbib, A. Berthon, 42V Power Net with supercapacitor and battery for automotive applications, J. Power Sources. 143 (2005) 275–283. doi:10.1016/j.jpowsour.2004.12.011.

[231] J. Bauman, M. Kazerani, A Comparative Study of Fuel-Cell–Battery, Fuel-Cell–Ultracapacitor, and Fuel-Cell–Battery–Ultracapacitor Vehicles, IEEE Trans. Veh. Technol. 57 (2008) 760–769. doi:10.1109/TVT.2007.906379.

[232] C. Ashtiani, R. Wright, G. Hunt, Ultracapacitors for automotive applications, 2006. doi:10.1016/j.jpowsour.2005.10.082.

[233] J. Jian Cao, A. Emadi, A New Battery/UltraCapacitor Hybrid Energy Storage System for Electric, Hybrid, and Plug-In Hybrid Electric Vehicles, IEEE Trans. Power Electron. 27 (2012) 122–132. doi:10.1109/TPEL.2011.2151206.

[234] F.S. Garcia, A.A. Ferreira, J.A. Pomilio, Control Strategy for Battery-Ultracapacitor Hybrid Energy Storage System, in: 2009 Twenty-Fourth Annu. IEEE Appl. Power Electron. Conf. Expo., IEEE, 2009: pp. 826–832. doi:10.1109/APEC.2009.4802757.

[235] A. Khaligh, Z. Zhihao Li, Battery, Ultracapacitor, Fuel Cell, and Hybrid Energy Storage Systems for Electric, Hybrid Electric, Fuel Cell, and Plug-In Hybrid Electric Vehicles: State of the Art, IEEE Trans. Veh. Technol. 59 (2010) 2806–2814. doi:10.1109/TVT.2010.2047877.

[236] A.C. Baisden, A. Emadi, ADVISOR-Based Model of a Battery and an Ultra-Capacitor Energy Source for Hybrid Electric Vehicles, IEEE Trans. Veh. Technol. 53 (2004) 199–205. doi:10.1109/TVT.2003.822004.

[237] J. Park, B. Raju, A. Emadi, Effects of an Ultra-Capacitor and Battery Energy Storage System in a Hybrid Electric Vehicle, SAE Int. (2006).

[238] A. Kuperman, I. Aharon, S. Malki, A. Kara, Design of a Semiactive Battery-Ultracapacitor Hybrid Energy Source, IEEE Trans. Power Electron. 28 (2013) 806–815. doi:10.1109/TPEL.2012.2203361.

[239] J.M. Miller, G. Sartorelli, Battery and ultracapacitor combinations — Where should the converter go?, in: 2010 IEEE Veh. Power Propuls. Conf., IEEE, 2010: pp. 1–7. doi:10.1109/VPPC.2010.5729216.

[240] R.A. Dougal, S. Liu, R.E. White, Power and life extension of battery-ultracapacitor hybrids, IEEE Trans. Components Packag. Technol. 25 (2002) 120–131. doi:10.1109/6144.991184.

[241] H.A. Catherino, J.F. Burgel, P.L. Shi, A. Rusek, X. Zou, Hybrid power supplies: A capacitor-assisted battery, J. Power Sources. 162 (2006) 965–970. doi:10.1016/j.jpowsour.2005.07.012.

[242] D. Shin, Y. Kim, Y. Wang, N. Chang, M. Pedram, Constant-current regulator-based battery-supercapacitor hybrid architecture for high-rate pulsed load applications, J. Power Sources. 205 (2012) 516–524. doi:10.1016/j.jpowsour.2011.12.043.

[243] S. Pay, Y. Baghzouz, Effectiveness of battery-supercapacitor combination in electric vehicles, in: 2003 IEEE Bol. Power Tech Conf. Proceedings, IEEE, 2003: pp. 728–733. doi:10.1109/PTC.2003.1304472.

[244] R. Carter, A. Cruden, P.J. Hall, Optimizing for Efficiency or Battery Life in a Battery/Supercapacitor Electric Vehicle, IEEE Trans. Veh. Technol. 61 (2012) 1526–1533. doi:10.1109/TVT.2012.2188551.

[245] D. Hoelscher, A. Skorcz, Y. Gao, M. Ehsani, Hybridized Electric Energy Storage Systems for Hybrid Electric Vehicles, in: 2006 IEEE Veh. Power Propuls. Conf., IEEE, 2006: pp. 1–6. doi:10.1109/VPPC.2006.364302.

[246] H. Farzanehfard, D.S. Beyragh, E. Adib, A bidirectional soft switched ultracapacitor interface circuit for hybrid electric vehicles, Energy Convers. Manag. 49 (2008) 3578–3584. doi:10.1016/j.enconman.2008.07.004.

[247] E. Schaltz, A. Khaligh, P.O. Rasmussen, Influence of Battery/Ultracapacitor Energy-Storage Sizing on Battery Lifetime in a Fuel Cell Hybrid Electric Vehicle, IEEE Trans. Veh. Technol. 58 (2009) 3882–3891. doi:10.1109/TVT.2009.2027909.

[248] T. Barlow, S. Latham, I. Mccrae, P. Boulter, A reference book of driving cycles for use in the measurement of road vehicle emissions, (2009) 280. http://www.trl.co.uk/online_store/reports_publications/trl_reports/cat_traffic_and_the_environment/report_a_reference_book_of_driving_cycles_for_use_in_the_measurement_of_road_vehicle_emissions.htm\nhttps://www.gov.uk/government/uploads/system/uploads/att.

[249] EPA, EPA Dynamometer Drive Cycles, (2008). http://www3.epa.gov/nvfel/testing/dynamometer.htm (accessed February 18, 2016).

[250] M. Ehsani, Y. Gao, J.M. Miller, Hybrid Electric Vehicles: Architecture and Motor Drives, Proc. IEEE. 95 (2007) 719–728. doi:10.1109/JPROC.2007.892492.

[251] J.P. Zheng, T.R. Jow, M.S. Ding, Hybrid power sources for pulsed current applications, IEEE Trans. Aerosp. Electron. Syst. 37 (2001) 288–292. doi:10.1109/7.913688.

[252] G. Sikha, B.N. Popov, Performance optimization of a battery–capacitor hybrid system, J. Power Sources. 134 (2004) 130–138. doi:10.1016/j.jpowsour.2004.01.054.

[253] J. Miller, Trends in Vehicle Energy Storage Systems: Batteries and Ultracapacitors to Unite, in: 2008 IEEE Veh. Power Propuls. Conf., IEEE, 2008: pp. 1–9. doi:10.1109/VPPC.2008.4685980.

[254] L. Gao, R.A. Dougal, S. Liu, Power Enhancement of an Actively Controlled Battery/Ultracapacitor Hybrid, IEEE Trans. Power Electron. 20 (2005) 236–243. doi:10.1109/TPEL.2004.839784.

[255] A.M. van Voorden, L.M.R. Elizondo, G.C. Paap, J. Verboomen, L. van der Sluis, The Application of Super Capacitors to relieve Battery-storage systems in Autonomous Renewable Energy Systems, in: 2007 IEEE Lausanne Power Tech, IEEE, 2007: pp. 479–484. doi:10.1109/PCT.2007.4538364.

[256] S. Lu, K.A. Corzine, M. Ferdowsi, A New Battery/Ultracapacitor Energy Storage System Design and Its Motor Drive Integration for Hybrid Electric Vehicles, IEEE Trans. Veh. Technol. 56 (2007) 1516–1523. doi:10.1109/TVT.2007.896971.

[257] M.B. Camara, H. Gualous, F. Gustin, A. Berthon, B. Dakyo, DC/DC Converter Design for Supercapacitor and Battery Power Management in Hybrid Vehicle Applications—Polynomial Control Strategy, IEEE Trans. Ind. Electron. 57 (2010) 587–597. doi:10.1109/TIE.2009.2025283.

[258] A. Mirzaei, A. Jusoh, Z. Salam, E. Adib, H. Farzanehfard, Analysis and design of a high efficiency bidirectional DC–DC converter for battery and ultracapacitor applications, Simul. Model. Pract. Theory. 19 (2011) 1651–1667. doi:10.1016/j.simpat.2011.04.007.

[259] E. Adib, H. Farzanehfard, Soft switching bidirectional DC–DC converter for ultracapacitor–batteries interface, Energy Convers. Manag. 50 (2009) 2879–2884. doi:10.1016/j.enconman.2009.07.001.

[260] A. Emadi, A New Battery/UltraCapacitor Hybrid Energy Storage System for Electric, Hybrid, and Plug-In Hybrid Electric Vehicles, IEEE Trans. Power Electron. 27 (2012) 122–132. doi:10.1109/TPEL.2011.2151206.

[261] A. Emadi, A New Battery/UltraCapacitor Hybrid Energy Storage System for Electric, Hybrid, and Plug-In Hybrid Electric Vehicles, IEEE Trans. Power Electron. 27 (2012) 122–132. doi:10.1109/TPEL.2011.2151206.

[262] A. Kuperman, I. Aharon, Battery–ultracapacitor hybrids for pulsed current loads: A review, Renew. Sustain. Energy Rev. 15 (2011) 981–992. doi:10.1016/j.rser.2010.11.010.

[263] J. Miller, G. Sartorelli, Battery and ultracapacitor combinations—Where should the converter go?, Veh. Power Propuls. …. (2010). http://ieeexplore.ieee.org/xpls/abs_all.jsp?arnumber=5729216 (accessed December 4, 2013).

[264] R. Carter, A. Cruden, Strategies for control of a battery/supercapacitor system in an electric vehicle, in: 2008 Int. Symp. Power Electron. Electr. Drives, Autom. Motion, IEEE, 2008: pp. 727–732. doi:10.1109/SPEEDHAM.2008.4581315.

[265] A. Kuperman, I. Aharon, A. Kara, S. Malki, A frequency domain approach to analyzing passive battery–ultracapacitor hybrids supplying periodic pulsed current loads, Energy Convers. Manag. 52 (2011) 3433–3438. doi:10.1016/j.enconman.2011.07.013.

[266] S. Underwood, Design DC-DC Converters with Reliability in Mind, PowerElectronics.com. (2002).

[267] M.M. B. Eckardt, A. Hofmann, S. Zeltner, Automotive Powertrain DC/DC Converter with 25kW/dm^3 by using SiC Diodes, Erlangen, 2008.

[268] Johnson Controls lithium-ion batteries power hybrid luxury SUVs, (n.d.). http://www.jsonline.com/blogs/business/286225371.html (accessed February 18, 2016).

[269] Saft - Mercedes Batteries Contract, (n.d.). http://news.thomasnet.com/companystory/saft-mercedes-batteries-contract-531224 (accessed February 18, 2016).

[270] Johnson Controls-Saft Announces BMW Li-ion Battery Contract, (n.d.). http://www.sustainablebusiness.com/index.cfm/go/news.display/id/16942 (accessed February 18, 2016).

[271] L. Rao, J. Newman, Heat-Generation Rate and General Energy Balance for Insertion Battery Systems, J. Electrochem. Soc. 144 (1997) 2697. doi:10.1149/1.1837884.

[272] A. Burke, M. Miller, The power capability of ultracapacitors and lithium batteries for electric and hybrid vehicle applications, J. Power Sources. 196 (2011) 514–522. doi:10.1016/j.jpowsour.2010.06.092.

[273] Maxwell Technologies, BC Series Ultracapacitors Datasheet, (2014) 5. http://www.maxwell.com/images/documents/bcseries_ds_1017105-4.pdf (accessed July 13, 2015).

[274] M. Lord, Market Acceptance of xEVs in Europe , the U.S, and Japan, in: Adv. Automot. Batter. Conf. 2015, Advanced Automotive Battery Conference 2015, Mainz, 2015: pp. 1–44.

[275] N. Omar, M.A. Monem, Y. Firouz, J. Salminen, J. Smekens, O. Hegazy, H. Gaulous, G. Mulder, P. Van den Bossche, T. Coosemans, J. Van Mierlo, Lithium iron phosphate based battery – Assessment of the aging parameters and development of cycle life model, Appl. Energy. 113 (2014) 1575–1585. doi:10.1016/j.apenergy.2013.09.003.

Appendix

A1 – Battery Heat Transfer Area Calculation

A simple Matlab script was used to define the parameters for the heat transfer model. The script is shown below.

```
%% Calculate Thermal Model Parameters

%% Properties Setup

% Material Properties
Anode_thickness=75e-6; %m
Cathode_thickness = 55e-6; %m
Separator_thickness = 40e-6; %m
Cu_CC_Thickness = 12e-6; %m
Al_CC_Thickness = 18e-6; %m
Cathode_Density = 3238; %kg m^-3 - [213]
Anode_Density = 700; %kg m^-3 - [213]
Separator_Density= 1009; %kg m^-3 - [213]
Al_Density = 2770; %kg m^-3
Cu_Density = 8933; %kg m^-3
Cu_Conductivity = 398; %W m^-1K^-1
Al_Conductivity = 220; %W m^-1K^-1
EandS_Conductivity=0.8; %W m^-1K^-1 - anode 1.04, LFP 0.2, Sep 0.33
E_S_Heat_Capacity= 1403; % J kg^-1 K^-1, LFP 750, Anode 1440 Sep 1978
Al_Heat_Capacity = 875; % J kg^-1 K^-1
Cu_Heat_Capacity = 385; % J kg^-1 K^-1
Pigtail_width= 2e-3; %m
Negative_pigtail_length = 25e-3; %m
Positive_pigtail_length = 52e-3; %m
Pigtail_thickness=1e-3; %m
Neg_Terminal_Thickness = 2e-3; %m
Can_diameter = 18e-3; %m
Can_Mass=4.2e-3; %m
Can_length=60e-3; %m
Can_thickness=0.3e-3; %m
Can_OD = 18e-3; %m
Can_ID = Can_OD - Can_thickness; % Inner diameter
Can_Insualtion_Mass=1e-3; %kg
Insulation_Heat_Capacity = 1015; % J kg^-1 K^-1 - Assumed PP
Insulation_Conductivity=0.7; %W m^-1K^-1

% Axial Discretisation
Ax_N=5;

%Mass of Cell - Measured
M_cell= 45e-3; %kg
% Mass of non-jelly roll - Measured
M_case=7e-3; %kg
M_tab_cathode=0.18e-3; %kg
M_tab_anode=M_tab_cathode*0.66;
% Mass of jelly roll
M_JR=M_cell-M_case-M_tab_cathode-M_tab_anode;

% Diameter of hole at middle of cell
D_in=2e-3; %m,  Measured
D_out=18e-3 - Can_thickness; %Measured OD subtract can_thick

% length of sep
Length=0.696; %m
Width = 0.06; %m

%% Calculate lengths around spiral

% Estimate number of turns of spiral
z_rad = (D_out - D_in)/2;
% Anode-Cu CC-Anode-Sep-Cathode-Al CC-Cathode-Sep
Single_Layer_Thickness = Anode_thickness + Cu_CC_Thickness + Anode_thickness + Separator_thickness +
Cathode_thickness + Al_CC_Thickness + Cathode_thickness + Separator_thickness;

% Number of Layers - For calculation validation
Layer_N=z_rad/Single_Layer_Thickness;

% Diameter of First Layer
L_1_thick = D_in + ((Anode_thickness + Cu_CC_Thickness + Anode_thickness)*2);
```

```
% Inner - First third of spiral, need length of spiral

for i = 1:21
Length_i = (L_1_thick + (Single_Layer_Thickness*2*(i-1)))*pi;
end

Total_Core_Length=Length_1+Length_2+Length_3+Length_4+Length_5+Length_6+Length_7;


Total_Mid_Length=Length_8+Length_9+Length_10+Length_11+Length_12+Length_13+Length_14;

Total_Outer_Length=Length_15+Length_16+Length_17+Length_18+Length_19+Length_20+Length_21;

Total_Length=Total_Outer_Length+Total_Mid_Length+Total_Core_Length; % For calculation validation

%% Thermal Mass of Electrode and Sep


% Length * Width * Material thickness * 2 * density

Core_Mass_EandS = (Total_Core_Length * Width * ((Anode_thickness)*2) * Anode_Density)+...
    (Total_Core_Length * Width * ((Cathode_thickness)*2) * Cathode_Density)+...
    (Total_Core_Length * Width * ((Separator_thickness)*2) * Separator_Density);

Mid_Mass_EandS = (Total_Mid_Length * Width * ((Anode_thickness)*2) * Anode_Density)+...
    (Total_Mid_Length * Width * ((Cathode_thickness)*2) * Cathode_Density)+...
    (Total_Mid_Length * Width * ((Separator_thickness)*2) * Separator_Density);

Outer_Mass_EandS = (Total_Outer_Length * Width * ((Anode_thickness)*2) * Anode_Density)+...
    (Total_Outer_Length * Width * ((Cathode_thickness)*2) * Cathode_Density)+...
    (Total_Outer_Length * Width * ((Separator_thickness)*2) * Separator_Density);

Cal_EandS_Mass = Core_Mass_EandS + Mid_Mass_EandS + Outer_Mass_EandS;

%% Thermal mass of CC's

Core_Mass_Al_CC = (Total_Core_Length * Width * ((Al_CC_Thickness)*2) * Al_Density);
Core_Mass_Cu_CC = (Total_Core_Length * Width * ((Cu_CC_Thickness)*2) * Cu_Density);

Mid_Mass_Al_CC = (Total_Mid_Length * Width * ((Al_CC_Thickness)*2) * Al_Density);
Mid_Mass_Cu_CC = (Total_Mid_Length * Width * ((Cu_CC_Thickness)*2) * Cu_Density);

Outer_Mass_Al_CC = (Total_Outer_Length * Width * ((Al_CC_Thickness)*2) * Al_Density);
Outer_Mass_Cu_CC = (Total_Outer_Length * Width * ((Cu_CC_Thickness)*2) * Cu_Density);

CC_Mass = Core_Mass_Al_CC+Core_Mass_Cu_CC+Mid_Mass_Al_CC+Mid_Mass_Cu_CC+...
    Outer_Mass_Al_CC+Outer_Mass_Cu_CC;

Calc_JR_Mass = Cal_EandS_Mass + CC_Mass;

%% Heat transfer area - axial electrode and separator

% Cross sectional area of Core
Core_area = pi * ((((D_out-D_in)/3)+ D_in)^2 - (D_in)^2) * 0.25;
% Cross sectional area of CC
CC_Core_CSA=Total_Core_Length * (Al_CC_Thickness + Cu_CC_Thickness);
Cu_Core_CSA=Total_Core_Length * (Cu_CC_Thickness);
Al_Core_CSA=Total_Core_Length * (Al_CC_Thickness);

% Cross sectional area of core - area of CC's
Core_EandS_CSA = Core_area - CC_Core_CSA;

% Cross sectional area of Core
Mid_area = pi * ((2*((D_out-D_in)/3)+ D_in)^2 - ((((D_out-D_in)/3)+ D_in)^2)) * 0.25;

% Cross sectional area of CC
CC_Mid_CSA=Total_Mid_Length * (Al_CC_Thickness + Cu_CC_Thickness);
Cu_Mid_CSA=Total_Mid_Length * (Cu_CC_Thickness);
Al_Mid_CSA=Total_Mid_Length * (Al_CC_Thickness);

% Cross sectional area of core - area of CC's
Mid_EandS_CSA = Mid_area - CC_Mid_CSA;

% Cross sectional area of Core
Outer_area = pi * (((D_out)^2 - ((2*((D_out-D_in)/3)+ D_in)^2))) * 0.25;

% Cross sectional area of CC
CC_Outer_CSA=Total_Outer_Length * (Al_CC_Thickness + Cu_CC_Thickness);
Cu_Outer_CSA=Total_Outer_Length * (Cu_CC_Thickness);
Al_Outer_CSA=Total_Outer_Length * (Al_CC_Thickness);
```

```
% Cross sectional area of core - area of CC's
Outer_EandS_CSA = Outer_area - CC_Outer_CSA;

% Heat Transfer area between anode and Cu CC

% double sided hence *2
Anode_CC_Area_Core=Total_Core_Length*Width*2;
Cathode_CC_Area_Core=Total_Core_Length*Width*2;

Anode_CC_Area_Mid=Total_Mid_Length*Width*2;
Cathode_CC_Area_Mid=Total_Mid_Length*Width*2;

Anode_CC_Area_Outer=Total_Outer_Length*Width*2;
Cathode_CC_Area_Outer=Total_Outer_Length*Width*2;

%% Radial HT

% Heat transfer area CC Core to mid
Cu_Radial_Area=Width * Cu_CC_Thickness;
Al_Radial_Area=Width * Al_CC_Thickness;

%% Pigtails & Can

% CC - Pigtail - width * length

Pigtail_HT_Area= Pigtail_width*Pigtail_thickness;

%Mass = density * volume
Neg_terminal_mass = Al_Density * (pi*((Can_diameter^2)*0.25)*Neg_Terminal_Thickness);
Pos_terminal_mass=Neg_terminal_mass;

Can_axial_HT_Area = pi * ((Can_OD^2)-(Can_ID^2))*0.25;

Cu_CC_Pigtail_Area = Pigtail_width * Negative_pigtail_length;
Al_CC_Pigtail_Area = Pigtail_width * Positive_pigtail_length;

%% convection Area & Conduction to terminals

Case_Area=(pi*Can_OD)* (Can_length/3);

Term_conduction = (10e-3 * Pigtail_width); %m^2 Pigtail contact area with brass blocks
Term_conduction_pos = (5e-3 * Pigtail_width); % Different to neg as difficult to balance contact
areas  without touching tab weld during experiment - pos has less contact area

%% Diameters

D_Core  = Length_7/pi;
D_Mid   = Length_14/pi;
D_Outer = Length_21/pi;

%% Radial Heat Transfer

Core_Mid_HT=(Length_7 * Width / 5); % Perimieter * Width / Discretisation
Mid_Outer_HT=(Length_14 * Width / 5);
Mid_thick = D_Mid-D_Core;
Outer_thick= D_Outer - D_Mid;
Eq_conductivity = ((190/220)*EandS_Conductivity) + ((12/220)*Cu_Conductivity) +
((18/220)*Al_Conductivity);

% Anode to can
Neg_to_can_HT_Area = (Length_21 * (Width - 24e-3) / 3) - (5e-3*12e-3); % (Exposed Area /
discretisation) - pigtail kapton tape area
```

A2 – Battery Model Electrical Parameters

$SoC/_{Current}$	-15A	-12A	-9A	-3A	-15mA	15mA	3A	6A
0.0	164.8	164.8	157.1	93.3	93.3	171.3	171.3	318.7
0.1	102.1	1000.0	1015.4	1210.1	1210.1	4277.7	4277.7	4946.7
0.2	4952.1	9567.6	9234.1	8048.3	8048.3	3243.6	3243.6	3206.9

0.3	7945.9	5869.9	4332.4	4790.5	4790.5	2719.0	2719.0	1832.5
0.4	7928.0	4562.8	8757.9	9999.4	9999.4	2526.3	2526.3	5087.3
0.5	8290.3	8054.4	4988.4	3590.6	3590.6	7685.2	7685.2	3930.0
0.6	3877.8	4608.3	4762.2	3369.9	3369.9	7749.3	7749.3	4459.7
0.7	4351.0	2951.6	2951.6	4916.4	4916.4	5994.6	5994.6	6932.8
0.8	4918.3	4559.7	4559.7	3110.5	3110.5	4718.0	4718.0	4731.6
0.9	5009.8	5459.4	5013.2	4774.6	4774.6	2919.8	2919.8	2919.8
1.0	1293.1	1953.9	3050.9	4527.7	4527.7	3096.9	3096.9	3096.9

Table 29: Battery Model Electrical Parameters - Capacitor C1 (F), 40℃

$SoC/_{Current}$	-15A	-12A	-9A	-3A	-15mA	15mA	3A	6A
0.0	1947.6	1947.6	1982.7	2036.1	2036.1	21777.8	21777.8	52409.6
0.1	4513.2	5744.8	9224.2	8889.1	8889.1	23364.8	23364.8	32034.4
0.2	22832.6	96860.5	66450.5	68165.8	68165.8	29695.2	29695.2	10233.4
0.3	94862.7	36629.9	38169.0	19784.2	19784.2	78293.3	78293.3	46740.2
0.4	77288.7	50580.1	70270.1	56595.3	56595.3	66608.1	66608.1	41587.0
0.5	34554.0	72774.6	83268.8	78329.0	78329.0	27352.7	27352.7	20614.7
0.6	93493.4	70954.4	75810.8	30389.6	30389.6	70953.7	70953.7	84347.8
0.7	36302.8	72932.9	72932.9	57801.9	57801.9	75137.3	75137.3	95754.6
0.8	12904.4	13924.2	13924.2	23710.4	23710.4	100000.0	100000.0	99870.5
0.9	68237.1	63910.1	61120.8	60844.0	60844.0	60530.9	60530.9	60530.9
1.0	77762.1	76933.5	73581.5	92025.3	92025.3	71249.5	71249.5	71249.5

Table 30: Battery Model Electrical Parameters - Capacitor C2 (F), 40℃

$SoC/_{Current}$	-15A	-12A	-9A	-3A	-15mA	15mA	3A	6A
0.0	68.1	68.1	63.9	64.7	64.7	624.6	624.6	729.3
0.1	50.1	583.6	4548.7	4529.7	4529.7	185.9	185.9	710.0
0.2	1564.4	579.6	106.4	86.5	86.5	80.4	80.4	95.0
0.3	2680.0	792.7	364.8	197.9	197.9	250.1	250.1	162.7
0.4	1341.4	1248.2	3407.0	3745.2	3745.2	1261.0	1261.0	1535.9
0.5	1057.0	1575.7	1110.9	1026.0	1026.0	3054.1	3054.1	3000.5
0.6	518.5	771.5	77.3	167.8	167.8	75.0	75.0	74.0
0.7	442.7	101.1	101.1	93.8	93.8	163.4	163.4	349.3
0.8	899.0	826.2	826.2	791.1	791.1	476.8	476.8	566.4
0.9	704.3	727.3	710.1	626.7	626.7	3089.0	3089.0	450.0
1.0	2474.2	2815.9	3712.4	3975.8	3975.8	4548.4	4548.4	600.0

Table 31: Battery Model Electrical Parameters - Capacitor C3 (F), 40℃

$SoC/_{Current}$	-15A	-12A	-9A	-3A	-15mA	15mA	3A	6A
0.0	164.8	100.0	100.0	100.0	100.0	106.0	106.0	124.9
0.1	101.1	7330.6	7332.0	7332.0	7332.0	5090.7	5090.7	2249.9
0.2	1865.8	9545.9	7059.5	3118.7	3118.7	3707.5	3707.5	2552.6
0.3	9727.7	9915.7	5291.2	2103.3	2103.3	2340.4	2340.4	2041.9
0.4	7149.8	6875.1	6856.8	4192.5	4192.5	3363.0	3363.0	2587.9

0.5	3684.6	1766.9	3886.3	5426.9	5426.9	8227.3	8227.3	6567.3
0.6	7373.6	2892.1	2416.4	2258.1	2258.1	45375.6	45375.6	4133.0
0.7	2764.9	2166.6	3051.5	2849.3	2849.3	2398.5	2398.5	3741.1
0.8	8646.2	2834.9	2326.0	2418.4	2418.4	3333.7	3333.7	5616.5
0.9	5822.1	6048.4	4520.8	1411.0	1411.0	5470.2	5470.2	5470.2
1.0	1237.7	5247.7	3542.2	8617.3	8617.3	3677.0	3677.0	3677.0

Table 32: Battery Model Electrical Parameters - Capacitor C1 (F), 25℃

$SoC/Current$	-15A	-12A	-9A	-3A	-15mA	15mA	3A	6A
0.0	1947.6	4000.0	4000.0	4000.0	4000.0	359947.0	359947.0	41427.6
0.1	65000.0	6044.0	6049.8	6049.8	6049.8	10456.6	10456.6	13827.3
0.2	55257.6	32643.4	35409.5	30029.4	30029.4	36792.3	36792.3	17117.6
0.3	12026.9	19803.8	23725.8	37429.3	37429.3	35728.3	35728.3	31911.7
0.4	76577.4	65658.3	24155.8	37607.2	37607.2	37706.8	37706.8	32857.7
0.5	59436.6	71994.7	67359.0	48272.9	48272.9	30700.0	30700.0	20095.8
0.6	62208.4	61977.7	64967.0	60772.5	60772.5	62862.9	62862.9	68704.3
0.7	38302.5	28535.4	15088.6	20002.2	20002.2	52046.4	52046.4	42116.4
0.8	11170.3	18796.1	38987.9	27274.5	27274.5	35882.8	35882.8	40401.7
0.9	56570.6	61539.4	59983.7	42434.2	42434.2	35457.7	35457.7	35457.7
1.0	71927.0	36561.3	39906.7	62568.1	62568.1	39992.9	39992.9	39992.9

Table 33: Battery Model Electrical Parameters - Capacitor C2 (F), 25℃

$SoC/Current$	-15A	-12A	-9A	-3A	-15mA	15mA	3A	6A
0.0	68.1	100.0	100.0	100.0	100.0	566.1	566.1	652.2
0.1	50.5	366.1	356.3	356.3	356.3	207.1	207.1	325.3
0.2	56.8	147.5	141.7	220.7	220.7	76.7	76.7	42.8
0.3	2403.4	1725.2	758.9	174.3	174.3	137.0	137.0	208.3
0.4	1005.1	1184.0	3822.3	3294.6	3294.6	2782.9	2782.9	2408.2
0.5	1842.1	1900.4	1668.9	1631.0	1631.0	2762.0	2762.0	2189.2
0.6	1590.4	528.0	136.2	84.1	84.1	96.7	96.7	106.1
0.7	1169.2	744.9	740.7	127.0	127.0	136.0	136.0	161.7
0.8	1392.0	2603.3	3985.2	482.2	482.2	430.9	430.9	403.4
0.9	1520.1	1146.5	737.5	18.6	18.6	18.8	18.8	18.8
1.0	2111.1	988.3	76.9	11.9	11.9	21.3	21.3	21.3

Table 34: Battery Model Electrical Parameters - Capacitor C3 (F), 25℃

$SoC/_{Current}$	-15A	-12A	-9A	-3A	-15mA	15mA	3A	6A
0.0	3.08E-01	3.08E-01	1.85E-01	1.85E-01	1.85E-01	7.42E-02	7.42E-02	4.96E-02
0.1	3.95E-02	5.77E-02	6.54E-02	6.45E-02	6.45E-02	5.04E-02	5.04E-02	4.14E-02
0.2	5.31E-02	4.20E-02	3.56E-02	4.19E-02	4.19E-02	2.73E-02	2.73E-02	2.95E-02
0.3	3.72E-02	3.52E-02	3.14E-02	3.22E-02	3.22E-02	2.64E-02	2.64E-02	2.92E-02
0.4	3.46E-02	3.46E-02	3.69E-02	3.85E-02	3.85E-02	4.46E-02	4.46E-02	3.62E-02
0.5	3.39E-02	3.43E-02	3.36E-02	4.67E-02	4.67E-02	4.47E-02	4.47E-02	3.69E-02
0.6	3.57E-02	3.26E-02	2.57E-02	2.91E-02	2.91E-02	2.62E-02	2.62E-02	2.74E-02
0.7	2.95E-02	2.82E-02	2.82E-02	2.36E-02	2.36E-02	2.15E-02	2.15E-02	2.97E-02
0.8	3.47E-02	3.47E-02	3.47E-02	3.71E-02	3.71E-02	3.93E-02	3.93E-02	3.70E-02
0.9	3.47E-02	3.18E-02	3.46E-02	3.41E-02	3.41E-02	1.44E-02	1.44E-02	1.44E-02
1.0	3.72E-02	3.85E-02	3.88E-02	3.89E-02	3.89E-02	8.25E-03	8.25E-03	8.25E-03

Table 35: Battery Model Electrical Parameters - Resistor R0 (Ω), 40℃

$SoC/_{Current}$	-15A	-12A	-9A	-3A	-15mA	15mA	3A	6A
0.0	1.38E-01	1.60E-01	1.93E-01	4.34E-01	4.34E-01	1.29E-02	1.29E-02	9.31E-03
0.1	1.46E-02	6.15E-02	7.28E-02	9.05E-03	9.05E-03	1.40E-02	1.40E-02	1.12E-02
0.2	1.42E-02	2.88E-02	7.41E-03	7.58E-03	7.58E-03	5.80E-03	5.80E-03	5.21E-03
0.3	1.15E-03	1.32E-03	1.41E-02	1.88E-02	1.88E-02	1.39E-02	1.39E-02	8.60E-03
0.4	2.31E-03	1.01E-03	2.61E-02	6.32E-02	6.32E-02	1.23E-02	1.23E-02	7.77E-03
0.5	3.88E-03	6.07E-03	4.75E-04	9.92E-04	9.92E-04	9.53E-03	9.53E-03	5.36E-03
0.6	7.06E-03	8.27E-03	4.82E-03	2.45E-03	2.45E-03	6.60E-03	6.60E-03	6.46E-03
0.7	7.02E-03	9.27E-03	9.27E-03	1.18E-02	1.18E-02	4.22E-03	4.22E-03	1.38E-02
0.8	1.11E-02	9.86E-03	9.86E-03	1.24E-02	1.24E-02	1.07E-02	1.07E-02	3.49E-03
0.9	6.85E-03	7.34E-03	8.07E-03	7.50E-03	7.50E-03	3.12E-02	3.12E-02	3.12E-02
1.0	3.29E-03	3.52E-03	3.09E-03	3.08E-03	3.08E-03	8.55E-03	8.55E-03	8.55E-03

Table 36: Battery Model Electrical Parameters - Resistor R1 (Ω), 40℃

$SoC/_{Current}$	-15A	-12A	-9A	-3A	-15mA	15mA	3A	6A
0.0	2.71E-01	2.71E-01	9.31E-03	1.92E-02	1.92E-02	1.66E-02	1.66E-02	2.00E-03
0.1	1.03E-03	2.59E-03	6.70E-03	3.64E-03	3.64E-03	1.78E-01	1.78E-01	6.34E-03
0.2	4.76E-01	1.19E-01	5.60E-02	4.20E-02	4.20E-02	2.28E-02	2.28E-02	1.22E-02
0.3	1.35E-02	1.74E-02	1.33E-02	1.20E-02	1.20E-02	7.56E-03	7.56E-03	1.82E-03
0.4	3.38E-03	5.55E-03	7.44E-03	2.61E-01	2.61E-01	2.61E-02	2.61E-02	8.70E-03
0.5	3.55E-03	1.58E-03	2.69E-03	1.00E-03	1.00E-03	6.21E-02	6.21E-02	3.50E-02
0.6	2.34E-02	2.38E-02	8.16E-02	2.29E-01	2.29E-01	2.97E-03	2.97E-03	7.06E-03
0.7	1.63E-02	2.22E-02	2.22E-02	4.32E-02	4.32E-02	3.16E-03	3.16E-03	5.45E-02
0.8	7.98E-04	8.64E-04	8.64E-04	6.35E-04	6.35E-04	1.50E-02	1.50E-02	7.63E-02
0.9	1.07E-03	1.12E-03	1.01E-03	1.00E-03	1.00E-03	4.24E-02	4.24E-02	4.24E-02
1.0	3.80E-01	4.64E-01	4.66E-01	5.20E-01	5.20E-01	6.23E-01	6.23E-01	6.23E-01

Table 37: Battery Model Electrical Parameters - Resistor R2 (Ω), 40℃

$SoC/_{Current}$	-15A	-12A	-9A	-3A	-15mA	15mA	3A	6A
0.0	1.35E-02	1.35E-02	3.82E-03	2.48E-03	2.48E-03	2.98E-03	2.98E-03	2.03E-03
0.1	4.93E-02	1.40E-02	7.99E-03	6.69E-03	6.69E-03	1.52E-02	1.52E-02	1.11E-02
0.2	6.37E-03	1.01E-02	1.50E-02	1.79E-02	1.79E-02	2.06E-02	2.06E-02	1.08E-02
0.3	4.57E-03	8.21E-03	9.95E-03	1.02E-02	1.02E-02	7.66E-03	7.66E-03	7.56E-03
0.4	5.11E-03	6.93E-03	7.49E-03	9.84E-03	9.84E-03	7.74E-03	7.74E-03	4.44E-03
0.5	6.86E-03	7.77E-03	9.95E-03	1.22E-02	1.22E-02	1.47E-02	1.47E-02	6.90E-03
0.6	1.16E-03	4.80E-03	1.06E-02	1.47E-02	1.47E-02	1.25E-02	1.25E-02	1.02E-02
0.7	8.07E-03	1.02E-02	1.02E-02	2.25E-02	2.25E-02	1.65E-02	1.65E-02	1.31E-02
0.8	4.80E-03	4.83E-03	4.83E-03	5.94E-03	5.94E-03	6.51E-03	6.51E-03	1.10E-02
0.9	5.80E-03	5.79E-03	6.37E-03	8.79E-03	8.79E-03	2.20E-02	2.20E-02	2.20E-02
1.0	5.64E-03	5.66E-03	5.96E-03	6.69E-03	6.69E-03	2.00E-02	2.00E-02	2.00E-02

Table 38: Battery Model Electrical Parameters - Resistor R3 (Ω), 40℃

$SoC/_{Current}$	-15A	-12A	-9A	-3A	-15mA	15mA	3A	6A
0.0	3.08E-01	1.00E+00	1.00E+00	1.00E+00	1.00E+00	8.74E-02	8.74E-02	6.92E-02
0.1	1.03E-01	2.33E-01	2.34E-01	2.34E-01	2.34E-01	5.77E-02	5.77E-02	5.20E-02
0.2	4.91E-02	5.71E-02	5.38E-02	7.68E-02	7.68E-02	3.42E-02	3.42E-02	3.68E-02
0.3	4.75E-02	5.07E-02	4.94E-02	4.74E-02	4.74E-02	3.74E-02	3.74E-02	3.86E-02
0.4	4.39E-02	4.50E-02	5.04E-02	5.12E-02	5.12E-02	4.60E-02	4.60E-02	4.35E-02
0.5	4.32E-02	4.32E-02	4.43E-02	4.72E-02	4.72E-02	3.82E-02	3.82E-02	4.56E-02
0.6	4.36E-02	4.32E-02	3.99E-02	3.70E-02	3.70E-02	2.55E-02	2.55E-02	3.42E-02
0.7	4.32E-02	4.33E-02	4.41E-02	3.65E-02	3.65E-02	1.72E-02	1.72E-02	2.94E-02
0.8	4.42E-02	4.56E-02	4.66E-02	5.02E-02	5.02E-02	4.91E-02	4.91E-02	4.62E-02
0.9	4.57E-02	4.59E-02	4.59E-02	1.82E-02	1.82E-02	1.86E-02	1.86E-02	1.86E-02
1.0	4.75E-02	4.86E-02	4.11E-02	2.92E-02	2.92E-02	2.78E-02	2.78E-02	2.78E-02

Table 39: Battery Model Electrical Parameters - Resistor R0 (Ω), 25℃

$SoC/_{Current}$	-15A	-12A	-9A	-3A	-15mA	15mA	3A	6A
0.0	1.35E-02	2.50E-01	2.50E-01	2.50E-01	2.50E-01	1.44E-02	1.44E-02	1.20E-02
0.1	4.01E-02	1.89E-03	1.24E-02	1.24E-02	1.24E-02	1.66E-02	1.66E-02	1.90E-02
0.2	5.23E-03	9.45E-03	1.40E-02	4.73E-03	4.73E-03	5.76E-03	5.76E-03	6.94E-03
0.3	1.18E-03	6.66E-02	1.04E-02	2.55E-02	2.55E-02	1.26E-02	1.26E-02	1.06E-02
0.4	6.57E-03	9.43E-03	1.99E-02	9.43E-03	9.43E-03	7.80E-03	7.80E-03	6.08E-03
0.5	7.84E-03	2.06E-03	6.11E-03	1.19E-03	1.19E-03	1.42E-03	1.42E-03	1.32E-03
0.6	1.07E-02	8.93E-03	7.76E-03	8.35E-03	8.35E-03	1.05E-02	1.05E-02	9.81E-03
0.7	6.70E-03	1.90E-02	1.29E-02	1.58E-02	1.58E-02	2.50E-02	2.50E-02	1.23E-02
0.8	1.23E-02	8.76E-03	1.21E-02	1.85E-02	1.85E-02	2.18E-02	2.18E-02	1.57E-02
0.9	1.32E-02	1.27E-02	7.60E-03	2.02E-02	2.02E-02	3.08E-02	3.08E-02	3.08E-02
1.0	1.10E-02	1.44E-02	1.81E-02	2.08E-02	2.08E-02	1.82E-02	1.82E-02	1.82E-02

Table 40: Battery Model Electrical Parameters - Resistor R1 (Ω), 25℃

$SoC/Current$	-15A	-12A	-9A	-3A	-15mA	15mA	3A	6A
0.0	2.71E-01	3.79E-02	3.79E-02	3.79E-02	3.79E-02	9.74E-03	9.74E-03	6.51E-03
0.1	5.00E-04	3.49E-01	5.03E-02	5.03E-02	5.03E-02	3.88E-02	3.88E-02	2.12E-02
0.2	1.37E-01	1.11E-01	3.23E-01	3.98E-01	3.98E-01	1.41E-02	1.41E-02	1.59E-02
0.3	1.51E-01	1.23E-01	5.55E-02	7.87E-02	7.87E-02	5.90E-03	5.90E-03	4.87E-03
0.4	1.99E-02	3.08E-02	5.12E-02	3.55E-02	3.55E-02	1.16E-02	1.16E-02	1.45E-02
0.5	1.32E-02	1.64E-02	2.31E-02	2.36E-02	2.36E-02	4.43E-02	4.43E-02	4.94E-02
0.6	5.30E-02	4.53E-02	3.06E-02	4.61E-02	4.61E-02	3.11E-02	3.11E-02	2.76E-02
0.7	2.40E-02	3.27E-02	6.56E-02	4.51E-02	4.51E-02	2.77E-02	2.77E-02	1.36E-01
0.8	4.62E-04	2.58E-02	1.02E-03	1.02E-03	1.02E-03	1.03E-03	1.03E-03	8.14E-02
0.9	3.13E-03	2.97E-03	4.56E-03	1.12E-02	1.12E-02	1.45E-01	1.45E-01	1.45E-01
1.0	4.51E-01	3.04E-03	1.29E-03	4.95E-02	4.95E-02	2.42E-01	2.42E-01	2.42E-01

Table 41: Battery Model Electrical Parameters - Resistor R2 (Ω), 25℃

$SoC/Current$	-15A	-12A	-9A	-3A	-15mA	15mA	3A	6A
0.0	1.35E-02	1.35E-02	1.35E-02	1.35E-02	1.35E-02	4.50E-02	4.50E-02	2.35E-03
0.1	4.01E-02	8.45E-02	8.43E-02	8.43E-02	8.43E-02	3.30E-02	3.30E-02	1.06E-02
0.2	5.23E-03	3.01E-02	2.53E-02	1.64E-02	1.64E-02	2.65E-02	2.65E-02	1.59E-02
0.3	1.18E-03	2.23E-02	1.22E-02	1.38E-02	1.38E-02	1.06E-02	1.06E-02	7.60E-03
0.4	6.57E-03	1.06E-02	1.14E-02	1.49E-02	1.49E-02	1.12E-02	1.12E-02	7.92E-03
0.5	7.84E-03	1.19E-02	1.25E-02	1.82E-02	1.82E-02	2.03E-02	2.03E-02	1.46E-02
0.6	1.07E-02	3.71E-03	7.28E-03	1.79E-02	1.79E-02	3.42E-02	3.42E-02	1.38E-02
0.7	6.70E-03	5.12E-03	6.64E-03	2.24E-02	2.24E-02	3.32E-02	3.32E-02	1.59E-02
0.8	1.23E-02	6.69E-03	4.03E-03	7.13E-03	7.13E-03	9.85E-03	9.85E-03	6.15E-03
0.9	1.32E-02	1.04E-02	8.20E-03	2.78E-02	2.78E-02	4.49E-02	4.49E-02	4.49E-02
1.0	1.10E-02	9.29E-03	1.30E-02	4.34E-02	4.34E-02	7.75E-02	7.75E-02	7.75E-02

Table 42: Battery Model Electrical Parameters - Resistor R3 (Ω), 25℃